Scale-bridging micromagnetic evaluation of surface integrity and conditioning mechanisms in deep hole drilled AISI 4140 steel

Zur Erlangung des akademischen Grades eines
Dr.-Ing.
von der Fakultät Maschinenbau
der Technischen Universität Dortmund
genehmigte Dissertation

Simon Strodick, M.Sc.
aus
Salzkotten

Tag der mündlichen Prüfung: 10.06.2024
1. Gutachter: Prof. Dr.-Ing. habil. Frank Walther
2. Gutachter: Prof. Dr.-Ing. Prof. h.c. Dirk Biermann

Dortmund, 2024

Preface

Although the concept of surface integrity and its fundamental impact on component performance was first described by Field and Kahles sixty years ago, it has never received more attention than it does today, given the current challenges of increasing cost pressures, heightened quality requirements, and global warming. Targeted surface conditioning has been identified as a key strategy for improving the capability, reliability, and lifespan of components. In light of these developments, the Chair of Materials Test Engineering (WPT) at TU Dortmund University has recently established the department of “Process Control”, led by the author of this doctoral thesis, to acknowledge the growing importance of this field. The central objective of this research group is the holistic investigation of process-structure-property relationships in machining and forming processes. Building on a profound understanding of the governing mechanisms, the group explores ways to capitalize on targeted surface conditioning, allowing for simultaneous improvements in product quality, cost efficiency, and environmental sustainability.

Within this context, the present work focuses on targeted surface conditioning in BTA deep hole drilling of quenched and tempered AISI 4140. Since this process is typically used for machining components that are particularly costly and often employed in highly safety-critical applications, controlling surface integrity during BTA deep hole drilling is especially beneficial. However, the limited accessibility of the borehole wall presents a major obstacle, necessitating the use of sensors small enough to be implemented inside the bores. Under these conditions, this thesis presents a scale-bridging micromagnetic evaluation of surface integrity and conditioning mechanisms within borehole walls, using Magnetic Barkhausen Noise analysis. This non-destructive method is proposed for detecting and characterizing hard and brittle white etching layers. Given that this technique is sensitive to various aspects of surface integrity that may overlap and interfere, additional advanced approaches are employed to thoroughly characterize both the microstructure and the magnetic structure. To fully leverage the discovered correlations, a miniature sensor was developed in close collaboration with Stresstech, designed to be integrated into a geometrically adapted BTA drill head and used on the deep hole drilling machine. Additionally, a method is established for characterizing the capability of BTA deep drilled specimens under quasi-static and cyclic compression. The present work represents a significant advancement in the field of “Process Control” at the Chair of Materials Test Engineering and makes a valuable contribution to global research on targeted surface conditioning in machining.

Dortmund Frank Walther
November 2024

Foreword

This research was conducted between August 2018 and January 2024 as part of a project within the framework of the priority program SPP 2086 “Surface Conditioning in Machining Processes”, funded by the German Research Foundation (DFG). Besides acknowledging the DFG for its financial support, I want to express my deep gratitude to all the people who have contributed to this work. I would like to thank the following people in particular:

My doctoral supervisor, Prof. Dr.-Ing. habil. Frank Walther, for his profound confidence in me and the excellent professional and personal guidance throughout the entire process. His commitment and dedication were highly inspirational. Prof. Dr.-Ing. Prof. h.c. Dirk Biermann, for supporting my work as a second assessor. By employing me as a student assistant at the Institute of Machining Technology in 2015, he allowed me to gain initial experience in the academic working environment and obtain valuable insights into the fields of machining technology and measurement engineering. Prof. Priv.-Doz. Dr.-Ing. habil. Peter Starke and Jun.-Prof. Dr.-Ing. Peer Woizeschke, for their participation in my doctoral assessment and their interest in my work.

All of my colleagues at the Chair of Materials Test Engineering and the Institute of Machining Technology, for an ideal working environment, and innumerable inspiring discussions. My project partner, Dr.-Ing. Robert Schmidt, for performing the deep hole drilling experiments and providing me with the specimens and the in-process data. Dr.-Ing. Tom Jäpel of TESCAN, for carrying out transmission Kikuchi diffraction. My long-term office mate, Dr.-Ing. Nikolas Baak, for consistently offering highly-appreciated advice on both, professional and personal matters. My student assistants, Felix Hühn and Thomas Kröger, as well as my student workers throughout the years, for their valuable contributions to this work.

I am wholeheartedly grateful to my family, who have supported me from the very beginning in pursuing my academic career, and have paved the way for my success and growth. To my aunt Karin Müller, for reviewing the linguistic quality of this thesis. To my uncle Rudolf Weinstock, for his encouragement. To my mother Bettina, for always believing in me and shaping who I am today; to my brother David, for serving as a role model in many respects; and to my sister Lena, for being a constant source of support. My heartfelt thanks go to my partner Gesa, for her unconditional understanding and patience, for always having my back when push comes to shove, and for persistently looking after me.

Dortmund Simon Strodick
November 2024

Abstract

In the face of global warming, modern production engineering is confronted with the pressing challenge of developing methods for a more sustainable production. A key strategy in manufacturing with vast potential for climate change mitigation is to improve material and resource efficiency by enhancing the surface integrity of components through adapted manufacturing processes. As numerous surface and subsurface properties are closely linked to performance, tailoring surface integrity enables the production of components with significantly improved capability, reliability and lifetime. This general connection between the design of machining processes, the resulting surface integrity of components and their performance also applies to the field of deep hole drilling. A widely employed process for machining large diameter bores with high length-to-diameter ratios is Boring Trepanning Association (BTA) deep hole drilling. This process is commonly used in fields like aerospace engineering or petroleum industry to machine components, such as landing gears, drill collars, or hydraulic cylinders.

A major obstacle in assessing the surface integrity at the critical inner surface of deep drilled components is the hindered accessibility of the borehole wall, as it complicates or fully prevents the use of many conventional approaches, such as X-ray diffraction. In addition to this, some of the most common methods for assessing aspects of surface integrity like microhardness testing or optical microscopy of cross-sections are either fully-destructive or semi-destructive and thus their application is restricted to a limited amount of spot checks, while damaging the workpiece. In contrast, magnetic Barkhausen noise (MBN) analysis is an entirely nondestructive technique, based on relatively compact sensors that can be positioned inside of deep drilled boreholes. Consequently, this method is a particularly promising approach for a holistic evaluation of surface integrity in ferromagnetic deep drilled components. On this account, this thesis aims at qualifying MBN for the nondestructive, efficient, and reliable assessment of the surface integrity in deep drilled components. Since MBN is affected by multiple aspects of surface integrity which overlap and interfere, the mechanisms governing the MBN analysis need to be elucidated and separated. Therefore, in a first step, a thorough evaluation of surface integrity in BTA deep hole drilling is performed. This includes interconnected analyses of the microstructure, the microhardness gradients and the residual stress states in subsurfaces of deep drilled specimens. To analyze the impact of cutting parameters on surface integrity, the cutting speed and the feed in drilling are varied.

It is observed that white etching layers (WEL) form at the surface of bores, when using relatively high cutting speeds and feed rates. These WEL bring about a significant increase in hardness. For instance, it is found that the microhardness inside the WEL can exceed the microhardness of the bulk material by more than three times. To investigate further into the microstructural evolution in the subsurface during deep hole drilling, electron backscatter diffraction analyses are performed. The results indicate a strong refinement of the grains resulting from severe plastic deformation as well as swept grains in the material adjacent to the WEL. As the nanocrystalline structures observed are close to the limit of the lateral resolution in electron backscatter diffraction, transmission Kikuchi diffraction is carried out additionally to validate the findings obtained by electron backscatter diffraction. In addition to this, electron channeling contrast imaging and scanning transmission electron microscopy are used to evaluate grain size gradients, grain morphologies, voids, and lattice defects such as dislocation structures and stacking faults.

Building on these fundamental findings on surface integrity, scale-bridging micromagnetic approaches are combined in the next step, to identify interrelations between the different aspects of surface integrity and the micromagnetic properties. The evolution of the magnetic microstructures in external magnetic fields is evaluated by magneto-optic Kerr effect microscopy. In addition to this, magnetic domain structures are evaluated by the Bitter technique. Magnetic force microscopy is employed for an analysis of the magnetic microstructure with particularly high spatial resolution. Inside of white etching layers, no distinct magnetic domains are observed by any of the approaches. In specimens free of WEL, domain patterns are found, which expand to the very surface. These multi-instrumental investigations provide the scientific basis for the application of MBN. In MBN analysis, it is observed that WEL lead to significantly lower maximum MBN amplitudes, due to the inherent structure and properties of WEL. The high number of dislocations, stacking faults and grain boundaries inside the WEL, evidenced by the microstructural analyses, all act as pinning sites for domain wall motion. Based on these observations, it is assumed that the WEL barely contributes to the generation of Barkhausen noise in MBN analysis and that this results in the particularly low MBN amplitudes for specimens with WEL. Based on these findings, a multi-sensory MBN-based test stand is developed, which allows for the rapid characterization of surface integrity in BTA deep drilled components. It is used to compare the results of different systems for MBN analysis, employing both multipurpose sensors and a sensor designed to fit a drill head for BTA deep hole drilling.

To analyze the impact of WEL on the mechanical properties of deep drilled components a procedure is developed, inspired by the tube flattening test according to ISO 8492. Results are provided for the compression of components when applying quasi-static and cyclic loads.

Kurzfassung

Vor dem Hintergrund der globalen Erwärmung steht die moderne Produktionstechnik vor der Herausforderung, die Nachhaltigkeit in der industriellen Fertigung zu erhöhen. Hierbei kommt der gezielten Einstellung der Randzonenbeschaffenheit von Komponenten durch angepasste Fertigungsprozesse eine Schlüsselrolle zu, da diese ein enormes Potenzial zur Steigerung der Nachhaltigkeit bietet. Da die Leistungsfähigkeit von Komponenten entscheidend durch ihre Oberflächen und Randzonenbeschaffenheit beeinflusst wird, ermöglicht deren belastungsangepasste Einstellung die Fertigung von Bauteilen mit erhöhter Zuverlässigkeit und Lebensdauer.

Dieser allgemeine Zusammenhang zwischen der Gestaltung von Produktionsprozessen, der resultierenden Randzonenbeschaffenheit der gefertigten Bauteile und deren Leistungsfähigkeit gilt auch für das Tiefbohren. Ein weit verbreitetes Verfahren zur Erstellung von Bohrungen mit hohem Länge-zu-Durchmesser Verhältnis ist das Boring Trepanning Association- (BTA-) Tiefbohren. Dieser Prozess ist weit verbreitet in Bereichen wie der Luft- und Raumfahrt, sowie der Erdölindustrie und wird hier zur Herstellung von Komponenten wie Flugzeuglandebeinen, Schwerstangen und Hydraulikzylindern eingesetzt.

Eine zentrale Hürde bei der Charakterisierung der Oberflächenbeschaffenheit der Bohrungswand tiefgebohrter Komponenten besteht in ihrer stark eingeschränkten Zugänglichkeit. Diese erschwert oder verhindert gänzlich den Einsatz zahlreicher konventioneller Verfahren wie der Röntgendiffraktometrie. Zusätzlich hierzu sind viele der weit verbreiteten Methoden zur Bewertung der Randzonenbeschaffenheit entweder vollständig oder semi-zerstörend und ihre Anwendung ist somit beschränkt auf punktuelle Analysen, wobei das Werkstück beschädigt wird. Im Gegensatz hierzu ermöglicht die Analyse des Barkhausen-Rauschens eine vollständig zerstörungsfreie Werkstoffcharakterisierung. Da diese Methode hierüberhinaus auf besonders kompakten Sensoren basiert die in Bohrungen platziert werden können, ist sie ein vielversprechender Ansatz zur ganzheitlichen Analyse der Randzonenbeschaffenheit in ferromagnetischen tiefgebohrten Bauteilen.

Vor diesem Hintergrund zielt diese Dissertation darauf ab, die Analyse des Barkhausen-Rauschens für eine zerstörungsfreie, zeiteffiziente und zuverlässige Charakterisierung der Randzonenbeschaffenheit tiefgebohrter Komponenten zu qualifizieren. Da das magnetische Barkhausen-Rauschen durch eine Vielzahl von Teilaspekten der Randzonenbeschaffenheit beeinflusst wird, deren Einflüsse sich überlappen und interferieren, müssen die dem Barkhausen-Rauschen zugrunde liegenden Mechanismen hierfür aufgeklärt und separiert werden.

Aus diesem Grund wird in einem ersten Schritt eine ausführliche Betrachtung der Randzonenbeschaffenheit im BTA-Tiefbohrprozess durchgeführt. Diese beinhaltet zusammenhängende Analysen der Mikrostruktur, der Mikrohärtegradienten und des Eigenspannungszustands in der Randzone BTA-tiefgebohrter Bauteile. Um den Einfluss zentraler Bohrparameter zu untersuchen, wird hierbei die Schnittgeschwindigkeit und der Vorschub variiert.

Es wurde beobachtet, dass weiße Randschichten (WEL) in der Bohrungsrandzone gebildet werden, wenn relativ hohe Schnittgeschwindigkeiten und Vorschübe verwendet werden. Diese weißen Randschichten bewirken eine signifikante Randzonenaufhärtung. So konnte gezeigt werden, dass die Härte in der weißen Schicht die Härte des Grundgefüges um mehr als das Dreifache übertrifft.

Um die mikrostrukturelle Entwicklung im Tiefbohrprozess tiefergehend zu untersuchen, wurden Elektronenrückstreubeugungs-Untersuchungen durchgeführt. Die Ergebnisse zeigen eine starke Kornfeinung als Ergebnis von starker plastischer Verformung (engl.: Severe Plastic Deformation (SPD)). Das an die weiße Schicht angrenzende Gefüge zeigt stark verformte Körner auf.

Da die beobachteten nanokristallinen Strukturen nah an der Grenze der Auflösung in der Elektronenrückstreubeugung liegen, wurde zusätzlich Transmission Kikuchi Diffraction eingesetzt, um die Ergebnisse zu validieren. Zusätzlich wurden Electron Channeling Contrast Imaging und Rastertransmissionselektronenmikroskopie durchgeführt, um Korngröße und -morphologie sowie Poren und das Auftreten von Gitterstörungen wie Versetzungen und Stapelfehlern in der Randzone zu analysieren.

Aufbauend auf den grundlegenden Erkenntnissen zur Randzonenbeschaffenheit wurden in einem nächsten Schritt skalenübergreifende mikromagnetische Verfahren kombiniert, um Korrelationen zwischen Aspekten der Randzonenbeschaffenheit und mikromagnetischen Eigenschaften aufzudecken. Die Evolution magnetischer Strukturen bei Aufbringen eines externen magnetischen Feldes wurde mit magneto-optischer Kerreffekt-Mikroskopie untersucht. Zusätzlich wurden magnetische Domänenstrukturen durch die Bittertechnik charakterisiert. Magnetkraftmikroskopie ermöglichte die Analyse magnetischer Strukturen mit besonders hoher Auflösung.

Mit keiner der eingesetzten Methoden wurden innerhalb der weißen Randschichten klare magnetische Domänenstrukturen detektiert. Im Gegensatz hierzu wurden bei Prüfkörpern ohne weiße Randschicht Domänenstrukturen nachgewiesen, die sich bis an den Rand der Prüfkörper erstrecken. Diese multiinstrumentellen Untersuchungen bieten die wissenschaftliche Basis zum Einsatz der Barkhausen-Rauschen-Analyse. Hierbei wurde beobachtet, dass weiße Randschichten in den

Prüfkörpern durch die Eigenschaften dieser Schichten zu deutlich kleineren maximalen Barkhausen-Rauschen-Amplituden führen. Die hohen Dichten an Versetzungen, Stapelfehlern und Korngrenzen innerhalb der weißen Randschichten, wie sie in den mikrostrukturellen Untersuchungen nachgewiesen wurden, fungieren als Pinning-Stellen für die Blochwand-Bewegung. Aus diesen Beobachtungen wird geschlussfolgert, dass die weiße Randschicht wenig zum Barkhausen-Rauschen beiträgt und dass hierin der Grund für die niedrigen Barkhausen-Rauschen-Amplituden zu finden ist. Aufbauend auf den Erkenntnissen wurde ein multisensorischer Prüfstand für die Barkhausen-Rauschen-Analyse entwickelt, der die zeiteffiziente Charakterisierung BTA-tiefgebohrter Komponenten ermöglicht. Mit Hilfe des Prüfstandes wurden verschiedene Barkhausen-Rauschen-Prüfsysteme gegenübergestellt. Hierbei kamen sowohl Mehrzwecksensoriken als auch ein speziell angepasster Barkhausen-Rauschen-Sensor zur Applikation in Bohrköpfen zum Einsatz.

Um den Einfluss der weißen Randschichten auf die mechanischen Eigenschaften der tiefgebohrten Prüfkörper zu untersuchen, wurde eine Methodik in Anlehnung an den Ringfaltversuch nach ISO 8492 entwickelt. Ergebnisse werden für quasistatische und zyklische Untersuchungen vorgestellt.

Contents

Abbreviations

+QT	Quenched and tempered
0D	Zero-dimensional
1D	One-dimensional
2D	Two-dimensional
AFM	Atomic force microscopy
AISI	American Iron and Steel Institute
ANSI	American National Standards Institute
BCC	Body-centered cubic
BCT	Body-centered tetragonal
BHN	Brinell hardness
BOZA	Cutting fluid supply apparatus
BSE	Backscattered electron
BTA	Boring Trepanning Association
CAT	Constant amplitude test
CCD	Charge coupled device
CCT	Continuous cooling transformation
CIRP	Collège International pour la Recherche en Productique
CO_2	Carbon dioxide
CRC	Collaborative Research Center
DFG	Deutsche Forschungsgemeinschaft
EBSD	Electron backscatter diffraction
ECCI	Electron channeling contrast imaging
EDX	Energy-dispersive X-ray spectroscopy
FCC	Face-centered cubic
FEM	Finite element method

FIB	Focused ion beam
GL	Grey level
HCF	High cycle fatigue
HRC	Rockwell hardness
HV	Vickers hardness
ISF	Institute of Machining Technology
ISO	International Organization for Standardization
LCF	Low cycle fatigue
MBN	Magnetic Barkhausen noise
MFM	Magnetic force microscopy
MOKE	Magneto-optic Kerr effect
OIM	Orientation imaging microscopy
OPS	Oxide polishing suspension
RMS	Root mean square
SEM	Scanning electron microscopy
SI	Surface integrity
SLD	Single-lip deep hole drilling
S-N	Stress amplitude-life
STEM	Scanning transmission electron microscopy
TEM	Transmission electron microscopy
TKD	Transmission Kikuchi diffraction
WEL	White etching layer
XRD	X-ray diffraction

Symbols

Latin symbols

Symbol	Meaning	Unit
A	Area	mm^2
A_{c1}	Lower critical temperature for heating	°C
A_{c3}	Upper critical temperature for heating	°C
A_{r1}	Lower critical temperature for cooling	°C
A_{r3}	Upper critical temperature for cooling	°C
A_{WEL}	Area covered by WEL	mm^2
AWF	Area-weighted fraction	%
b	Slope in the S-N curve in the HCF region	-
B	Magnetic flux density	T
B_r	Remanence	T
d_0	Strain free lattice spacing	nm
d_{hkl}	Lattice spacing	nm
d_{offset}	Offset	nm
d_{surf}	Distance to the surface	µm
d_{wd}	Working distance	mm
D	Diameter	mm
D_{cryst}	Crystallite size	nm
D_g	Grain size	nm
D_{in}	Inner diameter	mm
D_{out}	Outer diameter	mm
E	Young’s modulus	GPa
f	Feed	mm
f_{bp}	Band-pass filter frequency	kHz

f_{cyc}	Frequency	Hz
f_{mag}	Magnetization frequency	Hz
f_{max}	Maximum frequency	kHz
f_{min}	Minimum frequency	kHz
$f_{resonance}$	Resonance frequency	Hz
$f_{setpoint}$	Setpoint frequency	Hz
F	Force	N
F_a	Force amplitude	kN
F_m	Mean force	kN
F_{QS}	Force applied in quasi-static compression	kN
FWHM	Full width at half maximum	°
h	Height	mm
H	Magnetic field strength	A/m
H_c	Coercive field strength	A/m
H_{cM}	Derived coercive field strength	A/m
H_m	Micro hardness	-
I_B	Intensity of Background noise	-
I_i	Intensity of peaks	-
I_{max}	Maximum intensity	-
IW	Integral breadth	°
k	Shape factor	-
l	Length	mm
l_b	Length of the bore	mm
m_{atom}	Atomic magnetic moment	Am^2
M	Magnetization	A/m
M_0	Saturation magnetization	A/m
M_b	Torque	Nm

M_f	Martensite finish temperature	°C
M_{max}	Maximum MBN amplitude	mV
M_r	MBN amplitude at remanence	mV
M_s	Martensite start temperature	°C
n_{atom}	Number of atoms per unit volume	m^{-3}
N	Number of cycles	-
N_{peak}	Number of peaks	
p	Pressure	bar
R	Load ratio	-
Ra	Arithmetic average roughness	µm
R_e	Yield strength	MPa
R_m	Tensile strength	MPa
RMS	Root mean square of MBN	mV
s	Step size	nm
s_{QS}	Displacement	mm
t	Time	s
t_{dw}	Thickness of domain walls	nm
t_{tp}	Tempering time	h
T_{tp}	Tempering temperature	°C
T_Q	Quenching temperature	°C
t_{WEL}	Thickness of the WEL	µm
U_{acc}	Acceleration voltage	kV
$\dot{V}$	Volume flow rate	l/min
v_c	Cutting speed	m/min
v_f	Feed speed	mm/min
v_{scan}	Scan speed	µm/s
w	Width	mm

Greek symbols

Symbol	**Meaning**	**Unit**
α	Angle	°
δ	Dislocation density	cm^{-2}
δ_{skin}	Skin depth	mm
ΔF_a	Difference in force amplitude	kN
ΔN	Difference in cycles	-
ΔM_b	Difference in torque	Nm
$\Delta\sigma_a$	Difference in stress amplitude	MPa
ε	Strain	-
ε_{hkl}	Lattice strain	-
η	Complementary angle of θ	°
θ	Bragg angle	°
λ	Wavelength	Å
μ	Permeability	H/m
μ_0	Permeability in vacuum	H/m
μ_f	Coefficient of friction	-
μ_r	Relative permeability	-
ν	Poissons ratio	-
σ	Stress	MPa
σ_a	Stress amplitude	MPa
σ_{axial}	Axial residual stress	MPa
σ_{cond}	Electrical conductivity	S/m
σ_m	Mean stress	MPa
σ_{max}	Maximum stress	MPa
σ_{min}	Minimum stress	MPa
σ_{tang}	Tangential residual stress	MPa

φ	Azimuthal angle	°
Φ	Magnetic flux	µVs
Φ_{cm}	Coercive field strength derived from MBN	µVs
χ	Angle of tilt	°
ψ	Polar angle	°

1 Introduction

This chapter outlines the general context, framework, and aim of this thesis. The enormous significance of the global steel industry in mitigating climate change is highlighted in chapter 1.1. In chapter 1.2 reliable surface conditioning in machining, e.g. in BTA deep hole drilling, is presented as a cornerstone for enhancing material efficiency and sustainability in the future production of steel components. In addition to the ecological aspects, increasing the reliability and guaranteeing the capability of deep drilled steel components is a highly relevant topic, due to the costly, and oftentimes safety-relevant applications.

1.1 Background and motivation

At the beginning of the 21st century, global megatrends like climate change, resource scarcity, and increasing worldwide energy consumption have been sweeping the globe for decades, confronting mankind with unprecedented challenges. As a result, fighting human-induced global warming has become a key societal aim, which found its way into the sustainable development goals of the United Nations [1]. In response to this situation and the pressing tasks associated with it, strategies for mitigating climate change and increasing global environmental sustainability are urgently required.

One of the largest contributors to anthropogenic greenhouse gas emissions is industry. According to the International Energy Agency, the industrial sector accounted globally for a quarter (9.0 Gt) of energy system CO_2 emissions in 2022 and 37% (166 EJ) of the total global final energy consumption [2]. With 2.62 Gt of CO_2 emitted by the iron and steel industry in 2022, this sector is key to achieving global decarbonization targets [2,3]. With a total worldwide annual production of approx. 1.7 Gt of steel per year, leading researchers consider iron making as the largest single cause of global warming [4,5]. These numbers provide evidence that industries and particularly the iron and steel sector have considerable leverage in the fight against climate change. In terms of resource scarcity, particularly common alloying elements like chromium and molybdenum are crucial in the steel industry, e.g. in steels for quenching and tempering.

The global demand for iron and steel is expected to multiply in the upcoming decades. For instance, the production of crude steel is expected to exceed 2.5 Gt of steel per year by 2050 [3]. Thus, the enormous impact of this sector on increasing global environmental sustainability will certainly get even larger in the future. Nowadays, the end-use of steel is dominated by the construction business. In 2008

42% of global steel was used for buildings and 14% for infrastructure. Mechanical equipment ranks third. In total 13% of global steel was used in this field [6]. Given the sheer volume of steel used worldwide, even relatively small improvements in the various fields of application of steel can yield far-reaching, and massive savings on the global scale, e.g. in terms of energy invested and CO_2 emitted.

Besides persistent efforts in green steelmaking, modern production engineering plays a pivotal role in reducing the environmental impact of steel components. Scientists and engineers involved in the manufacturing of steel components are faced with increasing calls for strategies that will contribute to rapid, large-scale industrial climate mitigation. For instance, there is a pressing need to find a remedy for the current overexploitation of natural resources and significantly reduce the energy invested and greenhouse gases emitted in manufacturing. In response to the global situation, and in the light of the numerous national and international laws, policies, and declarations for climate mitigation like the European Green Deal of the European Commission, persistent efforts have been made by industry and academia over the course of the past decades, to identify and implement ways of making steel manufacturing more efficient, resilient, and sustainable.

In their sixth assessment report, the Intergovernmental Panel on Climate Change of the United Nations identifies material and resource efficiency as key drivers for mitigating the impact of industrial production on climate change in the future [7]. Strategies for material efficiency include e.g. fostering light-weighting, extending product and servicing lifetimes, making post-treatment redundant, enhancing properties, and improving manufacturing yields [8]. According to Allwood, the most promising, physically realistic options for delivering resource efficiency are avoiding both scrap and over-design as well as producing goods that are smaller and have a longer life [9]. So far, however, options for mitigating climate change and achieving resource efficiency oftentimes lack pace and scalability and thus up to this day fail to yield the required substantial improvements on a large scale [7,9].

A key to a more sustainable, resource-efficient manufacturing of steel products in the future can be found in the surface integrity (SI) of components. This term comprises topographical, metallurgical, and mechanical properties of surface and subsurface volumes, such as residual stresses, microstructure, and microhardness. All these aspects of SI are altered during machining, due to the mechanical, thermal, and chemical loads occurring. The various properties of SI significantly influence a component's in-service functionality, longevity, and performance [10–12]. In view of these interrelations, tailoring SI during manufacturing is a particularly promising approach for enhancing sustainability in manufacturing. This way, e.g. the life of a component can be extended, without the need for additional postprocessing [13] and its weight might be reduced by reliably reducing safety factors.

The general motivation behind this thesis, located within the historical context presented, is illustrated in Figure 1.1.

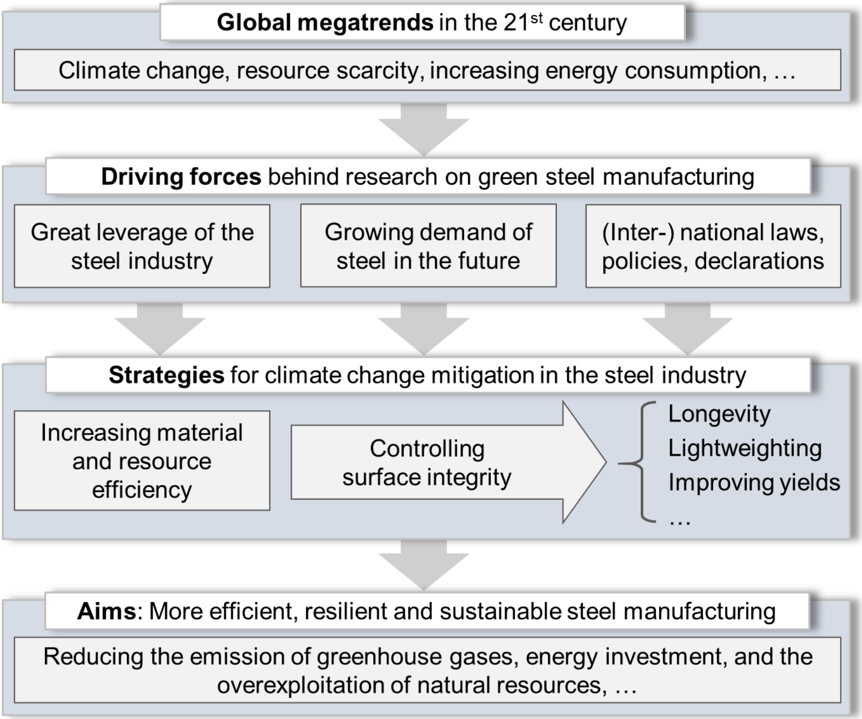

Figure 1.1 General motivation behind research on green steel manufacturing and surface intregrity

Since Field and Kahles published their pioneering work on SI of machined and ground high-strength steels, outlining that “the nature of the surface layer is […] requiring added attention in research and development, design and manufacturing” [14], SI has evolved into a major topic of research in production engineering. Particularly in recent years, the field of SI has received added attention, due to its leverage in the light of sustainable machining. Jawahir et al. propose a sustainability dashboard as a sustainability rating system that can be used for multi-objective process optimization [15].

Besides the vast importance of SI in terms of sustainable manufacturing, additional motivations for research on SI include economical, legal, and safety-related aspects. Profound, mechanism-based knowledge of surface technology can allow for reducing manufacturing costs in the face of global competition. In the light of product liability and catastrophic failures, controlling SI can guarantee and even significantly enhance the quality of components. [16,17].

As a result of the relatively long history of this subject, many correlations between the design of machining processes, the SI generated in steels, and the resulting properties of the machined components have been identified over the years. Many correlations are relatively well understood for common machining processes like turning and milling. Such a mechanism-based process know-how can be used as a base for controlling and tailoring SI. For other machining processes, like drilling, less is known about the complex interrelation [11]. A reason for this can be found in the hindered accessibility of the tool and the generated surface during machining, which makes drilling particularly challenging to investigate. This is especially the case for deep hole drilling processes, which are used for machining bores with large length-to-diameter ratios, such as Boring Trepanning Association (BTA) deep hole drilling [18]. This advanced machining process is used in fields such as aerospace engineering, petrol exploration, and the chemical industry, for machining high-performance components like landing gears, drill collars, and tube sheets of steam generators [18,19]. Such components tend to be very costly and are oftentimes used in safety-critical systems. Guaranteeing their SI for reliably ensuring their performance throughout their lifetime is of vital importance, otherwise, this can potentially lead to disastrous consequences. Particularly quenched and tempered steels for landing gears, which are used at very high stress levels, require meticulous attention in processing, fabrication, design, and maintenance [20]. Accordingly, components like landing gears have failed due to impermissible alteration of microstructure in drilling [14].

1.2 Aims and objectives

The main objective of this thesis is to identify the interrelations between the arrangement of the BTA deep hole drilling process and the generated SI in bores. Due to the hindered accessibility of the borehole wall, assessing SI is particularly challenging in bores. Magnetic Barkhausen noise (MBN) analysis is qualified as a nondestructive method for SI inspection, which allows for assessing the subsurface of bores, without the need of any special preparation. For an enhanced understanding of the micromagnetic structure in the subsurface of the borehole wall, complementary micromagnetic approaches and advanced crystallographic techniques will allow for a mechanism-based understanding of MBN analysis. The findings are linked to the performance of drilled specimens under quasi-static and cyclic compression. Based on this general modus operandi, this thesis aims to bridge the gap between the microscale structure of BTA deep drilled components and their macroscale properties. This way, understanding of SI alteration in BTA deep hole drilling and its impact on a component's capability is enhanced. The governing mechanisms of SI generation in BTA deep hole drilling are elucidated, by a variation of key drilling parameters and process design. The generated knowledge will serve as a base for a reliable conditioning of subsurfaces of high-performance components and will thus pave the way for greater resource efficiency and reliability in BTA deep hole drilling.

In drilling, the selection of the cutting speed v_c and the feed f significantly influence the thermomechanical loads at the surface and subsurface of bores. Thus, investigations focus on the impact of these two key parameters on SI as a consequence of the temperatures and mechanical loads in the subsurface of the bore.

This work presents a multi-scale analysis of SI resulting from BTA deep hole drilling, considering micromagnetic properties, microstructure, microhardness, and residual stresses. In terms of microstructural alterations, the investigations focus specifically on the formation of white etching layers (WEL) and swept grains in the subsurface. A segmentation-based evaluation of micrographs obtained by optical microscopy is performed, to separate WEL from the bulk material. The separated images are further analyzed to assess the extent of WEL.

The techniques employed for the characterization of subsurfaces range from conventional, well-established techniques such as optical microscopy, scanning electron microscopy (SEM), X-ray diffraction (XRD), electron backscatter diffraction (EBSD) and microhardness evaluation to more advanced technologies. These include for instance the use of a focused ion beam scanning electron microscope (FIB-SEM) for scanning transmission electron microscopy (STEM), transmission Kikuchi diffraction (TKD), electron channeling contrast imaging (ECCI), magneto-optic Kerr effect (MOKE) microscopy, and atomic force microscopy (AFM), including magnetic force microscopy (MFM).

Building on the findings obtained by these techniques, MBN analysis is qualified for quick and reliable detection of WEL. This micromagnetic technique is based on the observation of Barkhausen jumps and is applicable for an assessment of various properties and structural features, such as residual stresses [21,22], microstructural alterations [23,24], and hardness [25]. The structure of this thesis and interrelations between the topics covered are illustrated in Figure 1.2.

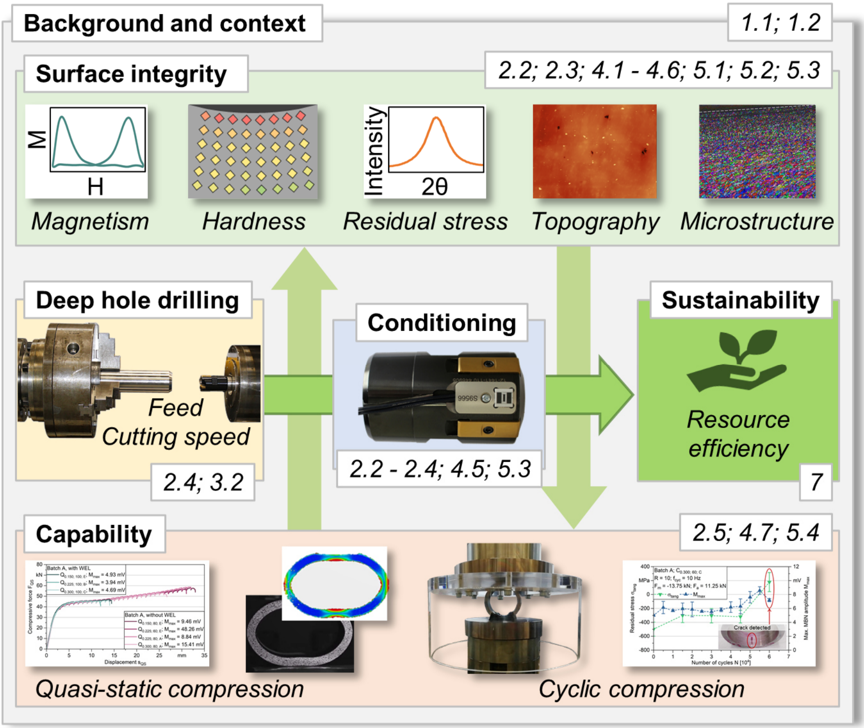

Figure 1.2 Structure of this research thesis and interrelations between the topics covered

2 State of the Art

In this chapter, the state of the art is presented. In 2.1 quenched and tempered steels are pointed out as a vital group of steels for numerous applications. The concept of SI in machining is introduced in chapter 2.2, outlining the fundamentals and the impact on the performance of components. In addition to this, methods for the destructive and nondestructive evaluation of SI are presented, with an emphasis on approaches for a holistic micromagnetic and diffractographic inspection of SI. A characteristic feature of SI, which can be found in steels, titanium and nickel-based superalloys are white etching layers. Information on their properties, formation mechanisms, and their impact on the performance of components is provided in chapter 2.3. In chapter 2.4 BTA deep hole drilling is presented as the dominant process for machining bores with high length-to-diameter ratios and relatively large diameters. Methods for mechanically characterizing bores are introduced along with the fundamentals of fatigue in 2.5.

2.1 Quenched and tempered steels

2.1.1 Quenching and tempering

Quenching and tempering of steels is a two-stage heat treatment process, which consists of hardening and subsequent tempering. Combining these two stages leads to steels with higher toughness and ductility as well as improved dimensional stability, compared to steels in an as-quenched state. These positive effects of tempering go along with a reduction in hardness, tensile strength and yield strength [26]. Thus, properties after quenching and tempering can be considered a compromise of sufficiently high yield strength and relatively high toughness.

Quenching

For quenching, the steel is heated to a temperature above austenitization temperature. It is kept at that temperature for a defined time to ensure a complete transformation to austenite. During this stage it is vital to avoid overheating and burning [27,28]. When holding time has passed, the steel is rapidly cooled below martensite start temperature M_s. The rate for cooling needs to be higher than a critical rate, to ensure the formation of martensite in the desired depth and avoid the formation of bainite, ferrite and pearlite [27,28]. With higher cooling rates, however, the risk of quench cracks increases [29]. Usually a continuous cooling transformation (CCT) diagram is used to determine the cooling rate. Based on the critical cooling rate, the quenching medium is selected. The most common quenchants are water and various types of oil [29]. Quenching results in the transformation of the austenitic microstructure into a distorted body-centered tetragonal (BCT) martensitic lattice. This microstructure is excessively hard and too brittle for applications [30]. To overcome this, subsequent tempering of quenched steels is used to make them tougher, while ensuring sufficiently high yield strength [30].

Tempering

Tempering is usually performed as soon as possible after quenching, to reduce the risk of quench cracks [26,31]. When the steel has cooled down to between T = 50-75°C and room temperature, the steel is reheated. This allows carbon atoms to diffuse from the distorted BCT lattice and form iron carbides [26]. With higher tempering temperatures, the movability of carbon and iron atoms increases. The diffusion of carbon atoms results in a transformation of as-quenched martensite into tempered martensite, which is more cubic and less distorted. The number of dislocations subsequently decreases [27,30]. Tempering is done at temperatures below the lower critical temperature (A_1), usually between T = 180-680°C [26,29,32]. Higher tempering temperatures result in a more severe loss in hardness [33]. At temperatures between T = 100-200°C, ε-carbides are precipitated [30]. At temperatures higher than T = 260°C, ε-carbides are transformed into cementite [34]. The tensile strength and hardness are significantly reduced, whereas the yield strength is less affected. At tempering temperatures higher than T = 400-450°C additional alloy carbides start to form [30].

The most commonly used tempering temperatures are in the range of T = 550-650°C [30]. Tempering is usually performed for a time of 30 minutes to 4 hours, which is approximately twice as long as holding times for austenitizing [29,30]. In general, alloying elements increase the time needed for tempering and reduce the loss in hardness [29,33]. The tempering temperature is considered to be much more significant than the tempering time [30,33]. Cooling after tempering is performed in water, oil or air [30]. Temper embrittlement oftentimes results at temperatures between 450 and 550°C for relatively slow cooling after tempering, particularly for steels containing manganese, chromium or nickel. Temper embrittlement can be avoided by adding molybdenum, or by cooling rapidly in this temperature range [35]. For alloy steels sometimes additional tempering stages are added, to temper the martensite formed on cooling from the first tempering stage [33]. It has been shown for AISI 4140 steel that double quenching and tempering can significantly increase impact toughness [36]. An exemplary continuous cooling transformation diagram is displayed for the steel analyzed in this thesis (AISI 4140) in Figure 2.1 [37,38]. The approximate critical temperatures for this steel are displayed in Table 2.1.

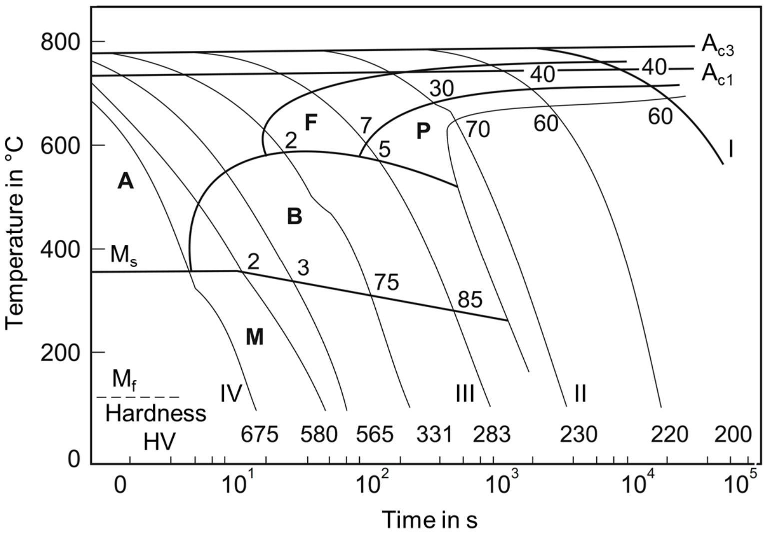

Figure 2.1 Continuous cooling diagram for AISI 4140 steel, presenting the regions of the formation of austenite (A), ferrite (F), pearlite (P), bainite (B) and martensite (M), along with the temperatures for martensite start M_s, martensite finish M_f, the Vickers hardness (HV) and the lower and upper critical transformation temperatures (A_{c1} and A_{c3}). According to [37,38][1]

Table 2.1 Characteristic temperatures of AISI 4140 steel: A_{c1} (lower critical temperature for heating), A_{c3} (Upper critical temperature for heating), A_{r1} (lower critical temperature for cooling), A_{r3} (Upper critical temperature for cooling), T_Q (Quenching temperature), M_s (Martensite start temperature) [26]

A_{c1}	A_{c3}	A_{r1}	A_{r3}	T_Q	M_s
749°C	793°C	693°C	743°C	816°C	338°C

---

[1] Reproduced with permission from Springer Nature BV from Berns, H.; Theisen, W.: Eisenwerkstoffe - Stahl und Gusseisen (2006); permission conveyed through Copyright Clearance Center, Inc.

2.1.2 Steels for quenching and tempering

Quenching and tempering is usually performed for hypoeutectoid non-alloy and low-alloy steels [39]. These steels are specified in the standards DIN EN ISO 683-1 (non-alloy steels) and DIN EN ISO 683-2 (alloy steels). In addition to these, steels in various other standards are subjectable to quenching and tempering [35]. Quenched and tempered steels are oftentimes divided into four subgroups: non-alloy steels, alloy steels containing manganese, chromium-molybdenum alloy steels (chromoly), and nickel-chromium-molybdenum alloy steels [30]. Their carbon content usually ranges from 0.25 to 0.6% [30]. Lower carbon contents lead to insufficient hardenability, whereas higher carbon contents result in insufficient toughness after quenching and tempering [31]. Tensile strength of conventional steels after quenching and tempering is usually up to $R_m = 1400$ MPa [30]. Alloying elements can be used to lower the critical cooling rate. Thus, they are oftentimes added for relatively thick components [35]. The alloying elements tungsten, molybdenum, chromium, vanadium, niobium and titanium form alloy carbides at temperatures higher than $T = 400\text{-}450°C$ and inhibit carbon diffusion [30]. These carbides are finer than iron carbides and their formation causes an additional increase in strength [30]. Thus, they are oftentimes added to reduce the loss in hardness during tempering stage [32]. Molybdenum can be added to reduce temper embrittlement [30]. Boron increases hardenability even in very small amounts of approx. 0.005% [30].

2.1.3 Applications

Due to their excellent toughness, quenched and tempered steels are used extensively for dynamically loaded components, which are required to have relatively high strength and a good resistance to fatigue [28,30]. They are commonly used for components which have to withstand cyclic loads, randomly distributed variable loads and impact loads. Quenched and tempered steels are oftentimes employed, when the non-alloy structural steels specified in DIN EN 10025-2 would lead to inappropriately high dimensions [35]. Typical components made of quenched and tempered steels include general-purpose machine elements, such as gears, axles, bolts, springs and screws. In the automotive industry, quenched and tempered steels are used for components such as crankshafts, camshafts, transmission shafts and steering knuckles [37,40]. In aerospace engineering, quenched and tempered steels are employed for critical structural components such as landing gears, flap tracks or airframe parts [41,42]. Other fields in which quenched and tempered steels are frequently used include the mining industry, defense and civil construction [43]. For applications at elevated temperatures, it is vital to ensure that temperature in service is below tempering temperature, to avoid a reduction in strength. Usually the tempering temperature exceeds the maximum temperature a component faces in service by at least 50°C [31]. Limitations for the applications of quenched and tempered steels are caused by their relatively poor weldability [44].

2.1.4 Machining

Most components made of quenched and tempered steels are machined after quenching and tempering. Only in some cases, quenching and tempering is performed after rough machining and before finishing, to reduce tool wear. Machinability of quenched and tempered steels is mostly determined by the design of the heat treatment and the resulting microstructure of components. Thus, key aspects with regard to machinability are tempering times and temperatures. Alloying elements are usually less important for machinability. However, the machinability of quenched and tempered steels can be significantly enhanced by adding sulfur (usually 0.06-0.1% for turning, drilling and milling) and lead [40]. Resulting from the huge impact of sulfur content on machinability, many of the steels for quenching and tempering can be purchased with a defined amount of sulfur [30]. The key mechanisms of wear when machining quenched and tempered steels are abrasion and thermally induced wear [40]. Usually coated cemented carbide tools are used for rough machining and cermets for finishing of quenched and tempered steels [40]. Exemplary cutting parameters for machining AISI 4140+QT under given tool life criterions can be found in [45]. In addition to this, a comparison of machinability between quenched and tempered steels and bainitic steels is presented.

2.2 Surface integrity in machining

2.2.1 Historical development and fundamentals

In 1964, Michael Field and John F. Kahles of Metcut Research Inc., Cincinnati Ohio, subsumed various topographical and metallurgical features of workpieces after manufacturing under the umbrella of the newly coined term “surface integrity”. In their pioneering work, they provided evidence that machining and grinding of high strength steels can induce significantly altered properties in surface layers, e.g. in terms of microstructure, hardness and residual stresses. This groundbreaking research followed thousands of years of studies in the field of surface science. The history of this branch of science is comprehensively summarized in [46]. By identifying the need for considerably more research on SI, Field and Kahles set the stage for their successors [14].

Ever since those days, SI has evolved into a matter of great concern and a major topic of research in production engineering, leading to a CIRP (Collège International pour la Recherche en Productique) conference series dedicated to this topic and an enormous amount of literature that is updated regularly. Some of the most comprehensive publications on SI include the works of Field [14,47], Griffiths [16], Rech [11], M'Saoubi [48], Davim [46], Jawahir [49], Sales [50], Liao [51], and la Monaca [10]. Key topics related to the field of SI are the methods for destructive and nondestructive evaluation and quantification of the various aspects of SI (chapter 2.2.2) and the impact of SI on the performance of components (chapter 2.2.3).

Since machining-induced material modifications are not strictly limited to surfaces, the term SI includes the subsurface. Astakhov describes a surface in a rather straight-forward way "to be the outermost layer of an entity" [52]. In the CIRP encyclopedia of production engineering, Breidenstein suggests following the definition of "surface" given in the standard DIN 4760 for the context of production technology. According to him, the term "subsurface" comprises the volume below the surface, in which properties have been modified by machining [53]. Brinksmeier states that the depth of a component's subsurface depends on the machining process. He proposes considering the depth beneath the surface, up to which the material properties have an impact on the performance of a component [17].

Following the early works of Field, some of the first in-depth studies on SI were commissioned by the United States department of defense. William P. Koster et al. published the results in a detailed technical report on the evaluation of SI of various steels, titanium and nickel base structural alloys. They considered grinding, milling, turning, drilling, electrical discharge machining, and electrochemical machining. In their report, they proposed a minimum data set, a standard data set and an extended data set for SI evaluation [54], similarly proposed by Field et al. in [47]. Based on these investigations, the American National Standards Institute published the "American National Standard on Surface Integrity" ANSI B211.1 in 1986, recommending data for SI assessment, as well as appropriate methodologies for assessing SI. Though this standard was withdrawn in 1996 without replacement, it is still frequently referenced, due to a lack of alternative standards in the field [46,55,56]. One major aspect of criticism is the classification of properties into the groups "mechanical, metallurgical, chemical, thermal and electrical", which lacks consistency and completeness. In addition to this, no clear distinction is drawn between properties and their origin [17].

In 1991, Brinksmeier developed a dataset for the inspection of ground surfaces and subsurfaces in his postdoctoral lecture qualification (Figure 2.2). This concept is referenced by Breidenstein in the entry for SI in the CIRP Encyclopedia of Production Engineering [53]. Brinksmeier states that there are various strategies for classifying the aspects of SI. A function-oriented perspective considers all the properties of surfaces and subsurfaces which have an impact on the performance of a component. He also proposes an origin-oriented perspective, which rather focuses on the mechanisms which govern SI formation. In machining, SI is defined by the kinematic, physical and chemical impact of the process. According to Brinksmeier, the origin-oriented perspective is thus particularly beneficial when analyzing SI resulting from machining processes [17]. In his monograph, published in 2001, Griffiths distinguishes between “internal” and “external” features (Figure 2.2). He divides the machined surface into three regions: the uppermost region contains deposits, adsorptions and oxides. Beneath this layer is the altered subsurface material, which is usually composed of different zones, e.g. for electric-discharge machining, this zone can consist of up to 6 zones. The altered subsurface material is followed by the bulk material that remains unchanged by manufacturing [16].

Table 2.2 summarizes the aspects of SI as pointed out in some of the aforementioned major contributions to the field of SI. The table shows a huge overlap between the publications. Some of the properties, such as residual stresses can be found in all the listed publications and, thus can be considered in the center of research in SI throughout the decades. Other aspects of SI, such as “topography” are broken down into various sub-aspects in some of the publications.

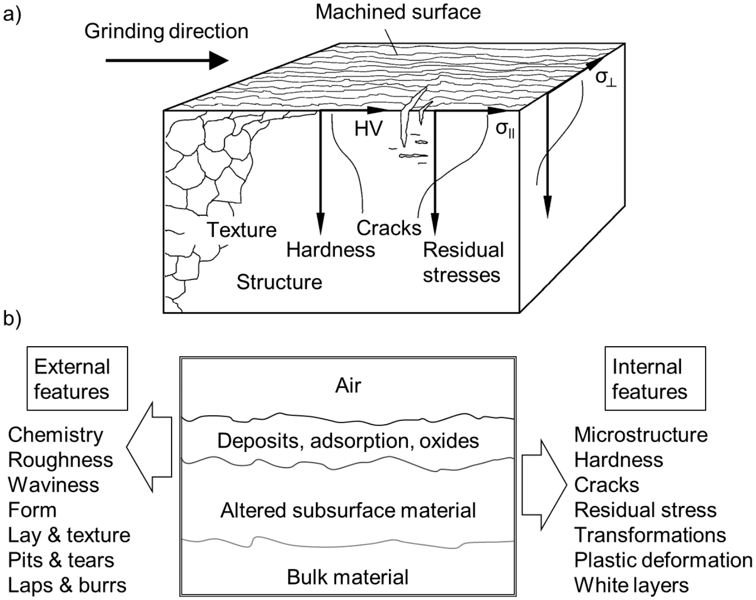

Figure 2.2 Surface and subsurface properties according to a) Brinksmeier; b) Griffiths. According to [16,17,53][2]

Following the previous remarks, it can be concluded that no definite, universally applicable standard or code of practice exists, which covers the entire field of SI. However, there are standards for some of the aspects of SI. Griffiths gives a comprehensive overview of these in his monograph. He states that the standards together provide a reasonable base for the SI requirements of surfaces. However, there is no internationally relevant ISO standard, which defines the subsurface aspects of SI [16]. Brinksmeier hypothesizes that the reason for this lack of one universally applicable standard for SI assessment, is that basically all properties of workpieces can potentially be considered surface or subsurface properties if they have an impact on performance [17].

---

[2] a) Reproduced with permission from E. Brinksmeier and Springer Nature BV from Breidenstein, B.: Surface Integrity. In: Laperrière, Reinhart – CIRP Encyclopedia of Production Engineering (2019); b) Reproduced with permission from Elsevier Science & Technology Journals from Griffiths, B.: Manufacturing surface technology: surface integrity & functional performance (2001); permission conveyed through Copyright Clearance Center, Inc.

Table 2.2 Properties of surfaces and subsurfaces, as summarized in some of the major contributions to the field of SI assessment

Publication	Surface and subsurface properties
M. Field et al. (1964) [14]	Plastic deformation, temperature gradient, residual stress, metallurgical transformation, overtempering, spattered molten metal, macrosurface cracks, tears, voids and inclusions, surface finish, surface texture
W. P. Koster et al. (1972) [54]; *M. Field* et al. (1972) [47]	Surface finish, macrostructure (macrocracks, macroetch indications), microstructure (microcracks, plastic deformation, phase transformations, intergranular attack, pits, tears, laps, protrusions, built-up edge, melted and redeposited layers, selective etching, depletion by vaporization (only in [54])), microhardness, fatigue tests, stress corrosion tests, residual stress and distortion, additional mechanical tests (tensile, stress rupture, creep, other specific tests)
E. Brinksmeier (1991) [17]	Profile, orientation of machining grooves, topography, roughness, texture, microstructure, hardness, cracks, residual stresses
B. Griffiths (2001) [16]	External features: Chemistry, roughness, waviness, form, lay, texture, pits, tears, laps, burrs; Internal features: microstructure, hardness, cracks, residual stress, transformations, plastic deformation, white layer
B. Breidenstein (2019) [53]	Topography; chemical composition; phase composition; hardness; microstructure; residual stress; texture

Surface and subsurface generation in manufacturing depends on the thermal, mechanical and chemical loads acting on a workpiece. These loads are defined by the five constituents of a machining process: workpiece, tool, machine tool, environment and process variables. A general overview of how these characteristics of a manufacturing process affect SI is given in [57]. Liao et al. propose categorizing surface generation mechanisms into the four categories: mechanical dominant, thermal dominant, chemical dominant and combined loading mechanisms [51]. Rech states that most processes involve a combination of mechanical, thermal and chemical mechanisms. Only a few processes can be assigned to one single mechanism [11].

For conventional machining processes, such as turning, grinding, milling, and drilling it is mostly mechanical and thermal loads which govern SI generation. As these usually overlap and interfere in machining, their effects always have to be considered in conjunction [58]. This can be shown by the example of residual stresses. In general, mechanical loads propagate compressive residual stresses, whereas high thermal loads usually result in tensile residual stresses. In machining, however, residual stresses are generated by the combined thermomechanical loads acting on the workpiece, thus both effects need to be respected. Outeiro summarizes the state of the art of residual stresses in machining in [59].

During machining, severe plastic deformation occurs in all three shear zones at the interface between tool, chip and workpiece. It is assumed that the SI of a workpiece is affected only in the primary shear zone and the tertiary shear zone [56]. High mechanical loads in machining are usually associated with favorable SI features. Based on this, processes belonging to the mechanical dominant category, such as shot peening or burnishing, are oftentimes used to improve SI of highly loaded components after machining.

The high deformation ratio in a limited region can lead to very high temperatures in the interface between tool, chip and workpiece during machining [50]. The thermal energy is dissipated by the chip, the workpiece, the tool and the environment. The biggest share of the heat generated flows to the chip. According to Sales et al., a relatively small share of 8-10% of the generated temperature is transferred to the tool, when machining with defined tool geometries. The rest of the heat generated is split between the workpiece and the environment [50]. For machining steels, it can roughly be estimated that 75% of the heat generated is dissipated by the chip, 18% by the tool and 7% by the workpiece [40]. However, the exact distribution is very challenging to determine and depends on various aspects, such as the materials for tool and workpiece and the conditions of cutting. High temperatures in the workpiece during machining can lead to a significant reduction of shear stresses due to the thermal softening effect. High thermal loads, however, are well known to accelerate tool wear and cause poor SI features, such as white etching layers, tensile residual stresses, microcracks, warping, phase transformation, recrystallisation and microhardness variation. Since these properties can lead to deficient component performance, it is oftentimes particularly crucial to control temperature in machining [50].

When describing machining conditions in the context of SI, “abusive” and “gentle” are two frequently employed adjectives, as these terms were already used by Field et al. in their pioneering works [14,47,54]. According to Griffiths, abusive machining is associated with high cutting parameters, worn tools, little lubrication and inadequate machine tools. These conditions generally result in high temperatures, strains and strain rates in cutting and thus typically cause poor SI. Conversely, gentle machining is associated with cutting parameters that promote long tool life, sharp tools, appropriate lubrication and rigid machine tools. Since usually little heat is generated in machining under such machining conditions, gentle machining typically leads to more favorable SI compared to abusive machining [16].

2.2.2 *Destructive and nondestructive evaluation*

In general, two strategies are employed for analyzing the SI of workpieces. The SI can be evaluated directly by means of an inspection of the workpiece through appropriate techniques. In addition to this approach, SI can also be assessed indirectly, by monitoring and diagnosing the process. Both strategies demand a profound understanding of the mechanisms of SI generation in machining and the measurement techniques employed [17,60]. Thus, the field of SI evaluation links the fields of manufacturing technology, materials science, and metrology. This general framework is illustrated in Figure 2.3, along with some exemplary techniques for direct SI evaluation and examples of process variables, which can be monitored for indirect SI assessment [17].

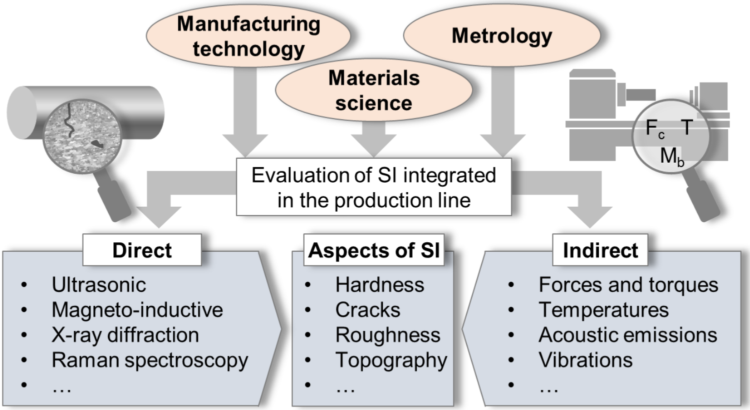

Figure 2.3 General framework for the evaluation of surface integrity (SI), giving examples of direct and indirect SI evaluation

There are numerous well-established techniques for evaluating surface topography. Many of these are widely available, well researched and internationally standardized. Griffiths gives an overview of some of the most common techniques, such as 2D and 3D profilometers with scanning contact mechanical styli or non-contact optical styli. In the past decades, optical approaches have been gaining importance, including approaches based on interferometry and focus variation. In addition to this, various microscopy techniques can be used for assessing topography with high precision, such as SEM, AFM, confocal laser scanning microscopy, scanning tunnel microscopy or vertical scanning interference microscopy [16]. The topic of nanoscale roughness assessment by approaches in light scattering has been gaining significance in the past decades. This matter is covered extensively in [61]. A summary of techniques applicable for an in-process on-line measurement of roughness is given by Dong. He presents methods based on fiber optics, light scattering, speckle contrast, dark and bright ratio as well as machine vision-based data [62].

Compared to the assessment of topography, the evaluation of the metallurgical and mechanical aspects of SI in subsurfaces is in many ways more challenging and less standardized. One of the most common techniques for SI evaluation is the microscopic analysis of etched sections, which usually are extracted from the workpiece. This technique provides information on multiple aspects of SI and remains the widely accepted standard in some fields, such as grinding burn detection, as specified in ISO 14104 „Surface temper etch inspection after grinding, chemical method". Nevertheless, there are many downsides of metallographic inspection. Thus, calls for advanced, nondestructive techniques for evaluating SI are increasing. Looking at the examples of grinding burn detection, MBN analysis has been qualified in the past decades as a fast and nondestructive alternative to metallographic etching [63]. This example illustrates that in SI evaluation there oftentimes are multiple techniques, which can all yield the desired information. However, there are assets and drawbacks for all of the competing approaches. Therefore, it is vital to thoroughly analyze the demands, a technique for SI evaluation is expected to meet in a specific application.

Since the integrability of inspection techniques in a production line has been gaining importance in the past decades, the focus in research nowadays lies mostly on approaches which allow for a process-oriented, nondestructive, fast, and reliable evaluation of SI. Brinksmeier comprehensively presents the demands, nondestructive and process-oriented evaluation techniques are expected to meet. He distinguishes between physical requirements, technological requirements and requirements in the field of information technology. Assessing the suitability of the available nondestructive inspection techniques, he states that particularly ultrasound and magneto-inductive testing are applicable for SI inspection in a process-oriented fashion [17]. Goch et al. identify the accuracy, robustness, costs, measuring time, and integrability in a production line as key demands for nondestructive evaluation techniques [64]. Many of the articles and standards on fundamentals of SI mentioned in 2.2.1 also propose destructive and nondestructive techniques for evaluating SI. Table 2.3 summarizes inspection techniques suggested in some of these contributions.

Table 2.3 Techniques for surface integrity (SI) inspection proposed in some of the major contributions

Authors	**SI inspection**
M. Field et al. (1964) [14]	Surface finish analyzer, visual inspection, microscopic examination of etched sections, magnetic particle inspection, dye penetrant inspection, X-ray diffraction, ultrasonic testing
W. P. Koster et al. (1972) [54]; *M. Field* et al. (1972) [47]	Visual examination, macroscopic examination, microscopic examination, microhardness testing, immersion etching, magnetic particle inspection, penetrant inspection, ultrasonic testing, eddy current, X-ray diffraction, etch techniques
E. Brinksmeier (1991) [17]	Ultrasound (pulse-echo, transit time, absorption, scattering), magneto-inductive (micromagnetic, eddy current, magnetic flux leakage), grazing incidence X-ray diffraction, total reflection x-ray fluorescence, Raman Spectroscopy, photothermal spectroscopy, instrumented microhardness testing, scanning tunneling microscopy
B. Breidenstein (2019) [53]	Roughness testing (tactile, optical or scanning probe microscopic methods), energy dispersive X-ray analysis (EDX), Auger electron spectroscopy, microprobe analysis, X-ray photoelectron spectroscopy, glow discharge optical (emission) spectroscopy, X-ray diffraction, electron backscatter diffraction, scratch test, hardness testing (Vickers, Brinell, Rockwell), rebound analysis, etched sections, "indirect method" for residual stress measurements by strain gauges or optical interference

It can be observed that the techniques summarized in Table 2.3 have developed from fairly straightforward inspection, to rather complex and mechanism-based analyses of SI. Comprehensive overviews of the most common methods for a direct evaluation of SI can be found in numerous review papers [47,64,65]. A particularly detailed account is given by Lucca et al. in their paper for CIRP Annals [66]. Recently emerging approaches in the area of SI evaluation are summarized by Liao et al. in [51].

In the field of indirect SI evaluation, Teti et al. extensively report on methods for monitoring and diagnosing processes, which allow for controlling SI. The aspects of SI covered by the approaches include surface finish and roughness, WEL formation, surface damage, residual stress and delamination damage. For assessing these SI features, process variables such as cutting forces, vibrations, acoustic emissions and temperatures were monitored [67].

Schulze et al. and Stampfer et al. present findings on soft sensor-based approaches for targeted subsurface conditioning in machining, through dynamic process controls. The processes turning, grinding and drilling are considered. The findings presented were obtained in projects of the priority program 2086 "Surface conditioning in machining processes", funded by the German Research Foundation (DFG) [12,68,69].

In the interdisciplinary Collaborative Research Center (CRC) 136 "Function-oriented manufacturing based on characteristic process signatures", funded by the DFG, German and American scientists researched into the novel concept of characteristic process signatures. Process signatures assess the energy which is converted and dissipated in a process. Based on this, interactions between a manufacturing process and the workpiece material are identified. Process signatures can thus be used for predicting SI of components and subsequently allow for function-oriented manufacturing [70,71]. In the CRC 926 "Microscale morphology of component surfaces", funded by the DFG, scientists researched into the microscale integrity of component surfaces with a specific functionality. The focus in this CRC lay in the fields of surface creation, morphology and properties [72].

A particularly significant technique for SI assessment, which can be found in all the publications, mentioned in Table 2.3 is X-ray diffraction. This technique remains the gold standard for the assessment of residual stresses in machining and can additionally be used for analyzing phase distribution, grain size and topographical aspects. Because of its significance for this work, X-ray diffraction is covered in detail in chapter 2.2.4. In addition to this, micromagnetic testing is portrayed in chapter 2.2.3, as a means for a fast and reliable, holistic characterization of various aspects of SI.

2.2.3 Micromagnetic inspection

The field of micromagnetic inspection comprises all the techniques in nondestructive testing and evaluation, which are based on the analysis of magnetic dipoles [73]. Throughout the past decades, this versatile technology has been gaining importance in various fields of SI assessment [74]. Reasons for this are particularly the nondestructive character and the flexibility of micromagnetic inspection, as well as the relatively short time that needs to be invested for performing measurements. In addition to this, instrumentation is usually cheap and measurements are fairly automatable. Various techniques in micromagnetic inspection can be used for evaluating numerous aspects of SI. Adapting the frequency of excitation f_{mag} or the analyzing frequency of a band-pass filter f_{bp} allows for depth-resolved characterization of materials [73,75]. In general, inspection depths are rather small. Thus, micromagnetic inspection is particularly adequate for evaluating the near-surface of materials.

The dominant technique in micromagnetic testing is the analysis of magnetic Barkhausen noise (MBN). In 1917 Prof. Heinrich Georg Barkhausen discovered that a crackling sound is emitted when iron is magnetized inside a coil connected to an amplifier, attached to a speaker. Two years later, in 1919, he published his findings in the article “Zwei mit Hilfe der neuen Verstärker entdeckte Erscheinungen“ (“Two phenomena discovered with the help of new amplifiers”) [76]. In this publication, Barkhausen already identified that the effect discovered by him might be beneficial for investigating iron. This way he set the stage for further research on the application of MBN for materials inspection [76]. However, apart from a few isolated studies, it wasn’t until the early 1970s that research on the applicability of MBN for nondestructive testing really gained momentum. A detailed overview of the history of MBN analysis is given in [77].

Up to this day, Barkhausen noise inspection has not been specified in any international ISO standard, despite its far-reaching significance in nondestructive testing. However, there are a few guidelines and codes of practice available, such as “FVA 594” by Forschungsvereinigung Antriebstechnik e.V. (Research Association for Drive Technology) [78], as well as an SAE aerospace recommended practice “ARP 4462” [79], and a good practice guide by Tomkowski et al. [80].

As a result of the many upsides of MBN inspection technology, numerous systems have been developed in the past decades. Due to the fairly straightforward design and the cheapness of the required components, it is common to use custom-designed, in-house instruments and sensors, such as the ones presented in [22,81,82]. Besides these, there are various commercially available systems. These include the devices 3MA-II [77], 3MA-X8 [83], BEMI [84] (all by Fraunhofer IZFP, Germany), FracDim (Fraunhofer IKTS, Germany) [85], Rollscan (Stresstech, Finland) [86], µmagnetic (Qass, Germany) [87], MagStress5c (NNT, Poland) [88], and MEB4-C (Mag-Lab, Poland) [25]. A comprehensive review of the design of Barkhausen noise probes is given in [89]. Customized sensor geometries have been developed for the inspection of components such as gears, camshafts, or crankshafts [85]. Tschuncky et al. present multicoil probes in [90]. Sensors for micromagnetic inspection can be used manually or in combination with automated, or robot-based handling systems [85].

One of the major limitations of micromagnetic inspection in general, and MBN analysis in particular, is that it does not allow for a direct assessment of single topographical, metallurgical, and mechanical properties. Instead, the magnetic properties are assessed and used as a base for drawing conclusions about the various aspects of SI. Since the relations between the magnetic properties and the topographical, metallurgical, and mechanical properties of materials are highly ambiguous and oftentimes unsteady, effects can overlap and interfere in MBN-based inspection. This requires calibration efforts and calls for a genuine separation of mechanisms governing MBN by additional complementary techniques. In addition to this, it is a common procedure to perform a micromagnetic multiparameter analysis, considering more than a single isolated parameter [17,73,86]. In interlaboratory tests, it was found that MBN analysis can lead to similar results and correlations, despite different methodologies used by the laboratories involved [23].

The underlying, fundamental principle of micromagnetic inspection techniques, such as MBN analysis, can be observed in the magnetic hysteresis loop. When a ferromagnetic material is subjected to an external magnetic field, with a field strength H, the magnetic flux density B inside the material changes according to its magnetic properties [91]. Based on this, the magnetic hysteresis loop of ferromagnetic materials can be obtained by plotting the magnetic flux density B for various field strengths. This way, the magnetic hysteresis loop illustrates the macroscopic magnetic properties of ferromagnets [91]. The interrelations between the magnetic flux density B, the magnetic field strength H, and the magnetization M are modeled by the equation:

$$B = \mu_0 (H + M) \tag{2.1}$$

where B is the magnetic flux density, μ_0 is the permeability in a vacuum, H is the magnetic field strength and M is the magnetization.

An exemplary hysteresis loop of a ferromagnetic material is depicted in Figure 2.4. In the initial, unmagnetized state, when no magnetic field is applied, there is no induction ($B = H = 0$). When the field strength of the magnetic field is increased, the magnetic flux density increases in the field direction until it reaches saturation (Figure 2.4). In this state, all magnetic dipoles are oriented in the direction of the magnetic field. Saturation magnetization M_0 is neither structure-sensitive nor is it temperature-sensitive, as it depends on only two factors: the magnitude of atomic magnetic moments m_{atom} as well as the number of atoms per unit volume n_{atom} [91].

$$M_0 = n_{atom} m_{atom} \qquad 2.2$$

When the field strength is lowered to zero, magnetic flux density remains, called remanence B_r. To remove magnetic flux density, a reverse magnetic field is applied with a field strength called coercivity H_c. When the field strength of the reverse magnetic field is increased, a saturation in the opposite direction is achieved when all magnetic dipoles are aligned with the magnetic field in the opposite direction. Removing the reverse magnetic field leads to the remanence in the opposite direction. To remove magnetic flux density from this point, magnetic field strength needs to reach coercivity [91].

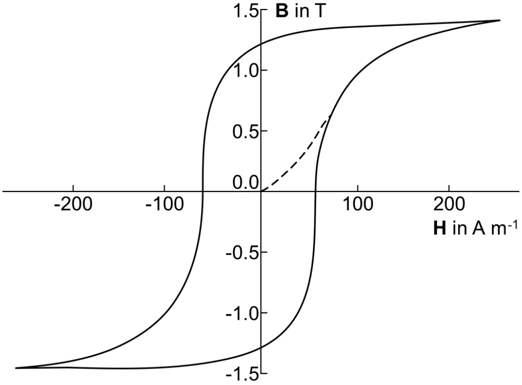

Figure 2.4 Characteristic magnetic hysteresis loop of a ferromagnetic material. According to [91][3]

Based on the shape of the hysteresis loop, various mechanical and microstructural properties can be approximated. An example of this can be seen in Figure 2.5 a), which presents typical hysteresis loops of hardened steel and soft iron. Some general tendencies that have been observed in the past include that stress states cause a sheering behavior of the hysteresis loop, whereas a change in hardness in many cases implies a change in coercivity [92]. This corresponds to the observation, that the predominant factor for coercivity H_c is the microstructure of a material, whereas saturation magnetization M_0, is dominated by the elemental composition.

---

[3] Reproduced with permission from Taylor and Francis Group LLC through PLSclear from Jiles, D.: Introduction to magnetism and magnetic materials (2015).

In general, residual stresses affect both, coercivity H_c, as well as saturation magnetization M_0 [17]. The predominant restriction of using these correlations in the actual practice of SI evaluation is that it is particularly challenging to measure the magnetic hysteresis loop for any given workpiece. This cannot be achieved by employing surface-mounted bobbin coils, which are usually used in industrial contexts. Reproducible and reliable hysteresis measurements usually demand special specimen geometries, like spheres or cylinders with coils wrapped around them for measuring magnetic flux density [75]. In response to this, techniques in micromagnetic testing have been developed, which do not require measuring the full hysteresis loop, such as MBN analysis. These approaches allow for the use of surface-mounted coils and can thus be adapted to given workpieces more easily [92].

When having a closer look into the hysteresis loop and monitoring it with higher resolution, discontinuities can be observed. When the field strength H is increased continuously, the magnetic flux density B does not change continuously and smoothly, but rather jerky and discontinuously in discrete jumps, this phenomenon is called the Barkhausen effect (Figure 2.5 b).

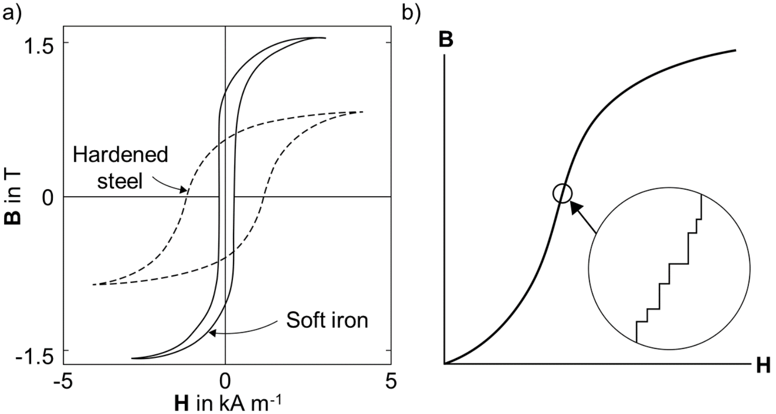

Figure 2.5 Fundamentals of micromagnetic testing: a) magnetic hysteresis for soft iron and hardened steel; b) magnetic Barkhausen noise phenomenon. Modified version of [91][4]

The origin of the Barkhausen effect and MBN can be found in the nature of magnetic domains, particularly domain wall movement and domain rotation. As discovered by Weiss in 1906, ferromagnets are composed of small regions, which are

---

[4] Reproduced with permission from Taylor and Francis Group LLC through PLSclear from Jiles, D.: Introduction to magnetism and magnetic materials (2015).

spontaneously magnetized to saturation. These are called magnetic domains. In each of the domains, the direction of magnetization is everywhere parallel. However, an unmagnetized ferromagnet in total reveals no net magnetization, because the direction of magnetization of all the domains is such that they cancel each other out. This is displayed in Figure 2.7 a) (marked I) [93]. During the magnetization of a ferromagnetic material to saturation, domains first expand due to reversible and irreversible domain wall motion (II). With increasing magnetic fields, the orientation of the magnetic domains rotates (III). Through these mechanisms of domain wall motion and domain rotation, the material is converted from a multi-domain to a single-domain state. At saturation magnetization, the remaining domain is aligned in the orientation of the applied field (IV) [93,94].

In a multi-domain state, before saturation, domains are separated by interfaces, called domain walls. Inside these finite transition regions, the direction of magnetizations changes gradually with position. The total angular displacement between the domains in iron is either 180° or 90°. Inside the domain walls, it changes over many atomic planes [17]. For a 180° domain wall in iron, Jiles calculates e.g. a thickness of approx. $t_{dw} = 38$ nm, which corresponds to 130 atomic layers [91]. There are two types of domain walls, called Bloch walls and Néel walls, named after Felix Bloch and Louis Néel. Néel walls can be found in very thin films with a thickness below a certain critical value, whereas Bloch walls can be found in bulk materials. The difference between a Néel wall and a Bloch wall is that for Néel walls magnetization rotates orthogonally to the normal of the domain wall, thus all magnetic moments are oriented in the plane of the thin film. Conversely, in Bloch walls, some of the magnetic moments face normally to the plane. This concept is illustrated in Figure 2.6.

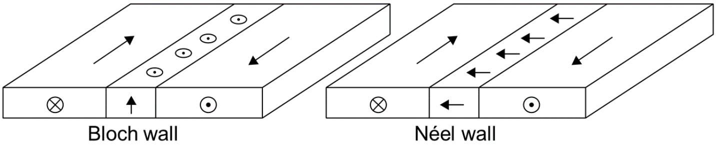

Figure 2.6 Difference between a Bloch wall and a Néel wall [91][5]

Based on the previous remarks, discontinuities in induction when applying a constantly increasing magnetic field strength, as observed by Barkhausen, derive from domain rotation and discontinuous domain wall motion, the latter factor being the

---

[5] Reproduced with permission from Taylor and Francis Group LLC through PLSclear from Jiles, D.: Introduction to magnetism and magnetic materials (2015).

more significant one [91]. Cullity and Graham state that wall movement dominates up to the knee of the magnetization curve and that domain rotation is the decisive factor from that point on to saturation [93]. Domain wall motion and magnetization rotation are depicted in Figure 2.7.

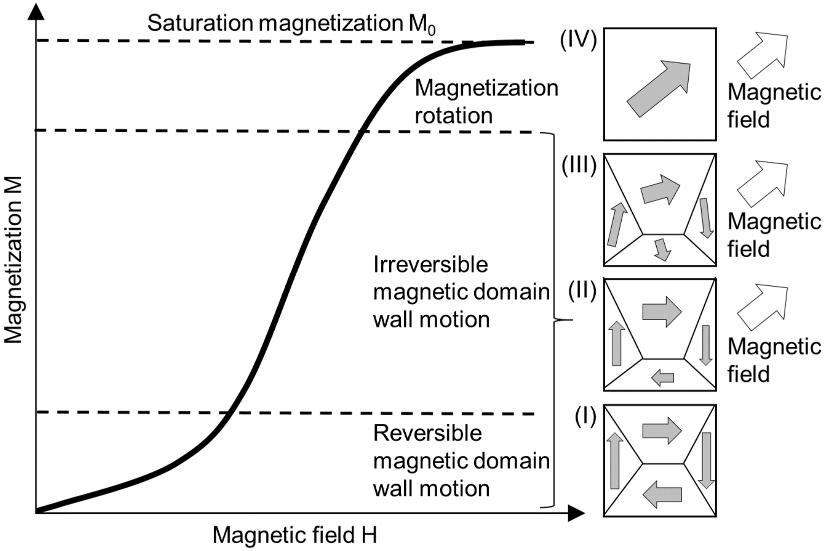

Figure 2.7 Domain wall motion and magnetization rotation in the initial magnetization curve: a) (I) demagnetized state, (II) domain wall motion, (III) magnetization rotation, (IV) single domain. According to [94][6]

Domain wall movement is hindered by imperfections in the crystal lattice, such as inclusions, dislocations, and their associated stress fields. Magnetic inclusions are isolated regions that differ magnetically from the bulk material such as impurities, e.g. oxides, carbides or sulfide particles, pores, voids, or cracks. These imperfections can act as pinning sites for domain walls. Thus, e.g. high dislocation density in a ferromagnet results in high impedance to domain wall motion and subsequently high coercivity and hysteresis loss [91]. The process of domain wall pinning is illustrated in [82]. Increasing the magnetic field strength can result in a sudden unpinning of the domain walls, causing MBN. A key diagram in MBN

---

[6] Reproduced with permission from Springer Nature BV, from Akagi, F.: Magnetic domain structures and techniques in micromagnetics simulation. In: Fujisaki, K. Magnetic material for motor drive systems. Engineering materials (2021); permission conveyed through Copyright Clearance Center, Inc.

analysis is the MBN envelope curve. It is obtained by plotting the summed-up intensity of MBN for varying field strength. An exemplary MBN envelope curve is depicted in Figure 2.8 a). The two most frequently analyzed parameters of MBN analysis are the maximum amplitude of the MBN envelope M_{max} and the field strength applied at M_{max} which is called coercive field strength derived from MBN H_{cM}. For martensite the field strength derived from MBN is close to the coercive field strength H_c, thus this field strength is usually referred to as coercive field strength as well [75]. In multiple studies, evidence has been provided that M_{max} is particularly sensitive to stresses and residual stresses, whereas H_{cM} tends to be especially sensitive to microstructural aspects, such as hardness. [17]. Examples of these correlations are depicted in Figure 2.8. Figure 2.8 b) presents a correlation between H_{cM} and Rockwell hardness HRC for C45E (AISI 1045). It can be observed that with increasing hardness, coercive field strength obtained from MBN analysis H_{cM} increases as well. Figure 2.8 c) presents a correlation between residual stresses and the micromagnetic parameters M_{max} and H_{cM} for annealed martensite with a hardness of 250 HV30. It can be observed, that M_{max} increases and H_{cM} decreases with increasing tensile stresses. For martensite which was not subjected to annealing (527 HV30), Altpeter et al. report a correlation with residual stresses only for M_{max}, whereas H_{cM} stayed on an almost constant level. The reason for this is the higher dislocation density of the non-annealed martensite, which results in more pinning sites compared to the annealed material [75].

Aspects of SI that have been assessed by MBN analysis include hardness [25], residual stresses [21,22], and microstructural alterations, such as phase transformations [24], changes in grain size [23,95], WEL formation [81,96] or grinding burn [63]. Baak et al. developed an approach for fatigue life prediction of deep drilled components [73,97]. Applications of MBN-based inspection in the field of structural health monitoring include the evaluation of stress states in landing gears of airplanes [21] and the assessment of steel embrittlement in reactor pressure vessels, caused by neutron irradiation [90,98]. Further correlations between micromagnetic parameters and mechanical properties are summarized in numerous review articles. A comprehensive overview of discovered correlations in the early days of research on MBN analysis is given in [92]. Altpeter et al. report on correlations between micromagnetic parameters and numerous aspects of SI, such as grain size, phase composition, hardness, hardness depth, texture, residual stresses, and the effects of aging in [75,90]. More recently, Baak et al. summarized applications of micromagnetic testing for various tasks in the fields of microstructure analysis and capability assessment in [85]. A crucial task in research on MBN is the quantitative description of MBN. This is particularly challenging, due to the random nature of MBN. One of the most breakthrough studies was published by

Bertotti et al., who in 1990 developed a stochastic process model, which tested well against experiments [91,99].

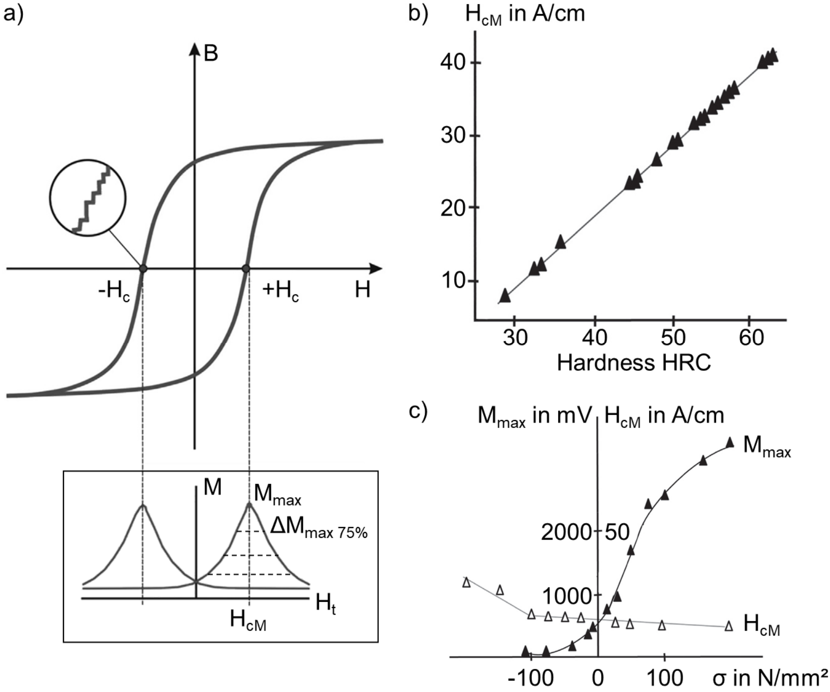

Figure 2.8 Magnetic Barkhausen noise (MBN) analysis for the assessment of material properties: a) MBN profile curve as derived from the magnetic hysteresis loop; b) exemplary correlation between coercive field strength H_{cM} and Rockwell hardness HRC for AISI 1045; c) exemplary correlation between the maximum MBN amplitude M_{max}, the coercive field strength H_{cM}, and residual stresses for annealed martensite (250 HV30). Modified version of [75][7]

Jiles et al. later extended Bertotti's model. By combining the basic model with the theory of hysteresis of the Jiles-Atherton model [100], they identified a way to

---

[7] Reprinted with permission from Elsevier from Altpeter, I. et al.: Electromagnetic techniques for materials characterization. In: Hübschen, G., Altpeter, I., Tschuncky, R., Herrmann, H.-G. Materials characterization using nondestructive evaluation (NDE) methods, 225–262 (2016); permission conveyed through Copyright Clearance Center, Inc.

model the sum of discontinuous changes in magnetization around the entire hysteresis loop. They found that MBN can be described as a combination of a deterministic, reproducible component and a stochastic component [101,102].

Inspection tasks, such as analyzing case hardening depth, or assessing residual stress gradients, demand a depth-resolved analysis of properties. Precisely determining the reading depth in MBN analysis has thus been a key challenge and also a highly debated, controversial topic throughout the past decades. In general, the depth of the interacting material in MBN analysis is governed by eddy current damping according to the skin effect. Exposing electrically conducting materials to an alternating field generates eddy currents. These have a damping effect on both, magnetic flux density and magnetic field strength. As a consequence, the values of magnetic flux density and magnetic field strength inside a material can decrease significantly with increasing distance to the surface. This way eddy current damping attenuates BN pulses [103]. As a result, detected MBN signals come from the near-surface layers. The frequency of MBN emissions ranges from a few kilohertz to a few hundred kilohertz. Based on the previous remarks, particularly the higher frequency parts of the received MBN signal are generated in near-surface regions [102].

The skin-depth δ_{skin} is defined as the depth below the surface of a material, at which the magnetic flux density B, or the magnetic field strength H drops to 1/e (approx. 37%) of its intensity at the surface. This quantity can be modeled by equation 2.3, in which the skin depth of the alternating magnetic field applied is inversely proportional to the square root of its frequency [90,93].

$$\delta_{skin} = \frac{1}{\sqrt{\pi f_{mag} \sigma_{cond} \mu_0 \mu_r}} \tag{2.3}$$

In equation 2.3 δ_{skin} is the skin depth, f_{mag} is the frequency of excitation, σ_{cond} is the electrical conductivity, μ_0 is the permeability in a vacuum and μ_r is the relative permeability [102]. Based on this equation, the thickness of the reading depth in MBN analysis is determined by the frequency, the conductivity and the permeability of a material. Usually, the frequency, conductivity and permeability in a vacuum are relatively easy to assess. Determining the relative permeability, however, is challenging [91].

Stupakov et al. published an in-depth, two-part work on reading depth in MBN analysis. They investigated martensitic steel ribbons with varying thicknesses and found that MBN reaches saturation at a ribbon thickness of t = 200 µm when using a sample wrapping coil. For industrial surface-mounted coils, they observed saturation already at t = 50 µm and observed significant suppression of the signal in the low-frequency part of the spectra. For softer ferritic steel with large grains they report reading depths of t = 200 µm for both, the sample wrapping coils as well as the surface-mounted coils [103,104].

As stated initially, an additional evaluation of SI is usually performed to complement micromagnetic inspection and calibrate the micromagnetic parameters. For this purpose, the most commonly employed procedures include metallographic analyses, microhardness measurements, and X-ray diffraction-based assessments of residual stresses. In addition to these, additional techniques for analyzing the structure of magnetic domains, domain rotation and domain wall movement, such as MOKE microscopy and MFM can be of particular merit. They allow for analyzing the magnetic properties governing micromagnetic inspection on a much smaller scale and with higher resolution and thus allow for a rather mechanism-based interpretation of the results of micromagnetic inspection.

Bitter technique

Perhaps the most straightforward and most common way of visualizing magnetic domains is the method developed by Bitter in the early 1930s, which is nowadays referred to as colloidal Bitter technique. Bitter suggested inspecting polished samples by applying a suspension containing colloidal magnetic particles to the surface and covering it with a coverslip. The magnetic particles then are attracted to the localized stray fields above the specimen and agglomerate at domain walls due to the magnetic moments. When the colloidal particles agglomerate, they highlight the domain walls for optical microscopy [105–107]. Many specialized procedures have been developed based on the classic Bitter method, such as a dry Bitter technique. In the dry Bitter technique, the need for using a coverslip is eliminated by letting the solution dry before optical microscopy. This way it extends the applicability of the classic colloidal Bitter technique in optical microscopy by allowing the observation of domain patterns at higher magnification. With specialized approaches based on the classic Bitter technique, analyses can also be performed at particularly high magnification in SEM and TEM [108].

Magneto-optic Kerr effect (MOKE) microscopy

Another approach for observing domain walls and their movement is to use magneto-optic methods. Both magneto-optic effects, the Faraday effect as well as the MOKE can be exploited for this purpose. The magneto-optic effects are based on the interaction of light with magnetic fields, which was first observed by Michael Faraday in 1845. In his studies, Faraday found that a magnet can rotate the polarization plane of transmitted light. In 1877 John Kerr discovered the MOKE effect, analyzing light reflected from an electromagnet pole. Kerr found that during reflection of light at a magnetized specimen, its plane of polarization is rotated. Since the Faraday effect requires light to be transmitted through magnetized specimens, it is limited to particularly thin or transparent specimens. This restriction does not apply for the MOKE. Thus, this effect is in general more frequently used when studying magnetic domains. Based on the effect discovered by Kerr, MOKE microscopy allows for visualizing the small rotation of the polarization plane of reflected light in greyscale images. This way, the domain structure can be visualized as a function of the magnetic field applied [105,109].

Figure 2.9 a) presents an exemplary result of MOKE microscopy of a thin film of permalloy. Domains which are magnetized in opposite direction can be clearly distinguished as light and dark regions [93].

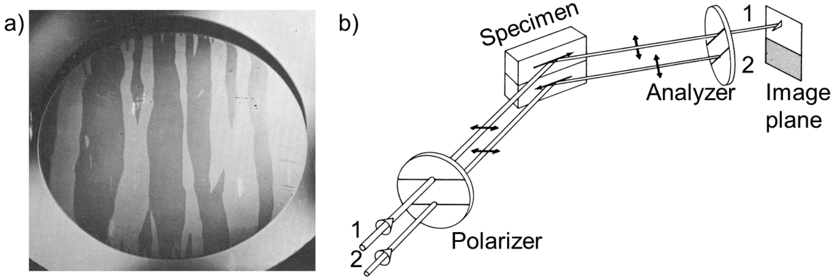

Figure 2.9 Oberservation of magnetic domains by magneto-optic Kerr effect (MOKE) microscopy: a) domains magnetized in opposite direction in a film of 81 permalloy observed using MOKE microscopy; b) domain observation by the MOKE. Modified version of [93][8]

The underlying principle of MOKE microscopy is illustrated in Figure 2.9 b) for a specimen with two antiparallelly magnetized domains. As light passes through a polarizer, light is obtained which is plane polarized. Due to the oppositely magnetized domains, the plane of polarization of beam one and beam two are rotated differently during reflection [93]. The reflected light is filtered by an analyzer and reaches a microscope. It can be seen that beam two is extinguished by the analyzer, due to its plane of rotation: Conversely beam one passes through the analyzer. As a result, the upper domain appears light, whereas the lower domain appears dark.

---

[8] Reproduced with permission from John Wiley & Sons - Books, from B. D. Cullity, C. D. Graham: Introduction to Magnetic Materials (2010); permission conveyed through Copyright Clearance Center, Inc.

A comprehensive review on MOKE and the related surface MOKE along with examples of common applications in materials characterization is given in [109].

Magnetic force microscopy (MFM)

In addition to the previously presented Bitter method and the approaches based on magneto-optic effects, MFM allows for observing magnetic structures. MFM is an approach in scanning probe microscopy which can be used for recording 2D images of local magnetic field gradients at the surface of specimens with particularly high resolution. First results obtained by MFM were published in 1987 by Martin and Wickramasinghe [110]. MFM derived from atomic force microscopy (AFM). Subsequently, the operating procedure is fairly similar. The general principle of scanning probe microscopy and MFM is presented in Figure 2.10.

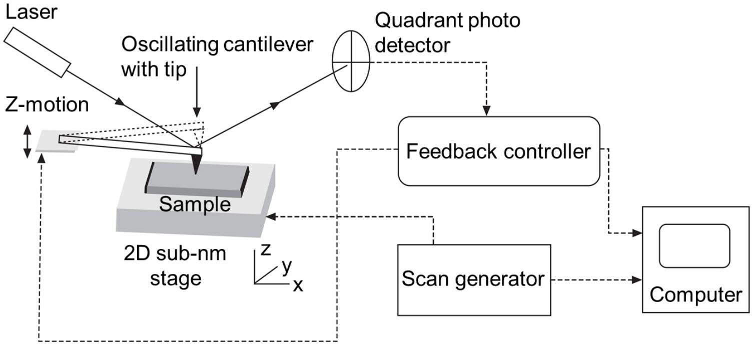

Figure 2.10 Experimental setup for scanning probe microscopy. In magnetic force microscopy (MFM) the interaction between the magnetic tip at the oscillating cantilever and the stray magnetic fields emanating from the specimen are recorded [111][9]

In MFM a magnetized tip is mounted to an oscillating cantilever. This tip ideally is a small particle with a single domain and constant magnetization. The cantilever is moved to scan the surface of the specimen either at constant height or at variable height. While the cantilever is in motion the amplitude, phase angle, and frequency of oscillation can change, due to the interaction between the magnetic tip and the stray magnetic fields emanating from the specimen. These changes in oscillation are recorded and used as a base for drawing conclusions about the magnetic force gradients at the surface. By also considering the topography of the specimen,

---

[9] Reprinted with permission from Elsevier from Thomson, T.: Magnetic properties of metallic thin films. In: Metallic films for electronic, optical and magnetic applications (2014); permission conveyed through Copyright Clearance Center, Inc.

which is obtained by the same instrument oftentimes in a first pass of the cantilever, magnetic effects and geometrical effects can be distinguished [111]. One of the downsides of MFM is that interpreting results is challenging, since the correlations between the stray magnetic fields above the specimen and the forces on the tip are rather complex and highly dependent on the design of the tip. As the tip in MFM is magnetic, there is the potential risk that it might cause domain walls inside the specimen to move, particularly in soft magnetic materials. By rule of thumb, Thomson estimates the magnetic field caused by the tip to have a strength of approx. $H = 100$ Oe at the surface of the specimen. Conversely, the magnetic stray fields emanating from the sample can also affect the magnetization of the tip [93,111].

2.2.4 X-ray diffraction

Fundamentals

Soon after Wilhelm Conrad Röntgen discovered X-rays in 1895 [112], numerous applications were developed, exploiting this type of electromagnetic radiation in fields such as medicine and industry. Röntgen's groundbreaking discovery also paved the way for novel fields of science, such as radiography or X-ray spectroscopy. Another discipline of research on X-rays that soon emerged was X-ray crystallography. This discipline is based on the diffraction of X-rays, which was discovered in 1912 by Max von Laue, Paul Knipping, and Walter Friedrich. Based on their works, William Henry Bragg and William Lawrence Bragg formulated Bragg's law, which up to this day is considered the fundamental law in XRD. A more detailed account of the history and the fundamentals of XRD is given in [113].

XRD in a crystal is based on the interplay between X-rays and the electrons of atoms. When X-rays encounter the electrons, they are diffracted as a function of the atomic structure of the crystal, leading to typical diffraction patterns. The interaction of crystalline substances with X-rays can thus be considered their unique fingerprint [113]. Based on the diffraction pattern, various microscopic and macroscopic properties of samples can be assessed. Nowadays, XRD is used to qualitatively and quantitatively assess properties such as phase composition [114], microstrains and -stresses [115], crystallite size [116,117], X-ray elastic constants [118] , and texture [119]. In addition to these applications, XRD has become the common standard for the nondestructive assessment of residual stresses in crystalline materials [120–122]. The general procedure for assessing properties based on diffraction patterns, which result from the crystal structure of a sample, is presented in Figure 2.11. To perform depth-resolved measurements, e.g. for obtaining depth profiles of residual stresses, usually electropolishing is performed intermittently to XRD. A major disadvantage of this method is that it involves the partial destruction of the workpiece. In addition to this, depth-resolved information can be obtained by special setups. For instance, grazing-incidence XRD allows for analyzing the crystal structure in very close distance to the surface [123].

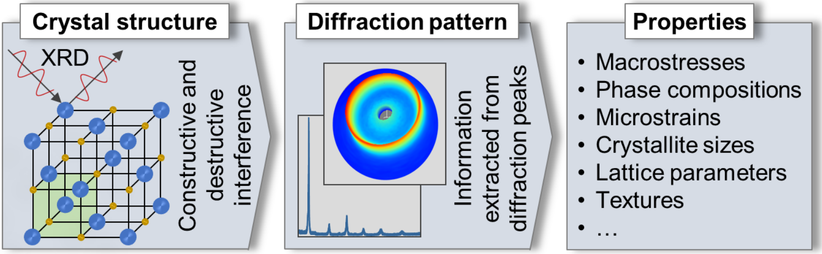

Figure 2.11 Interrelations between the crystal structure, the resulting diffraction patterns, and the properties that can be assessed based on X-ray diffraction (XRD)

In laboratory devices, X-rays are created by sealed tubes or rotating anodes. A tungsten filament is heated up and the electrons emitted are accelerated towards a target with an acceleration voltage of usually $U_{acc} = 20$ to 60 kV [119]. This results in the emission of X-rays by two atomic effects. When the electrons are decelerated, X-ray photons are emitted. This type of X-rays has a continuous spectrum and is called by its German name "Bremsstrahlung". In addition to this, atoms struck by the accelerated electrons are ionized and photons are emitted which have a characteristic energy [119]. As a result of these two mechanisms, the spectrum of X-rays emitted by the target is composed of a continuous curve resulting from the Bremsstrahlung and spikes at the discrete wavelengths resulting from the characteristic radiation. Usually, $K\alpha$ radiation is used in XRD, as this has the highest intensity. The remaining radiation, e.g. $K\beta$ is oftentimes absorbed by means of appropriate filters and monochromators. The composition of the spectrum of X-rays, produced by a sealed-tube is displayed in Figure 2.12 a) [113,119]. The underlying fundamental principle of XRD and Bragg's law is presented in Figure 2.12 b). When monochromatic X-rays with a wavelength of λ strike a crystal, they are scattered on different planes in all directions. The angle of incidence and reflection are identical. In Figure 2.12 b) two parallel beams with a wavelength of λ are reflected on different crystal planes. As it is reflected on a lower crystal plane, beam two travels a longer distance compared to beam one. The difference in distance travelled by the two beams is $\overline{ADC}$. When the scattered beams, travelling in the same direction, meet, they either undergo constructive or destructive interference. Given that the two beams are in phase, meaning that the distance $\overline{ADC}$ is a multiple of the wavelength λ and an integer n, constructive interference of the beams occurs and they are captured by the detector (equation 2.4) [113]:

$$\overline{ADC} = n\lambda \tag{2.4}$$

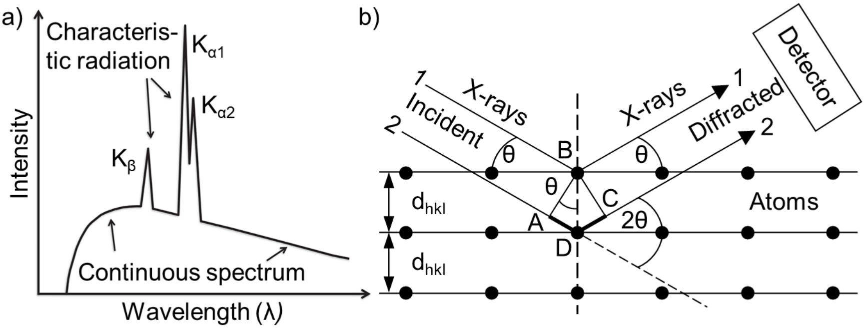

Figure 2.12 Fundamentals of X-ray diffraction: a) Continuous spectrum of the Bremsstrahlung and spikes at the wavelengths of the characteristic radiation; b) X-ray diffraction according to Bragg’s law. Modified version of [113,119][10]

Constructive interference can only occur for certain values of the angle θ, which is called the glancing angle. This angle depends on the lattice spacing d_{hkl} and the wavelength of X-rays λ. If the two beams are completely out of phase, destructive interference occurs and the reflected beams cancel each other out. Resulting from the periodicity of crystalline structures, constructive and destructive interference both occur in XRD. In the case of constructive interference, Bragg’s law (equation 2.5) can be obtained, based on the geometric conditions illustrated in Figure 2.12 b) and trigonometric functions [113,119]:

$$n\lambda = 2d_{hkl}\sin(\theta_{hkl}) \tag{2.5}$$

---

[10] a) Reprinted with permission from Elsevier from J. Epp.: X-ray diffraction (XRD) techniques for materials characterization. In: Hübschen, G., Altpeter, I., Tschuncky, R., Herrmann, H.-G. Materials characterization using nondestructive evaluation (NDE) methods (2016), b) reproduced with permission from Springer Nature BV from L. Spieß: Moderne Röntgenbeugung: Röntgendiffraktometrie für Materialwissenschaftler, Physiker und Chemiker (2019); permission conveyed through Copyright Clearance Center, Inc.

with n being the order of diffraction, λ the wavelength of X-rays, d_{hkl} the lattice spacing, and θ_{hkl} the angle of the diffracted beam. If the values of wavelength and Bragg angle are known, Bragg's law can be used for calculating the lattice spacing. Based on this general principle, numerous properties of crystalline materials can be analyzed in XRD experiments. The most common way of presenting diffraction patterns is by diffractograms, which usually plot the intensity of detected X-rays for 2 times θ. Information that is derived from diffraction patterns includes the number of peaks N, their position θ_i, their intensity I_i, their width, usually described by their full width at half maximum, and the line profile.

An exemplary peak of a diffractogram is presented in Figure 2.13. Between θ_1 and θ_2, intensity of the X-rays detected is significantly higher than the background noise. This range is called measuring interval. The maximum intensity I_{max} is detected at the glancing angle θ. Background noise is subtracted in the analysis of peaks, e.g. by a linear function through I_{B1} and I_{B2}. This way, the net maximum intensity I_0 is calculated by subtracting I_{B0}, which is the background intensity at the glancing angle θ, from I_{max}. The most common parameter to describe the shape of a peak is its width at half the net maximum intensity $I_0/2$. This parameter is called the full width at half maximum (FWHM). Since peaks are usually not perfectly symmetrical, the area under the peaks is oftentimes calculated. A parameter used to describe this area is the integral width IW, which multiplied by I_0 equals the area under the peak [113].

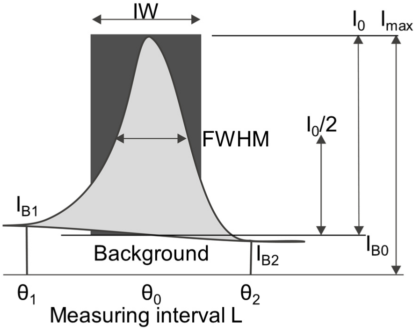

Figure 2.13 Characteristic parameters of a peak in X-ray diffraction (XRD). Modified version of [113][11]

---

[11] Reproduced with permission from Springer Nature BV from L. Spieß: Moderne Röntgenbeugung: Röntgendiffraktometrie für Materialwissenschaftler, Physiker und Chemiker (2019); permission conveyed through Copyright Clearance Center, Inc.

Figure 2.14 illustrates, how the characteristic parameters used to describe XRD patterns correspond to the crystallographic structure and thus to various properties of the material. It can be observed that the material properties can be assessed by different parameters. When assessing stresses, for example, the line profile, the width and the position of peaks should be considered. Conversely, the determination of particle sizes requires evaluating the width of peaks as well as the line profile. Here the position of peaks is not considered. As a result of these interrelations, it is vital to analyze which characteristic parameters of diffraction patterns matter the most for a given task, when designing an XRD experiment. Two opposing aspects in this regard are the time that is invested in measurements and the resulting accuracy. Subsequently, meticulous attention to detail is required in designing an experiment, to obtain all desired information with sufficient accuracy in as little time as possible [113].

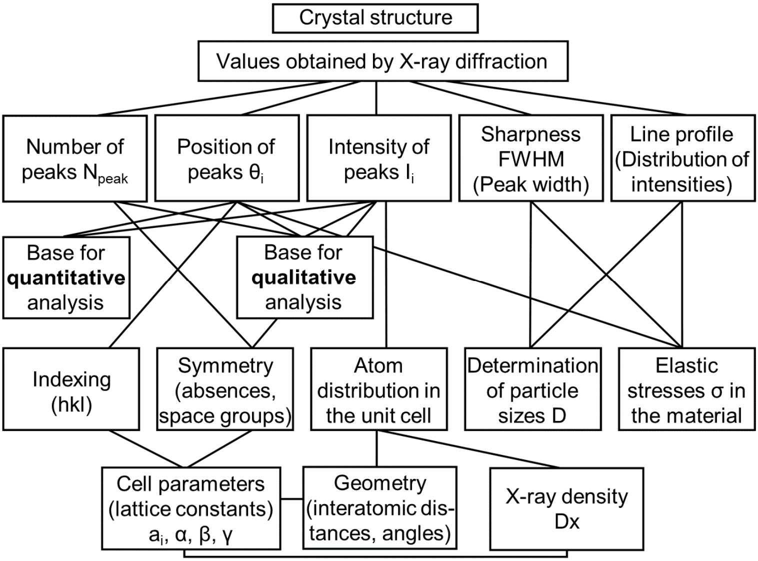

Figure 2.14 Information directly obtained or derived from X-ray diffraction (XRD) experiments. Modified version of [113][12]

---

[12] Reproduced with permission from Springer Nature BV from L. Spieß: Moderne Röntgenbeugung: Röntgendiffraktometrie für Materialwissenschaftler, Physiker und Chemiker (2019); permission conveyed through Copyright Clearance Center, Inc.

When X-ray beams are diffracted from a polycrystalline sample with a large number of crystals, the diffracted X-rays create a series of characteristic diffraction cones. The reason for this is that the incident beam is diffracted by the numerous randomly oriented crystals. Observing larger areas of diffraction cones requires advanced detector technology.

In XRD, detectors allow for registering the intensity of the diffracted beam. They can be categorized by their detection area as point detectors (0D), line detectors (1D), and area detectors (2D). There are various types of detector technologies, exploiting different physical phenomena. In gas detectors, incoming X-ray photons ionize a gas [119]. Solid detectors observe the fluorescence of special materials. Besides these, there are detectors based on semiconductor technologies [119]. In the past decades, immense progress has been made particularly in the 2D detector technology [124]. An extensive review of the state of the art in XRD based on 2D detector technology is given by He [124].

Besides detectors, performing XRD experiments requires several other key components, such as an X-ray source, usually a monochromator, and a goniometer [113]. The goniometer allows for precisely moving the X-ray source, the detector, and the sample. The most common arrangement of the components is the Bragg-Brentano geometry, as presented in [119].

Crystallite size

In the past decades, multiple techniques have been developed for the determination of crystallite size, based on data obtained in XRD. One of the most widespread equations for this purpose is the Scherrer equation 2.6 [125].

$$D_{cryst} = \frac{k\lambda}{FWHM \cos\theta} \qquad 2.6$$

where D_{cryst} is the crystallite size in nm, k is a constant that depends on the particle shape (k = 0.94 for spherical particles), λ is the wavelength of X-rays, FWHM is the full width at half maximum of the peaks (FWHM) and θ is the Bragg angle [117,126]. Based on the calculated crystallite size, the dislocation density is oftentimes roughly approximated using the equation 2.7 [117].

$$\delta = \frac{1}{{D_{cryst}}^2} \qquad 2.7$$

Residual stresses

Mechanical stresses that exist at ambient temperature in materials that are entirely free of any temperature gradients, external forces, or torques are called residual stresses [119,121]. Residual stresses are composed of stresses of the first, second, and third kind. The kind of residual stresses depends on their scope of action. Residual stresses of the first kind are constant for larger regions of the material, usually multiple grains. These are considered the residual macrostresses. Residual stresses of the second kind are constant for smaller regions, usually one grain or a subset of a grain. They are referred to as homogeneous microstresses. Residual stresses of the third kind are marked by slight submicroscopic differences [119]. They are inconstant for very small regions of the material, usually multiple atomic distances. Thus, they are called inhomogeneous microstresses. The sum of residual stresses of the first, second, and third kind are the locally effective residual stresses at a given spot [119,121].

Stresses in a specimen can be presented by a symmetric third-order tensor $\sigma_{ij,}$ where i is the direction of the acting force and j is the area the force acts on, as displayed in 2.8 [119]. The stresses on the main diagonally are the normal stresses, whereas the remaining ones are considered shear stresses.

$$\sigma_{ij} = \begin{pmatrix} \sigma_{11} & \sigma_{12} & \sigma_{13} \\ \sigma_{21} & \sigma_{22} & \sigma_{23} \\ \sigma_{31} & \sigma_{32} & \sigma_{33} \end{pmatrix} \qquad 2.8$$

Residual stresses in a material are linked to elastic lattice strains in a distorted crystal structure by Hooke's law of isotropic elasticity [120]. Subsequently, different values of the lattice spacing d_{hkl} can be observed for crystals affected by stresses, when compared to the same crystals free of stresses. Following Bragg's law 2.5 a change in the lattice spacing d_{hkl} results in a change in the angle of the diffracted beam θ, given that all other values stay constant. Based on this underlying principle, various approaches have been developed in XRD for assessing residual stresses. A comprehensive review on the fundamentals of X-ray-based assessment of residual stresses and the history of this discipline is given by Eigenmann and Macherauch in [127]. A particularly detailed account of the assessment of residual stresses in mechanically deformed subsurfaces is given by Scholtes in [122].

For a Bragg angle which has been determined in a diffraction experiment, lattice spacing can be calculated, using Bragg's law (2.5). Depending on the stress state in a specimen, lattice spacing can either increase or decrease. The lattice spacing is linked to the elastic lattice strains according to 2.9:

$$\varepsilon^{hkl}(\varphi,\psi) = \frac{d^{hkl}(\varphi,\psi) - d_0^{hkl}}{d_0^{hkl}} \quad 2.9$$

where $\varepsilon^{hkl}(\varphi,\psi)$ is the elastic lattice strain for the hkl planes and a specimen orientation specified by the azimuthal angle φ and the polar angle ψ, $d^{hkl}(\varphi,\psi)$ is the lattice spacing measured at any given φ and ψ angle, and d_0^{hkl} is the lattice spacing in the crystal free of strains [119].

As the exact values of lattice spacing and Bragg's angle for crystals free of strains are usually not known, alternative ways for calculating $\varepsilon^{hkl}(\varphi,\psi)$ are desired, which do not require the precise value of d_0^{hkl} or θ_0^{hkl}. One method, which requires only an approximate value of d_0^{hkl} is the $\sin^2\psi$-approach [119]. The method was first proposed by E. Macherauch in 1958 [127]. Throughout the past decades, this method has been the most frequently employed approach for calculating residual stresses, based on diffraction data. The $\sin^2\psi$-method is used for biaxial, surface parallel stress states. The values of the normal stress σ_{33} and the corresponding shear stresses subsequently are zero. This applies to the surface of materials due to equilibrium conditions. When using laboratory XRD systems, this assumption can usually also be made for the outer subsurface, as a result of the relatively shallow penetration depth of X-rays [127]. In the $\sin^2\psi$-method, usually point or line detectors are employed to determine the evolution of lattice spacing for varying sample orientations, specified by the polar angle ψ. Based on the data in diffraction experiments, the residual stress state can be calculated, using several methods, which will be tackled in the following paragraphs.

In the first step, the diffraction data obtained in experiments is processed by various mathematical operations. Usually, the background noise is subtracted, the $K_{\alpha2}$-peak is removed and the peaks are fitted, e.g. by the Pearson VII algorithm [113]. The fundamental principle of the $\sin^2\psi$-method is depicted in Figure 2.15 [119]. When plotting the lattice spacing or the Bragg's angle for various values of $\sin^2\psi$, the slope of the graph can be used to analyze the stress state in the sample (Figure 2.15 b). Figure 2.15 c) presents various typical shapes of curves, plotting lattice spacing as a function of $\sin^2\psi$. It can be seen that shear stresses cause a typical ψ-splitting of the curve as a result of asymmetric strain distribution for positive and negative ψ-tilts. Nonlinearity is observed when residual stress gradients or crystallographic texture are present in the penetration depth of X-rays. In such cases, specialized approaches, e.g. grazing-incidence diffraction, are oftentimes preferable [119,123].

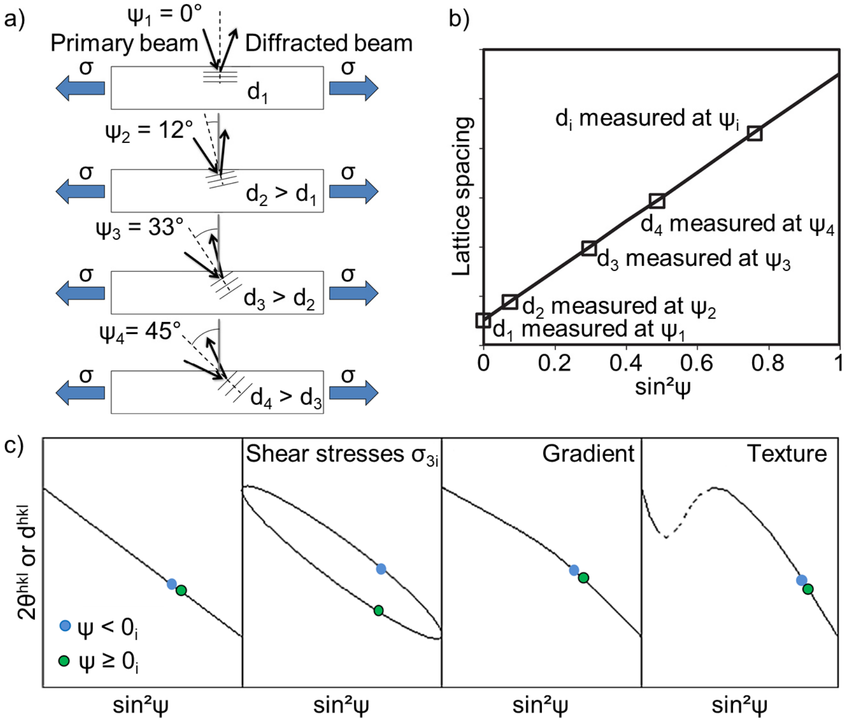

Figure 2.15 Fundamental principle of sin²ψ-method in X-ray diffraction (XRD): a) evolution of lattice spacing as a function of orientation for longitudinal tensile stresses, b) plot of lattice spacing as a function of sin²ψ for tensile residual stresses, c) types of sin²ψ distributions for different materials. Modified version of [119][13]

The major downsides of the sin²ψ-method include that the procedure is time-consuming and requires specialist skills and knowledge by the operators [74]. In addition to this, complex and relatively costly instrumentation is required, as precision is vital in this method, e.g. when setting the angles.

---

[13] Reprinted with permission from Elsevier from J. Epp.: X-ray diffraction (XRD) techniques for materials characterization. In: Hübschen, G., Altpeter, I., Tschuncky, R., Herrmann, H.-G. Materials characterization using nondestructive evaluation (NDE) methods (2016); permission conveyed through Copyright Clearance Center, Inc.

An alternative approach, which is based on modern 2D detectors, is the cosα-method. This approach was proposed in the late 1970s. Throughout the first decades after its development it was used only on a very limited scale and primarily in academic contexts in Japan. However, the advent of novel 2D detector technology, particularly image plates, recently gave rise to cosα-method on a global scale. Thus, in the past years, the method has rapidly been gaining importance, as a commercial system exploiting the principle was released by Pulstec Industrial Co., Ltd. in 2012 [74,118,120]. An extensive review of the cosα-method is given by Tanaka [120].

The cosα-method is also commonly referred to as the single-exposure method since it is based on the observation of one single intersection of the diffraction cone with a 2D detector. The resulting ring at the intersection is called a Debye-Scherrer ring. Stresses in a specimen cause the Debye-Scherrer ring to deform. In the cosα-method, this deformation of the ring is analyzed and compared to the perfectly circular ring which can be observed for unstressed specimens [118]. Just like the $\sin^2\psi$-method, the cosα-method is based on linking the strain distribution assessed by XRD to the stress state following Hook's law of isotropic elasticity [120]. An extensive review of the mathematical fundamentals of cosα-method, including the application of the method for triaxial residual stress states is given by Tanaka [120]. Many scientists provided evidence that the $\sin^2\psi$-method and the cosα-method lead to corresponding results. Delbergue et al. found a smaller scatter and better repeatability when using the cosα-method [74,118,120].

2.2.5 Advanced approaches for crystallographic analysis in SEM

Many advanced approaches have been developed in scanning electron microscopy that allow for a crystallographic analysis of microstructural features. For instance, properties such as grain morphologies, grain size gradients, and dislocation densities can be assessed using a variety of techniques. These include relatively well-established approaches, such as EBSD, as well as rather novel, emerging techniques, such as TKD. The following sections cover the fundamentals underlying the methods EBSD, TKD, ECCI, and STEM and present the main fields of application along with current challenges and major limitations of these methods.

Figure 2.16 presents a schematic illustration of the respective instrumentations and setups employed for the techniques. It can be observed that for some of the approaches (STEM and TKD) electron-transparent thin films are required, whereas for other methods (EBSD and ECCI) usually relatively thick bulk samples are analyzed. In addition to this, it can be seen that some methods, such as EBSD and TKD, require tilting of the samples by a defined angle. This is usually done by using appropriate sample holders.

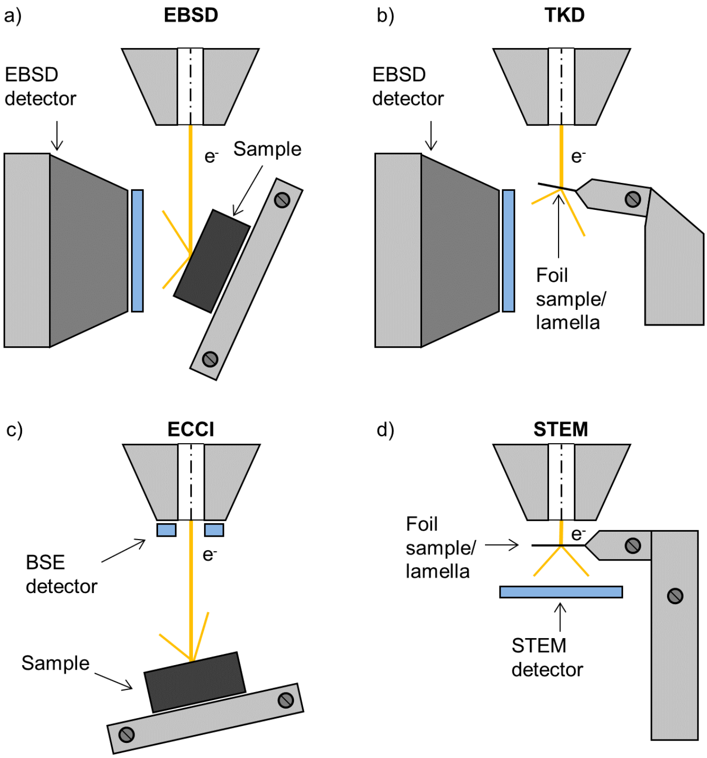

Figure 2.16 Illustration of the experimental setup for crystallographic analyses in SEM: a) electron backscatter diffraction (EBSD); b) transmission Kikuchi diffraction (TKD); c) electron channeling contrast imaging (ECCI); d) scanning transmission electron microscopy (STEM). Modified version of [128]

Electron backscatter diffraction (EBSD)

Building upon the studies of Seishi Kikuchi and other pioneers in the field, automated EBSD was developed in the 1980s and early 1990s [128]. Ever since then, this technique has gained enormous importance in various fields of materials science research for tasks such as phase identification, grain morphology and grain size distribution assessment, as well as the quantitative characterization of crystallographic texture on micro and macro scale [128]. Today, EBSD is considered to be the most popular method in orientation imaging microscopy (OIM) [129].

The basic principle underlying this technique is the detection and evaluation of backscatter Kikuchi diffraction patterns. These are formed when an incident beam strikes a specimen and in response, the backscattered electrons are elastically diffracted, losing energy. For EBSD the specimen is usually tilted at 70° so that the electron beam hits the surface of the specimen under an angle of 20°. The backscattered electrons are captured using a phosphor screen and the formation of Kikuchi patterns on the screen is observed, e.g. by a charge-coupled device (CCD) camera [129]. For OIM, the beam is scanned across the surface to obtain Kikuchi patterns for the entire surface region of interest. To assess the crystal orientation, the patterns detected are evaluated, usually by Hough-transform, and matched to reference patterns of the material under investigation.

One of the major limitations of EBSD can be found in spatial resolution, particularly when it comes to nanocrystalline materials. The lateral resolution of this technique goes down to approx. 50 to 200 nm, some give an estimate of 120 nm, as it depends on numerous parameters, such as the material of the specimen, the primary beam energy used, and the type of microscope employed [129,130]. Despite continued efforts to enhance the resolution and persistent and significant progress in this field throughout the past decades, TEM-based analyses remain oftentimes superior to EBSD for particularly fine-grained materials [128,129].

Transmission Kikuchi diffraction (TKD)

To overcome the shortcomings of traditional EBSD techniques, for instance the limited spatial resolution, transmission-EBSD, commonly referred to as TKD was proposed by Keller and Geiss in 2010. They provided evidence that TKD allows for considerably enhanced spatial resolution and diffraction pattern quality compared to conventional EBSD. Keller and Geiss reported that TKD can be used for characterizing nanostructures down to 10 nm [130–132]. Nowadays, the technique is mainly employed for analyzing materials with grain sizes ranging from $D_g = 10$ to 200 nm [128]. The major difference between TKD and conventional EBSD can be found in the design of specimens. Whereas in conventional EBSD relatively thick bulk specimens are used, thin foils are analyzed in TKD. This results in a significantly smaller interacting volume between electron beam and specimen for TKD compared to EBSD. In an on-axis geometry instrumentation, thin foils are placed perpendicularly to the incident beam and the detector is positioned right under the specimen to obtain the Kikuchi patterns. Conversely, in an off-axis geometry, thin foils are slightly tilted, usually by 20°, so that the detector is shifted to the side. A systematic and comprehensive review of these two approaches in TKD is given by Niessen et al. They report on faster acquisition rates and subsequently lower drift-related issues in on-axis geometry. The off-axis geometry, however, was found to be less sensitive to changes in beam current and beam energy [133].

Electron channeling contrast imaging (ECCI)

ECCI is a common approach for monitoring local imperfections in the crystal lattice, such as dislocations or stacking faults. Conversely to TEM, this technique can be used to study relatively thick, bulk samples instead of thin foils. This significantly facilitates sample preparation, making ECCI a relatively fast and non-destructive approach. In addition to this, the observable area is relatively large compared to TEM. On the other hand, the spatial resolution in ECCI usually does not match that of TEM-based analysis. In recent years, however, results have been reported which indicate that high-resolution ECCI using state-of-the-art instrumentation may well compete with the resolution of TEM, with a defect image width of about 15 nm [134–136].

Electron channeling contrast of backscattered electrons in SEM was first observed by Coates in 1967. However, the limited resolution of the instruments available at the time severely limited the applicability of the technique. With the advent of high-performance SEM in recent decades, the range of applications for ECCI has increased significantly and the method has gained momentum [136].

The underlying fundamental principle of ECCI using conventional backscattered electron detectors is the visualization of the shift in intensity of backscattered electrons at local defects in the crystal lattice. The angle between the lattice planes and the incident beam determines the intensity of the backscattered electrons [128]. When the angle between the lattice planes and the primary beam is close to the Bragg angle, there is limited interaction between electrons and the crystal lattice, and the electrons pass relatively deep into the material. This is referred to as the electron channeling mechanism [135]. The corresponding grain subsequently appears relatively dark in the backscattered electron (BSE) image, as few electrons are backscattered and the grain is considered to have a good channeling contrast. At local defects in the crystal lattice, such as dislocations, the channeling of the electrons is disturbed and the intensity of backscattered electrons significantly increases at the defects. As a result, local defects influencing the intensity of backscattered electrons can be observed as bright features in ECCI [128,135].

ECCI can be performed in low-tilt and high-tilt configurations, using a pole-piece mounted detector, or a side-mounted detector respectively [136]. To enhance the dislocation and interface contrast of this technique, and thus its general applicability and merit, controlled ECCI was developed. This approach couples traditional ECCI with an EBSD mapping of the surface, which is used to determine the optimum tilting of the sample and perform ECCI under controlled diffraction conditions [135].

Scanning transmission electron microscopy (STEM)

STEM can be considered a hybrid of SEM and TEM in many ways, as it monitors scattered transmitted electrons passing through a raster-scanned specimen [137]. Resulting of this underlying principle, STEM requires an electron-transparent specimen. Usually, thin-foils with a thickness of less than $t = 50$ nm are examined, similar to the ones for the previously presented method of TKD. After passing the specimen, the scattered electrons are detected by STEM detectors. STEM allows for particularly high spatial resolution, down to the sub-nanometer regime [138]. A comprehensive review of STEM is given by Nellist in [137].

2.2.6 Impact on performance

The various aspects of SI as pointed out in 2.2.1 can significantly impact the performance of components. SI can e.g. extend or shorten the life of components decisively. Even modifications that appear relatively small and are erroneously considered insignificant, can significantly undermine the in-service performance of a component. In critical cases, this can potentially yield disastrous consequences. As a consequence, the impact of SI on the performance of components has evolved into a major topic of research. Altered SI was found to impact aspects such as fatigue performance, creep, corrosion resistance, stress-corrosion cracking, and wear resistance [51].

A prime example of detrimental alteration of SI is grinding burn, which is an undesired modification of microstructure and residual stresses, due to excessive temperatures in grinding. Grinding burn can shorten component lifetime significantly [53]. Examples of safety-critical components failing due to poor SI resulting from inappropriate grinding conditions are presented by Holshouser [20]. He reports on in-service failures of airplane landing gears made of quenched and tempered steels. Some of these failures resulted from SI-related aspects, such as grinding cracks. Holshouser concludes that quenched and tempered steels can be employed for such components subjected to ultra-high stress levels only, if meticulous care is given in processing and fabrication [20]. Examples like these, illustrate the vast importance of SI for applications in fields such as aerospace engineering or the automotive industry.

Fatigue cracks are well known to initiate at the surface in geometric features, thus the surface and subsurface conditions are vitally important with respect to fatigue performance [50]. Numerous aspects of SI were found to impact fatigue performance. Surface topography significantly affects fatigue when $R_a \geq 0.1$ µm [10]. In addition to this, residual stresses have a vast impact on fatigue performance. In general, when their nature is tensile, they are unfavorable for fatigue performance, since tensile residual stresses generally foster the generation and growth of cracks. Conversely, compressive residual stresses are favorable for fatigue performance as they can delay both, crack initiation and propagation [59]. The impact of residual stresses on fatigue performance in general depends on the hardness of materials. Whereas hardened materials clearly show the effect, the fatigue performance of recrystallized materials was not found to be affected by residual stresses [53]. Besides the residual stresses at the very surface, the residual stresses in the subsurface are of major importance. For instance, Breidenstein reports on hard turned specimens with tensile residual stresses at the surface that can have similar fatigue performance as ground specimens that show compressive surface residual stresses. The reason for this might be that the tensile residual stresses in the hard turned surface were found to evolve into compressive residual stresses below the surface [53]. Thus, it is vital to consider the evolution of residual stresses below the surface. In general, residual stresses affect rather high cycle fatigue (HCF) than low cycle fatigue (LCF) [51].

Surface defects like WEL formation were found to affect LCF and HCF fatigue, as they tend to promote early fatigue crack initiation. Other microstructural surface anomalies that can have a detrimental impact on fatigue performance are material drag, micro-cracking, and pitting [51]. Detailed summaries of studies reporting on the effects of SI on fatigue performance, corrosion performance, and wear resistance can be found in [10,50,59].

2.3 White etching layers in machining

Over the past few decades, considerable evidence has been provided that one of the characteristics of SI that is particularly detrimental to component performance and life is the formation of hard and brittle WEL. In the upcoming sections, the fundamentals and properties of this microstructural anomaly will be covered, along with the mechanisms that govern the formation of WEL. In addition to this, destructive and nondestructive methods for the detection of WEL will be presented as well as findings on their impact on component performance and life.

2.3.1 Fundamentals, formation mechanisms, and properties

WEL also named white layers, non-etching layers, white phase, or phase transformed material, are located immediately beneath the surface. They have been reported for steels [139–141], titanium [56,142], and nickel-based superalloys [143–145]. The generic term WEL derives from their appearance [146]. Under an optical microscope, they appear white, when using a SEM, they seem featureless [46]. The reason for the white and featureless appearance is debated. Some claim it is an enhanced resistance of the WEL to etching that makes them appear white [53,141,147]. Others question this hypothesis, arguing that the appearance of WEL results from the scattering of light in their nanocrystalline structure [139].

The first published reference to WEL is attributed to J. W. Stead, who, in 1912, published his findings on WEL in used steel wire ropes [146,148]. WEL can be generated in various ways. They can be induced by production processes such as grinding, blanking, reaming, drilling, milling, highspeed punching, explosive forming, and electrical discharge machining [139,148]. Besides WEL induced by production processes, such layers can also be observed in engineering components after these have been removed from their service environment. For instance, they have been reported for components such as leaf springs, turbine shafts, piston rings, liners, rail-heads, and roller bearings [148]. In these applications, WEL can form as a result of various types of loading, such as impact loading, abrasion or sliding at rubbed surfaces. They can also be found as a result of laboratory tests, simulating certain types of loading, e.g. wear in pin-on-disk tests or wear resulting from ballistic impacts [149]. In all these scenarios, WEL generation occurs as a result of either thermal, or mechanical loads, or various combinations of these and sometimes chemical loads [114,139,148].

As a result of the enormous spectrum of WEL, information available on their characteristics is oftentimes conflicting and appears contradictory. Numerous studies report findings on structures and properties of WEL which seem fundamentally opposing. For instance, Guo and Sahni compare WEL produced by turning and grinding and conclude that the layers differ substantially in surface structure characteristics, microstructural aspects, microhardness, and also their chemical composition [139,150]. It appears as if the generic term WEL lacks precision. Bulpett therefore suggests further distinguishing between the descriptive term WEL, indicating etch-resistance, and what he calls thermo-mechanically transformed white layers [151]. In attempts to pull together the disparate findings on the formation, structure, and properties of WEL, numerous review articles have been published on this subject. Some of the most comprehensive ones include the works of Eyre and Baxter [146], Griffiths [148], and Brown [56].

Given the complexity of the subject, in-depth and mechanism-based studies are required when analyzing WEL. This demands e.g. that the properties of WEL are analyzed in close conjunction with their structure and the mechanisms that govern their formation, considering particularly the thermal and mechanical loads. The interrelationship between the formation mechanisms, the structure and the mechanical properties of WEL is presented in Figure 2.17. Detailed information on these fields will be given in the following paragraphs.

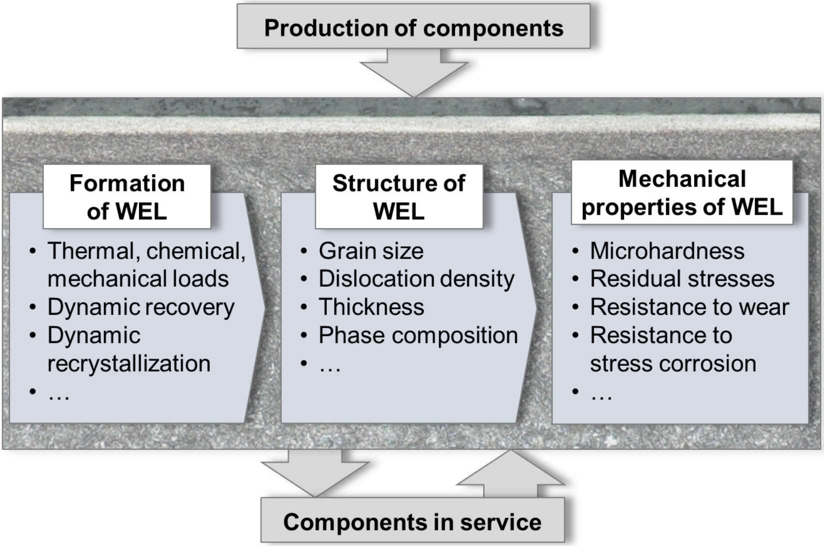

Figure 2.17 Interrelationship between the formation mechanisms, the structure and composition, and the mechanical properties of white etching layers (WEL)

Formation of white etching layers (WEL)

WEL formation is governed by the thermal, mechanical and chemical loads acting on surfaces. Usually, either thermal, mechanical, or combined thermo-mechanical mechanisms play the dominant role. Chemical loads are associated with certain types of white layers that result from surface reactions with the environment. Examples of such layers include the ones produced by carburizing, nitriding, and oxide plowing [148]. These layers, however, differ significantly from thermo-mechanically generated WEL in their formation, structure and properties. Despite the visual similarities of the layers in optical microscopy, such layers are oftentimes not included in the spectrum of WEL. The inherent differences between these different types of layers that appear white in optical microscopy were already recorded by Field and Kahles. In their pioneering work on SI, they analyzed WEL generated in the drilling of steels and observed severe differences to layers resulting from nitriding [14].

It is widely agreed that the formation of WEL in machining processes is caused by two fundamental mechanisms, which originate from the combination of temperatures, stresses, strains, and strain rates in cutting [56,145,152]. WEL can either result from the mechanism of phase transformation or due to grain refinement, resulting from severe plastic deformation plus dynamic recrystallization [153]. Moreover, a combination of both mechanisms is oftentimes proposed. This underlying concept of WEL formation is depicted in Figure 2.18.

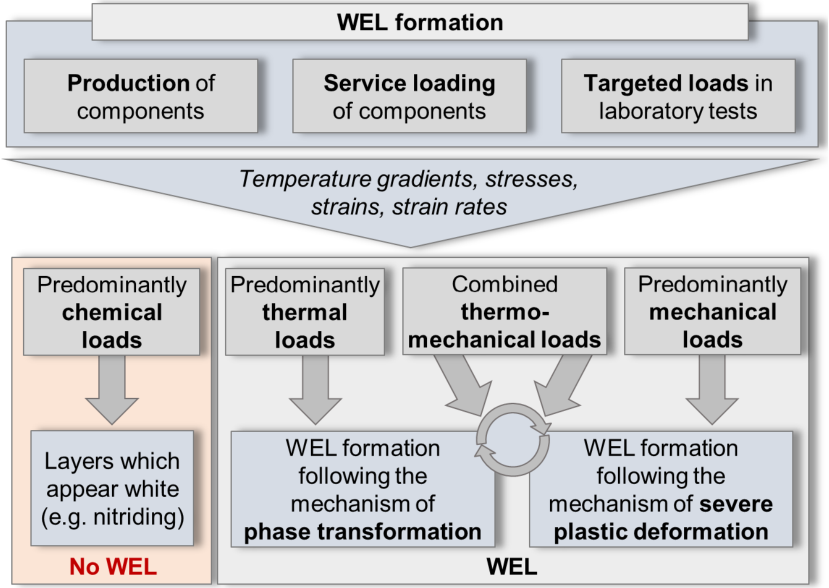

Figure 2.18 Concepts of white etching layer (WEL) formation

The mechanism of phase transformation is governed by the temperatures in machining. As comprehensively discussed in chapter 2.2.1, high temperatures can occur at the interface between tool, chip, and workpiece, as a result of the high deformation in a very constrained region [50]. The actual cutting process is followed by rapid cooling, particularly when using coolants. The heat generated is dissipated by the chip, the workpiece, the tool, and the environment. When machining steels, nickel-base alloys, and titanium, the heat is usually localized very closely to the surface, as a result of the relatively modest thermal conductivity of these materials [56]. This typically causes steep temperature gradients in the subsurface. As a result, evidence has been provided in numerous experimental and model-based approaches that phase transformation temperatures can be transgressed in the near surface of the workpiece in machining, despite the fact that only a small share of the heat generated is dissipated by the workpiece [50,152]. In addition to this, it was observed in various works that phase transformation in

WEL can occur at temperatures well below the nominal phase transformation temperature A_{c1} [154]. Analyzing machining of AISI 52100, Zhang et al. hypothesize that increasing strains and stresses in machining reduce austenitization temperature [152]. This agrees with the findings of Du et al., who record a reduction in phase transformation temperature, due to large strains and strain rates in highspeed machining of a nickel-base superalloy [145]. The previous examples mostly present WEL resulting from combined thermal and mechanical loads. However, WEL can result from purely thermal loads as well. For instance, Griffiths reports on WEL formed in electrical discharge machining as a result of thermal loads, without any mechanical contact at all [16].

For steels, the reverse martensite transformation is oftentimes observed when WEL are formed [155]. Subsequently retained austenite inside the layers is indicative of WEL formation due to the phase transformation mechanism. In addition to this, a dark layer is oftentimes observed right beneath a WEL in steel. Since this dark layer has only been reported for WEL formed by the phase transformation mechanism, this also serves as evidence of this type of WEL generation [56,154].

Hosseini et al. present an in-depth study on the structure of WEL as a result of their formation, comparing primarily thermally and primarily mechanically induced WEL. They found that the microstructural evolution during surface generation in predominantly thermally-induced WEL was initiated by dynamic recovery and then evolved to dynamic recrystallization at higher temperatures [156]. Such a transition from dynamic recovery to dynamic recrystallization is also proposed by Barry and Byrne for predominantly thermally induced WEL in steels. According to them, dynamic recrystallization is favored by the decrease in the stacking fault energy of the material due to reverse martensite transformation in the WEL [155]. Liao et al. provide evidence of a graded microstructure inside WEL in a nickel-based superalloy. They found that the WEL is composed of a layer resulting from dynamic recrystallization and a layer caused by dynamic recovery, which extends further into the subsurface [157].

When phase transformation temperature is not transgressed, WEL can form according to the mechanism of grain refinement caused by severe plastic deformation. An in-depth study on this formation mechanism is given by Hossain et al., who analyzed WEL formed as a result of dynamic impact loads. [114]. Hosseini et al. provide evidence that dynamic recovery is the dominating factor in this formation mechanism. In their investigations, they observed that plastic deformation causes the martensite/bainite platelets of the bulk material to reorient along the shear direction. The platelets are broken down into elongated subgrains as a result of dynamic recovery [156]. In this mechanism, dislocations pile up within the grains and concentrate into tangles, forming subgrain boundaries [149,158].

Various other studies report on WEL formation by combined phase transformation, severe plastic deformation, and additional mechanisms, such as carbide dissolution. Akcan et al. hypothesized that the governing mechanism in WEL formation is the deformation to very large strains combined with effects such as dynamic recrystallization and cementite decomposition and dissolution [139]. Du et al. propose that WEL can form as a result of a coupled deformation-phase transformation mechanism [145]. This agrees with the findings of Zhang et al. [152], who identified WEL as a result of combined phase transformation and plastic deformation. Hossain reports that WEL form as a combination of phase transformations, strain hardening, and grain refinement [114]. Many works report on similarities between WEL and adiabatic shear bands. It has been observed, that the mechanisms governing the formation of WEL and adiabatic shear bands are rather similar, e.g. carbide dissolution, phase transformations, dynamic recovery, and dynamic recrystallization. These common formation mechanisms result in similarities in structure and crystallography [149,155,156]. Based on this, Barry and Byrne consider WEL generation to be an adiabatic shear process, in which the dominant metallurgical process is dynamic recovery [155].

In machining the selection of cutting parameters, such as feeds and cutting speeds governs the strains, strain rates, and temperatures. Subsequently, these parameters, by extension, also have a decisive impact on WEL formation and the mechanisms dominating it. Mehmedović et al. propose a flowchart for the analysis of WEL in hard turning of steels [159]. Ramesh et al. provided evidence that WEL produced at low to moderate cutting speeds result mostly from grain refinement as a result of severe plastic deformation. For higher cutting speeds, they reported WEL due to phase transformation driven by elevated temperatures [160]. Besides cutting speed and feed, another parameter that has a decisive impact is the cooling regime. Since thermal loads play the key role in WEL formation according to the phase transformation mechanism, coolants or even cryogenic machining as well as the use of sharp, unworn tools leading to lower temperatures can significantly mitigate WEL formation [50,154,155].

Structure of white etching layers (WEL)

One feature that WEL share, regardless of their formation mechanisms, is that they are composed of submicrometer grains. The range of grain sizes on the nanoscale, however, is rather large. In general, it was found that grain size decreases when the phase transformation mechanism is accompanied by plastic deformation [142]. Analyzing machined AISI 52100, Ramesh et al. found grain sizes of $D_g = 5$ nm inside the WEL when using low cutting speeds and coarser grains of $D_g = 20$ nm when using higher cutting speeds [160]. This corresponds to the findings of Zhang et al., who observed an increasing grain size in WEL with increasing cutting speeds and increasing flank wear. Most grains in the WEL observed by them had a grain size of less than $D_g = 100$ nm [152]. Akcan et al. report grain sizes of $D_g = 30\text{-}500$ nm inside white etching layers formed in steels [139]. For machined Ti-6Al-4V Brown et al. report average grain sizes of less than $D_g = 200$ nm [142]. Besides their particularly small grain size, WEL usually have a particularly high dislocation density and a large number of defects resulting from shear deformations [50,158].

Depending on the design of the machining process e.g. the level of wear of the tool, the geometry of the tool, and cutting parameters such as cutting speed and feed, the thickness of WEL in machining can vary greatly. Information on WEL thicknesses indicates huge variations. Whereas some state that the average thickness of WEL is in the range of 1-10 µm [56], other studies report on much thicker layers with a thickness of typically less than 50 µm [139]. Like the mechanisms of WEL formation, the thickness of WEL depends on the thermomechanical loads in machining and, by extension, the design of the process employed. Zhang et al. found an increase in the thickness of the WEL, with increasing flank wear in orthogonal cutting of AISI 52100. In their experiments, an increase in cutting speed led to an increase in WEL thickness for relatively low cutting speeds, whereas for high cutting speeds, an increase in cutting speed resulted in a decrease in WEL thickness. They hypothesized that this observation resulted from higher temperatures with higher cutting speeds for relatively low speeds, whereas in the high cutting speed regime a decrease in plastic deformation and subsurface temperatures with increasing speeds resulted in thinner WEL [152]. This agrees with the findings of Du et al., who analyzed highspeed machining of a Nickel-base superalloy and recorded increasing thicknesses of WEL with increasing cutting speeds up to a cutting speed of $v_c = 2000$ m/min, and a decrease in the thickness of WEL when increasing the cutting speed even further [145]. Zemzemi et al. found that WEL thickness rises with increasing cutting speed, feed rate and tool wear, using a multi physics model [161]. This agrees to the experimentally obtained findings of Capellini et al., who analyzed orthogonal turning of AISI 52100 and provided evidence that the thickness of WEL increases with cutting speed, feed, and tool wear [162]. Besides the wear of the tool, its microgeometry influences WEL formation, e.g. it has been reported that WEL thickness increases with increasing chamfer widths and lengths [50].

Another structure-related topic in research on WEL is their phase composition. In general, studies on phase composition inside of WEL come to very disparate findings. In the early days of research on WEL, Field and Kahles considered WEL resulting from drilling to consist of untempered martensite [14,47]. In recent years authors found WEL to be a mixture of fine martensite lath with finely dispersed carbides and retained austenite [158], whereas others observe that WEL consist mostly of severely deformed pearlite lamellae and a mixture of martensite, cementite and austenite [163], and others conclude that WEL bear no similarities to conventional martensite at all [155]. The reason for this wide range of results might be found in the multitude of parameters influencing WEL formation and particularly in the strong interrelationship between phase composition inside of WEL and the underlying mechanisms governing their formation.

Hosseini found that predominantly thermally induced layers consisted of body-centered cubic (bcc) martensite, face-centered cubic (fcc) austenite and orthorhombic cementite. Conversely, predominantly mechanically induced WEL were found by them to consist of bcc-ferrite and orthorhombic cementite [156]. In general, stronger thermal loads during machining, e.g. caused by increasing tool wear, were found to lead to more retained austenite inside the WEL [154,155,160]. A refinement in the size of carbide particles is oftentimes observed within the layers, regardless of the formation mechanism [155,156]. Ramesh et al. reported that in WEL carbon was retained fully in solution for high cutting speeds, whereas for low cutting speeds they observed carbides [160]. Hossain et al. provide evidence of a hybrid structure of WEL, consisting of a very thin layer of nano-sized austenite grains and nano-sized martensite grains [114].

Mechanical properties of white etching layers (WEL)

Besides their nanocrystalline structure, the various types of WEL also have in common that their hardness clearly exceeds the hardness of the bulk material. Eyre et al. state that the hardness of WEL in steels and cast iron is usually in the range of 700-1200 HV [146]. However, even higher values have been observed in some studies. For instance, Griffiths reports on WEL formed in BTA deep hole drilling, which exceed a hardness of 1300 HV, which is more than four times the hardness of the bulk material [164]. Hence, the hardness of WEL can significantly exceed the hardness of untempered martensite produced by heat treatment processes [16,139].

In terms of residual stresses WEL are less uniform, as they exhibit a broad range of residual stresses, depending on the formation mechanisms. Oftentimes WEL are associated with particularly large residual stresses, which can be either of compressive or tensile nature [56]. Zhang et al. reported compressive residual stresses in WEL when using relatively low cutting speeds as a result of plastic deformation. When using high cutting speeds, they observed tensile residual stresses in WEL as a result of higher thermal loads in cutting. In addition to this, they found that increasing flank wear, causing higher temperatures, resulted in higher tensile stresses [152]. This example illustrates that the nature of residual stresses in WEL is significantly influenced by the thermal and mechanical loads. Layers formed primarily by plastic deformation due to high mechanical loads tend to have compressive residual stresses. Conversely, WEL generated as a result of high thermal loads and according to the phase transformation mechanism are usually associated with tensile residual stresses [56].

Besides experimental approaches, various simulative approaches have been developed to model the formation of WEL. Arfaoui et al. propose a finite element model (FEM) based on the mechanism of phase transformation. The modeled WEL depth are consistent with experimentally obtained findings. They identify cutting speed, feed, flank wear, and hardness of the workpiece as the key parameters for WEL formation [140]. Zemzemi et al. propose an analytical multi-physics model for predicting the thickness of WEL and dark layers based on the phase transformation mechanism [161].

2.3.2 Destructive and nondestructive evaluation

A comprehensive review of destructive and nondestructive characterization of WEL is given by Brown et al. [56]. Up to this day, the prevalent gold standard for the detection of WEL is a metallographic etching of cross-sections followed by optical microscopy. Due to the relatively long history of this technique, it is well-established and standards have been developed to identify alterations of SI, such as WEL or grinding burn, to prevent potentially catastrophic failures. For instance, the Society of British Aerospace companies developed etch inspection standards in the late 1960s and early 1970s [16]. Nital etching is labeled “pseudo-nondestructive” as the workpiece is not fully destroyed, but its surface is altered by removing layers during etching [165]. Compared to most truly nondestructive approaches, the method is costly in terms of time invested and parts sacrificed. In addition to this, nital etching requires operator interpretation and thus involves a certain bias [166]. Motivated by these downsides of conventional metallographic etching, truly nondestructive alternative approaches for the detection of WEL have been developed in the past decades. For instance, analyses based on eddy currents, surface acoustic waves, acoustic emissions, laser ultrasonics, and positron emission spectroscopy were evaluated [56,166].

In addition to these techniques, magnetic Barkhausen noise analysis has been applied for the detection of thermally and mechanically induced WEL in ferromagnetic materials in some works. This technique is already well established for the detection of grinding burn for academic as well as for industrial contexts [78,80,90]. Since grinding burn is a metallurgical machining defect that bears similarities to WEL, the application of MBN for the nondestructive detection and characterization of WEL seems particularly promising [165]. Numerous works have provided evidence that MBN analysis in general is sensitive to various aspects of WEL. The properties of WEL, which MBN analysis is sensitive for are depicted in Figure 2.19, along with the parameters in MBN analysis that can be employed for WEL detection and characterization.

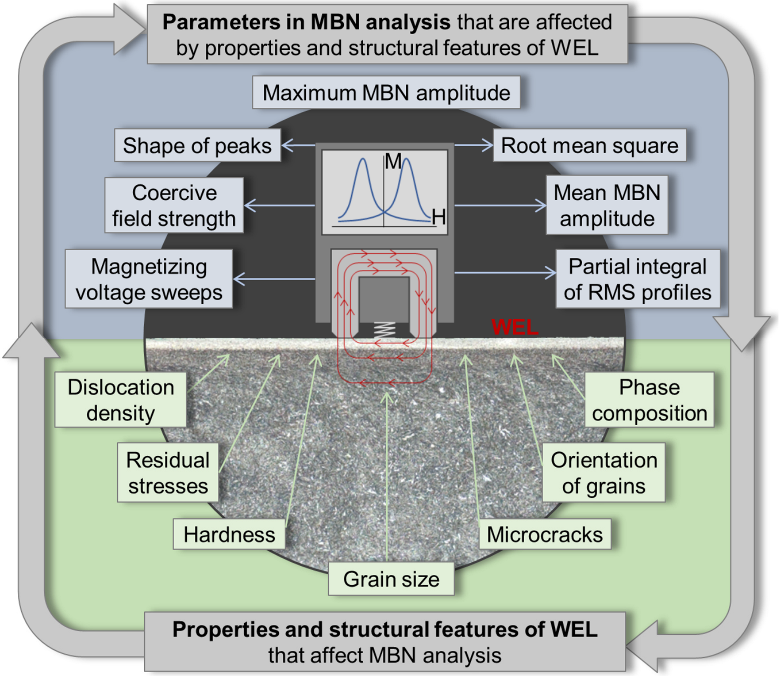

Figure 2.19 Interrelation between the parameters of magnetic Barkhausen noise (MBN) and the properties and structural features of white etching layers (WEL)

Stupakov et al. analyzed WEL in milled AISI 52100 by MBN analysis. They identified a second peak in the MBN envelope, when a WEL was present at the surface and were able to rank samples by WEL thickness. They state that the applicability of MBN analysis for WEL detection results from various aspects. They found that the WEL is not only mechanically but also magnetically particularly hard and exceeds the hardness of the material beneath the WEL. In addition to this, the martensitic matrix in the WEL has a favorable orientation and the increasing volume of retained austenite in thicker WEL can also be used as a base for detecting WEL. They suggest to use special parameters of MBN for WEL detection, such as the partial integrals of RMS profiles over field intervals, along with coercive field strength and root mean square (RMS) values of MBN [81]. This corresponds to the findings of Neslušan, who also observed a second peak originating from the WEL. In their work, the second peak originating from the WEL was more pronounced with increasing wear of the tool, and by extension increasing WEL thickness [96].

Brown et al. propose an approach for rapidly detecting and sizing WEL, based on the breadth and intensity of diffraction peaks [165–167]. They evaluated this approach against MBN-based WEL detection and nital etching [153,165]. Specimens with WEL were found to lead to increased XRD peak breadth relative to specimens free of WEL. This corresponds to the findings of Akcan et al., who state that peak broadening in XRD is most likely the result of lattice strains and small grain sizes in the WEL [139]. In MBN analysis, Brown et al. observed that a decrease in the FWHM of the envelopes indicated re-hardened layers [165]. In another work, Brown et al. observed a shift in the peak frequency of MBN, which was indicative of the compressive residual stresses associated with WEL [153]. An advantage of XRD and MBN-based WEL detection over nital etching is that the methods do not require operator interpretation. The major advantage of XRD-based WEL detection over MBN analysis is that it is not restricted to ferromagnetic materials.

All previously mentioned nondestructive approaches are used to evaluate fundamental properties that are intrinsic to WEL such as lattice strains and grain sizes or secondary properties, like residual stresses [165]. For instance, magnetic Barkhausen noise analysis is particularly sensitive to the elevated residual stresses, the high hardness and the small grain size of WEL.

In addition to optical microscopy, SEM is oftentimes used to detect WEL, as these appear featureless in SEM and can thus be distinguished from the bulk material [168]. Due to its very high resolution, transmission electron microscopy (TEM) is particularly adequate for investigating the nanocrystalline microstructure of WEL. In many studies, TEM has been employed for an in-depth assessment of mechanisms governing WEL formation and the resulting phase composition in the WEL. Examples include the works of Akcan et al. [139], Barry and Byrne [155], and Hosseini et al. [156].

X-ray diffraction according to the $\sin^2\psi$-method is the predominant technique for investigating the residual stress states in WEL, since this technique is nondestructive and particularly suitable for investigating the near surface regions, as comprehensively explained in chapter 2.2.4. Besides residual stresses, also the crystallographic structure of WEL can be analyzed in detail based on XRD. For instance, the amount of retained austenite inside of WEL can be quantitatively assessed by means of XRD [114,139,154].

With the advent of frontier technologies in microscopy in the past decades, advanced procedures have found application for the analysis of WEL. Hossain et al. employed TKD, FIB-SEM, nano indentation hardness measurements, and high-resolution EBSD techniques, to investigate the formation, structure, and properties of WEL in high-carbon steel [114]. Liao et al. characterized the mechanical properties of WEL in nickel-based superalloys by cyclic micro pillar testing and its structure by TEM, TKD, and ion channeling contrast. They found that WEL show a clearly distinct micro-plastic behavior and exhibit a significant loss in ductility on the micro- and nanoscale [157].

2.3.3 Impact on performance

Due to the vast spectrum of WEL, it is challenging to identify universally applicable correlations between WEL and the performance of components. WEL can have a severely detrimental impact, e.g. in terms of fatigue strength and life. However, also favorable implications have been reported in various works, such as increased wear resistance of WEL. Subsequently, understanding the formation mechanisms, the structure, and the properties of WEL is vital to assess their impact on the performance of components and ensure their life, capability, and reliability.

Numerous studies have provided evidence for steels, nickel-based superalloys, and titanium that fatigue life can significantly be reduced when WEL are present, as they usually tend to promote crack nucleation and propagation. [56,141]. Due to their enormous impact on fatigue life, Brown even considers WEL to be the metallurgical anomaly that is perhaps “the most feared by materials engineers” [56]. A particularly remarkable example of the detrimental impact of WEL is given by Herbert et al. for the example of drilled nickel-based superalloys. They provide evidence that a WEL with a thickness of approx. 10 µm can reduce fatigue life by up to 30 times when compared to the damage-free benchmark material [144]. A WEL with a thickness of approx. 5 µm reduced fatigue life by approx. four times. They found that an additional shot peening process after drilling is not capable of mitigating the negative impact of WEL. The compressive residual stresses induced by shot peening were found to not be stable under low-cycle fatigue. They hypothesize that this inability to maintain stresses might result from cracking and spalling of the brittle WEL. Based on their observations, Herbert et al. conclude that WEL are not tolerable to any extent [144]. Conversely to the findings of Herbert, evidence was provided by Koster et al. that the thickness of WEL does not necessarily have a major impact on fatigue performance. In their investigation, a WEL with a thickness of 12 µm reduced fatigue life similarly to layers which had a thickness of approx. 90 µm [16,169]. WEL can also significantly reduce resistance to rolling contact fatigue [56].

Besides the previously presented negative implications of WEL, numerous studies report on the beneficial properties of WEL. Favorable impacts of WEL have been reported in terms of tribological properties, such as improved wear resistance in sliding contact [141]. Griffiths and Furze report on reduced wear in block-on-ring tests when WEL were present at a surface [141]. Zhang et al. found that the nanocrystalline microstructure and the high hardness inside the WEL can improve abrasive wear resistance. They also found that specimens with WEL can have better fatigue wear resistance when compared to uncut specimens with lower hardness and coarse grains. The residual stress state in the layers had a major impact on fatigue life but not on abrasive wear resistance [168]. As a result of the beneficial properties of WEL in terms of wear resistance, Griffiths and Eyre propose taking advantage of controlled WEL formation, e.g. by substituting post-process heat treatment [141,146,148]. In addition to tribological aspects, WEL can have an impact on the formation and retention of passive layers, which are beneficial in terms of corrosion resistance. Subsequently, evidence has been provided indicating improved corrosion resistance through WEL. However, due to the vast complexity of the interrelationship between grain size and corrosion resistance, no general conclusions can be drawn based on the observation of WEL alone [10,170].

2.4 BTA deep hole drilling

2.4.1 Process characteristics and thermomechanical loads

The most common method of drilling is conventional twist drilling. The major reasons for the popularity of this method are that the required machines and tools are relatively cheap and usually fairly easy to apply. However, there are major limitations of this method when it comes to machining bores with high diameters or lengths. A key criterion which poses a constraint on the applicability of conventional twist drilling in this regard is the length-to-diameter ratio of boreholes. Due to the balance of forces in conventional twist drilling, this method is also restricted in terms of the achievable surface qualities, and the dimensional accuracy of the diameter and straightness of boreholes [18]. In response to these downsides of conventional twist drilling for some manufacturing tasks, specialized deep hole drilling techniques have been developed. These include single-lip deep hole drilling, BTA deep hole drilling, also called single-tube system drilling, and ejector drilling, also known as double-tube system drilling. The fields of application of conventional twist drilling and deep hole drilling methods are depicted in Figure 2.20 [171]. The encircled numbers in the figure refer to application examples given in [171].

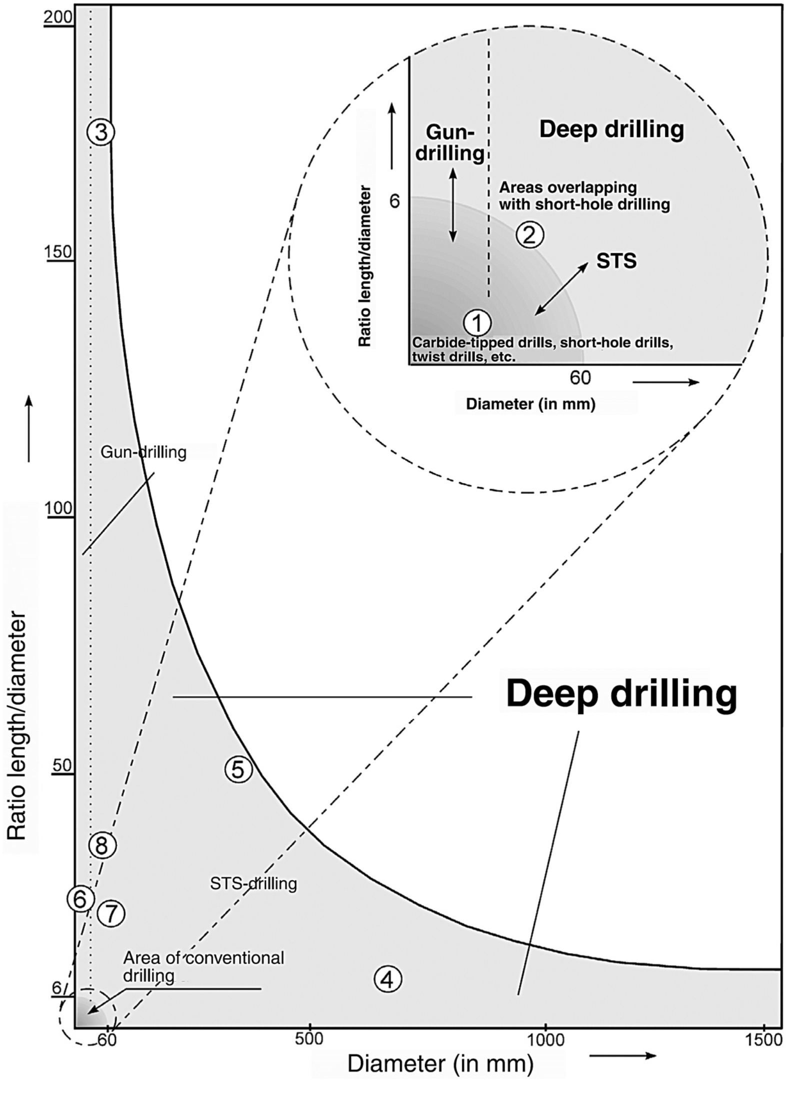

Figure 2.20 Field of application of conventional drilling and deep hole drilling [171][14]

---

[14] Reproduced with permission from Verein Deutscher Ingenieure e. V.

Although twist drilling is the most frequently used technique in drilling, the application area of deep hole drilling is significantly bigger [18]. Deep hole drilling methods are usually employed for machining boreholes with a length-to-diameter ratio larger than $l/D \geq 10$. However, the methods are also applied for smaller length-to-diameter ratios due to their high productivity, the achievable quality of boreholes, and the possibility of machining difficult-to-cut materials. In general, single-lip drilling is used for machining bores with relatively small diameters of D = 0.8-40 mm, whereas BTA and ejector drilling are used for larger diameters, usually $D \geq 40$ mm and in special cases diameters as small as D = 6 mm are machined by BTA deep hole drilling [18,171,172].

BTA deep hole drilling was developed in the late 1930s and early 1940s by the combined efforts of Burgsmueller and Beisner [40]. Nowadays, the method is employed in industries such as petrol exploration, aerospace engineering, and the chemical sector. Typical components machined by BTA deep hole drilling include drill collars, hydraulic cylinders, landing gears, extruder barrels, or tube sheets of steam generators [18,19,171]. One reason for the widespread use of BTA deep hole drilling is the achievable surface quality paired with the huge productivity. The fundamental principle of BTA deep hole drilling is presented in Figure 2.21.

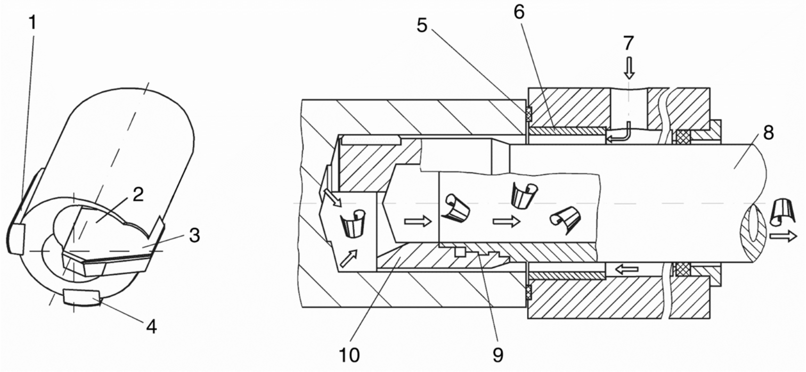

Figure 2.21 Tool and machine for BTA deep hole drilling: 1: Guide pad 2; 2: Chip mouth; 3: Cutting edge; 4: Guide pad 1; 5: Seal; 6: Drill bushing; 7: Coolant lubricant feed; 8: Boring bar; 9: Connecting thread; 10: Drill head [171][15]

A key characteristic of the method is the supply of a high volume of cutting fluid with high pressure through the cutting fluid supply apparatus (BOZA). The cutting

---

[15] Reproduced with permission from Verein Deutscher Ingenieure e. V.

fluid is supplied through a gap in between the machined borehole and the boring bar. It takes away the swarf through the chip mouth and the boring bar. This way, chips do not come into contact with the newly generated surface of the bore wall, and the risk of potential damage to the surface by the swarf is thus eliminated. This is a major advantage of BTA deep hole drilling over conventional twist drilling and single-lip deep hole drilling. In drilling the workpiece and the tool can both be rotated. Usually, the tool is rotated when the workpiece cannot be rotated. Counter rotation of the tool and workpiece allows for achieving high concentricity and straightness [173].

Mechanical loads

An extensive review of the acting forces and torques in BTA deep hole drilling for the example of a single-edged drill head, like the one presented in Figure 2.21 a) is given in [18,174].

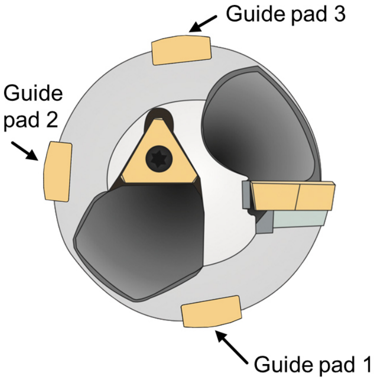

Figure 2.22 Assymetrical design of a BTA drill head, resulting in an imbalance of forces in drilling. According to [174][16]

The asymmetrical tools in BTA deep hole drilling, like the ones employed in this work, cause an imbalance of forces (Figure 2.22). The asymmetrical forces push the drill head against the newly generated borehole wall. To support the forces against the workpiece, guide pads are used. The guide pads are attached to the drill head at a fixed distance behind the cutting inserts, which is called the guide pad

---

[16] Reproduced with permission of H. Abrahams from H. Abrahams: Untersuchungen zum Führungsleistenverschleiß und zur Prozessdynamik beim BTA-Tiefbohren austenitischer Stähle (2016).

recess or the pad lag [175]. This design of drill heads allows for a self-guiding effect of the tool during drilling [164].

Initially, when the guide pads of the tool are not yet in contact with the borehole wall, the tool is guided by the drill bushing (Figure 2.21). As an alternative to drill bushes, a pilot hole can be used. Traditionally drill heads with two guide pads were used [164]. However, drill heads with three guide pads, such as the one displayed in Figure 2.22 were found to be more stable and lead to higher surface qualities [173]. By supporting the forces against the borehole wall, the guide pads burnish and smoothen the surface after it has been machined by the cutting inserts. Thus, the surfaces and subsurfaces of BTA deep drilled components are conditioned through effects of cutting inserts and guide pads. In consequence both mechanisms, cutting and burnishing, always need to be analyzed in close conjunction. Surface generation and conditioning through cutting inserts and guide pads in BTA deep hole drilling are illustrated in Figure 2.23. It can be seen that in front of the guide pads, a ridge piles up [164]. A review of the role of the guide pads in BTA deep hole drilling is given by Richardson and Bhatti [176].

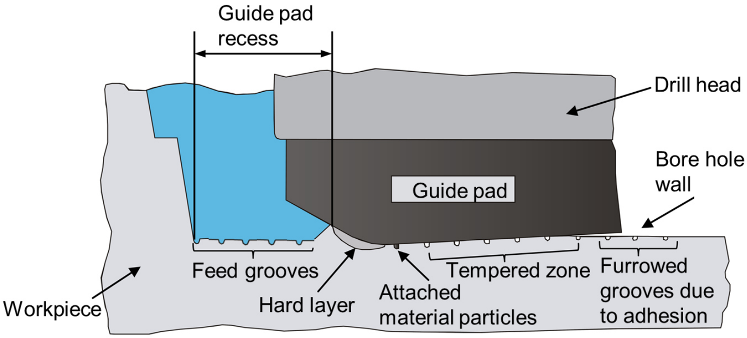

Figure 2.23 Surface generation in BTA deep hole drilling through the combined conditioning mechanisms of cutting insert and guide pad. According to [147,174][17]

The normal forces in BTA deep hole drilling are significantly determined by the angle of the guide pads as well as by the friction coefficient. The normal forces acting on the guide pads have been assessed through calculations based on cutting

---

[17] Reproduced with permission from H. Abrahams from H. Abrahams: Untersuchungen zum Führungsleistenverschleiß und zur Prozessdynamik beim BTA-Tiefbohren austenitischer Stähle (2016) and with permission from H. Fuß from H. Fuß: Aspekte zur Beeinflussung der Qualität von BTA-Tiefbohrungen (1986).

forces and data obtained in analogy experiments [164,174]. In addition to these approaches, normal forces have been measured in experiments by strain gauges and piezoelectric sensors [147,174,177]. The feed forces at the guide pads are considered to be insignificant [18]. Torques and forces in the feed direction during BTA deep hole drilling have been assessed by strain gauges applied to the boring bar [174,177]. An innovative approach for contactless torque measurement based on the Villari effect is presented by Schwersenz [178].

Thermal loads

As for other machining processes, such as turning, and milling, the heat generated in BTA deep hole drilling is split between the chip, the workpiece, the tool, and the environment. In BTA deep hole drilling, thermal loads are exerted on the workpiece not only due to the machining through cutting inserts but also as a result of the friction and burnishing by the guide pads. Usually, the temperatures at the outer cutting inserts are significantly higher than the temperatures at the inner cutting insert [18]. The temperatures at the first guide pad exceed the temperatures at the second guide pad. Temperatures at the third guide pad, which is only relevant at the start phase and the bore-through phase, are even lower. Numerous scientists report on increasing temperatures impinged on the workpiece with higher cutting speeds and higher feed rates [18].

One of the most common techniques for assessing workpiece or tool temperatures in BTA deep hole drilling is placing thermocouples in eroded boreholes in the workpiece or the tool, respectively. Besides thermocouple-based measurements, temperatures in BTA deep hole drilling were assessed by thermography [174]. More recently ratio-pyrometry was employed to assess temperatures immediately at the cutting inserts and guide pads [179].

Besides the thermomechanical loads in BTA deep hole drilling, other key topics that have been the focus of research on BTA deep hole drilling during the past years are e.g. the in-process observation and compensation of straightness deviations [180], the optimization of guide pads through microfinishing [181] and the development and use of novel guide pad coatings [174,182]

2.4.2 Surface integrity

Figure 2.24 presents a scheme proposed by Fuß for the evaluation of the quality of boreholes [147]. Besides the geometry of bores, which includes aspects such as straightness and roundness, its quality is defined by the SI. Fuß divides aspects of SI into the categories of surface geometry, surface structure and physical properties.

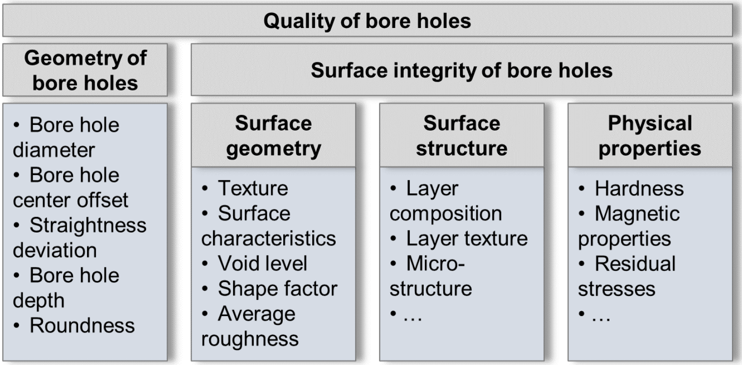

Figure 2.24 Scheme for the evaluation of the quality of boreholes. According to [147][18]

Evaluating SI in BTA deep hole drilling is particularly challenging for several reasons. Firstly, due to the highly restricted accessibility of the borehole wall, analyses are oftentimes limited to post-process, destructive methods. Secondly, as SI resulting from BTA deep hole drilling results from the overlapping effects of cutting inserts and guide pads, assessing how exactly the surfaces are generated during drilling is a very demanding but crucial task. In response to this, numerous efforts have been undertaken throughout the past decades to separate the effects of cutting inserts and guide pads, e.g. by quick stop devices [147,164,183].

Some of the first investigations into SI resulting from BTA deep hole drilling were performed by Griffiths [164] and Fuß [147]. Griffiths gives a comprehensive review of the research on SI in BTA deep hole drilling in [164]. According to him, Drewes was the first to publish findings on SI in BTA deep hole drilling. He reported on the plateau-valley structure of surfaces. Tiemann was the first to publish micrographs, indicating the severely deformed grains with an acicular structure parallel to the surface [164]. Following their pioneering works, Griffiths and Fuß presented extensive findings on SI resulting from BTA deep hole drilling of AISI 1040, AISI 5115, and AISI 1060 respectively, applying the minimum data set proposed by Field [147,164]. Rao then extended research on SI in BTA deep hole drilling by analyzing residual stresses [175]. These key contributions to the field of research on SI in BTA deep hole drilling are summarized in Table 2.4, along with some more recent studies on the subject.

---

[18] Reproduced from H. Fuß: Aspekte zur Beeinflussung der Qualität von BTA-Tiefbohrungen (1986) with permission from H. Fuß.

Table 2.4 Research on surface integrity (SI) resulting from BTA deep hole drilling

Authors	Material	Drilling parameters considered	SI inspection
Griffiths, B.J. (1982) [164]	AISI 1040, D = 22 mm	Cutting speed, feed, impact of cutting inserts and guide pads separated through a quick stop device	Surface finish, microstructure, microhardness
Fuß, H. (1986) [147]	AISI 5115, AISI 1060, D = 60 mm, D = 50 mm	Cutting speed, feed, design of the drill head, tool wear, impact of cutting inserts and guide pads separated through a quick stop device	Surface finish, microstructure, microhardness
Rao, P.K. (1987) [175]	AISI 1055 D = 20 mm	Cutting speed, feed, impact of cutting inserts and guide pads separated by interrupting the process	Surface finish, microstructure, microhardness, residual stress
Abrahams, H. (2016) [174]	AISI 304, AISI 1060, D = 60 mm	Cutting speed, feed, design of the tool, coating of the guide pads	Surface finish, microstructure, microhardness,
Zhang, H. (2017) [183]	Cast iron, D = 80 mm	Cutting speed, feed, impact of cutting inserts and guide pads separated by interrupting the process	Surface finish, microstructure, nanohardness
Li, B. (2023) [19]	SA 508, D ≈ 18 mm	Cutting speed, feed	Surface finish, microstructure, microhardness,
Li, X. (2023) [184]	SA 5083 D ≈ 18 mm	Cutting speed, feed, impact of cutting inserts and guide pads separated by interrupting the process	Surface finish, microstructure, microhardness, residual stress

Surface finish

A BTA deep drilled surface is composed of regular valleys and plateaus in between. An exemplary profile is depicted in Figure 2.25. Depending on the process forces, and by extension the level of burnishing through the guide pads, an open, partially closed, or closed profile is generated in drilling. In an open profile, the feed marks are not fully closed due to incomplete burnishing as a result of insufficient normal forces. Conversely, if the normal forces are too high, spalling and outbreaking of the material can occur in burnishing [18].

A BTA deep drilled surface is oftentimes characterized by defects such as plowing grooves, furrows, pittings, and surface tearing [19]. These can be alleviated by adapting the cutting parameters [183]. Depending on the selection of cutting parameters, rifling marks are generated [185]. Due to the topography of deep drilled surfaces, a stylus-based assessment can oftentimes lead to false results, as outlined by Griffiths in [186]. In general, no universally applicable statements about the impact of cutting speed and feed rate on surface topography in BTA deep hole drilling can be made, due to the complexity of the mechanisms in surface generation. Many authors reported a decrease in roughness with higher cutting speeds. This was often accounted to an increasing burnishing effect at higher cutting speeds [19,175]. However excessively high cutting speeds might damage the surface due to over-plowing and increasing system vibration [183]. Li states that in general the effect of feed rate on roughness is lower than the effect of cutting speed [19].

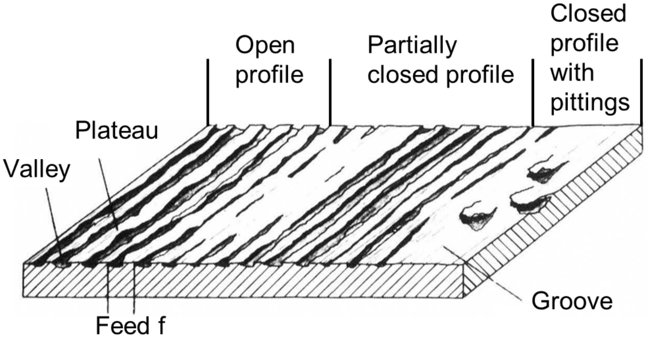

Figure 2.25 Surface finish in BTA deep hole drilling. According to [147][19]

---

[19] Reproduced from H. Fuß: Aspekte zur Beeinflussung der Qualität von BTA-Tiefbohrungen (1986) with permission from H. Fuß.

Numerous studies report on a severely deformed microstructure of BTA deep drilled specimens, which results from the burnishing effect of the guide pads [18,19,183]. The deformed grains in this layer have an acicular structure and their axis is parallel to the borehole wall [164]. In addition to the deformed layer, oftentimes a layer with an ultrafine grain structure is observed right below the surface of the bore [19,183]. Li et al. provide evidence that this layer is recrystallized in drilling. In their studies, the amount of low-angle grain boundaries rises with increasing distance to the surface of the borehole. They found that the thickness of the gradient layer rises with increasing feeds and cutting speeds. [19]. The ultrafine grain structure in the layer observed by Zhang et al. and Li et al. clearly resembles WEL, however, no definite results are given in the publications to support this assumption, e.g. micrographs obtained by optical microscopy [19,183]. Griffiths and Fuß report on the formation of WEL in BTA deep hole drilling [147,164]. Fuß presents evidence of a three-layered structure composed of a fragmented layer, a severely deformed layer, and the bulk material. The fragmented layer was sometimes replaced by a WEL, potentially due to higher temperatures in machining [147]. Griffiths observed WEL in BTA deep hole drilling, in spite of gentle machining parameters. He hypothesizes that WEL might have formed due to recrystallization as a result of the thermomechanical loads. He provides evidence that WEL form mostly by the influence of the guide pads [164].

The microhardness in the subsurface is strongly connected to the microstructural alterations previously described. Due to the high deformation in drilling, severe work hardening was reported in the subsurface of BTA deep drilled components in many works [164,175]. In the investigations of Li, higher feeds and higher cutting speeds lead to larger depths of the hardened layer [19]. In the investigations of Griffiths and Fuß, WEL at the surface were found to have a hardness of up to 1304 HV and 1280 HV respectively, which is more than 4 times greater than the bulk hardness[147,164]. Rao states that burnishing enhances microhardness by 30-40% in comparison with the original hardness [175]. Zhang presents nanohardness investigations of BTA deep drilled surfaces and found that a burnished, ultrafine-grained layer exceeds the hardness of the cutting zone by 56% and the hardness of the bulk material by 140% [183].

Up to this day, research on the residual stresses resulting from BTA deep hole drilling remains particularly limited. Rao provides evidence of tensile residual stresses when machining with the cutting inserts only and compressive residual stresses for burnished specimens. For machined and for burnished surfaces, the intensity of residual stresses was found to increase with increasing speed [175]. This agrees with the findings of Li et al., who also observed the correlations between residual stresses and cutting speed [184].

2.5 Mechanical characterization of bores

2.5.1 Fundamentals of fatigue

When components are subjected to time-variant loads repeatedly, they can fail as a result of damage accumulation well before their (quasi-) static ultimate tensile strength and yield strength are reached. This phenomenon is referred to as fatigue and has been known to mankind for centuries [187]. Loading conditions that can lead to fatigue include axial loads, bending, torsion, internal or external pressure, thermal loads, or a combination of overlapping loads. For instance, many components face a combination of cyclic thermal and mechanical loads throughout their service life, which can occur periodically, or aperiodically. Fatigue poses a particular danger because usually no macroscopic plastic deformation can be observed in components before they fail. Throughout the past centuries, this has led to numerous catastrophic accidents that gave rise to investigations on the matter. Besides engineering components in industries such as railway, aerospace, and automotive, massive structures, such as bridges, can also suffer from fatigue. A review of numerous accidents caused by fatigue is given by Lancaster [188].

In the early days of research on fatigue, many catastrophic railroad accidents were attributed to the phenomenon of fatigue, such as the one that occurred in Versailles in 1842. In the middle of the 20th century, when civil and military aviation gained momentum, more and more fatigue-related accidents were reported in this sector as well, e.g. the crashing of De-Havilland Comet airplanes in 1954 [189]. Despite massive improvements in the quality of materials since those days, catastrophic accidents are caused by fatigue up to this day time and time again, since no metal is completely immune to fatigue [189].

The first to perform fatigue experiments was Albert in 1829, analyzing chains used in the mining industry [190]. Some decades later, August Wöhler conducted systematic fatigue experiments on railway axles between 1852 and 1870. He investigated axial loading, bending, and torsion and identified correlations between the load amplitudes applied to the specimens and the number of cycles to their failure. Wöhler's pioneering works paved the way for further research on methods for characterizing fatigue life and numerous procedures were developed for assessing the fatigue life of components under specified loading conditions.

2.5.2 Standardized procedures in fatigue testing

The most common way of investigating fatigue behavior is by performing tests with a constant cyclic stress amplitude which is applied at a certain frequency. In this method, the number of cycles to failure is observed for various stress amplitudes. For illustrating the results of such tests, stress amplitude-life (S-N) curves are usually employed [191,192].

An exemplary S-N curve for some groups of steels, e.g. ferritic-pearlitic or quenched and tempered steels, is depicted in Figure 2.26 a), showing the number of cycles to failure N_f resulting from the applied stress amplitude. It can be observed that a fatigue endurance limit is reached at some point. The concept of such a limit up to which a material does not fail regardless of the number of cycles, however, does not apply to all materials and remains a highly-debated, controversial issue [189]. According to Lee, the S-N curve for steels can be modeled by using the fatigue strength values at 1, 10^3, and 10^6 cycles. The slope b in the high-cycle fatigue region can be calculated by the equation 2.10 [192]. The inverse slope is given by k. An exemplary S-N curve of AISI 4140 steel components machined by drilling with varying feed rates is presented in Figure 2.26 b).

$$b = -\frac{1}{3}\log\frac{\sigma_{1000}}{\sigma_{be}} \tag{2.10}$$

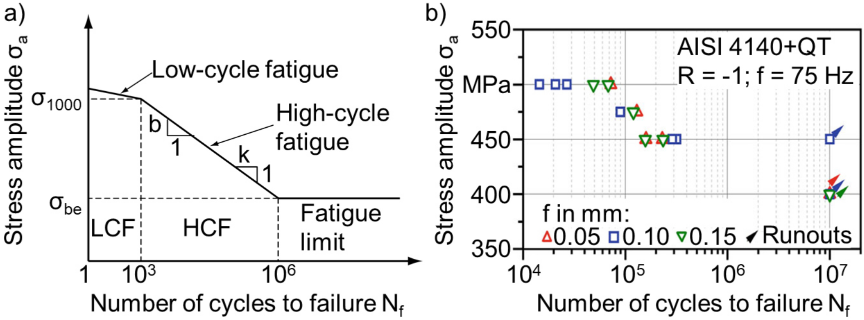

Figure 2.26 S-N curves for steels. a) Typical S-N curve for quenched and tempered or ferritic-pearlitic steels, both axis are in a logarithmic scale; b) S-N curve of deep drilled AISI 4140. According to [73,192][20]

---

[20] a) Reproduced with permission from Elsevier Science & Technology Journals from Lee, Y.-L. et al.: Fatigue testing and analysis: theory and practice (2004); b) reproduced with permission from Springer Nature BV from Baak, N.: Mikromagnetische Charakterisierung des Ermüdungsverhaltens und der Eigenspannungsrelaxation tiefgebohrter Proben des Vergütungsstahls 42CrMo4 (2023); permission conveyed through Copyright Clearance Center, Inc.

The main variables in fatigue testing are presented in Figure 2.27. In conventional fatigue testing, fatigue life is assessed as a function of various parameters, for instance, the applied stress range $\Delta\sigma$, the mean stress σ_m or the environment [190,191].

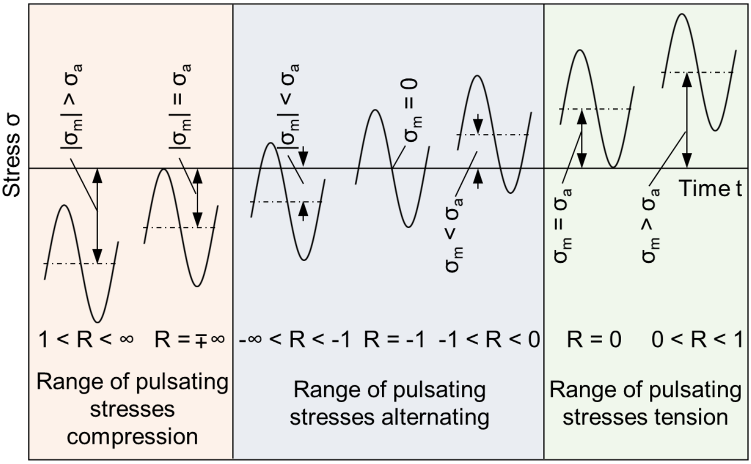

Figure 2.27 Parameters and load regimes in fatigue testing. According to [189][21]

A key parameter is the load ratio R, which is obtained by dividing the minimum stress by the maximum stress. The load amplitude is half of the stress range $\Delta\sigma$. In many engineering applications, mean stress is applied to components in addition to cyclic loads. Applying a mean stress has a major impact on fatigue behavior. Subsequently fatigue experiments are often carried out with a non-zero mean stress. The mean stress is defined as the sum of the maximum stress and the minimum stress divided by two. In addition to the previously presented stress-based approaches, strain-based methods are frequently used. In these, the total strain or the plastic strain are the controlled variables [189–191]. Besides conventional fatigue tests with constant amplitudes (CAT), other procedures have been developed that allow for saving time, costs, and specimens, such as load increase testing, or incremental step testing. In addition to these, specialized short-time procedures were developed, such as PHYBAL [193] and SteBLife [194].

---

[21] Reproduced with permission from Springer Nature BV from D. Radaj, M. Vormwald: Ermüdungsfestigkeit: Grundlagen für Ingenieure (2007); permission conveyed through Copyright Clearance Center, Inc.

2.5.3 Mechanical characterization of tube-shaped components

Countless specialized approaches in fatigue testing have been developed in academia and industry to assess the fatigue behavior of components with non-standard geometries. Since tube-shaped components are fairly common in many fields of engineering, numerous procedures exist for assessing their fatigue life. Baak presents an approach for evaluating the fatigue life of single-lip deep drilled components under axial loads. In instrumented fatigue tests, he studied the evolution of residual stresses, microstructure, and damage using MBN, XRD, and other approaches [73]. Many others performed similar fatigue tests, applying axial loading to relatively thin-walled, tube-shaped components, such as steam generator tubes. He et al. propose locally thinning such tubes for fatigue tests [195]. Besides axial loading, cyclic bending and rotating bending of tube-shaped components have been investigated extensively ever since Wöhler first investigated the fatigue behavior of railway axles. When it comes to tube-shaped components with particularly large diameters and relatively thick walls, these approaches are highly limited by the applicable forces of fatigue testing systems. For quasi-static testing of welded tube-shaped components, the tube flattening test according to ISO 8492 has been developed. In this testing procedure, tube segments are compressed to a defined height and inspected for cracks on the outer and inner surfaces of the tubes. Cyclic testing of tubes by applying internal and external pressure to components is a common procedure. However, like the previously presented approaches, this method is limited when tubes with relatively thick walls are tested. Cristea et al. present full scale internal pressure fatigue tests of seamless tubes. In addition to these, small scale fatigue testing was carried out, using a three point bending system and a specific specimen preparation. They found good agreement in fatigue limit between the full scale and the small scale tests [196].

In [197] the US Army Armament Research, Development and Engineering Center presents a two-stage method for assessing the fatigue life of cannon tubes. In contrast to many of the previously presented methods, this approach is also applicable for assessing the fatigue performance of relatively thick-walled tubes with large diameters. The method consists of pretest loading, through a specific number of live fire rounds, and subsequent hydraulic constant amplitude testing of the tubes at internal pressures [197]. Preconditioning of the tubes and crack formation prior to hydraulic testing is essential in this method. In addition to this, the approach is highly adapted to the thermal, mechanical and chemical loads the cannon tubes face in service. Thus, transferring the method to civil applications does neither seem beneficial nor feasible.

3 Materials and Specimens[22]

In this chapter, information on the batches of AISI 4140 steels used is provided, including details on the heat treatments, chemical compositions, and mechanical properties (3.1). Unetched micrographs of the bulk material are presented, which indicate the presence of manganese sulfides in the steels. Etched micrographs reveal the quenched and tempered microstructures. In addition to the materials, the manufacturing of specimens by the Institute of Machining Technology (ISF) of TU Dortmund University is presented in 3.2. The deep hole drilling machine and the tools are introduced. In addition to this, the key parameters used in drilling are outlined, and information on the thermomechanical loads during drilling is provided.

3.1 Materials

Two batches of quenched and tempered AISI 4140 steels were used. The chemical compositions are depicted in Table 3.1, the mechanical properties are given in Table 3.2. It can be observed, that both batches are relatively similar in their chemical compositions and mechanical properties. The tempering temperatures are in the upper range for tempering. Subsequently, the hardness and strength of both batches are relatively low, compared to quenched and tempered AISI 4140, which is tempered at lower temperatures [60].

Table 3.1 Chemical compositions of the two batches of AISI 4140 used [198]

	C	**Cr**	**Ni**	**Mn**	**S**	**Mo**	**Fe**
Batch A	0.430	1.05	0.10	0.74	0.021	0.22	Bal.
Batch B	0.420	1.05	0.17	0.77	0.024	0.19	Bal.

---

[22] Some of the contents presented in this section are prepublished in [198] and based on the student works [199–202].

Table 3.2 Mechanical properties of the two batches of AISI 4140 used [198]

	Tensile strength R_m in MPa	Yield strength $R_{p0.2}$ in MPa	Hardness Brinell BHN	Tempering temperature T_{tp} in °C	Tempering time t_{tp} in h
Batch A	972	876	294	640	3.25
Batch B	992	891	313	680	25

Figure 3.1 reveals unetched micrographs of the bulk material of both batches in cross-sections extracted in the longitudinal and transverse directions. It can be observed that manganese sulfides are present in the steels. These are oriented in the rolling direction. In Figure 3.2 cross-sections etched with nital are presented. These depict the quenched and tempered microstructures of the bulk materials.

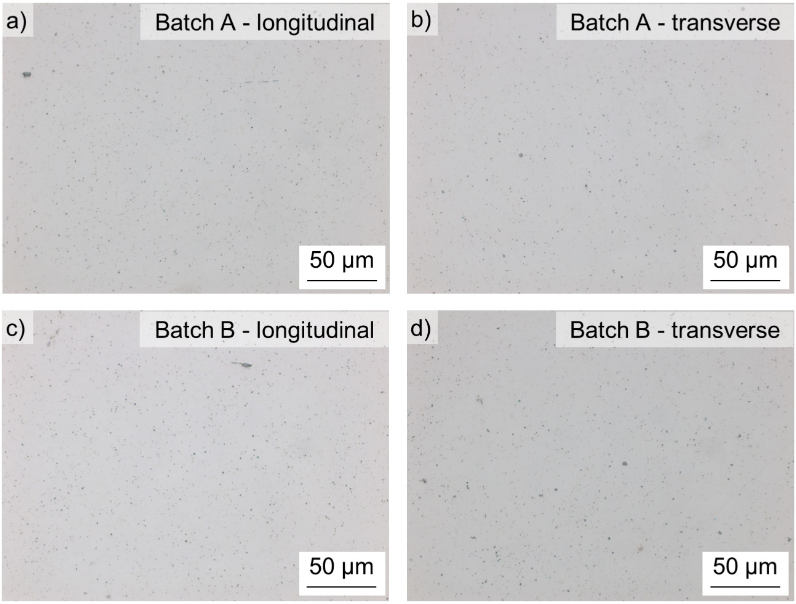

Figure 3.1 Micrographs obtained by optical microscopy of polished cross-sections of the bulk materials: a) batch A in the longitudinal direction; b) batch A in the transverse direction; c) batch B in the longitudinal direction; d) batch B in the transverse direction

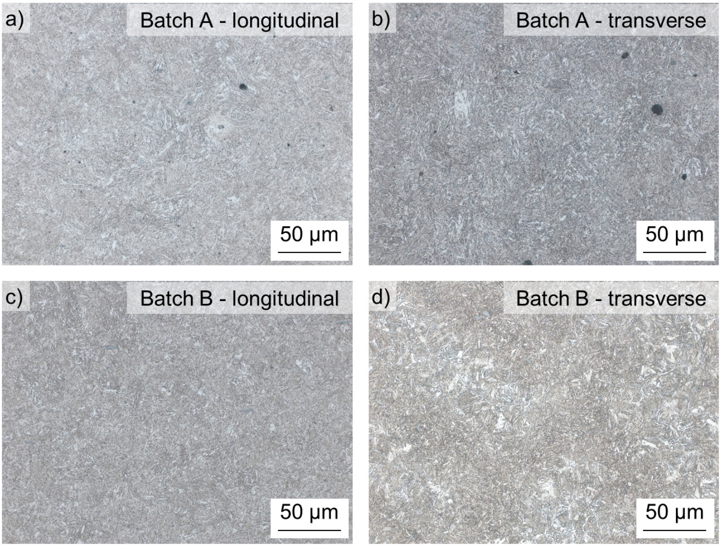

Figure 3.2 Micrographs obtained by optical microscopy of etched cross-sections of the bulk materials: a) batch A in the longitudinal direction; b) batch A in the transverse direction; c) batch B in the longitudinal direction; d) batch B in the transverse direction

3.2 BTA deep hole drilling

3.2.1 Machine, tools, and parameters

All BTA deep hole drilling experiments were performed by the ISF, using the deep hole drilling machine Giana GGB 560 (Giuseppe Giana s.r.l., Magnago, Italy). This machine is displayed in Figure 3.3. With a power of P = 125 kW, it can be used for machining bores with a maximum length of l = 3,000 mm and a diameter of up to D_{in} = 180 mm for full drilling [203]. The machine allows for the rotation of the workpiece, the tool, and counterrotating the workpiece and the tool.

For the experiments presented in this thesis, drilling was performed with a rotating workpiece and a non-rotating tool. For drilling, cutting speeds were selected in the range of v_c = 60-100 m/min and feeds were used in the range of f = 0.150-0.300 mm. In all experiments, the deep drilling oil Berucut RMO TC 22 was used. It was provided through the BOZA at a pressure of p = 11 bar and a flow rate of $\dot{V}$ = 300 l/min. For some of the experiments presented, a damper was used. The parameters employed in drilling are given in Table 3.3.

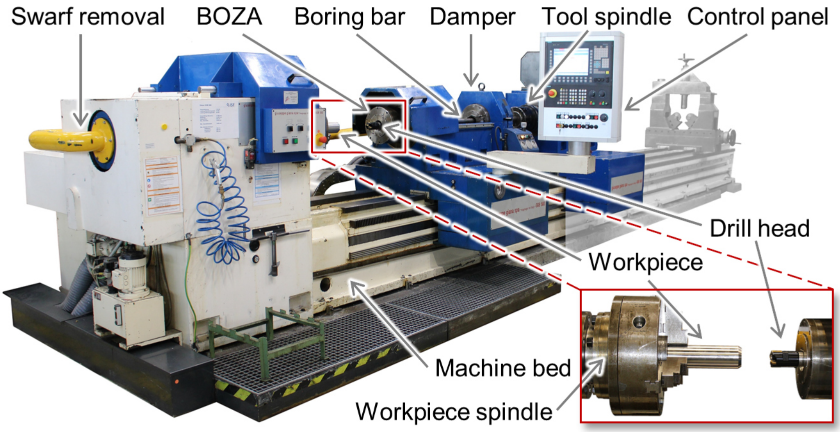

Figure 3.3 Deep hole drilling machine Giana GGB 560 used for BTA deep hole drilling experiments

Table 3.3 Parameters in BTA deep hole drilling

Feed f	0.150-0.300 mm	**Drill head**	Botek BTA type 12
Cutting speed v_c	60-100 m/min	**Deep drilling oil**	Berucut RMO TC 22
Oil flow rate $\dot{V}$	300 l/min	**Guide pads**	Cemented carbide, TiN-coated
Oil pressure p	11 bar	**Cutting inserts**	Cemented carbide, TiN-coated

For all experiments, a solid drill head type 12 by Botek (Botek Praezisionsbohrtechnik, Riederich, Germany) was used. This drill head is presented in Figure 3.4. It was equipped with an outer and an inner cutting insert and three guide pads. The inserts were made of cemented carbide and coated with Titanium nitride (TiN). For all experiments, the first and the second guide pad were replaced after every bore, if not stated differently. The third guide pad was not exchanged, after every experiment, as it is only relevant at the start and the end of bores and did not show significant wear.

The outer and the inner cutting inserts were replaced after every experiment as well. The wear of the inserts was documented by microscopy.

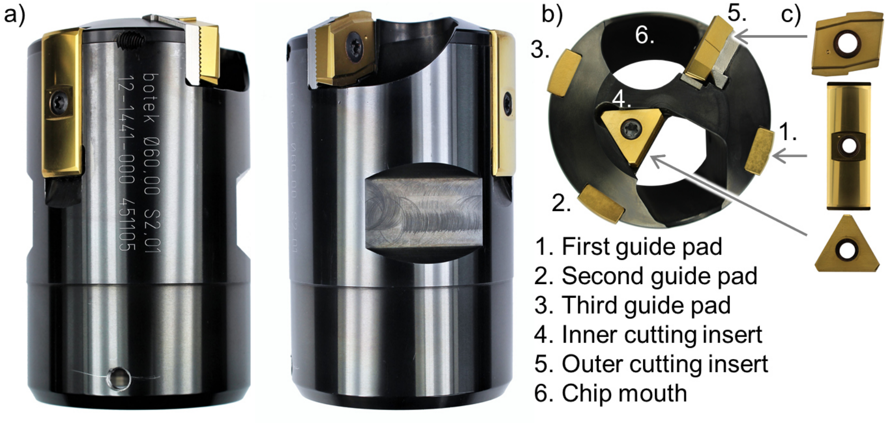

Figure 3.4 Drill head type 12 by Botek: a) side views; b) top view; c) cutting inserts and guide pads of the drill head

3.2.2 Specimen preparation

Figure 3.5 presents the sequence of steps in the manufacturing of the BTA deep drilled specimens. Initially, rolled round bars with a diameter of $d_{out} = 80$ mm and a length of $l = 1000$ mm were cut to a length of $l = 250$ mm (Figure 3.5 a). In preparation for drilling, the bars were turned to a diameter of approx. $d_{out} = 78$ mm. Then specimens were face-turned and a chamfer of $\alpha_{ch} = 30°$ was machined on one side of the bars (Figure 3.5 b).

Figure 3.5 Preparation of specimens: a) Rolled round bars; b) turned round bars; c) BTA deep drilled round bars; d) specimen geometry and direction of feed and cutting

This chamfer was required for centering the specimen in the cone of the BOZA during drilling. In the next step, the turned bars were machined by BTA deep hole drilling (Figure 3.5 c). This step is explained in detail in chapter 3.2.1. The specimen geometry is presented in Figure 3.6.

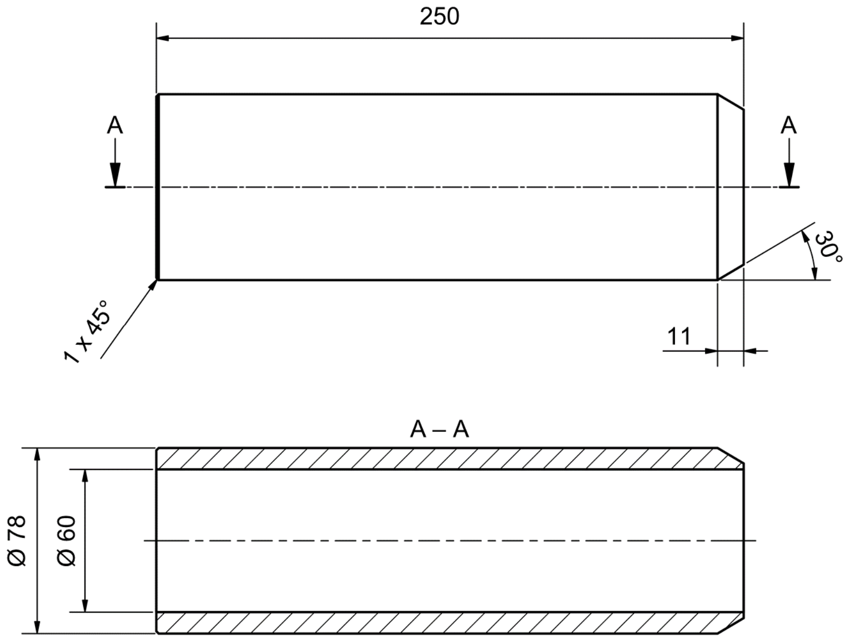

Figure 3.6 Technical drawing of the specimen geometry of the BTA deep drilled specimens

Due to the limited accessibility of the bores, segments were extracted after drilling by sawing and abrasive cutting, for metallographic etching, SEM, EBSD, microhardness testing, MFM, MOKE microscopy, Bitter technique and residual stress measurements. Specimens for SEM, EBSD, Bitter technique, MOKE, and MFM were polished using oxide polishing suspension (OPS) with colloidal silicon dioxide with a particle size of d = 0.05 µm. For the mechanical investigations and residual stress analyses, rings with a length of l = 30 mm were taken from the bores. Specimen preparation is presented in Figure 3.7.

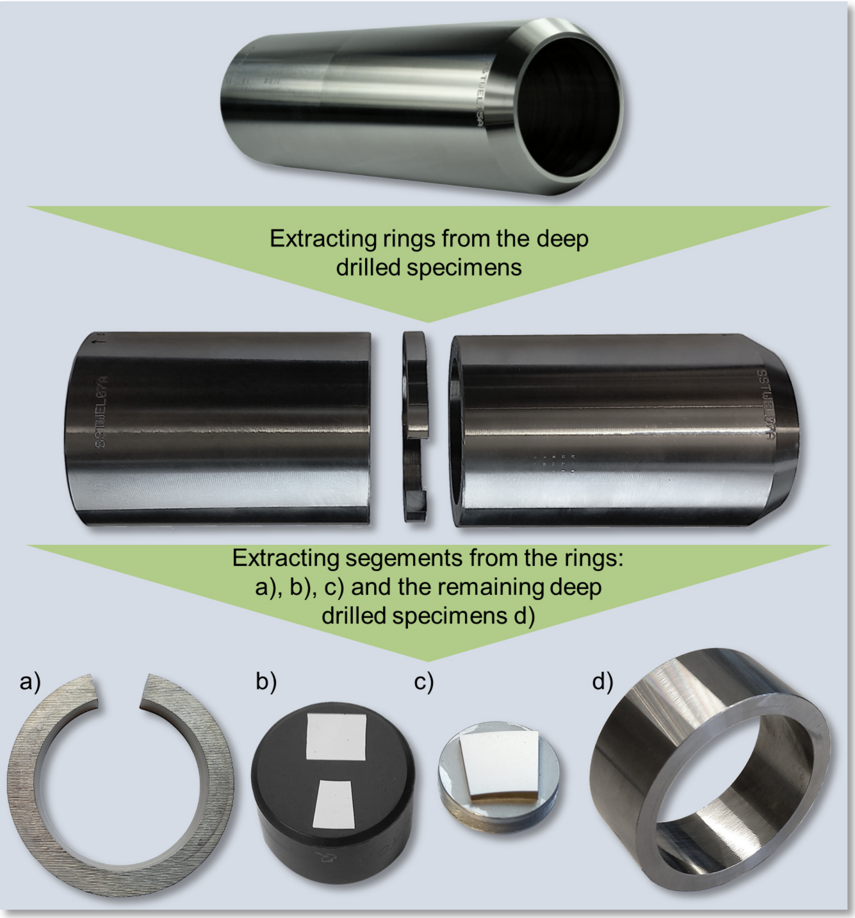

Figure 3.7: Extraction of segments from the bores and further preparation of the specimens: a) ring segments for X-ray diffraction (XRD), b) cross-sections in longitudinal and transverse directions for optical microscopy, electron backscatter diffraction (EBSD), scanning transmission electron microscopy (STEM), electron channeling contrast imaging (ECCI), transmission Kikuchi diffraction (TKD), Bitter technique, magnetic force microscopy (MFM) and microhardness mappings, c) particularly slim cross-sections in transvere direction for magneto-optic Kerr effect (MOKE) microscopy and MFM, d) large ring segments for mechanical tests and XRD

3.2.3 *Thermomechanical loads in drilling*

In drilling, forces, torques, temperatures and acoustic emissions were assessed. The instrumentation applied for these investigations is presented in Figure 3.8. A microphone was used to assess acoustic emissions. This served the purpose of analyzing the occurrence of torsional vibrations in drilling, which are usually referred to as chatter. These vibrations in the natural frequency of the boring bar were detected and further analyzed to conclude about the dynamics of the process. A detailed account of these investigations is given in [198].

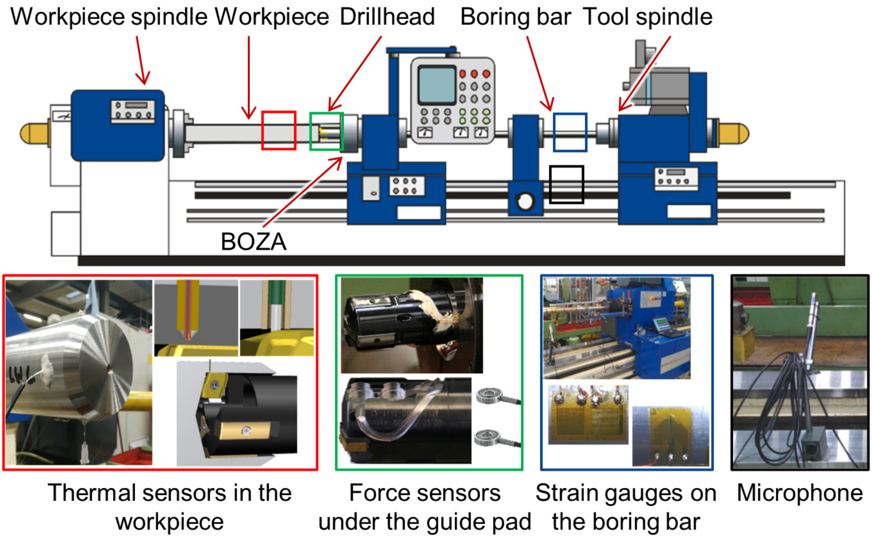

Figure 3.8 In-process assessment of forces, torques, temperatures, and acoustic emissions. According to [198]

Forces and torques were assessed by strain gauges and piezoelectric force sensors. To assess the forces in feed direction and the torque, strain gauges were applied to the boring bar in a full Wheatstone bridge. For assessing the normal forces acting on the first guide pad, a BTA drill head was modified by milling two pockets into the guide pad seat. Particularly slim piezoelectric force sensors were mounted inside these pockets and preloaded with a force of $F = 1000$ N via tightening the screw of the guide pad [177].

Exemplary results for torques and forces in BTA deep hole drilling obtained by these methods are presented in [177,198]. It was observed that an increase in feed results in significantly higher normal forces and torques. These observations were attributed to higher cutting forces with rising feeds. With higher cutting speeds, torques slightly decrease. The normal forces decrease significantly with increasing cutting speeds. The highest normal forces and torques were observed in drilling with a cutting speed of $v_c = 60$ m/min and a feed of $f = 0.300$ mm. In drilling with these parameters, chattering causes significant oscillations in torques and normal forces. In this example, the torque has an average value of approx. $M_b = 370$ Nm before and after chattering. When chattering starts, the torque starts oscillating strongly ($\Delta M_b = 330$ Nm). Besides the torque, also the axial force and the normal force are affected by chattering. The oscillation of values of the axial force increases with the beginning of chattering. Further information on the investigations on mechanical loads in BTA deep hole drilling and the integration of the piezoelectric sensors into the drill head are given in [177,198,204,205].

Assessing the temperature in BTA deep hole drilling is particularly challenging due to the limited accessibility of the surface of the bore and the tool during machining. Thermal loads in BTA deep hole drilling were monitored by type K thermocouples with a diameter of $D = 250$ µm, which were placed inside of bores in the workpiece in close proximity to the bore wall. In addition to the thermoelectric measurements, an innovative approach based on pyrometry was developed and employed to evaluate temperatures directly at the cutting inserts and guide pads. In the investigations, the pyrometer FIRE-3 by en2aix (Energy Engineering Aachen, Aachen, Germany) was used. An optical fiber with a diameter of $D = 300$ µm was placed inside small bores in the workpiece. During drilling this fiber was cut. By the time the cutting edge of the insert entered the area of the optical fiber, the emitted thermal radiation was detected and used as a base for drawing conclusions about the temperatures at the very surface of the cutting edge. This method has already been proven to be well applicable for assessing temperatures in other drilling processes, such as twist drilling [206] and single-lip deep hole drilling [58].

Exemplary results of thermoelectric and pyrometric investigations on temperatures in BTA deep hole drilling are illustrated in Figure 3.9. For these experiments, the tool was rotated instead of the workpiece. Both methods indicate that an increase in feed results in significantly higher temperatures in drilling. In general, the impact of the cutting speed on temperatures seems to be less strong compared to the impact of the feed. The temperatures detected by ratio-pyrometry right at the surface of the cutting edges range from $T = 242°C$ to 1,074°C. At the highest cutting speed of $v_c = 100$ m/min an increase in feeds resulted in an increase in the average temperatures from $T = 425°C$ to 789°C. At a feed of $f = 0.225$ mm raising the cutting speeds resulted in the rising of the average temperatures from $T = 402°C$ to 592°C [179]. The highest temperatures were observed for the highest cutting speed of $v_c = 100$ m/min combined with the highest feed of $f = 0.300$ mm.

As displayed in Figure 3.9, for most of the cutting speeds and feed rates investigated the maximum temperatures exceed the austenitization temperatures of AISI 4140, as presented in Table 2.1. Further information on these investigations on the thermal loads in BTA deep hole drilling of AISI 4140 is provided in [179].

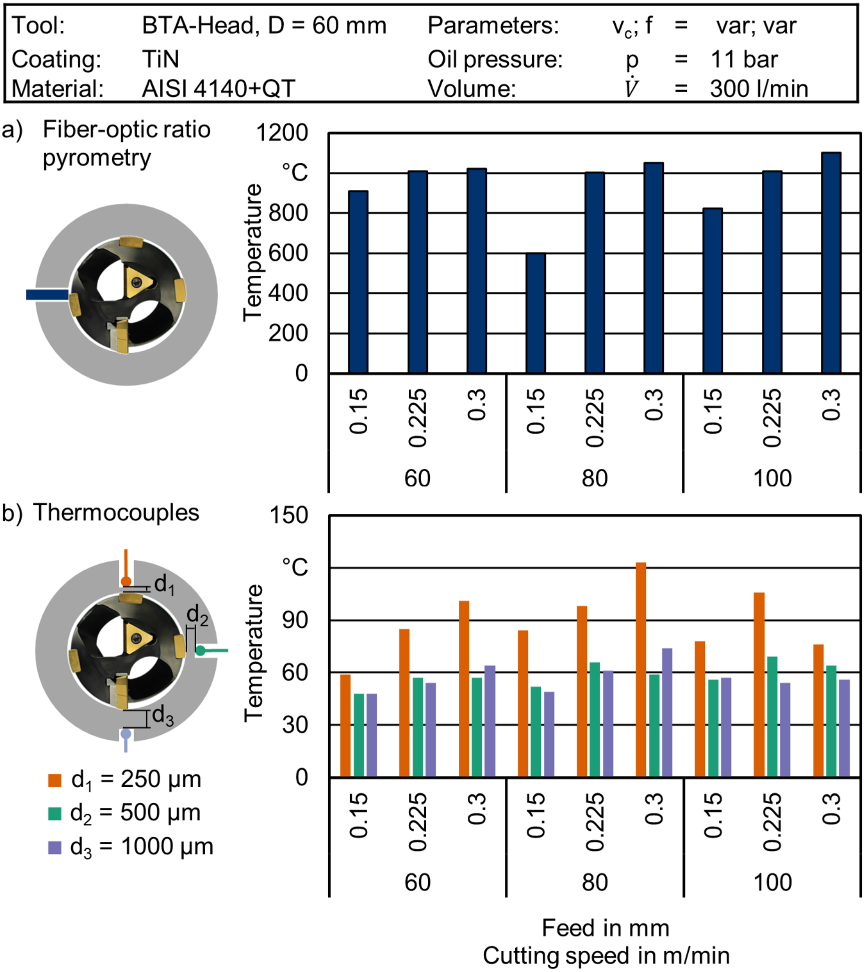

Figure 3.9 Temperatures in BTA deep hole drilling, obtained by a) ratio-pyrometry and b) thermocouples close to the bore wall [179,198]

4 Methodology[23]

This chapter presents the general methodology underlying this thesis (4.1) and the systems employed for evaluating SI are introduced. Information is provided on the methods and instrumentation used to assess the microstructure (4.2), the subsurface hardness (4.3), and the residual stresses (4.4) in BTA deep drilled specimens. In addition to this, the equipment used for multi-instrumental micromagnetic analyses based on MBN, Bitter technique, MOKE microscopy and MFM is introduced (4.5). An MBN-based test stand which allows for a rapid and holistic characterization of the BTA deep drilled specimens is presented (4.6). Additionally, the methods developed for analyzing the mechanical properties of BTA deep drilled components under quasi-static and cyclic loads are portrayed (4.7).

4.1 General procedure and modus operandi

Due to the limited accessibility of the bore wall, assessing the SI at the inner diameter of BTA deep drilled components is particularly challenging. However, aspects such as microstructure, microhardness, and residual stresses inside of bores are of particular importance, since they have a major impact on a component’s performance, as outlined in chapter 2.2.6. Subsequently, methods for a nondestructive inspection of SI are required, which can be employed to evaluate the crucial inner surface of bores, to ensure reliability and capability of a component throughout its service life.

In this thesis, MBN is qualified as a means for holistically assessing SI in BTA deep drilled components. Destructive and nondestructive methods are combined to gain a profound understanding of surface and subsurface conditioning in BTA deep hole drilling and elucidate the mechanisms governing surface generation. The results of these approaches are used to differentiate the effects of various aspects of SI on MBN. For instance, comprehensive microstructural investigations were performed by optical microscopy and SEM with a focused ion beam. These were linked to the values of FWHM obtained by XRD. Microhardness gradients in the subsurface of bores were assessed by microhardness mappings. Residual stresses in the BTA deep drilled specimens were assessed by two approaches based on XRD. To further elucidate the structure of magnetic domains in deep drilled

---

[23] Some of the contents presented in this section are prepublished in [207,198,208–210] and based on the student works [199–202].

specimens, MOKE microscopy and MFM were performed. The general methodology of the investigations presented in this thesis is presented in Figure 4.1. The specific procedures for the assessment of microstructure, microhardness, residual stresses, and magnetic domain structures are outlined in the following chapters.

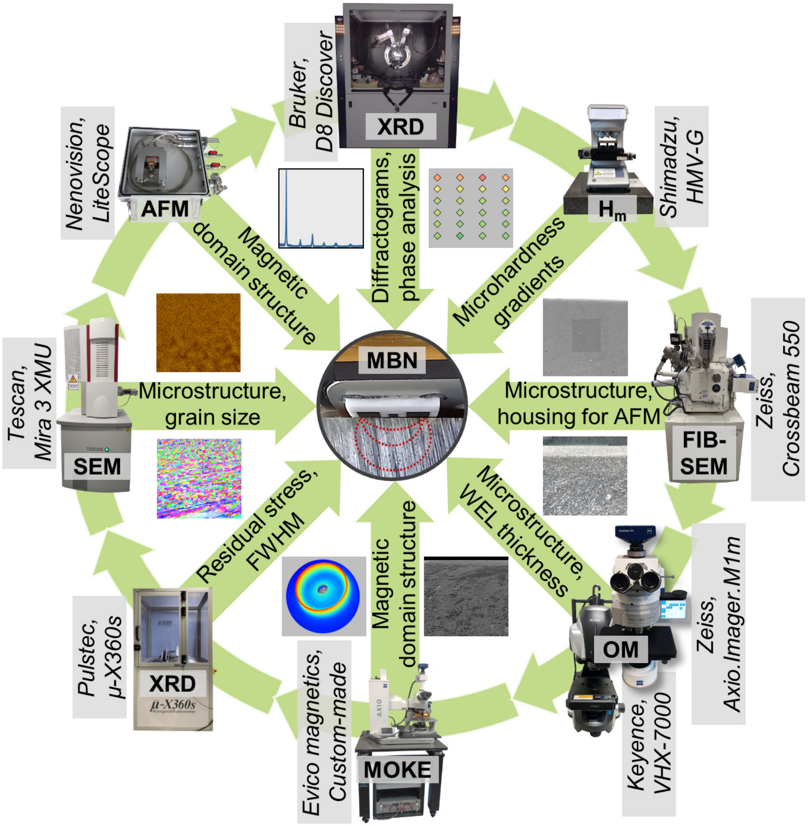

Figure 4.1 Holistic assessment of surface integrity (SI). According to [198]

4.2 Microstructural analyses

Microstructural analyses were performed by optical microscopy, SEM, and EBSD, TKD, ECCI and STEM. The optical microscopes and scanning electron microscopes used are presented in Figure 4.2. In addition to the ones depicted, the

FIB-SEM AMBER by TESCAN was used for TKD analyses. A method for digital micrograph inspection was developed which allows for precisely assessing the extent of WEL based on optical microscopy. In this approach, micrographs are first segmented, separating the WEL from the bulk material and the embedding resin. In the next step the segmented images are evaluated.

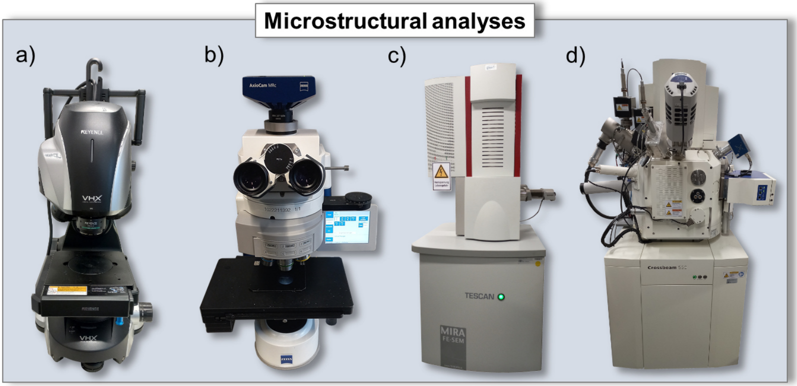

Figure 4.2 Optical microscopes and scanning electron microscopes: a) VHX-7000 (Keyence, Osaka, Japan); b) Axio Imager.M1m (Carl Zeiss, Oberkochen, Germany); c) Mira 3 XMU (Tescan, Brno, Czechia); d) Crossbeam 550 (Carl Zeiss, Oberkochen, Germany). Images of the systems according to [198]

4.2.1 Optical microscopy

Optical microscopy was performed using the microscopes VHX-7000 (Figure 4.2 a) and Axio Imager.M1m (Figure 4.2 b). Images were obtained by reflected light microscopy using bright field illumination. The magnification used was in the range of 100-1000-fold. Larger areas of workpieces were evaluated by stitching together micrographs. To automatically detect WEL, image segmentation was performed by partitioning micrographs into three classes. WEL were separated from the bulk material and the embedding resin by manual segmentation. The extent of WEL was then further evaluated by a set of algorithms implemented in NI LabVIEW. These allowed for a pixel-by-pixel calculation of the area covered by WEL in the micrographs, and the average thickness of the WEL. A more detailed account of this procedure is given in [211].

An example of this method is presented in Figure 4.3. A micrograph of a specimen drilled with a cutting speed of v_c = 60 m/min and a feed of f = 0.300 mm was segmented, highlighting the WEL in red. This segmented image is analyzed to obtain information on aspects such as the area covered by the WEL A_{WEL}, the average thickness of the WEL $t_{WEL,av}$, and the maximum thickness of the WEL $t_{WEL,max}$. In Figure 4.3 one of the flaws of this technique is highlighted with a circle marked A. It can be observed that material most certainly broke out of the WEL, however this region is not detected as WEL and subsequently not considered in the calculations. As a result, it is vital to prepare specimens as carefully as possible and ensure that no segments break out of the brittle WEL.

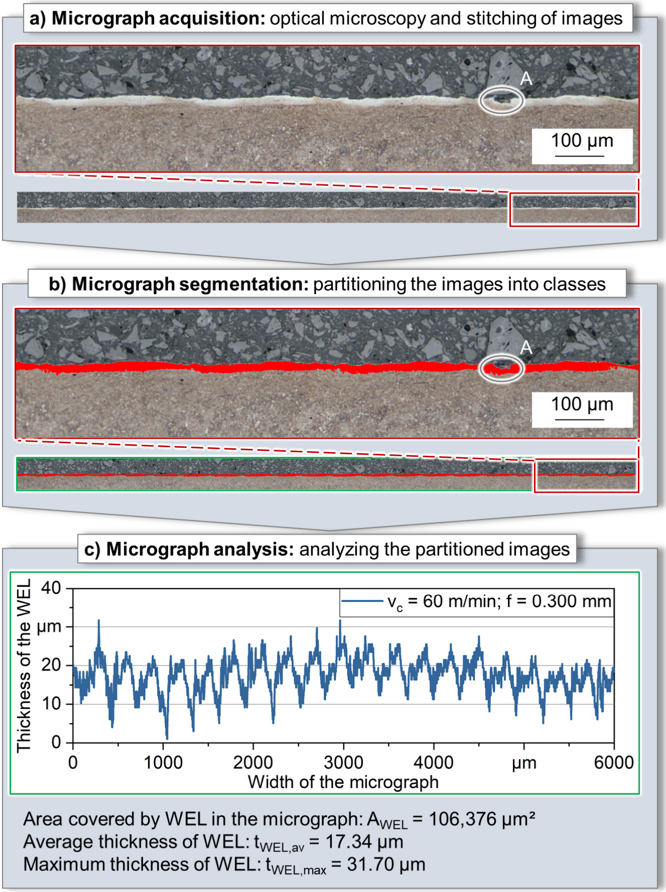

a) Micrograph acquisition: optical microscopy and stitching of images

b) Micrograph segmentation: partitioning the images into classes

c) Micrograph analysis: analyzing the partitioned images

Area covered by WEL in the micrograph: A_{WEL} = 106,376 µm²
Average thickness of WEL: $t_{WEL,av}$ = 17.34 µm
Maximum thickness of WEL: $t_{WEL,max}$ = 31.70 µm

Figure 4.3 Procedure and data processing in digital image analysis, consisting of: a) acquisition of micrographs by optical microscopy and stitching of images; b) segmentation of the stitched images; c) analysis of the partitioned micrographs to obtain data on the area covered by white etching layers (WEL), the average thickness of the WEL and the maximum thickness of the WEL

4.2.2 Advanced approaches for crystallographic analysis in SEM

For scanning electron microscopy, the SEM Mira 3 XMU, was used (Figure 4.2 c). Additionally, SEM in combination with a focused ion beam was performed by the device Crossbeam 550 (Figure 4.2 d). For EBSD analyses, both scanning electron microscopes presented were used. In the Mira 3 XMU an EDAX Velocity Plus detector was employed. For EBSD analyses in the Crossbeam 550, an Oxford Instruments NordlysMax3 detector was employed. Cross-sections extracted in the transverse direction were tilted by 70°, using an appropriate sample holder. This setup is presented in Figure 4.4. Acceleration voltage was set to U_B= 25 kV and a stepsize of s = 25 nm (Mira 3 XMU) and s = 5 nm (Crossbeam 550) was used. Working distance was set in the range of d_{wd} = 15 to 18 mm. Images were recorded with a width of w = 30 µm and a length of l = 30 µm in the Mira 3 XMU and a width of w = 4 µm and a length of h = 4 µm in the Crossbeam 550, respectively. Results were visualized in the software OIM analysis by EDAX (Mira 3 XMU) and AZtec by Oxford Instruments (Crossbeam 550). For ECCI analyses, a backscattered electron detector was used in the Crossbeam 550. Specimens were tilted in an angle of 5°, the working distance was set in between d_{wd} = 2 to 4 mm and an acceleration voltage of U_B = 25 kV was used. TKD was performed by Dr. Tom Jäpel of TESCAN, using the FIB-SEM AMBER by TESCAN with a Symmetry S3 detector by Oxford Instruments in an off-axis geometry. The step size for TKD was s = 0.03 µm. The preparation of the lamella for TKD will be presented along with the results in 5.2.3. STEM analyses were performed using the FIB-SEM Crossbeam 550. The preparation of an exemplary lamella for STEM analysis is presented in Figure 4.5.

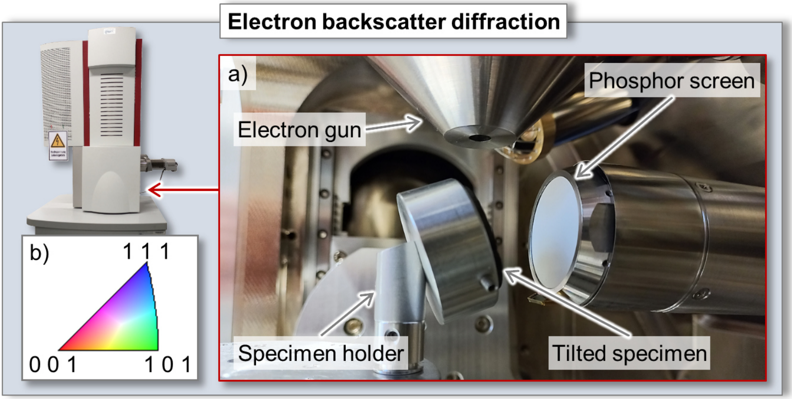

Figure 4.4 EBSD analysis: a) setup in the SEM Mira 3 XMU, b) color code of the inverse pole figures. Images of the system according to [198]

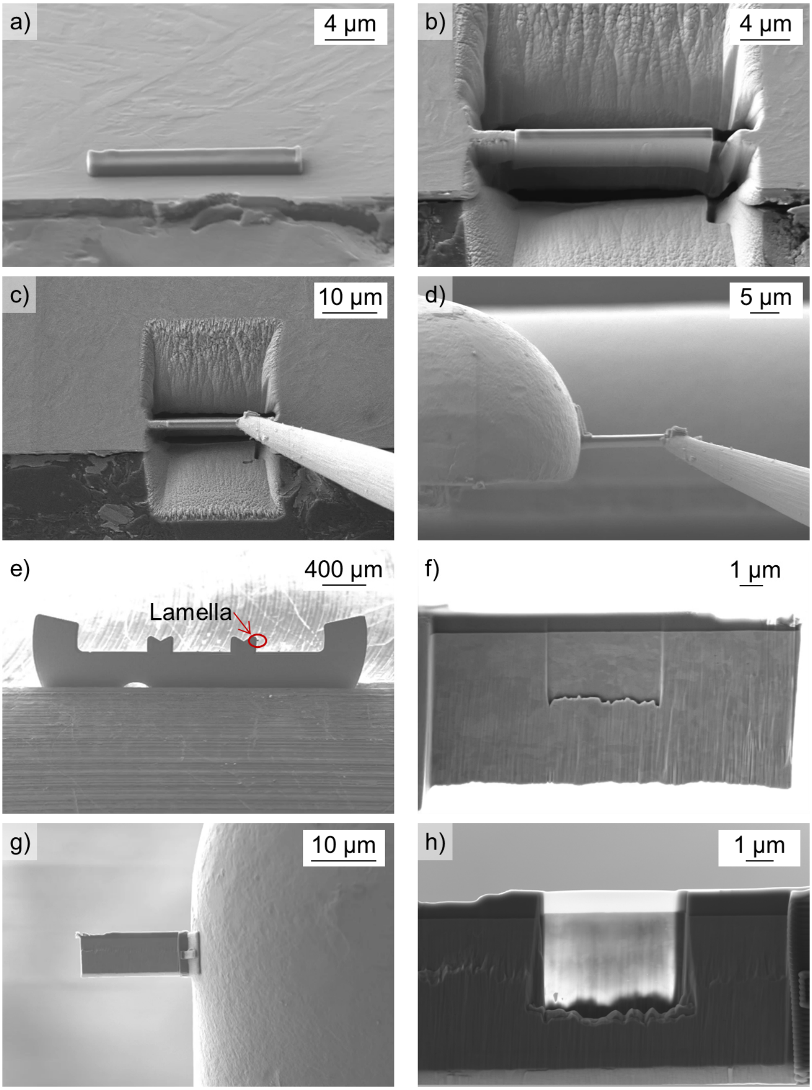

Figure 4.5 Preparation of a lamella for STEM analyses: a) applying a platinum deposition, b) milling of the lamella, c) attaching the lamella to the manipulator, d) attaching the lamella to the grid, e) lamella attached to the grid, f) polishing of one side, g) the grid is rotated to allow for polishing of the other side, h) lamella prepared for STEM

4.3 Subsurface hardness

Microhardness mappings were performed using the device HMV-G21 by Shimadzu. A force of F = 0.098 N was applied for a time of t = 10 s to assess Vickers hardness HV 0.01. Mappings were performed according to the schemes depicted in Figure 4.6, analyzing cross-sections in transverse direction (Figure 4.6). This positioning of the impressions transgresses the standard DIN EN ISO 6507-1 for Vickers hardness testing. However, small distances are required to assess the microhardness in very close proximity to the surfaces.

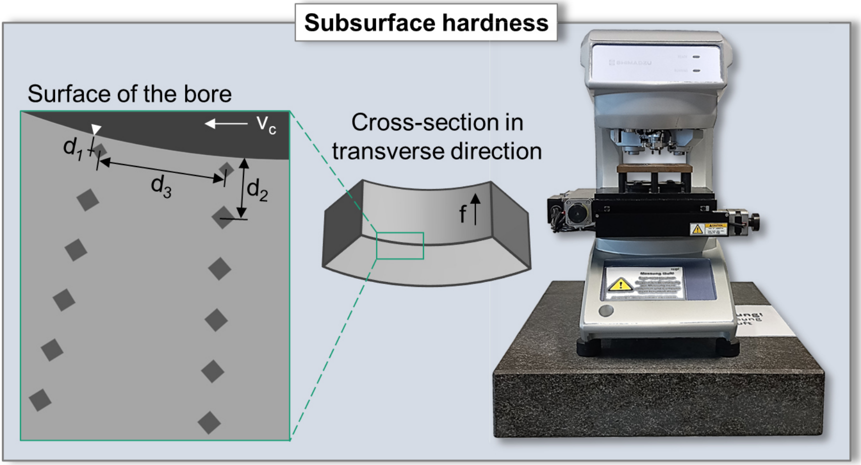

Figure 4.6 Microhardness testing system HMVG-21 by Shimadzu and scheme for the microhardness mappings in transverse sections, with $d_1 = 5$ µm, $d_2 = 20$ µm and $d_3 = 100$ µm. Images of the system according to [198]

4.4 X-ray diffraction

Two approaches in X-ray diffraction were used to analyze residual stress states and assess crystallite sizes based on FWHM. Residual stresses were obtained by XRD following the $\sin^2\psi$-method and by using the $\cos\alpha$-method. The equipment employed for the investigations is presented in Figure 4.7. The parameters used in X-ray diffraction are presented in Table 4.1.

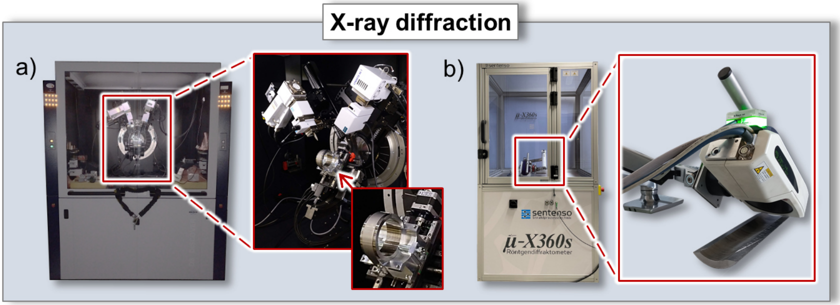

Figure 4.7 Instrumentation used for X-ray diffraction: a) D8 Discover (Bruker Corporation, Billerica, MA, United States); b) μ-X360s (Pulstec Industrial Co. Ltd., Japan). Images of the systems according to [198]

Table 4.1 Parameters in X-ray diffraction

	Bruker D8 Discover	**Pulstec μ-X360s**
Tube	Chromium	Chromium
2θ angle	106°	156°
Collimator diameter	1.0 mm	0.5 mm
Tilt	χ	-
Poisson’s ratio ν	0.33	0.28
Young’s modulus E	165 GPa	220 GPa

$\sin^2\psi$-method

For X-ray diffraction according to the $\sin^2\psi$-method the system D8 Discover was used (Figure 4.7 a). This is a fully radiation protected stationary system for XRD with several axes for accurately setting the required increments. For analyzing residual stresses, a chromium tube was used. For residual stress analyses, a 2θ angle of 106° was analyzed, to avoid shading of the radiation in the ring segments extracted.

cosα-method

The instrument μ-X360s was employed to assess residual stresses according to the cosα-method. The portable device is equipped with a chromium X-ray tube and collimators with varying diameters. An image plate is used to obtain a full Debye-Scherrer ring. Besides residual stresses, also FWHM values of the peak at 156.396° were obtained. For calculating grain sizes based on the Scherrer equation, k was assumed as 0.94, as this is the common value for spherical particles [117]. The wavelength of the X-rays was $\lambda = 2.291$ Å, FWHM was the full width at half maximum of the peak at a 2θ angle of $2\theta = 156.396°$, and θ was the Bragg angle of $\theta = 78.198°$.

4.5 Micromagnetics

Complementary systems were employed, to assess the micromagnetic structure of BTA deep drilled specimens on different scales and with varying spatial resolution (Figure 4.8). Magnetic Barkhausen noise analyses were performed using two commercial systems. These were employed to evaluate the magnetic properties of deep drilled specimens on a rather large volume scale, in a particularly time-efficient and straightforward way. To analyze the magnetic domains on a smaller scale, cross-sections prepared by Bitter etching were analyzed. In addition to this, MOKE microscopy was performed, for an enhanced understanding of the domain wall movement in response to an applied magnetic field, analyzing cross-sections extracted in transverse direction. MFM was done to evaluate the micromagnetic structure of BTA deep drilled specimens with particularly high resolution at the very surface to a depth of d = 20 μm and in the bulk material.

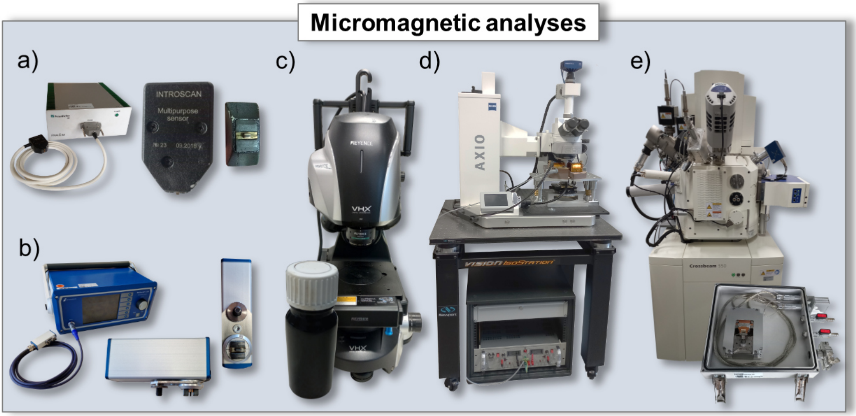

Figure 4.8 Micromagnetic instruments used: a) FracDim (Fraunhofer IKTS, Dresden, Germany), b) Rollscan 350 (Stresstech, Jyväskylä, Finland), c) VHX-7000 (Keyence, Osaka, Japan), d) MOKE microscopy (evico magnetics, Dresden, Germany), e) FIB-SEM Crossbeam 550 (Carl Zeiss, Oberkochen Germany) and AFM LiteScope 2.0 (NenoVision, Brno, Czechia). Images of the systems according to [198]

Magnetic Barkhausen noise

Magnetic Barkhausen noise was assessed by the devices FracDim (Figure 4.8 a) and Rollscan 350 (Figure 4.8 b). FracDim measurements were performed with a multipurpose sensor. The receiving coil in between the magnetic yoke is spring-loaded and thus in contact with the surface of the bores during measurements. The magnetic flux was controlled and set to $\phi_{mag} = 4.7\ \mu Vs$, a magnetization frequency of $f = 60$ Hz was used and a band-pass filter with $f_{low} = 10$ kHz to $f_{high} = 200$ kHz was employed for all analyses, if not stated differently in the results section. FracDim measurements were performed using the Software Modimag.

The Rollscan 350 was used with a multipurpose sensor as well. Just like in the sensor for the FracDim, the receiving coil in the middle of the magnetic yoke is spring-loaded and in contact with the borehole wall. For Rollscan measurements with the multipurpose sensor, a magnetization frequency of $f_{mag} = 200$ Hz was used in combination with a magnetization voltage of $V_{pp} = 10$ V and a band-pass filter of $f_{low} = 70$ kHz to $f_{high} = 200$ kHz.

Besides the multipurpose sensor, a custom-designed miniature sensor was developed in close collaboration with Stresstech Oy, which can be mounted inside a drill head. This sensor is displayed in Figure 4.9. A comprehensive account of how this sensor was designed and implemented is given in [205]. In contrast to the multipurpose sensors, the sensing coil is not spring loaded, but in a fixed position. In addition to this, the amplifying electronics are placed outside of the sensor housing. The length of the cable connecting the sensor to the amplifying electronics was l = 1000 mm, to allow for mounting the instrumented bore head onto the boring bar of the BTA deep hole drilling machine and feeding the cable through the BOZA. By separating some of the electronics, sensors with particularly small dimensions can be created. Based on its design, the sensor can be used in contact but also with a small air gap in between the sensing coil and the borehole wall. For Rollscan measurements, the software ViewScan was used as well as the analog output of the system.

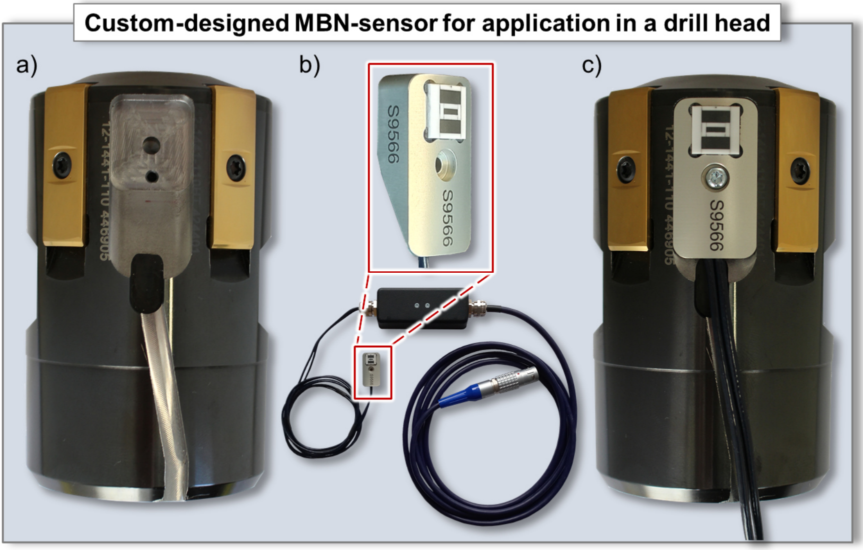

Figure 4.9 Mounting of a custom-designed MBN-sensor in a BTA drill head: a) BTA drill head with a milled pocked, a bore with a thread for fixing the sensor, and a groove for the positioning of the sensor cable, b) custom-designed miniature sensor for the Rollscan 350 with an external amplification, c) sensor mounted inside the BTA drill head

Bitter etching

Bitter etching was performed using commercially available oil-based ferrofluid with a particle size of approx. $D_p = 10$ nm. A drop of the ferrofluid was applied to the OPS-polished cross-sections. A coverslip was then placed onto the cross-sections. The agglomerating particles at the domain walls of the specimens were observed with a VHX-7000 digital microscope by Keyence (Figure 4.8 c).

Magneto-optic Kerr effect microscopy

MOKE microscopy was performed to enhance the understanding of the magnetic microstructures inside the BTA deep drilled specimens by in-situ monitoring of the magnetic domains during the magnetization process. Investigations were carried out with a custom-made system by evico magnetics, composed of an Axio Imager light microscope by Carl Zeiss, an ORCA-CMOS camera, LEDs, a magnetometer, and a magnet for the induction of the magnetic field by evico magnetics. A magnification of 50x was employed. The system is depicted in Figure 4.8 d) and Figure 4.10. During magnetization, the positioning of the specimen was controlled by piezo actuators in the x, y, and z directions. This way, specimens were kept from moving in spite of the magnetic pull of the induction magnets. To keep the magnetic attraction low, the OPS-polished cross-sections were cut to particularly small dimensions. Sections were mounted onto stubs (Figure 4.10). Two LEDs were used to illuminate the specimen, placed in orthogonal direction to the inner surface of the bore. For obtaining images, the following procedure was used: in the first step, the specimen is captured in the unmagnetized state. The obtained image is used as background level. To reveal the magnetic microstructure of the remanence point, specimens were magnetized first to the maximum and then to the minimum achievable magnetization field strengths. Afterwards, external magnetization was set to zero and the image subtraction function of the software was activated to differentiate the current magnetization state from the background level. Next, the external magnetic field strength is incrementally increased to record the evolution of the magnetic microstructure with increasing field strengths.

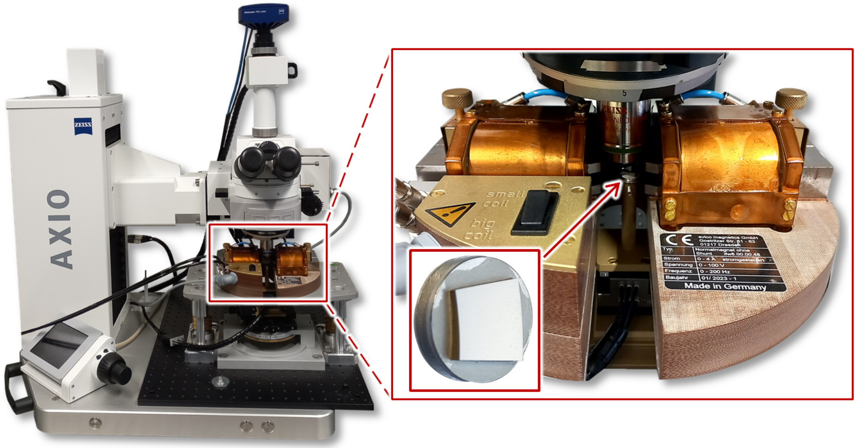

Figure 4.10 Instrumentation used for Magneto-optic Kerr effect (MOKE) microscopy

Images are obtained for varying magnetization, by incrementally increasing the magnetic field strength in steps of $H = 50$ kA/m. Specimens were analyzed at the inner surface of the bores, and in the bulk material at a distance of $d_{surf} > 1$ mm.

Magnetic force microscopy

The same OPS-polished cross-sections were used for MFM as for MOKE microscopy. Measurements were performed using the AFM LiteScope 2.0 by Nenovision and the software Nenoview (Figure 4.8 e). The instrument was mounted inside the FIB-SEM Crossbeam 550 by Zeiss to carry out the investigations under vacuum (Figure 4.12). The cantilever was equipped with a magnetic tip. The quality of the magnetic tip and its suitability were controlled by SEM (Figure 4.11).

The resonance frequency of the cantilever was approx. $f_{resonance} = 40{,}417$ Hz. A piezoelectric actuator was used to make the cantilever oscillate. The phase shift of the cantilever was monitored by a piezoelectric sensor. Images were obtained in a dual-pass scanning strategy. A first pass of the cantilever was performed to assess the topography in tapping mode. In a second pass, the cantilever was lifted by an offset in the z-axis, and the magnetic interaction between the tip and the specimen was assessed by measuring the phase shift without contact with the surface. If not stated differently in the corresponding part of the results section, the offset for the second pass was $d_{offset} = 80$ nm. The scanning speed was $v_{scan} = 3$ µm/s and a setpoint of approx. $f_{setpoint} = 6$ Hz was used in the first pass. Due to the nature of this method, specimens could not be analyzed at the very edge of the cross-sections, to avoid damaging the cantilever or the tip. Instead, cross-sections were analyzed at a distance of a few microns to the edge of the specimens. In addition to the subsurface of specimens, the bulk material was analyzed at a distance of approx. $d = 1$ mm to the edge. The areas scanned had a width of $w = 10$ µm and a length of $l = 10\text{-}20$ µm. Postprocessing of the data included tilt correction, scale adaption, and cropping and was performed using the software Gwyddion.

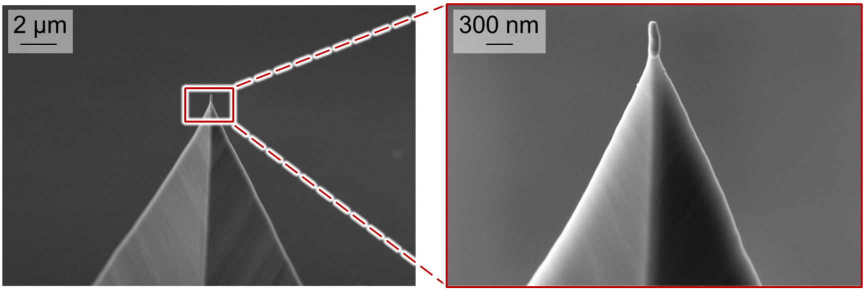

Figure 4.11 SEM image of the magnetic tip used for MFM analyses

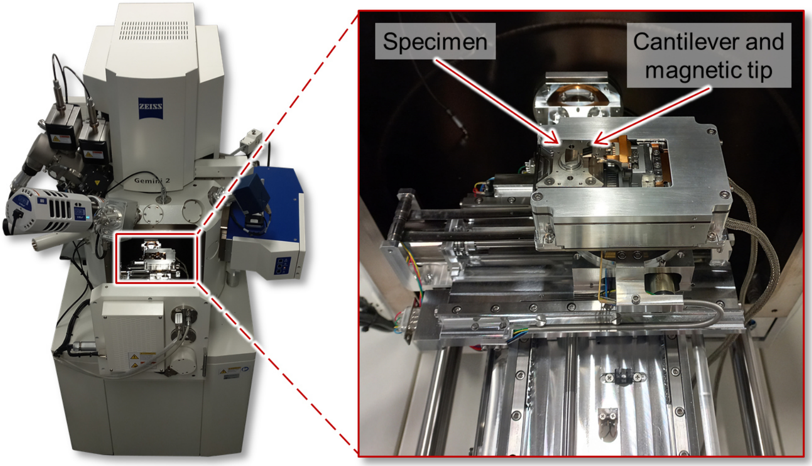

Figure 4.12 Atomic force microscope (AFM) mounted inside the focused ion beam scanning electron microscope (FIB-SEM) for magnetic force microscopy (MFM) measurements

4.6 MBN-based test stand

Based on the methods presented in 4.5, a test stand was developed which allowed a more precise MBN-based assessment of SI inside BTA deep drilled boreholes. This test stand is depicted in Figure 4.14. Specimens are fastened to a dividing head for accurately positioning them in axial and angular directions. This dividing head allows for precisely rotating the specimens in small increments with a dividing-ratio of 1:40. A custom-designed positioning device is mounted onto a linear bearing. This device is composed of an aluminum frame and a 3D-printed cantilever with a thread at the tip, similar to the threads at BTA boring bars. Customized sensor positioning devices were designed and 3D-printed. These are adapted for mounting the multipurpose sensors of FracDim and Rollscan 350 and can be attached to the cantilever of the positioning device by threads. In addition to these sensors, the instrumented drill head presented in Figure 4.9 c) can be mounted onto the cantilever. A draw wire sensor is fixed to the aluminum frame and its rope is attached to the dividing head. This way, the draw wire sensor can be used for monitoring the position of the MBN sensors inside the specimens in the axial direction. In addition to this, two linear potentiometers are applied to the positioning device of the Rollscan multipurpose sensor. One of these faces upwards and the other one is rotated by 90° and points to the side. These sensors allow for analyzing the distance between the positioning device and the borehole wall of the specimen. Thus, a misalignment of the specimen can be detected. The draw wire sensor and the positioning devices are supplied with an excitation voltage by NI myDAQ devices (National Instruments, Austin, TX, United States). Additionally, these devices are used for acquiring the data of the sensors. For this purpose, the myDAQ devices are connected to a control panel. This control panel runs a custom-made LabVIEW software, which allows for collecting data from the linear potentiometers, the draw wire sensor, and the analog output of the Rollscan 350. The graphical user interface of this software is depicted in Figure 4.13, showing an exemplary reading of the sensors. A status LED indicates, whether or not the reading of the MBN signal is in between the lower and the upper threshold levels, which are user-defined variables. The general working principle of the test stand is presented in [212].

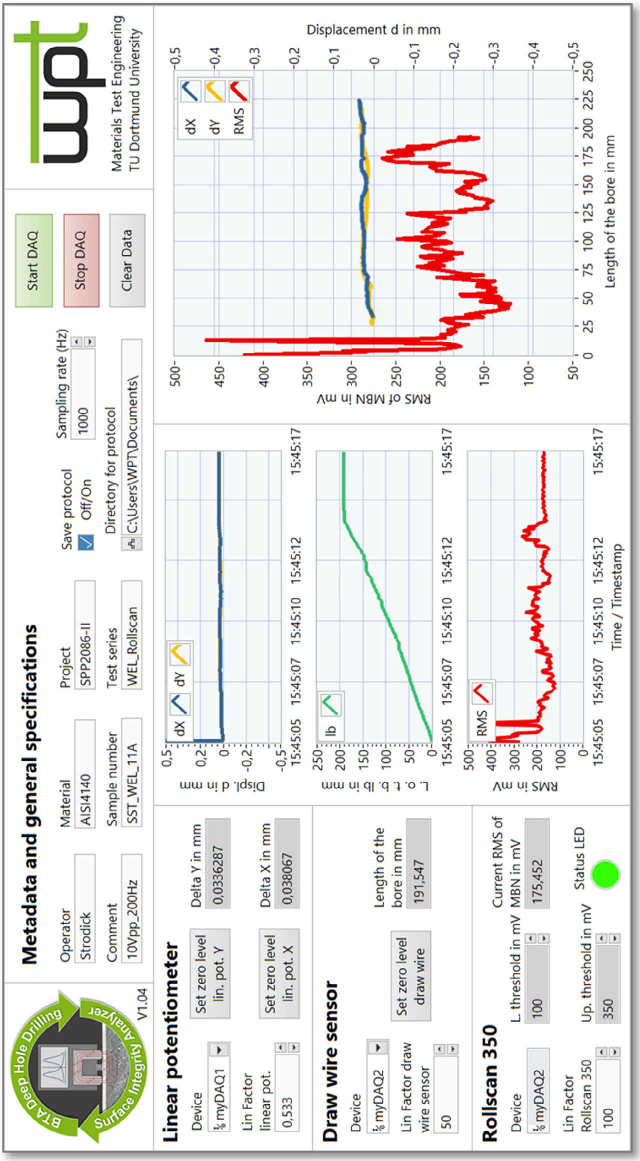

Metadata and general specifications

Operator: Strodick
Material: AISI4140
Project: SPP2086-II
Save protocol ☑ Off/On
Sampling rate (Hz): 1000
Comment: 10Vpp_200Hz
Sample number: SST_WEL_11A
Test series: WEL_Rollscan
Directory for protocol: C:\Users\WPT\Documents\

Linear potentiometer

Device: myDAQ1
Lin Factor linear pot.: 0,533
Delta Y in mm: 0,0336287
Delta X in mm: 0,038067

Draw wire sensor

Device: myDAQ2
Lin Factor draw wire sensor: 50
Length of the bore in mm: 191,547

Rollscan 350

Device: myDAQ2
Lin Factor Rollscan 350: 100
L. threshold in mV: 100
Up. threshold in mV: 350
Current RMS of MBN in mV: 175,452
Status LED ●

Figure 4.13 Graphical user interface of the software used for the control panel of the MBN-based test stand

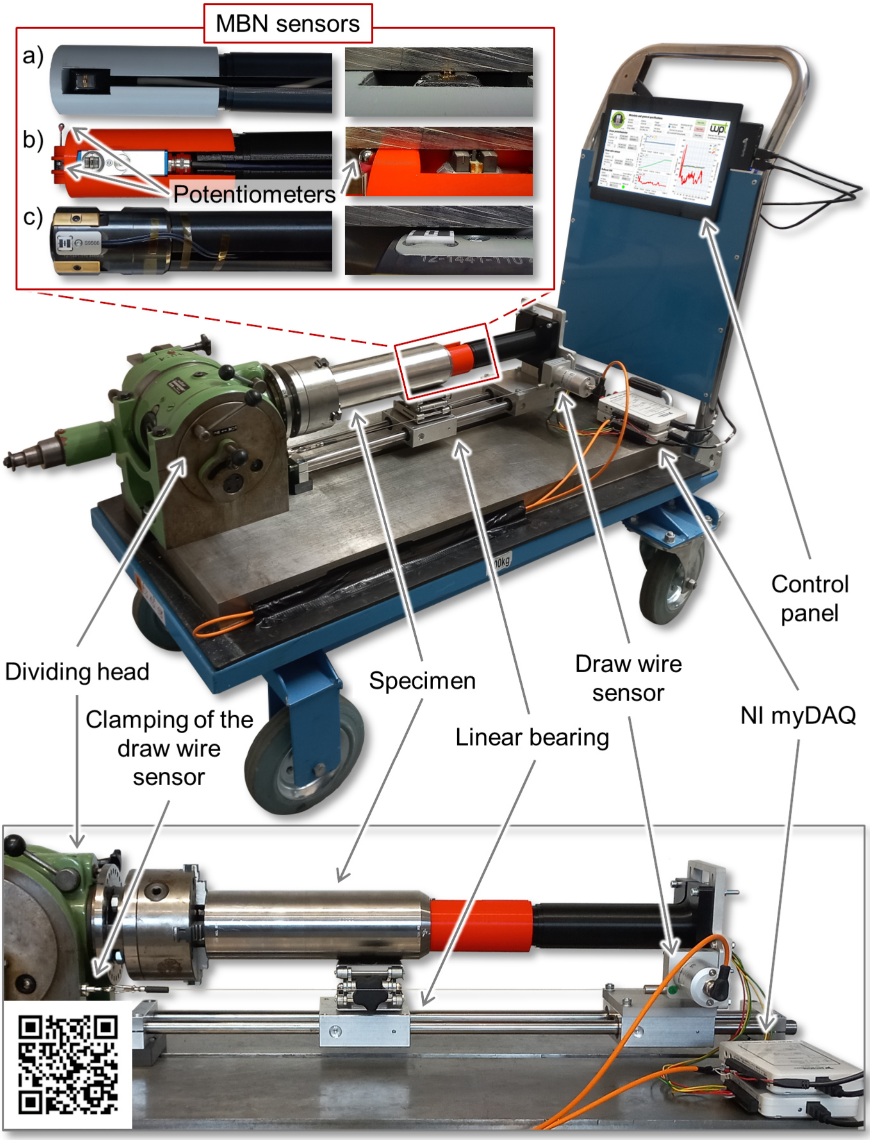

Figure 4.14 MBN-based test stand for the assessment of surface integrity (SI) in BTA deep drilled boreholes. The QR code links to an animation of the test stand [212]

4.7 Methods for mechanical characterization

A method was developed for assessing the performance of the BTA deep drilled specimens under quasi-static and cyclic compression, which was inspired by the tube-flattening test according to DIN EN ISO 8492. The general procedure of this method is illustrated in Figure 4.15 [207].

Deep drilled specimens, prepared following the methodology presented in 3.2.2, were divided into 5 segments with a length of $l_{seg} = 30$ mm per bore and turned to an outer diameter of $d_{out} = 74$ mm. The segments were then compressed by applying a force in a quasi-static or cyclic manner. The parameters used for quasi-static testing are presented in 4.7.1. Cyclic testing following this method is presented in 4.7.2.

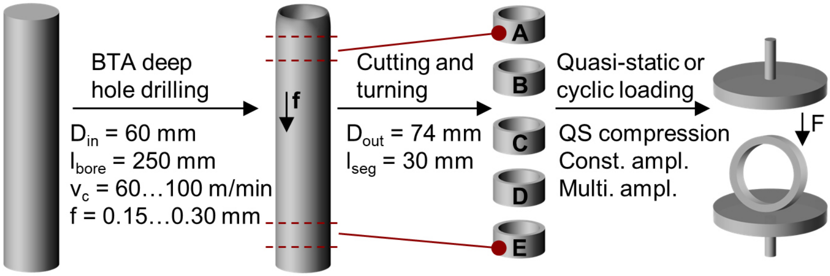

Figure 4.15 Mechanical characterization of BTA deep drilled specimens. According to [207]

4.7.1 Quasi-static compression

For all quasi-static and cyclic compression tests, a servohydraulic testing system Schenck PSB100 with an Instron 8800 controller was used. Forces were measured with a load cell with a limit of F = 75 kN. The testing system used is depicted in Figure 4.16. In quasi-static testing, the upper compression plate was lowered with a velocity of $v = 5$ mm/min.

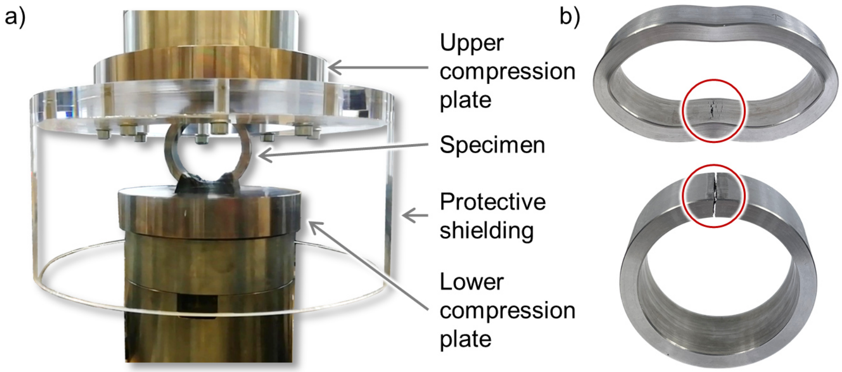

Figure 4.16 Quasi-static and cyclic compression of BTA deep drilled specimens: a) setup used at the servohydraulic testing system Schenk PSB 100, according to [207], b) two exemplary specimens after compression testing, the upper one was subjected to quasi-static loads, whereas the lower one was subjected to cyclic loads

4.7.2 Cyclic compression

Cyclic tests were performed analyzing compression-compression loading by applying constant amplitudes. Tests were carried out with a frequency of $f_{cyc} = 10$ Hz, a mean force of $F_m = -13.75$ kN, and a force amplitude of $F_a = 11.25$ kN. The stress ratio subsequently was $R = 10$ for all tests.

Intermittently during fatigue testing, the evolution of residual stresses was monitored by MBN analysis and X-ray diffraction, using the methods presented in (4.5) and in (4.4) respectively. For intermittent tests by X-ray diffraction, the specimens were subsequently removed from the machine and placed inside the Bruker D8 discover diffractometer. Here, the specimen design and the relatively low Bragg-angle of 106° allowed for nondestructively characterizing the residual stresses inside the bore.

5 Results and Discussion[24]

This chapter presents and discusses the results of the investigations, providing information on subsurface conditioning in BTA deep hole drilling in general and the applicability of methods in destructive and nondestructive testing for SI characterization. General findings on SI resulting from BTA deep hole drilling are presented in 5.1, considering microstructure (5.1.1), microhardness gradients (5.1.2) and residual stresses (5.1.3) in the subsurface of the deep drilled specimens. In 5.2, an in-depth analysis of WEL induced by deep hole drilling is provided. The extent of white etching layers at the surface of BTA deep drilled specimens is thoroughly evaluated by digital analysis of segmented images obtained by optical microscopy and manual segmentation (5.2.1). In 5.2.2 and 5.2.3 results are provided for advanced crystallographic analyses of WEL, including X-ray diffraction, STEM, ECCI, and TKD. Scale-bridging micromagnetic approaches are used for characterizing SI resulting from BTA deep hole drilling and particularly white etching layers in (5.3). These include a large-scale assessment via MBN analyses as well as particularly high-resolution MFM analyses. In 5.4, the capability of BTA deep drilled specimens is assessed, by applying quasi-static and cyclic compression loads.

5.1 Subsurface conditioning

Subsurface conditioning in BTA deep hole drilling is characterized by a rather high level of complexity, as it results from the combined thermomechanical loads exerted on the borehole wall by the cutting inserts and by the guide pads. As a result of cutting and subsequent plastic deformation in drilling, the material in the subsurface is altered in terms of e.g. microstructure, microhardness, and residual stresses. These fields of SI are strongly interconnected. For instance, evidence will be provided in this chapter that the microstructure induced by BTA deep hole drilling is closely linked to the microhardness and the residual stresses in the subsurface of bores. Subsequently, the following subchapters need to be considered in close conjunction with one another.

---

[24] Some of the contents presented in this section are prepublished in [198,208,209,213,210,204] and based on the student works [199–202].

5.1.1 Microstructure

Figure 5.1 presents exemplary results of optical microscopy. In a) the subsurface of a specimen drilled at a relatively low cutting speed and feed is presented. The specimen depicted in b) was drilled using relatively high cutting parameters. It can be observed that the specimens exhibit clearly distinct structures. The specimen depicted in Figure 5.1 b) reveals a three-layered subsurface. At the very surface, a WEL can be observed with a thickness of approx. $t_{WEL} = 16\ \mu m$. Beneath the WEL, traces of a swept microstructure can be observed. This transitional layer is followed by the bulk material. No clear boundary can be observed between the bulk material and the plastically deformed layer in the micrographs obtained by optical microscopy. This three-layered structure in the subsurface of BTA deep drilled steels, composed of a WEL, a transitional layer, and the bulk material has been reported for BTA deep hole drilling multiple times, for instance by Griffiths, who analyzed AISI 1040 [164], by Fuß, who investigated on AISI 5115 and AISI 1060 [147] and by Li, who assessed ASME SA508 steel [19]. Zhang observed a similar structure analyzing BTA deep drilled cast iron [183]. The specimen drilled using a relatively moderate cutting speed and feed rate does neither exhibit a WEL, nor a severely deformed layer in optical microscopy. The reason for these distinct structures of the two specimens might be found in the temperatures (Figure 3.9) and forces during drilling, since these were significantly lower when using a cutting speed of $v_c = 60$ m/min and a feed of $f = 0.150$ mm. This interconnection between forces, temperatures and the resulting microstructure in the subsurface of bores will be discussed further in this chapter as well as in chapters 5.2 and 5.3.

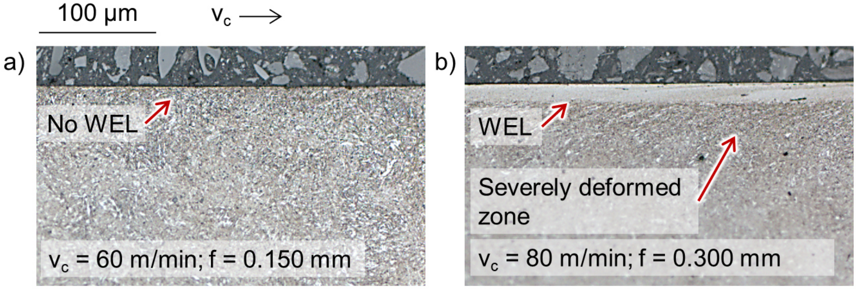

Figure 5.1 Micrographs with and whithout white etching layers (WEL): a) etched cross-section of a specimen, drilled at a cutting speed of $v_c = 60$ m/min and a feed of $f = 0.150$ mm; b) etched cross-section of a specimen, drilled at a cutting speed of $v_c = 80$ m/min and a feed of $f = 0.300$ mm (batch A)

To analyze the impact of feed and cutting speed on the microstructural alterations in the subsurface and particularly on the formation of WEL, nine combinations of drilling parameters were investigated. The results of optical microscopy of cross-sections extracted in transverse direction are presented in Figure 5.2. Micrographs of cross-sections extracted in the longitudinal direction are displayed in Figure 5.3. WEL were observed in both directions.

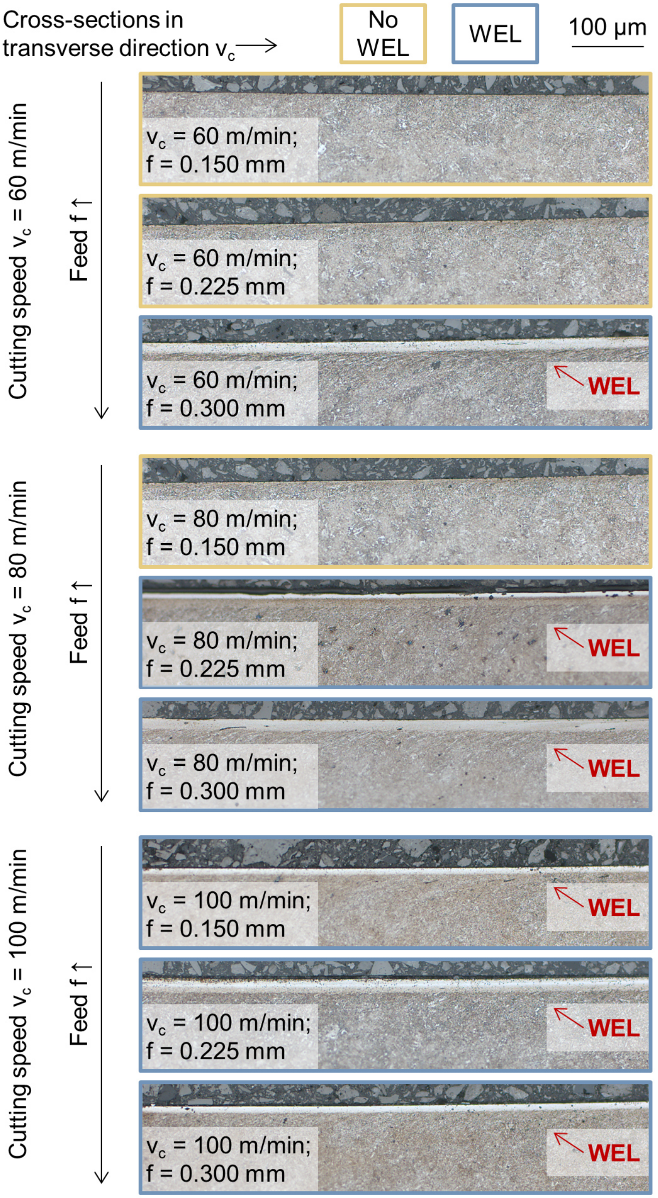

Figure 5.2: Etched cross-sections in the transverse direction of specimens drilled at varying cutting speeds (v_c = 60-100 m/min) and feeds (f = 0.150-0.300 mm) (batch A)

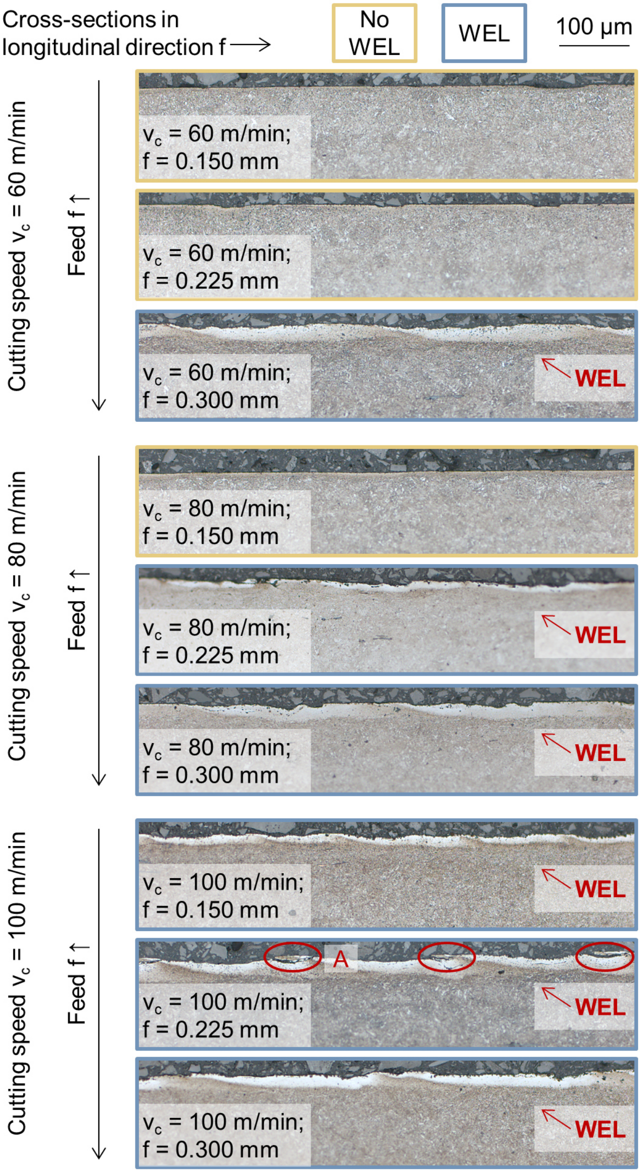

Figure 5.3 Etched cross-sections in the longitudinal direction of specimens drilled at varying cutting speeds (v_c = 60-100 m/min) and feeds (f = 0.150-0.300 mm) (batch A)

For three out of the nine combinations of cutting speed and feed, no clear WEL were observed. The other six parameter sets resulted in the formation of WEL. For the specimens without clear WEL, a very thin, scattered bright rim was observed at some parts of the surfaces (Figure 5.4). This bright rim might be considered a preliminary stage to the formation of clear, and significantly thicker WEL. It resembles the fragmented layers observed by Fuß in the BTA deep hole drilling of AISI 1060 and by Griffiths in BTA deep drilled AISI 1040. According to Griffiths, the original microstructure cannot be discerned inside these fragmented layers [164]. Fuß hypothesizes that the fragmented layers form when thermal loads in drilling are significantly elevated, but not high enough for a clear WEL to be formed [147]. Conversely to specimens with clear and thick WEL, specimens of this type will be categorized as largely free of WEL in the further course of this work. In cross-sections extracted in the transverse direction, the thickness of WEL is found to be relatively constant. Thicknesses range from approx. $t_{WEL} = 6$ µm ($v_c = 80$ m/min; $f = 0.225$ mm) to approx. $t_{WEL} = 22$ µm ($v_c = 100$ m/min; $f = 0.225$ mm). Some micrographs reveal a slightly darker layer beneath the WEL and signs of a swept microstructure resulting from plastic deformation Figure 5.2 ($v_c = 60$ m/min; $f = 0.300$ mm). However, compared to other machining processes, the darker layers between the WEL as well as the traces of severe plastic deformation seem less pronounced in the given micrographs.

The surfaces of the specimens in the transverse direction are rather smooth. In contrast, most surfaces in the longitudinal direction show geometrical defects. Some cross-sections reveal regular grooves in the longitudinal direction. The spacing between these marks corresponds to the feed employed in drilling. This observation fits the typical topography of BTA deep drilled specimens, composed of flat-topped plateaus and feed marks in between them (Figure 2.25) [147,164]. This is illustrated by the example of the specimen drilled at a cutting speed of $v_c = 60$ m/min and a feed of $f = 0.225$ mm in Figure 5.4.

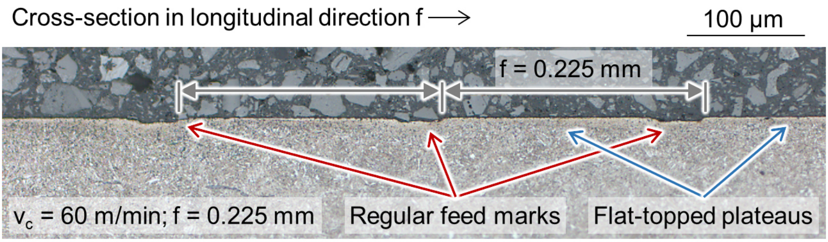

Figure 5.4 Typical topography of BTA deep drilled specimens, composed of regular grooves and flat-topped plateaus for a specimen drilled at a cutting speed of $v_c = 60$ m/min and a feed of $f = 0.225$ mm (batch A)

Besides the regular grooves, the thickness of the WEL in the longitudinal direction alters periodically with the feed in drilling. This will be analyzed and quantified later on in this thesis (5.2.1). The specimen drilled at a cutting speed of $v_c = 100$ m/min and a feed of $f = 0.225$ mm reveals cracks inside the WEL (Figure 5.3, marked "A"). This observation corresponds to the brittle nature of WEL and agrees with the general consensus that WEL are highly susceptible to crack initiation [73,143,151]. In general, longitudinal sections with WEL show more surface defects, compared to specimens free of WEL.

A periodicity in the shape of the WEL was also observed in the transverse direction. In Figure 5.7 two particularly large-scale stitched micrographs in the transverse and the longitudinal direction of a specimen machined with a cutting speed of $v_c = 100$ m/min and a feed of $f = 0.300$ mm are presented. It can be observed, that also in the direction of cutting, the thickness of the WEL increases and decreases regularly. This shape of the WEL results from the combined effects of the feed and the rotation of the tool, respectively the workpiece. Based on this observation, it can be concluded, that small-scale micrographs in transverse or longitudinal direction can only be used to a limited extend as a base for accurately assessing the thickness of WEL.

In some of the micrographs, for instance, that of the specimen drilled at a cutting speed of $v_c = 100$ m/min and a feed of $f = 0.225$ mm, a dark layer can be observed at the brink of the WEL (Figure 5.5). Such dark layers following a WEL have only been reported for WEL formed according to the phase transformation mechanism [56]. Consequently, their presence is indicative of phase transformation during BTA deep hole drilling. This corresponds to the findings of fiber-optic ratio pyrometry presented in Figure 3.9, which provide evidence that austenitization temperature is transgressed significantly, particularly when using high cutting speeds and high feed rates. Based on these observations, it can be hypothesized that the dark layers formed due to tempering caused by elevated temperatures which did not transgress phase transformation temperatures. It has oftentimes been observed, that the hardness of the dark layers is lower than the hardness of the bulk material. However, in the microhardness mappings provided later on in this thesis, no evidence of lower hardness close to the WEL was found. A reason for this might be found in the significant work hardening of the subsurface, induced by the plastic deformation by the guide pads.

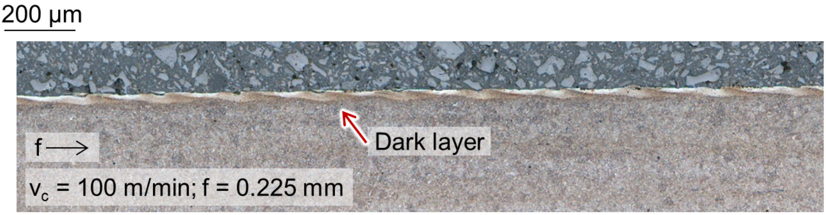

Figure 5.5 Micrograph indicating a dark layer at the brink of the white etching layer (WEL) for a specimen drilled at a cutting speed of $v_c = 100$ m/min and a feed of $f = 0.225$ mm (batch A)

In some micrographs, a post-conditioning of WEL after their formation is evident. Exemplary micrographs indicating this effect to a severe and a less severe degree are depicted in Figure 5.6 a), and b) respectively. It can be observed, that during one ration of the tool or the workpiece, the thickness of the WEL rises in the direction of the feed. After one revolution of the tool or the workpiece respectively, a new WEL section starts. It can be observed that the newly created WEL superimposes the WEL created during the previous revolution. Chipping of the WEL and cracks inside it indicate that this type of WEL post-conditioning is particularly detrimental to the surface topography and subsequently should be avoided in drilling. It can be observed that the section of the WEL that is close to the area superimposed by the WEL generated during the successive revolution is significantly darker than the rest of the WEL. It resembles the phenomenon of grinding burn. Subsequently, it can be assumed that the section of the WEL that is darker is tempered during the successive revolution.

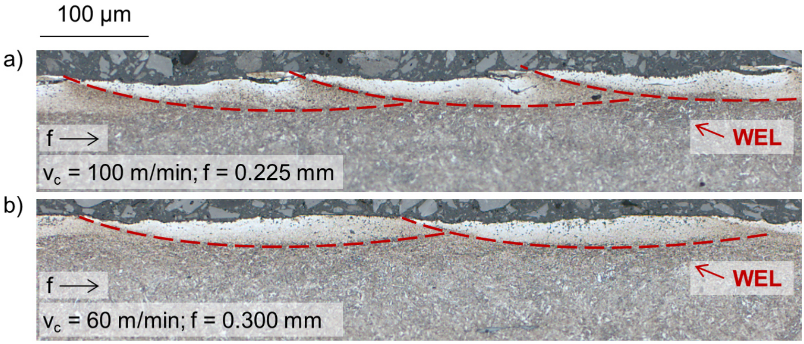

Figure 5.6 Post-conditioning of white etching layers (WEL) after their formation by repetitive transitions of the tool: a) particularly strong post-conditioning of WEL by successive revolutions; b) small level of post-conditioning of WEL (batch A)

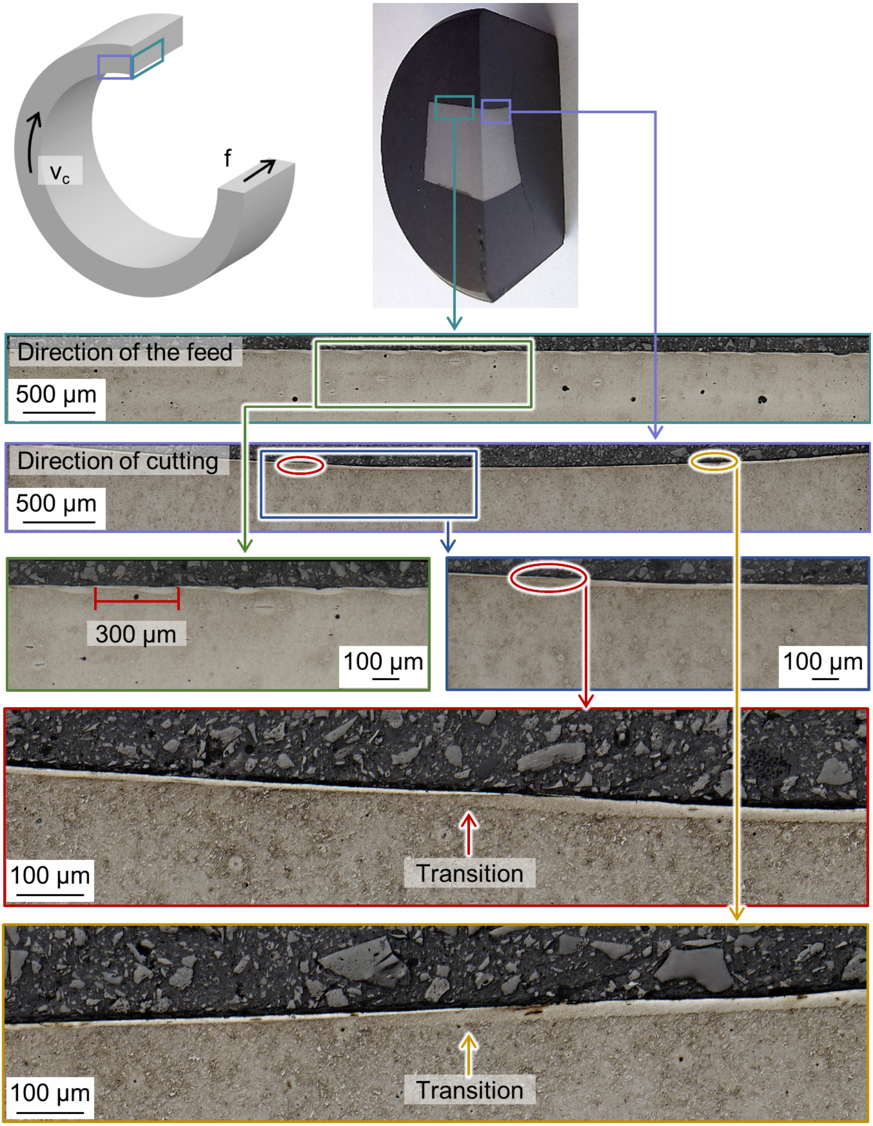

Figure 5.7 Particularly large-scale micrographs in transverse and longitudinal directions of a specimen with a white etching layer (WEL), machined at a cutting speed of v_c = 100 m/min and a feed of f = 0.300 mm (batch B). According to [198]

As explained in 3.2.3, dynamical disturbances are frequently observed in BTA deep hole drilling, particularly due to the slender design of the long boring bars which can lead to poor rigidity of the system. When drilling the specimens presented in Figure 5.2 and Figure 5.3, chattering was only observed in one experiment, when using a cutting speed of $v_c = 60$ m/min and a feed of $f = 0.300$ mm. This drilling experiment was therefore repeated with an additional damper to avoid chattering. Figure 5.8 presents the cross-sections in the transverse direction of the specimen drilled without a damper and a specimen drilled with a damper. It can be observed, that a thick WEL formed in drilling when no damper was used. Conversely, the specimen drilled with a damper is free of WEL. Based on this observation, it can be assumed that a damper might have a mitigating effect on WEL formation. Based on this observation, it can be concluded that the dynamic state in drilling must always be considered in conjunction with the parameters employed due to its vast impact on SI.

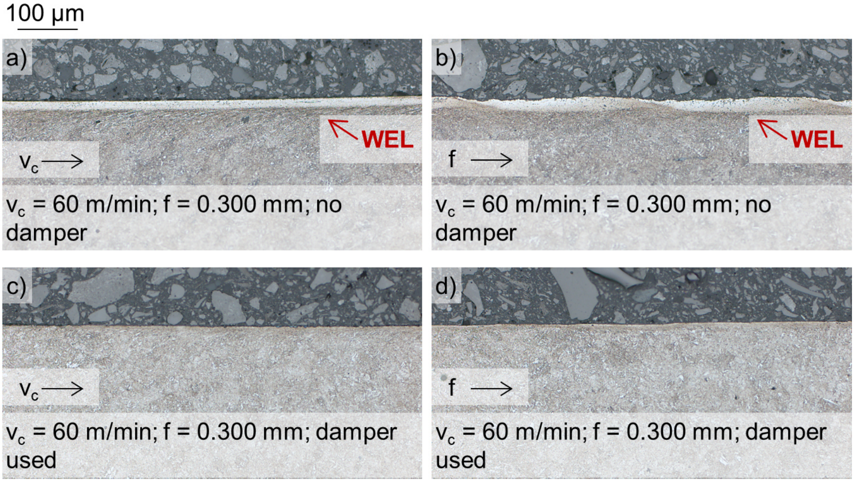

Figure 5.8 Etched cross-sections of two specimens drilled at a cutting speed of $v_c = 60$ m/min and a feed of $f = 0.300$ mm: (b, d) in the longitudinal direction; (a, c) in the transverse direction; (a, b) without using a damper in drilling; (c, d) using a damper in drilling (batch A)

In addition to optical microscopy, EBSD analysis were performed to assess the microstructural alterations induced by BTA deep hole drilling. In the first step, the microstructure of the bulk material was analyzed. For this, a specimen drilled at a cutting speed of $v_c = 60$ m/min and a feed of $f = 0.150$ mm was analyzed at a distance of a few millimeters to the surface of the bore. The results are presented in Figure 5.9.

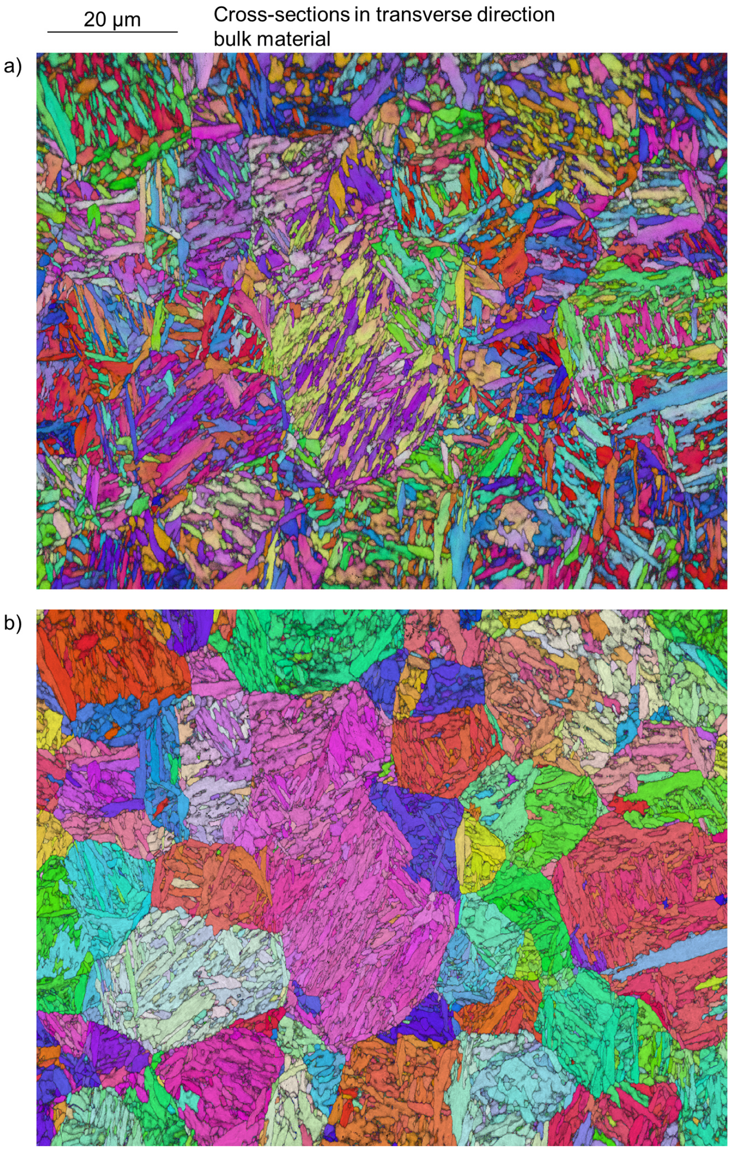

Figure 5.9 EBSD scan of the bulk material a) inverse pole figure and fit, b) reconstructed austenite grains using Nishiyama-Wassermann orientation relationship (batch A)

In Figure 5.11, EBSD scans of cross-sections in the transverse direction are presented for specimens that were found to be free of WEL in optical microscopy. In Figure 5.12 EBSD mappings of two specimens with WEL are presented. It can be observed that all four specimens reveal severely refined grains, particularly within the first few micrometers beneath the surface of the bore. In some of the maps, a severely deformed layer with a swept grain structure can be observed at a distance of approx. $d_{surf} = 15$ µm beneath the surface of the bore. This effect is marked in the example of Figure 5.12 b). In this region, grains tend to be slightly larger than right beneath the surface. These swept grains exhibit an acicular shape and run parallel to the surface of the bore. In addition to this, traces of crystallographic topography can be observed, as the elongated grains in this region have a relatively similar color code. To further assess the grain sizes in this region, squares with a length and width of $l = w = 10$ µm were extracted at the surface and analyzed. These squares are highlighted in white in the respective figures. It was found that the two specimens free of WEL reveal average grain sizes of $D_g = 328$ nm (Figure 5.11 a) and $D_g = 364$ nm respectively (Figure 5.11 b). Whereas for the specimens with WEL, average grain sizes were slightly smaller, as average grain sizes of $D_g = 241$ nm (Figure 5.12 a) and $D_g = 302$ nm (Figure 5.12 b) respectively were observed. More detailed results on the distribution of grain sizes are provided in Figure 5.10. For all four specimens analyzed, it can be observed that particularly small grains with a diameter of smaller than $D_g = 100$ nm were present in the inspected area.

The results correspond well with the findings of Zhang et al., who observed a strong grain size gradient in BTA deep drilled cast iron. They report on an ultrafine grained layer at the very surface followed by a transitional layer with grain sizes of up to $d = 2$ µm and the bulk material with grain sizes in the range of $d = 20\text{-}40$ µm [183]. Similar observations were made by Li et al. Analyzing BTA deep hole drilling of SA508 steel by EBSD, they identified a three-layered subsurface composed of a recrystallized layer with high dislocation density which is formed by dynamic recrystallization, followed by a layer marked by severe plastic deformation and the bulk material. With increasing cutting speeds, they identified increasing grain refinement and larger thicknesses of the recrystallized and severely deformed layers [19]. The images presented in Figure 5.11 and Figure 5.12 support these results. Accurately assessing the grain sizes at the very surface based on the given EBSD data, however, is particularly challenging, as the limits of the equipment might be reached. For this reason, advanced methods, such as TKD and STEM were performed and will be presented later on in this thesis (5.2.3). Confronting the results with EBSD mappings of subsurfaces machined by single-lip deep hole drilling, vast agreement is found. For instance, Baak provided evidence of severely refined grains at the surface of single-lip deep hole drilled surfaces.

Particularly small grains were observed for specimens with thick WEL. Further into the bulk, Baak observed slightly larger grains, with an acicular shape, parallel to the surface of the bore [73].

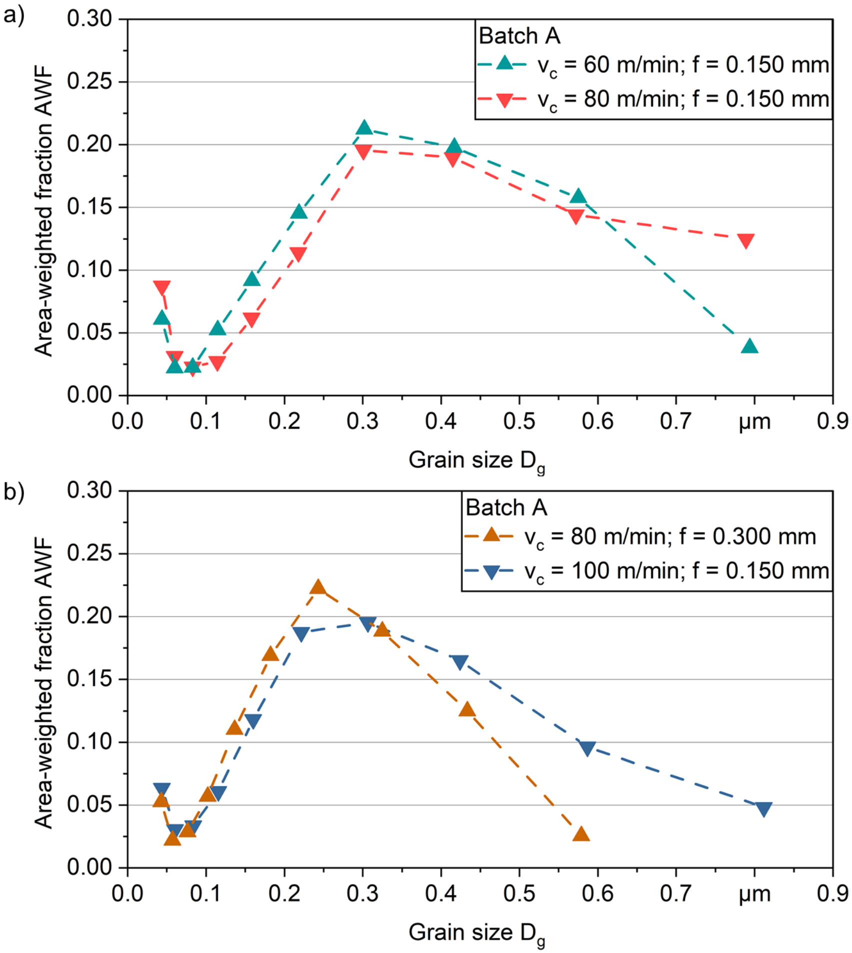

Figure 5.10 Calculated grain sizes for the regions marked with a white square in the electron backscatter diffraction (EBSD) mappings, a) for specimens without white etching layers (WEL) ($v_c = 60$ m/min; $f = 0.150$ mm and $v_c = 80$ m/min; $f = 0.150$ mm); b) for specimens with WEL ($v_c = 80$ m/min; $f = 0.300$ mm and $v_c = 100$ m/min; $f = 0.150$ mm) (batch A)

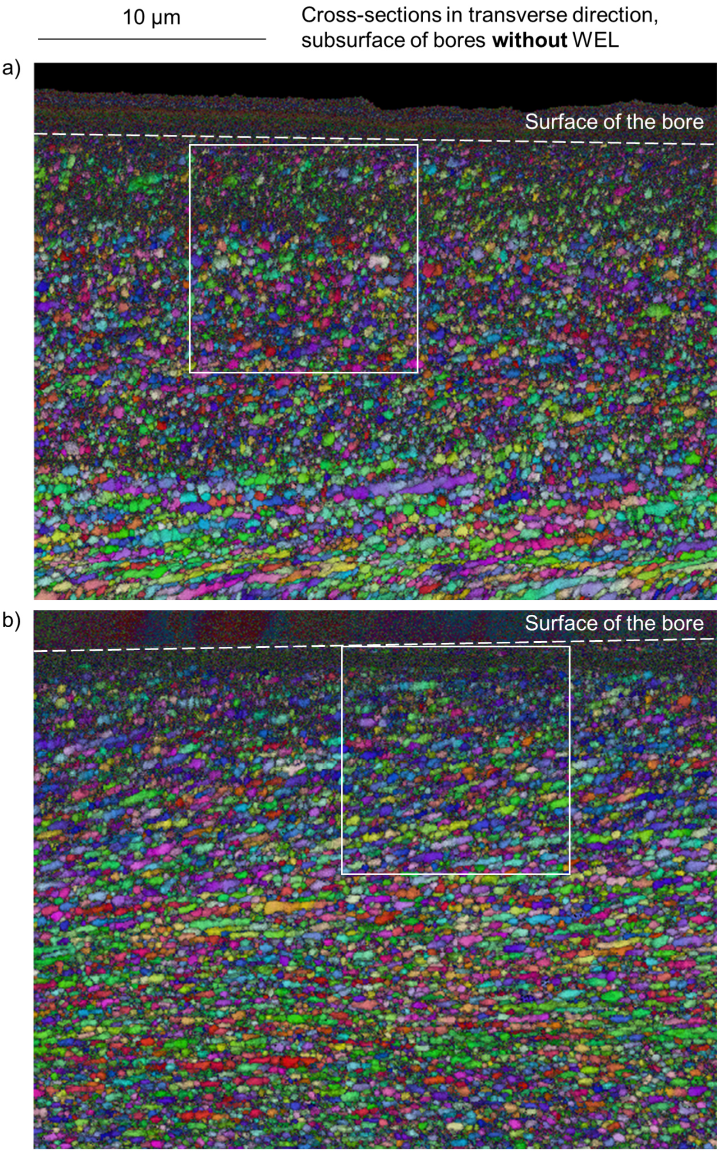

Figure 5.11 Electron backscatter diffraction (EBSD) for two specimens without a white etching layer (WEL): a) $v_c = 60$ m/min; f = 0.150 mm; b) $v_c = 80$ m/min; f = 0.150 mm. The white squares indicate the area for grain size analyses (batch A)

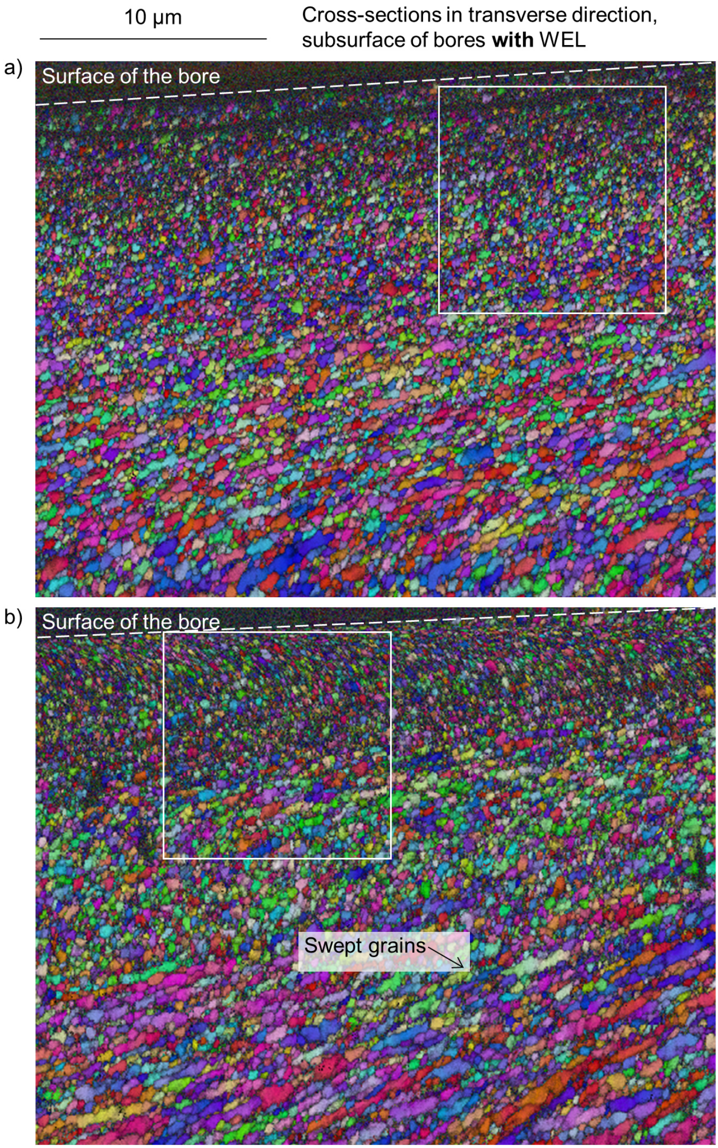

Figure 5.12 Electron backscatter diffraction (EBSD) for two specimens with a white etching layer (WEL): a) $v_c = 80$ m/min; $f = 0.300$ mm; b) $v_c = 100$ m/min; $f = 0.150$ mm. The white squares indicate the area for grain size analyses (batch A)

5.1.2 Microhardness

Figure 5.13 present the results of microhardness mappings. All specimens reveal microhardness gradients. The highest hardness is observed close to the surface. With increasing distance to the surface, the microhardness decreases.

It is found that specimens which showed WEL in optical microscopy have substantially greater hardness close to the surface, compared to specimens which are free of WEL. Elevated hardness is observed particularly in the first row of impressions at a distance to the surface of $d_{surf} = 5$ µm. In the second row of impressions at a distance of $d_{surf} = 20$ µm, higher hardness is observed particularly for specimens with relatively thick WEL, for instance, the one drilled at a cutting speed of $v_c = 100$ m/min and a feed of $f = 0.225$ mm. For some of the specimens, the hardness inside the WEL exceeds the hardness of the bulk material by more than three times. It is noticeable that the specimen drilled at a cutting speed of $v_c = 100$ m/min and a feed of $f = 0.300$ mm only shows a moderate increase in hardness, in spite of a WEL. The reason for this can be found in the particularly small extent of the WEL of this specimen at the position of the microhardness mapping. It was found that the thickness of the WEL in this section is smaller than $T_{WEL} < 5$ µm. Subsequently, the first row of microhardness impressions is placed behind the WEL for this specimen, leading to lower hardness compared to the other specimens with WEL [209]. The specimens free of WEL have slightly elevated hardness close to the surfaces as well, resulting from work hardening, however, it is significantly smaller than the hardness inside the WEL. In a distance to the surface of $d_{surf} = 80$ µm, the hardness is still slightly elevated for all specimens, compared to the hardness of the bulk material. This evidences that BTA deep hole drilling impacts the SI also relatively deep into the subsurface. This observation corresponds to the findings of Griffiths. He provides evidence of elevated hardness in BTA deep drilled specimens up to a depth of approx. $d_{surf} = 200$ µm [164].

Further information on these investigations, including micrographs of the specimens investigated, is provided in [209]. The microhardness inside the WEL of up to approx. 1340 HV 0.01 on average ($v_c = 100$ m/min; $f = 0.225$ mm), with readings for single impressions of up to approx. 1410 HV 0.01 clearly exceeds the hardness of hardened, fully-martensitic AISI 4140. Based on the observations presented in 5.1.1, and particularly the EBSD images presented, it can be concluded that the microhardness inside the WEL, cannot result entirely from grain refinement alone, as specimens free of WEL also exhibited significantly refined grains (Figure 5.11). It can be hypothesized that the particularly high amount of lattice defects such as dislocation and stacking faults inside the WEL contribute to the significantly elevated hardness.

The microhardness presented corresponds to the findings of Fuß and Griffiths. Fuß observed a maximum hardness of 1280 HV 0.02 inside a WEL in BTA deep drilled AISI 1060 [147]. Griffiths reported a hardness of up to 1304 HV in WEL in deep drilled AISI 1040, which is more than four times greater than the bulk hardness. He hypothesizes that reasons for the immense hardness inside the WEL might be found in a multi-stage thermo-mechanical hardening process at the guide pads [164].

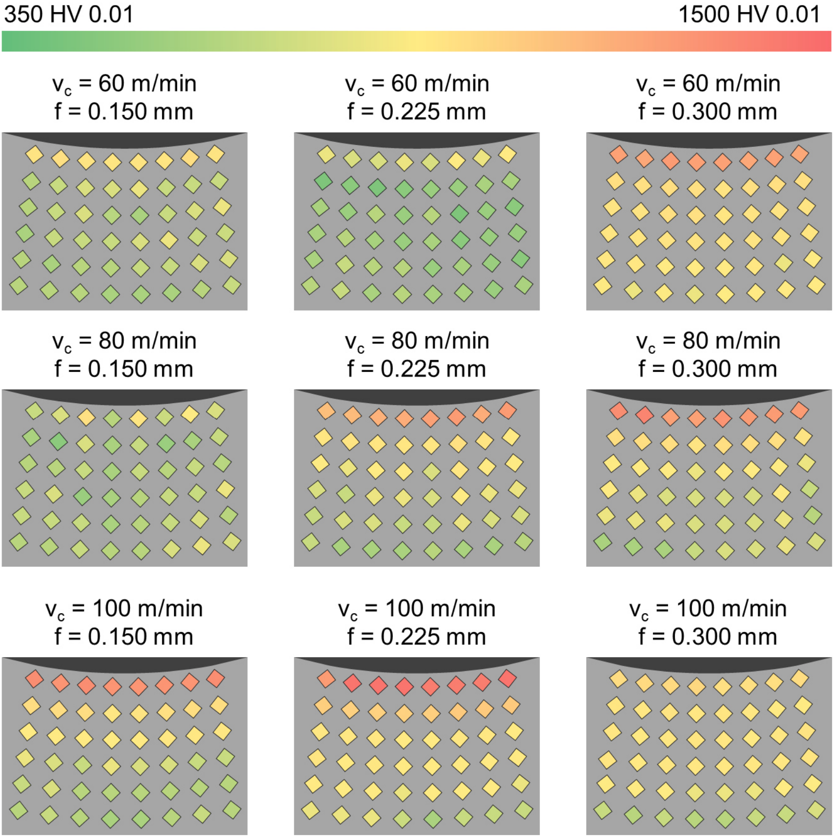

Figure 5.13 Microhardness mappings of cross-sections in the transverse direction of specimens drilled at varying cutting speeds (v_c = 60-100 m/min) and feeds (f = 0.150-0.300 mm) (batch A). Parts of the data are published in [209]

5.1.3 Residual stresses

In Figure 5.14 two exemplary depth profiles of residual stresses in the subsurface of a BTA deep drilled specimen are presented. These were obtained by analyzing the same specimen at two different lengths of the bore (l_b = 157 and 173 mm). Right after extracting a ring segment with a length of l = 30 mm from a deep drilled specimen (Figure 3.7 d), the residual stresses in the tangential direction were assessed according to the $\sin^2\psi$-method, using the D8 Discover. By selecting a Bragg angle of 106° instead of the usual 156°, shading of the X-rays by the upper part of the specimen was prevented. As a result, the X-rays generated were able to reach the surface of the bore and the diffracted X-rays could reach the detector. Assessing residual stresses in the axial direction, however, was not possible at this stage, due to shading of the X-rays. In the initial state, compressive residual stresses between σ_{tang} = -500 and -600 MPa were observed at both lengths of the bore (Figure 5.14 I). In the next step, specimens were cut in half (Figure 5.14 II). It can be seen that the tangential residual stresses remain relatively constant at the same level. Due to the removal of the upper part of the specimen, the residual stress state at this point could be assessed in the axial direction as well. It was found, that residual stresses in the axial direction significantly exceed the residual stresses in the tangential direction, as they have an intensity of approximately σ_{axial} = -900 MPa (Figure 5.14, II). In a next step, the surface was removed incrementally by electropolishing. It can be observed, that residual stresses in axial and tangential direction decrease rapidly below the surface (Figure 5.14 III). From a depth of d = 100 µm on, axial and tangential residual stresses are higher than σ = -200 MPa.

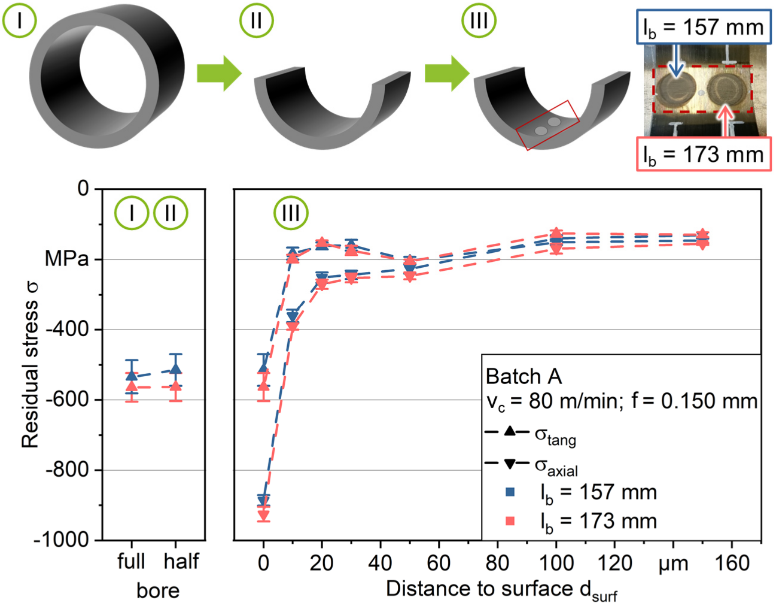

Figure 5.14 Residual stresses assessed by D8 Discover ($\sin^2\psi$-method) before (I) and after (II; III) cutting a specimen in half, which was drilled at a cutting speed of $v_c = 80$ m/min and a feed of $f = 0.150$ mm. Depth profiles of residual stresses at two lengths of the bore (batch A). According to [207]

Figure 5.15 presents two exemplary depth profiles of residual stresses in axial and tangential directions obtained by cosα-method for ring segments extracted from the bores. Based on the observations that residual stresses are concentrated at the surface and drop rapidly deeper into the subsurface, the increments in electropolishing were reduced to 5 µm for the first $d_{surf} = 30$ µm for these investigations. Following the results of optical microscopy (Figure 5.3), it can be assumed that the specimen depicted in Figure 5.15 a) is free of WEL, whereas the specimen depicted in b) has a WEL. The reason for this is that the ring segments analyzed are extracted from the same length of the bores as the specimens analyzed in optical microscopy but at different angles around the circumference of the bore. For both specimens, compressive residual stresses are observed in the axial direction. The specimen without a WEL has relatively moderate compressive residual stresses of $\sigma_{axial} = -450$ MPa, whereas the specimen with a WEL has compressive residual stresses of approx. $\sigma_{axial} = -800$ MPa. Just like for the specimen presented in Figure 5.14, residual stresses drop quickly with increasing distance to the surface of the bore. For the specimen free of WEL, the residual stresses in the axial direction drop relatively steadily within the first 20 µm of electropolishing. At this distance they exceed σ_{axial} = -100 MPa. Looking at the specimen with the WEL, it is remarkable that the residual stresses drop only very slightly within the first 10 µm of electropolishing. The reason for this can probably be found in the presence of the WEL. Based on this observation, it might be hypothesized that the high residual stresses inside the WEL are relatively uniformly distributed throughout the extent of the WEL. Behind the WEL residual stresses first drop rapidly but stay on a constant level of approx. σ_{axial} = -300 MPa in between d_{surf} = 40-100 µm.

For the specimen free of WEL, residual stresses in the tangential direction are found to be compressive, with relatively moderate intensity. Just like the residual stresses in the axial direction of this specimen, they drop steadily within the first 20 µm of electropolishing and then stay relatively constant on a level close to zero. The specimen with a WEL reveals tensile residual stresses in the tangential direction. These have relatively moderate intensity. In the first step of electropolishing they rise very slightly from approx. σ_{tang} = 100 MPa to σ_{tang} = 250 MPa. From that point on they drop relatively steadily with increasing distance to the surface.

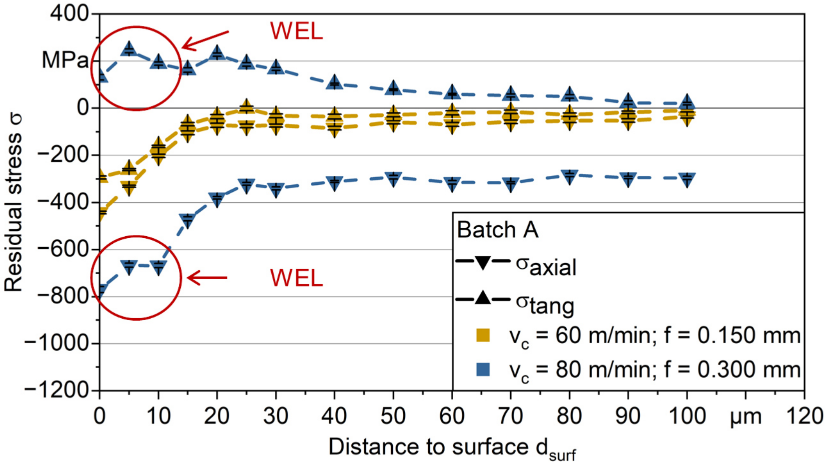

Figure 5.15 Depth profiles of residual stresses in the axial and the tangential directions for two specimens (v_c = 60 m/min; f = 0.150 mm and v_c = 80 m/min; f = 0.300 mm), assessed by µ-X360s (cosα-method) (batch A). According to [198]

To investigate further into the evolution of residual stresses along the length of the bore, small-step line-scans were performed for two exemplary segments with a length of $l = 30$ mm extracted from two different bores (Figure 3.7 d). Both specimens were machined with a feed of $f = 0.225$ mm. Cutting speed was 60 m/min (a) and 80 m/min (b). Residual stresses were assessed in the tangential direction for a length of $l = 20$ mm in increments of $\Delta l = 1$ mm. To assess the deviations of residual stresses around the circumference of the bore line-scans were performed at four angular positions for each of the specimens ($\alpha = 0°, 90°, 180°, 270°$). It is found that the tangential residual stresses at the surface vary greatly with the length of the bore. For the specimen drilled at a cutting speed of $v_c = 60$ m/min and a feed of $f = 0.225$ mm, residual stresses range from approx. $\sigma_{tang} = -800$ MPa ($l_b = 125$ mm) to $\sigma_{tang} = 200$ MPa ($l_b = 118$ mm). The tangential residual stresses in the specimen drilled at a cutting speed of $v_c = 80$ m/min and a feed of $f = 0.225$ mm vary in the range of approx. $\sigma_{tang} = -850$ MPa ($l_b = 117$ mm) to $\sigma_{tang} = 0$ MPa ($l_b = 127$ mm). The reason for this huge scattering of residual stresses in the tangential direction might be found in the relatively complex mechanisms governing the generation of residual stresses in BTA deep hole drilling. Comparing the residual stresses at the four angular positions, it can be observed that the deviation of the intensity of residual stresses around the circumference of the bore is relatively low. All of the four line-scans indicate the same profile of tangential residual stresses along the length of the bore.

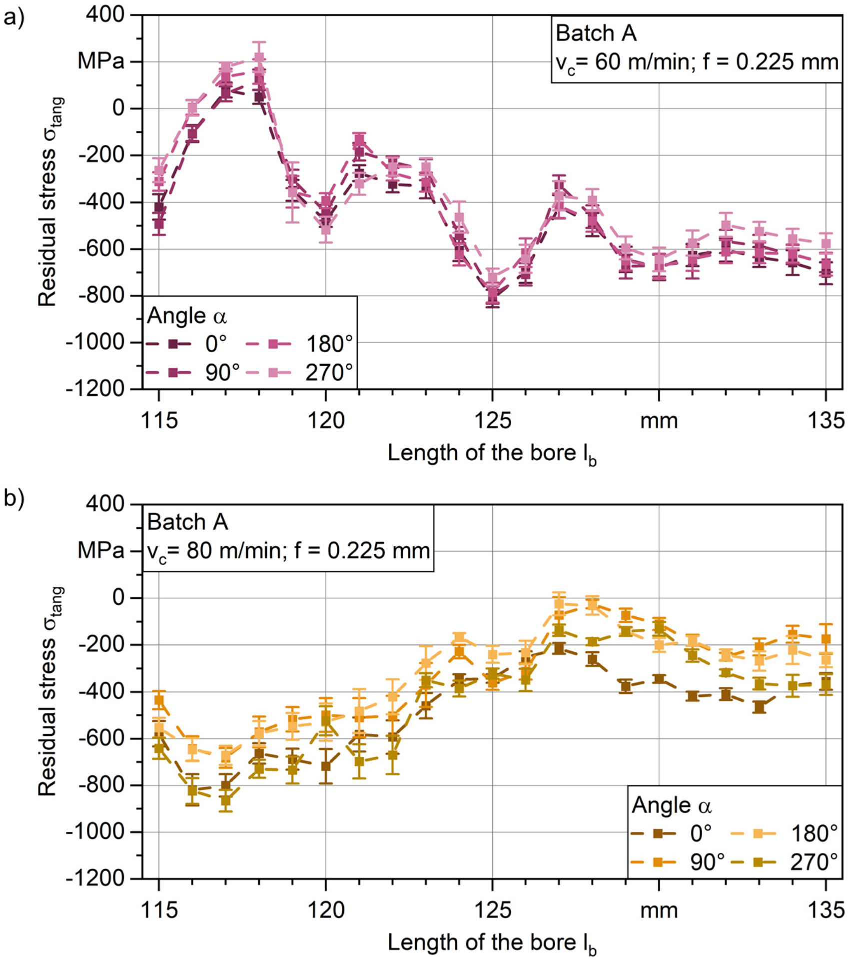

Figure 5.16 Evolution of tangential residual stresses along the length of the bore for two specimens : a) v_c = 60 m/min; f = 0.225 mm; b) v_c = 80 m/min; f = 0.225 mm, assessed by Bruker D8 Discover (batch A)

In general, research on residual stresses resulting from BTA deep hole drilling is far from conclusive, and literature on the matter is particularly limited, as only very few studies on BTA deep hole drilling consider this aspect of SI. Confronting the findings presented in this chapter with the few results available in literature, it can be concluded that the observations presented are in relatively good agreement with the previously published findings of other scientists. For instance, Griffiths hypothesizes that residual stresses induced by BTA deep hole drilling are most likely compressive, due to the known effects of burnishing on residual stresses. However, he does not provide evidence to back up this hypothesis [164]. Rao and Shunmugam analyze residual stresses in BTA deep hole drilling of AISI 1055 by X-ray diffraction. They report tensile residual stresses in the range of approx. $\sigma = 0$ to 400 MPa for surfaces which were machined by the cutting edge only and compressive residual stresses which range from approx. $\sigma = -600$ to -250 MPa for fully BTA deep drilled surfaces [175]. More recently, Li analyzed residual stresses in BTA deep drilled SA-508 steel in nuclear power tube plates as a function of cutting speed, feed, and drilling depth [184]. For the diffractographic investigations, the deep drilled specimens were cut in half. They observed compressive residual stresses with relatively moderate intensities in the range of $\sigma = -450$ to -50 MPa [184]. Besides these experimental studies, also simulative studies have provided evidence of compressive residual stresses induced by BTA deep hole drilling [198,214].

Given the limited number of results available for BTA deep hole drilling, it might be beneficial to also consider residual stresses assessed after single-lip deep hole drilling, due to the likeness between the processes. Baak provided evidence that the residual stress state in single-lip deep drilled specimens is compressive in the axial and in the tangential directions. Residual stresses in the tangential direction were slightly less intense compared to residual stresses in the axial direction. Depending on the cooling strategy he identified residual stresses in the axial direction in the range of approx. $\sigma_{\text{axial}} = -1250$ to -300 MPa and in the tangential direction in the range of $\sigma_{\text{tang}} = -850$ to -100 MPa [73].

5.2 Detection and assessment of white etching layers

As presented in the previous chapters, WEL play a dominant role in the field of SI resulting from BTA deep hole drilling. In light of the major importance and the vast gap of knowledge which remains up to this day, elaborate approaches were performed to detect and assess WEL. Besides optical microscopy, XRD-based analyses are qualified for the detection of WEL.

5.2.1 Digital analysis of micrographs

As presented in 5.1.1, optical microscopy is particularly suited for the detection of WEL at the surface of specimens. However, due to the periodicities observed in the deep drilled specimens in the longitudinal but also transverse directions, and the associated variation of WEL thickness (Figure 5.3), assessing the extent of

WEL in BTA deep drilled specimens requires added attention and particular effort. Subsequently, measuring the thickness of WEL at only a few limited positions in micrographs, which remains the most common practice, has proven to be insufficiently accurate. A method leading to far more robust results is the digital analysis of large-scale micrographs [211]. In the first step of digital analysis micrographs need to be segmented, separating the WEL from the embedding resin and from the surrounding material free of WEL. For this, various techniques can be used, such as thresholding-based approaches, machine learning-based segmentation, and manual segmentation. In previous studies, evidence has been provided that manual segmentation remains the gold standard when the amount of data is particularly limited [211]. The major reason for this is that WEL oftentimes cannot be separated easily from the surrounding material due to poor edge contrast and a general lack of clear borders. Thus, manual segmentation oftentimes remains the superior method, in spite of the downsides of this method, for instance, a certain operator-influence involved. In light of this bias, manual segmentation calls for clear standards. This necessity is illustrated in Figure 5.17. In a) an unsegmented image is displayed. At the spots marked with A, the WEL is darker, resembling a grinding burn. This is oftentimes observed in micrographs and is particularly challenging for classic segmentation approaches, such as grey-level (GL) thresholding as its appearance is clearly distinct from the rest of the WEL, e.g. in terms of grey-levels. These range from approx. 100 to 150 in this zone, and are thus closer to the average GL of the bulk material than the GL of the WEL. In Figure 5.17, the zone beneath the clear, bright WEL is marked with B. In very conservative manual segmentation, one might not include this zone into the WEL (Figure 5.17 b), conversely to less conservative segmentation (Figure 5.17 c). Just like for the area marked with A, GL in this layer are closer to the bulk material than to the GL of the WEL.

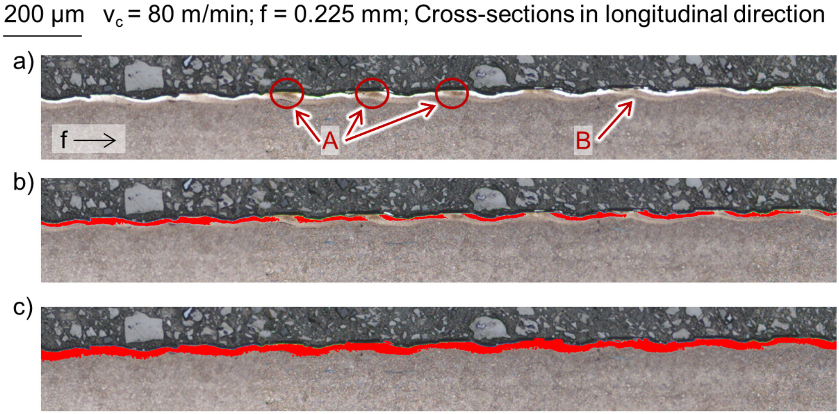

Figure 5.17 Segmentation of the white etching layer (WEL) in micrographs for the example of a specimen drilled at a cutting speed of v_c = 80 m/min and a feed of f = 0.225 mm. The segmented WEL is highlighted in red: a) unsegmented image; b) particularly conservatively manually segmented image; c) less conservative segmented image (batch A)

Figure 5.19 presents exemplary large-scale stitched micrographs of cross-sections in the longitudinal direction. In Figure 5.20 the segmented versions of the micrographs with a WEL are presented. These were used for assessing the maximum thickness, the average thickness, and the area covered by WEL in the micrographs. Due to space limitations, Figure 5.19 and Figure 5.20 only show approx. 3 mm out of the total approx. 6 mm analyzed. The results of digital image analysis are presented in Figure 5.18.

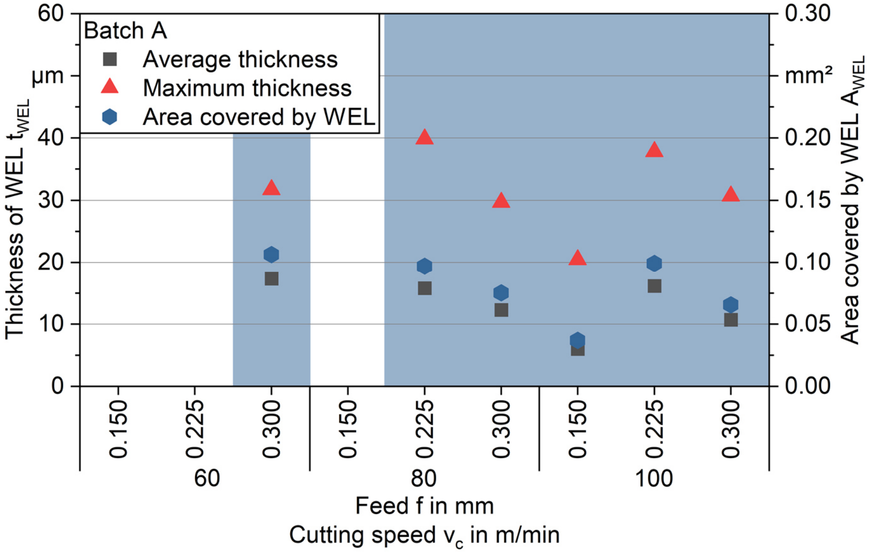

Figure 5.18 Digital image analysis of specimens drilled at varying cutting speeds (v_c = 60-100 m/min) and feeds (f = 0.150-0.300 mm), indicating average white etching layer (WEL) thickness, maximum WEL thickness and the area covered by WEL in micrographs in the longitudinal direction with a length of l = 6 mm (batch A)

It can be observed that out of the specimens with a WEL, the specimen drilled at a cutting speed of v_c = 100 m/min and a feed of f = 0.150 mm has the lowest average and maximum thicknesses and consequently the lowest area covered by WEL in the micrograph. This corresponds well to the temperatures assessed in drilling, as these were lower for this specimen, compared to the other specimens with WEL (Figure 3.9, a).

For cutting speeds of v_c = 80 and 100 m/min, the highest average thicknesses and subsequently also the largest areas covered by WEL were observed for a feed of f = 0.225 mm. A reason for this might be found in the longer time the tool is in contact with the generated surface of the bore when using lower feeds. Even if temperatures of the cutting edge are higher when using higher feed rates, as indicated in Figure 3.9 a), this does not necessarily imply that more heat is transmitted into the workpiece. For instance, the feed per minute for the parameter combination (v_c = 80 m/min; f = 0.225 mm) is v_f = 95.5 mm/min, whereas a higher feed of f = 0.300 mm in combination with a cutting speed of v_c = 80 m/min leads to a significantly higher feed per minute of v_f = 127.3 mm/min. Subsequently, using the latter parameter combination may result in higher temperatures of the cutting insert (Figure 3.9), however, the thermal energy dissipated into the workpiece is not necessarily higher, as the time the inserts of the tool are in contact with the generated surface is shorter.

In general, the cutting speed seems to have less of an impact on the thickness of WEL compared to the feed. For instance, the thicknesses of WEL are relatively similar when using a cutting speed of $v_c = 80$ m/min or a cutting speed of 100 m/min combined with a feed of f = 0.225 mm. The same observation applies to the two cutting speeds in combination with a feed of f = 0.300 mm.

The average thicknesses of WEL, ranging from approx. $t_{WEL} = 6$ to 17 µm are in good agreement with the results provided in the literature. Li et al. report on recrystallized layers at the surface of BTA deep drilled SA508 steel, with thicknesses in the range of $t_{WEL} = 12$-18 µm. They found that the thickness of the recrystallized layer increases with higher cutting speeds and feeds. However, they do not consider any periodicities of WEL and only cross-sections in transverse direction are assessed [19]. In addition to this, the thickness of severely recrystallized layers does not necessarily correspond to the thickness of WEL in optical microscopy, as outlined in 5.1.1

In general, drawing conclusions about the interrelations between drilling parameters in BTA deep hole drilling, and WEL formation is particularly challenging due to the number of influencing factors. For instance, wearing of the inserts might result in even higher temperatures at higher cutting speeds and feeds. In addition to this, the dynamic state of the process needs to be considered, as BTA deep hole drilling is highly susceptible to dynamic effects such as chattering. Subsequently, the correlations observed are not universally applicable.

Figure 5.19 Large-scale micrographs of cross-sections in the longitudinal direction of specimens drilled at varying cutting speeds (v_c = 60-100 m/min) and feeds (f = 0.150-0.300 mm) (batch A)

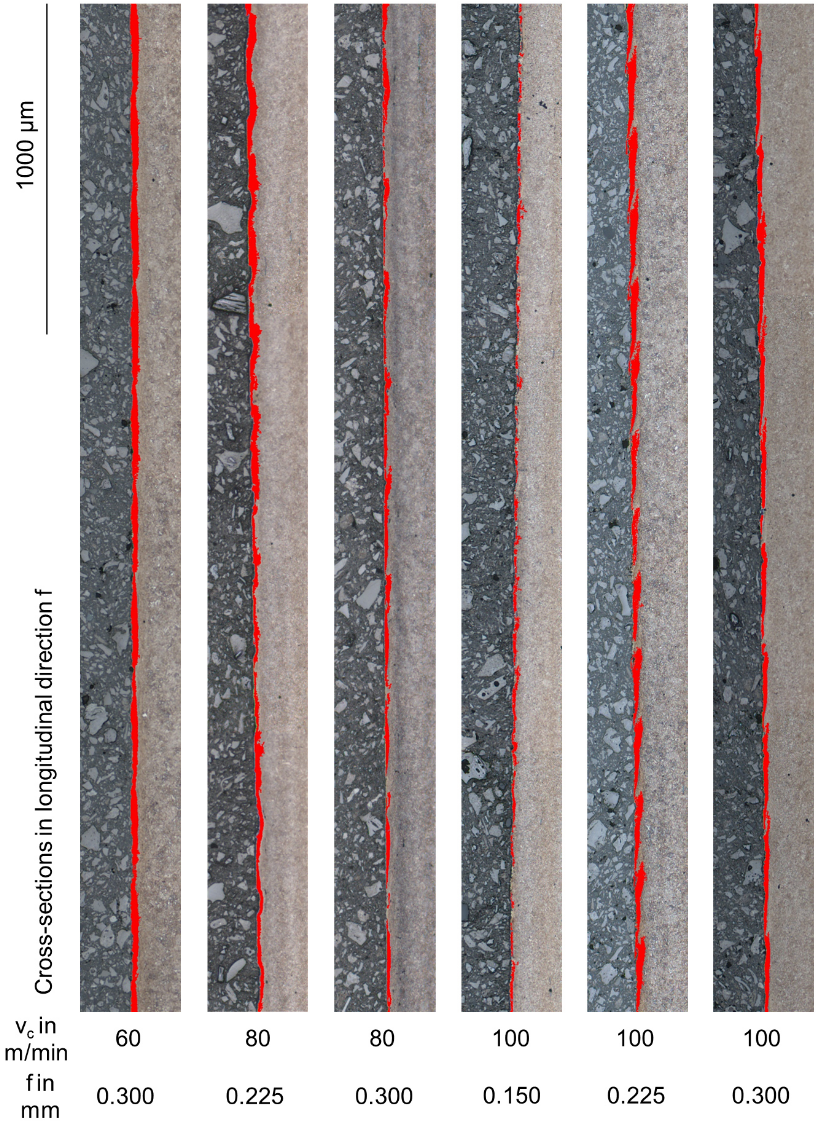

Figure 5.20 Manually segmented large-scale micrographs of cross-sections in the longitudinal direction of specimens drilled at varying cutting speeds (v_c = 60-100 m/min) and feeds (f = 0.150-0.300 mm) (batch A)

5.2.2 X-ray diffraction

Besides the assessment of residual stresses, X-ray diffraction was also performed to detect and characterize WEL at the surfaces of specimens. As the peak width in XRD is sensitive to e.g. grain size and dislocation density, the FWHM value can be used for detecting and evaluating the nanocrystalline WEL [167]. Depth profiles of FWHM values for two exemplary specimens with a WEL (v_c = 80 m/min; f = 0.300 mm) and without a WEL (v_c = 60 m/min; f = 0.150 mm) are depicted in Figure 5.21. Besides the FWHM, the figure presents crystallite sizes, which were calculated using the Scherrer equation 2.6. It can be observed that the specimen without a WEL has an initial FWHM of approx. 3.5°. After electropolishing, this value drops in the first 10 µm relatively quickly, before the slope becomes more shallow. Subsequently, the grain sizes calculated by Scherrer equation increase from approx. D_g = 18 to 23 nm. For the specimen with a WEL, the FWHM drops only slightly within the first 10 µm from approx. 5.0° to 4.5°. After the first 10 µm are removed, the FWHM drops stronger. Based on this observation, it can be assumed that inside the WEL only a small gradient in grain sizes might be found.

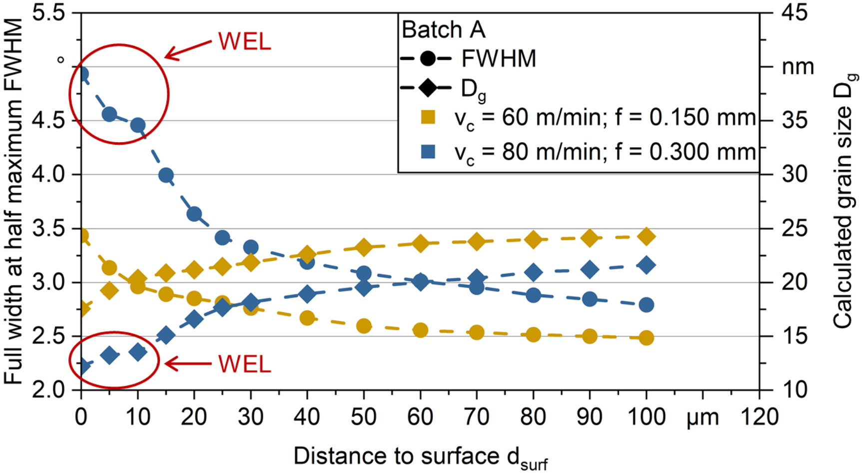

Figure 5.21 Depth profiles of full width at half maximum (FWHM) values, assessed by µ-X360s for a specimens without a white etching layer (WEL) (v_c = 60 m/min; f = 0.150 mm) and a specimen with a WEL (v_c = 80 m/min; f = 0.300 mm) (batch A). According to [198]

This agrees with the results for residual stresses presented in Figure 5.15, which indicate relatively homogenous residual stresses inside the WEL and a strong drop in their intensity further into the bulk material. In line with the FWHM values, the calculated crystallite sizes stay relatively stable at a size of approx. D = 13 nm within the first 10 µm. Further into the bulk material, they increase to a size of approx. D = 23 nm at a distance to the surface of d = 100 µm. The results correspond to the findings in the literature. For instance, Brown et al. assessed the presence and extent of WEL based on X-ray diffraction. They were able to rank specimens of Ti-6Al-4V in terms of WEL thickness, based on the peak breadth in XRD given by the FWHM. In their studies, higher FWHM values indicated thicker WEL [166,167].

Figure 5.22 presents the FWHM values obtained by the device µ-X360s for specimens machined with different cutting speeds and feeds. It can be observed that for all six specimens which were found to have WEL in optical microscopy (Figure 5.2, Figure 5.3), the FWHM values are significantly higher, compared to the values obtained for the three specimens free of WEL. Consequently, the calculated crystallite sizes are smaller and the calculated dislocation density using equation 2.7, is higher for specimens with WEL.

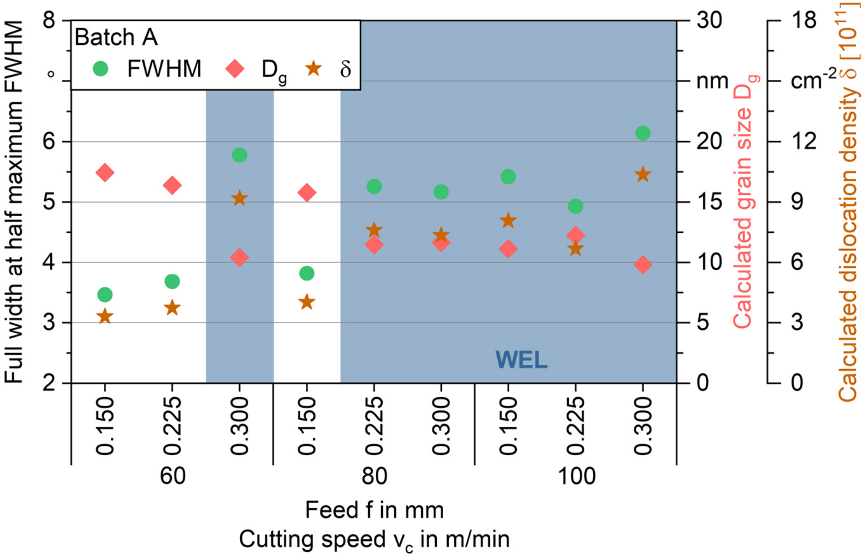

Figure 5.22 Full width at half maximum (FWHM) assessed by µ-X360s, along with the calculated grain size D_g and the calculated dislocation density δ of specimens drilled at varying cutting speeds (v_c = 60-100 m/min) and feeds (f = 0.150-0.300 mm) (batch A). According to [198]

5.2.3 Advanced approaches for crystallographic analysis in SEM: EBSD, TKD, ECCI, STEM

To overcome the shortcomings of the traditional crystallographic approaches, as observed and discussed in 4.2, advanced approaches were employed. These allow for further analyzing the subsurfaces conditioned by BTA deep hole drilling and assessing structural features such as grain sizes even within the nanocrystalline WEL. Exemplary specimens with and without a WEL were analyzed by means of EBSD following FIB-preparation, TKD, ECCI, and STEM. The results of these investigations will be presented in the following sections.

Electron backscatter diffraction (EBSD) following focused ion beam (FIB)-preparation

Cross-sections were prepared in a FIB-SEM for EBSD, by removing material with a focused ion beam up to a depth of approx. $d_{surf} = 1.9$ µm from the surface of the bore. This procedure allowed for analyzing the subsurface of specimens by EBSD, not only in transverse or longitudinal directions as conventionally performed but directly inside the crucial subsurface of the bore. The preparation of a specimen in the FIB-SEM for this procedure is illustrated in Figure 5.23.

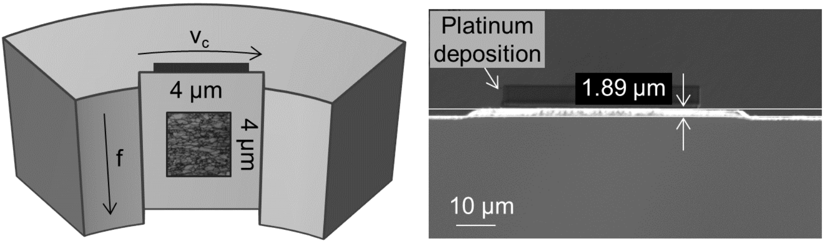

Figure 5.23 Schematic illustration of the preparation of specimens by a focused ion beam (FIB) for performing electron backscatter diffraction (EBSD) within the subsurface, analyzing a surface parallel to the surface of the bore

The results of the analyses are presented in Figure 5.24, in the form of band contrast images (a, d), Euler color maps (b, e), and phase maps (c, f). A specimen without WEL is depicted on the left, whereas on the right a specimen with WEL is presented.

It can be observed that for the specimen free of WEL, a significantly higher detection rate of 55% was achieved, compared to the specimen with WEL, for which the detection rate was 28%. For the specimen free of WEL, swept grains in the direction of cutting can be observed. In the previously presented EBSD-based investigations of cross-sections in the transverse direction, these elongated grains with an acicular shape running parallel to the surface of the bore could only be detected at larger distances to the surface of the bore (Figure 5.12).

In total, grain size is significantly smaller in the specimen with the WEL. In the specimen without WEL, slightly larger grains were observed in addition to particularly small grains with a diameter of D_g = 100 nm and less. In the specimen with WEL, exclusively particularly small grains were observed in EBSD following FIB-preparation. A detailed discussion of grain sizes in the subsurfaces will follow in the upcoming chapters, providing also results obtained by TKD and STEM.

For both specimens, the detected phase was exclusively bcc, with only a few scattered pixels classified as fcc (Figure 5.24 c, f). In contrast to this, previous XRD-based investigations have provided evidence for the presence of relatively small amounts of retained austenite inside of a specimen with a WEL [198]. The presence of retained austenite within a WEL would evidence the reverse-martensite transformation during machining as e.g. observed by Barry [155]. However, as the number of pixels classified as fcc was particularly limited, no clear evidence of austenite within the subsurfaces was found in EBSD mappings. The findings given in the literature on the retained austenite content within WEL are highly divergent. For instance, Akcan et al. report less than 10% of austenite within WEL in machined AISI 4340 and AISI 52100 steels [139], whereas Chou and Evans found 33% of austenite in hard turning of AISI 52100 [170]. Hossain provides evidence of different phase compositions of WEL, depending on the respective formation mechanisms. Whereas predominantly thermally induced WEL were found to be composed of austenite, cementite, and martensite, no austenite was observed in WEL which were predominantly mechanically induced [114]. Confronting the findings presented in this thesis with results from the literature, it can be concluded that the phase composition within the WEL formed during BTA deep hole drilling of AISI 4140 is composed mostly of bcc crystals. If any austenite is present in the WEL, the amount appears to be very limited.

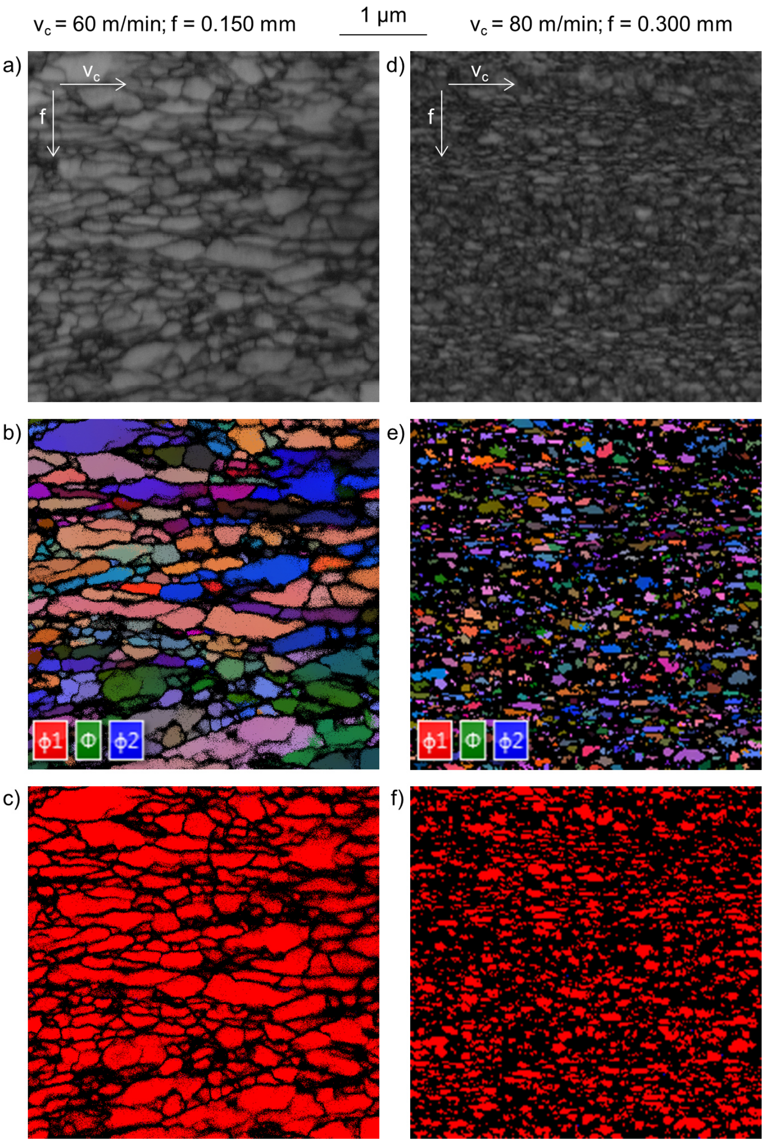

Figure 5.24 Electron backscatter diffraction (EBSD) mapping: a)-c) a specimen without a white etching layer (WEL) (v_c = 60 m/min; f = 0.150 mm); d)-f) a specimen with a WEL (v_c = 80 m/min; f = 0.300 mm); a), d) band contrast images; b), e) Euler color maps; c), f) phase maps (red: Fe-bcc, blue: Fe-fcc) (batch A)

Transmission Kikuchi diffraction (TKD)

To validate the results obtained by EBSD following FIB-preparation, off-axis TKD was performed for a specimen with a WEL, drilled at a cutting speed of $v_c = 80$ m/min and a feed of $f = 0.300$ mm. This way the microstructure inside of the WEL was assessed with particularly high resolution. In preparation for TKD, a lamella was extracted in the perpendicular direction to the borehole wall by FIB sectioning. This lamella is presented in Figure 5.25. TKD investigations were performed by Dr. Tom Jäpel of TESCAN.

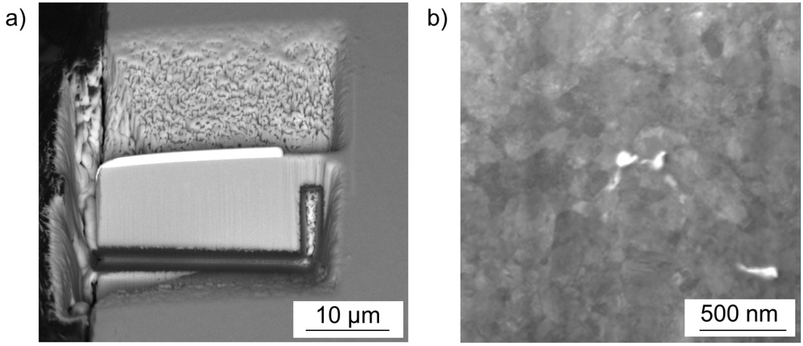

Figure 5.25 Preparation of a lamella for transmission Kikuchi diffraciton (TKD) by focused ion beam (FIB) sectioning: a) overview of the lamella, perpendicular to the borehole wall; b) dark field image of the lamella, after polishing with a gallium FIB (batch A)

In Figure 5.25 b) bright spots inside the lamella can be observed at grain boundaries. These spots might be voids, resulting from tearing of the material due to the brittle nature of the WEL. However, further analysis is necessary to back up this hypothesis, considering also the relaxation of stresses in the lamella which might have caused the formation of voids. The results of the TKD analysis are presented in Figure 5.26. Corresponding to the results of EBSD after FIB-preparation, it was shown that the lattice inside the WEL is mostly bcc. It can be observed that grain sizes within the WEL are particularly small. The detection rate in TKD is approx. 41% and thus better than the detection rate obtained for a similar specimen in EBSD after FIB sectioning. By pattern matching using dictionary indexing, the detection rate can be increased to 66% (Figure 5.26 d). When fitting the grains with ellipses, and considering the major diameter of the ellipses, an average grain size of approx. $D_g = 260$ nm is calculated with a standard deviation of approx. 110 nm. The area-weighted mean grain size is approx. $D_g = 350$ nm. The minimum major diameter of the fitted ellipses is approx. $D_g = 100$ nm and the maximum diameter is approx. $D_g = 700$ nm. Considering the maximum ferret diameter instead, the arithmetic mean of grain sizes increases to approx. $D_g = 290$ nm with a standard deviation of approx. 120 nm. The area-weighted fraction of the fitted grains is presented in Figure 5.27.

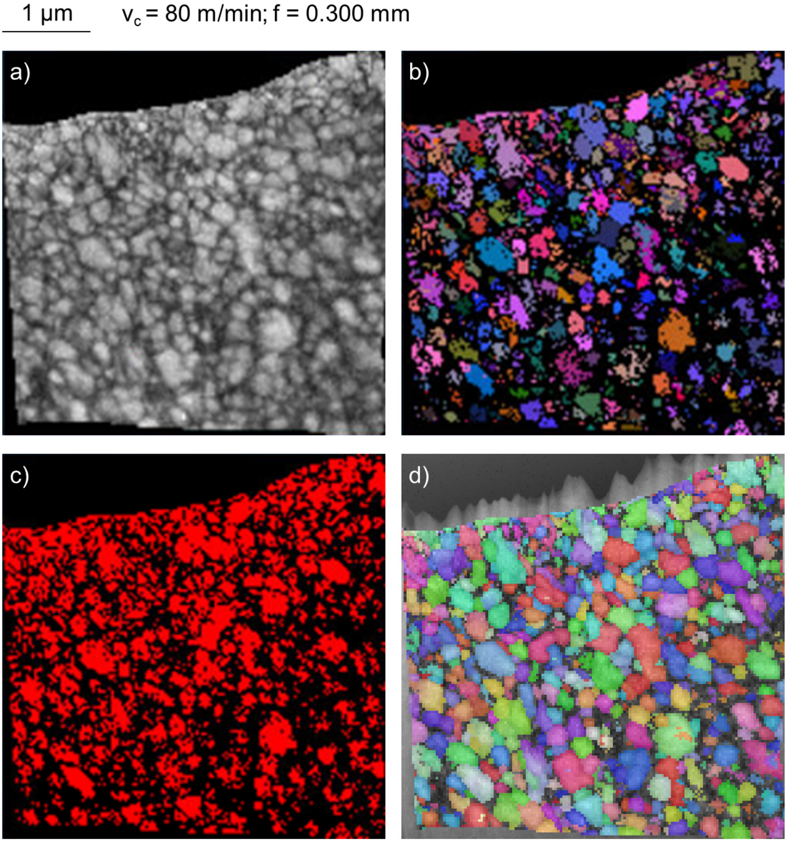

Figure 5.26 TKD mapping of a specimen with a white etching layer (WEL), drilled at a cutting speed of v_c = 80 m/min and a feed of f = 0.300 mm: a) band contrast image, b) Euler color map, c) phase map, d) pattern matching (dictionary indexing) (batch A)

Confronting the results with the calculated grain sizes based on the FWHM in X-ray diffraction using the Scherrer equation, it can be observed that the calculated grain sizes are smaller. For instance, for the specimen analyzed in TKD, a grain size of approx. D_g = 12 nm was calculated using Scherrer equation (Figure 5.22). This is much smaller than the average grain size (D_g = 260 nm) observed in TKD. Reasons for the deviation might be found in the practical limitations of the Scherrer equation. For instance, the approximation of the crystallite shape factor as k = 0.94 for spherical particles might be a source of errors. In addition to this, average grain sizes in the WEL as assessed by TKD might transgress the upper limit of acceptable grain sizes for using the Scherrer equation. In general, the Scherrer equation is limited to materials with an average grain size of up to approx. D_g = 100-200 nm. The reason for this limitation is that for larger crystallite sizes it is particularly challenging to separate additional sources of peak broadening in XRD from peak broadening due to the crystallite size [126]. Additional sources of peak broadening in the case of the experiments presented in 5.2.2 might be found in inhomogeneous elastic strains and a particularly high dislocation density inside the WEL. As these and other disruptive factors contribute to the broadening of peaks, crystallite sizes calculated by the Scherrer equation tend to be smaller, as the entire peak broadening is attributed to the grain size.

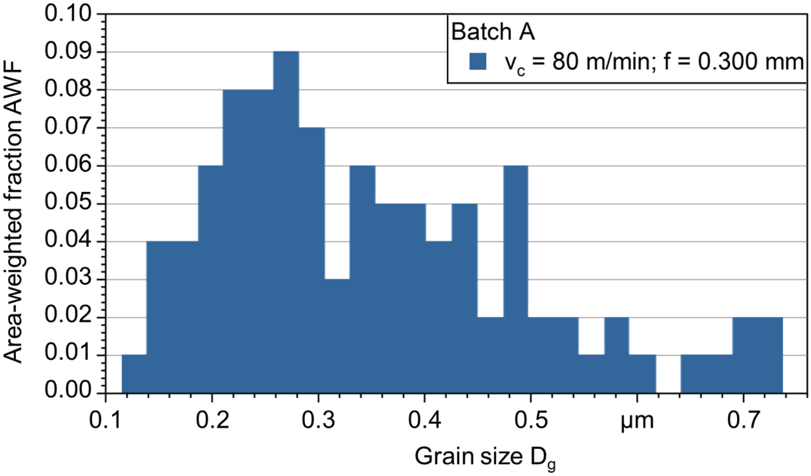

Figure 5.27 Area-weighted fraction of grain size obtained by transmission Kikuchi diffraction (TKD) in a specimen with a white etching layer (WEL), drilled at a cutting speed of v_c = 80 m/min and a feed of f = 0.300 mm (batch A)

Electron channeling contrast imaging (ECCI)

To further analyze grain size, dislocation density, and structures in the subsurfaces of the deep drilled specimens, ECCI analyses were performed. As dislocations and other defects distort the crystal lattice, they alter backscattered electron intensity and appear bright in grains with favorable channeling contrast [135]. Representative images obtained for a specimen free of WEL are displayed in Figure 5.28. Exemplary results for a specimen with a WEL are given in Figure 5.29 and Figure 5.30.

For both specimens, grains in a distance of a few microns to the surface were analyzed by means of ECCI, in order to characterize the regions, where SI is altered the most during BTA deep hole drilling. The precise position of the grains analyzed in ECCI is indicated in the large-scale images on top of the figures.

When analyzing these large-scale images obtained with relatively low magnification, clearly distinct structures can be observed in the subsurfaces of the two specimens. The specimen with a WEL shows a multi-layered subsurface in the images acquired with a BSE-detector. At the very surface, significantly refined grains can be observed within the WEL. This layer has a thickness of approx. $t_{WEL} = 15\ \mu m$. The WEL itself reveals a slight grain size gradient, with particularly small grains on the surface and slightly larger grains at the interface between WEL and the lower subsurface regions (Figure 5.30). Adjacent to the WEL, a severely deformed layer can be observed, which is composed of swept grains. This general structure corresponds well to the patterns observed in EBSD of specimens with WEL, for instance, the one presented in Figure 5.12 b).

Grain boundaries in the specimen free of WEL are rather clear. In this specimen, few subgrains are present (Figure 5.28). Conversely to this, in the subsurface zones of specimens with WEL grain boundaries are surrounded by nanosized grains (Figure 5.29). These indicate the formation of WEL according to the mechanism of dynamic recrystallization. This mechanism is comprehensively discussed in [215]. The findings correspond to the findings of Barry and Byrne, who identified dynamic recrystallization as the driving mechanism for WEL generation in the turning of steels, resulting from a reduction in stacking fault energy as a result of reverse martensite transformation [155]. In addition, this also agrees with the findings of Hosseini et al. who provide evidence of WEL generation due to dynamic recrystallization in hard turning of AISI 52100 [156].

For both specimens, crystal defects, such as dislocations, can be observed as bright patterns inside the dark grains. In the specimen without WEL, dislocations run mostly perpendicular to the grain boundaries. This is highlighted for instance, in Figure 5.28. In the specimen with the WEL, however, complex dislocation patterns can be seen at the grain boundaries and within the grains, as can be observed for example in Figure 5.30. Here the observed defects are found to run not only parallel to the grain boundaries but also in other directions, piling up and forming complex tangles. Due to overlapping and accumulating defect structures, it is challenging to differentiate between the kinds of lattice defects. It seems plausible that the dark dots which can be perceived at some of the grain boundaries are precipitates or nanosized grains with different orientations. However further evidence is required to back up this hypothesis.

In Figure 5.30 black patterns can be observed with a white surrounding, which run mostly parallel to the surface at a distance of a few microns. These structures are cracks and voids. This observation seems plausible, due to the hard and brittle nature of the WEL, which oftentimes results in the formation of cracks, as previously observed in optical microscopy (Figure 5.6).

The findings presented correspond to the findings of Fischer et al. [216]. They employed ECCI to analyze the microstructural evolution due to deep rolling and induction hardening in crankshafts of AISI 4140. Fischer et al. found a significant increase in defects after deep rolling. The electron channeling contrast images provided by them for the deep rolled state show very similar defect structures, compared to the results of ECCI provided in this thesis, although the findings presented by them show larger grains. The similarities in defect structures between conventional deep rolling and BTA deep hole drilling seems plausible, due to the similarities between the processes. For instance, the final step in the conditioning of subsurfaces in BTA deep hole drilling is burnishing through the guide pads, resulting in severe plastic deformation of the subsurface, similar to the effects of deep rolling.

Based on the results of ECCI, it can be concluded that the dislocation density in the specimen with the WEL was higher than in the specimen free of WEL. This observation corresponds well to the dislocation density assessed based on the diffractometric data (Figure 5.22). However, as ECCI can only be performed for a limited amount of adequate grains, quantitatively assessing dislocations by ECCI is particularly challenging, especially in deformed, fine-grained materials [135]. The applicability of this technique for a representative assessment of specimens is thus limited. To back up the findings of ECCI, further STEM-based analyses were performed, which will be presented in the upcoming section.

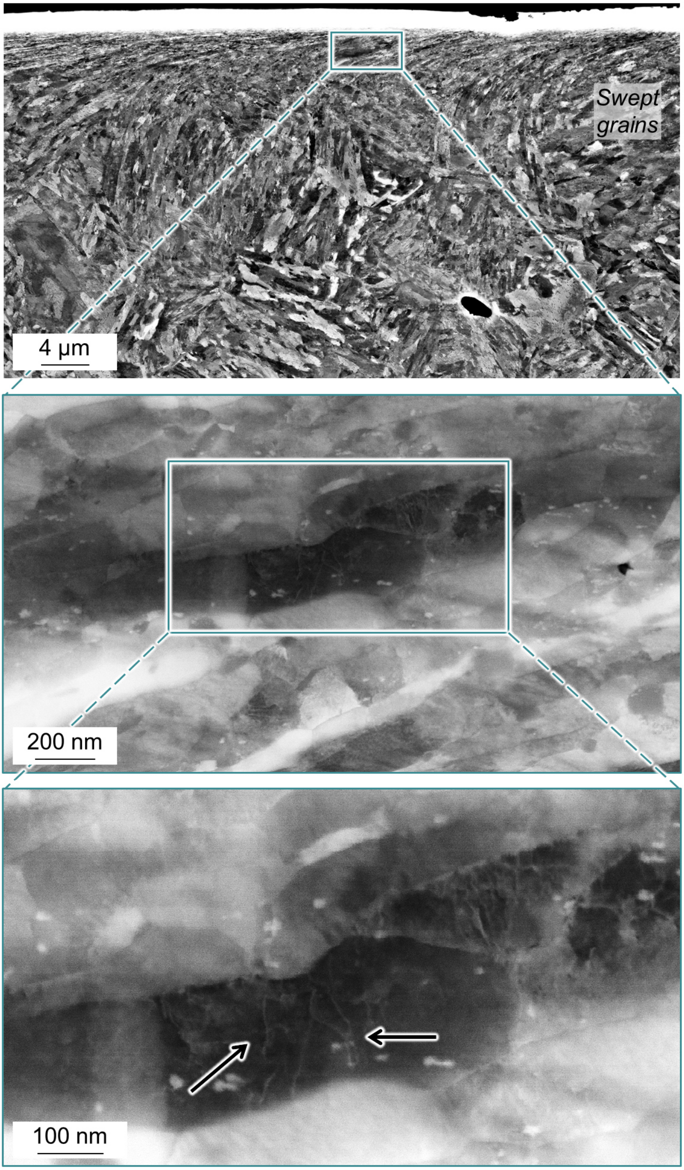

Figure 5.28 Electron channeling contrast images (ECCI) of the subsurface of a specimen without a white etching layer (WEL), drilled at a cutting speed of v_c = 60 m/min and a feed of f = 0.150 mm (batch A). Black arrows: dislocations

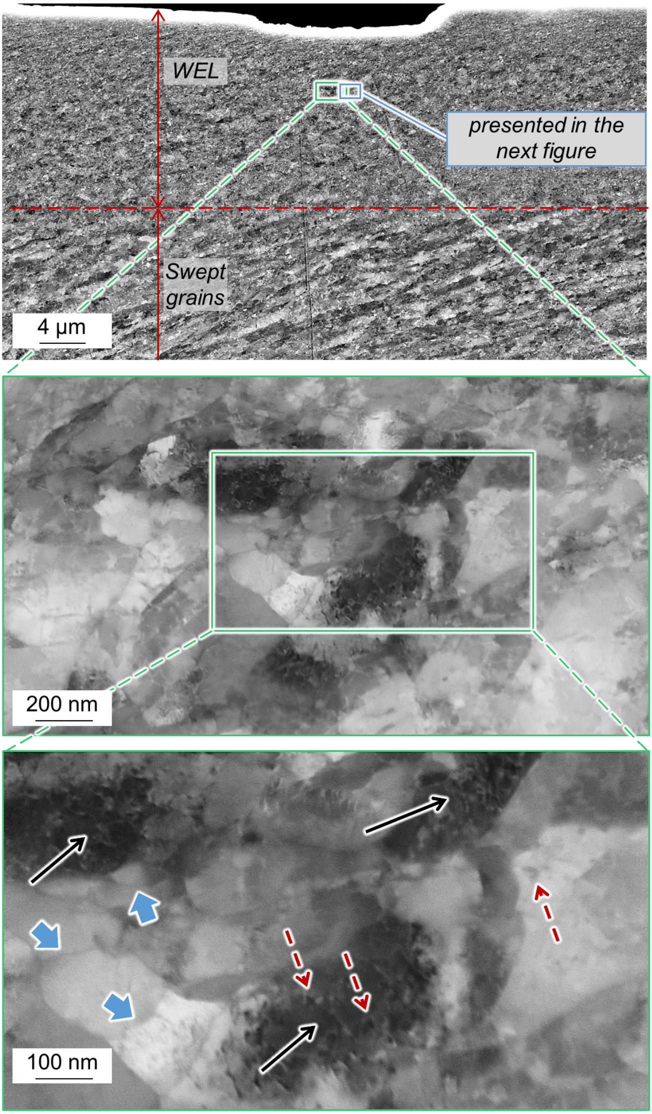

Figure 5.29 Electron channeling contrast images (ECCI) of the subsurface of a specimen with a white etching layer (WEL), drilled at a cutting speed of v_c = 80 m/min and a feed of f = 0.300 mm (batch A). Black arrows: dislocations, blue thick arrows: subgrains, red dashed arrows: potentially precipitates

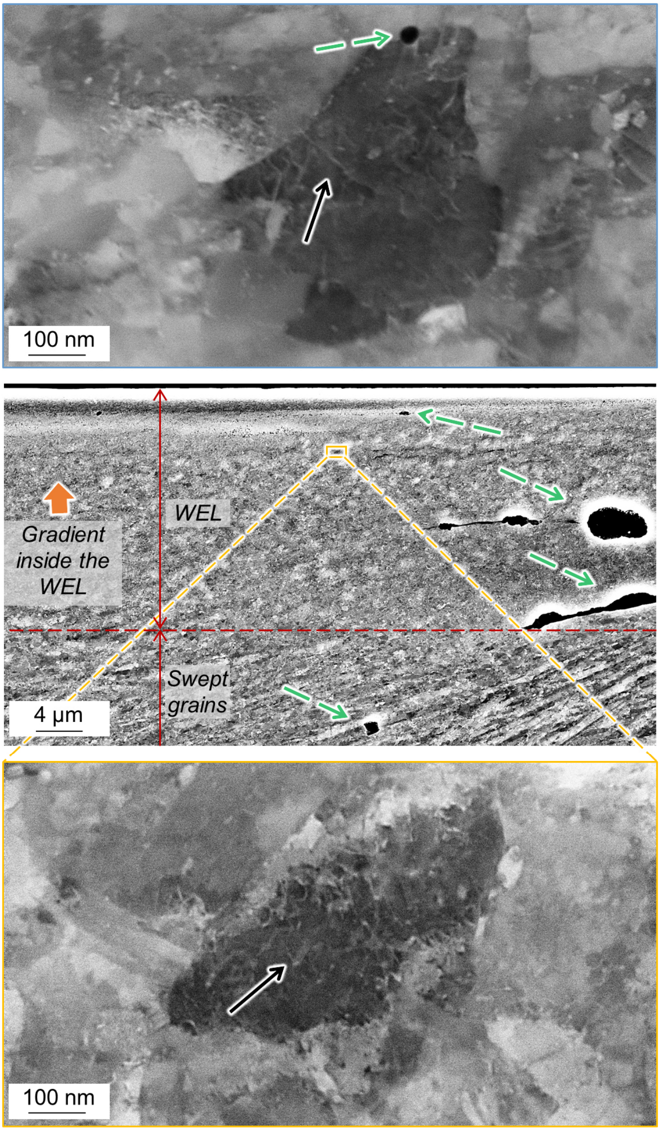

Figure 5.30 Electron channeling contrast images (ECCI) of the subsurface of a specimen with a white etching layer (WEL), drilled at a cutting speed of $v_c = 80$ m/min and a feed of $f = 0.300$ mm (batch A). Black arrows: dislocations, green dashed arrows: pores and cracks, orange thick arrow: gradient. ECCI images as presented in [217]

Scanning transmission electron microscopy (STEM)

For the STEM analyses, lamellae were extracted parallel to the surface of cross-sections in the transverse direction at a distance of approx. $d_{sub} = 3$ µm. This process is shown in Figure 4.5. The results of STEM analyses of the lamellae polished by a focused ion beam (FIB) are presented in Figure 5.31 and Figure 5.32 for a specimen free of WEL and in Figure 5.33 and Figure 5.34 for a specimen with WEL.

In terms of grain sizes and grain morphology in the subsurfaces, the STEM results support the findings obtained by EBSD, TKD, and ECCI. In the specimen free of WEL particularly small grains can be perceived in addition to some slightly larger grains. Some examples of these are highlighted in Figure 5.32. Conversely to this, in the specimen with the WEL exclusively particularly small grains can be observed. As in ECCI, the specimen with the WEL shows a particularly high dislocation density. Regular dislocation patterns can be observed, as dislocations pile up and form tangles. An example of this is marked with an arrow in Figure 5.34, for a grain at the very surface of the deep drilled specimen. In Figure 5.33, an indicator of WEL formation following the mechanism of dynamic recrystallization is presented. The arrows highlight stacking faults, which are a sign of severe plastic deformation.

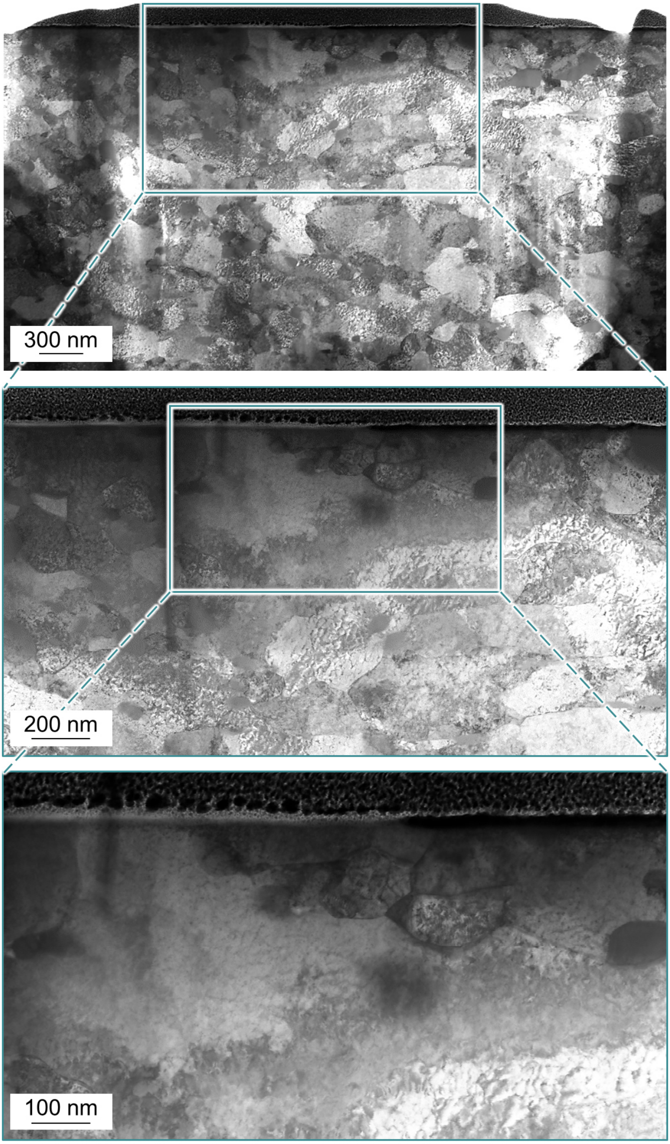

Figure 5.31 Scanning transmission electron microscopy (STEM) images of the subsurface of a specimen, without a white etching layer (WEL) drilled at a cutting speed of $v_c = 60$ m/min and a feed of $f = 0.150$ mm (batch A)

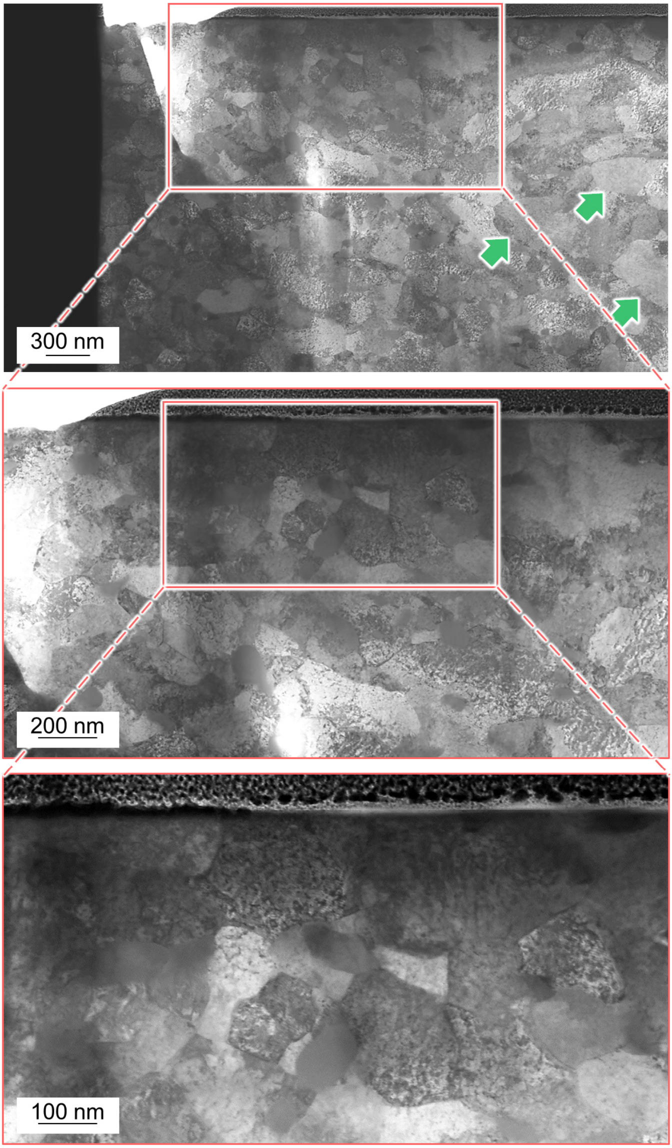

Figure 5.32 Scanning transmission electron microscopy (STEM) images of the subsurface of a specimen whitout a white etching layer (WEL), drilled at a cutting speed of $v_c = 60$ m/min and a feed of $f = 0.150$ mm (batch A). Green arrows: larger grains

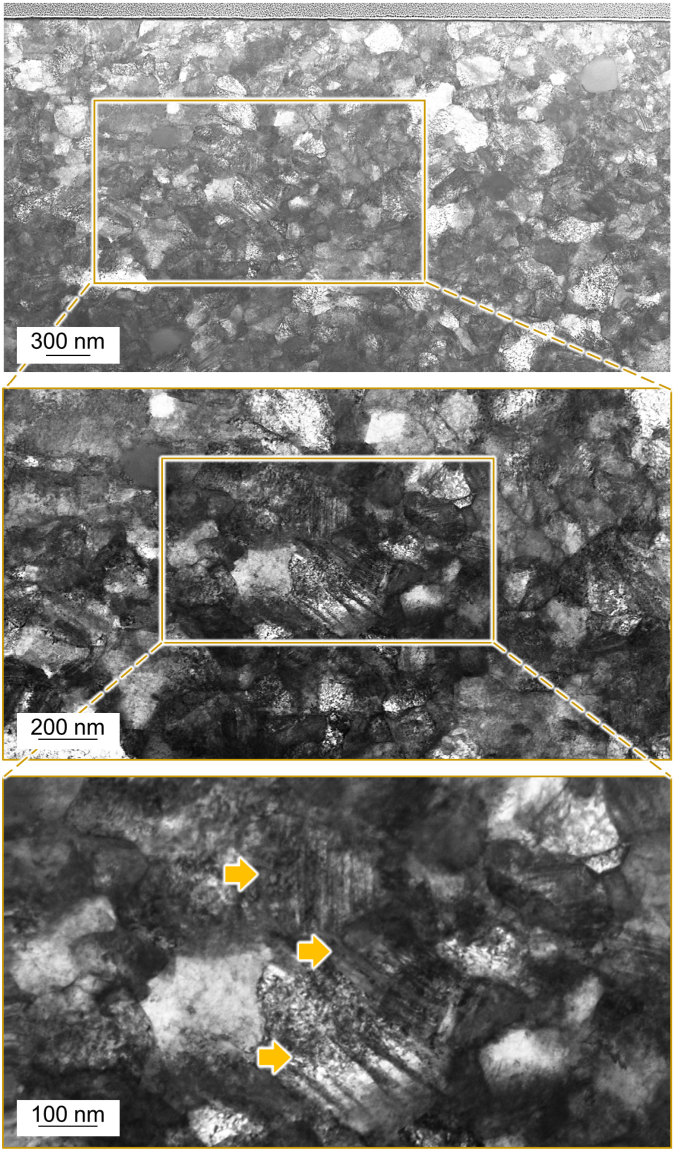

Figure 5.33 Scanning transmission electron microscopy (STEM) images of the subsurface of a specimen with a white etching layer (WEL), drilled at a cutting speed of $v_c = 80$ m/min and a feed of $f = 0.300$ mm (batch A). Yellow arrows: stacking faults

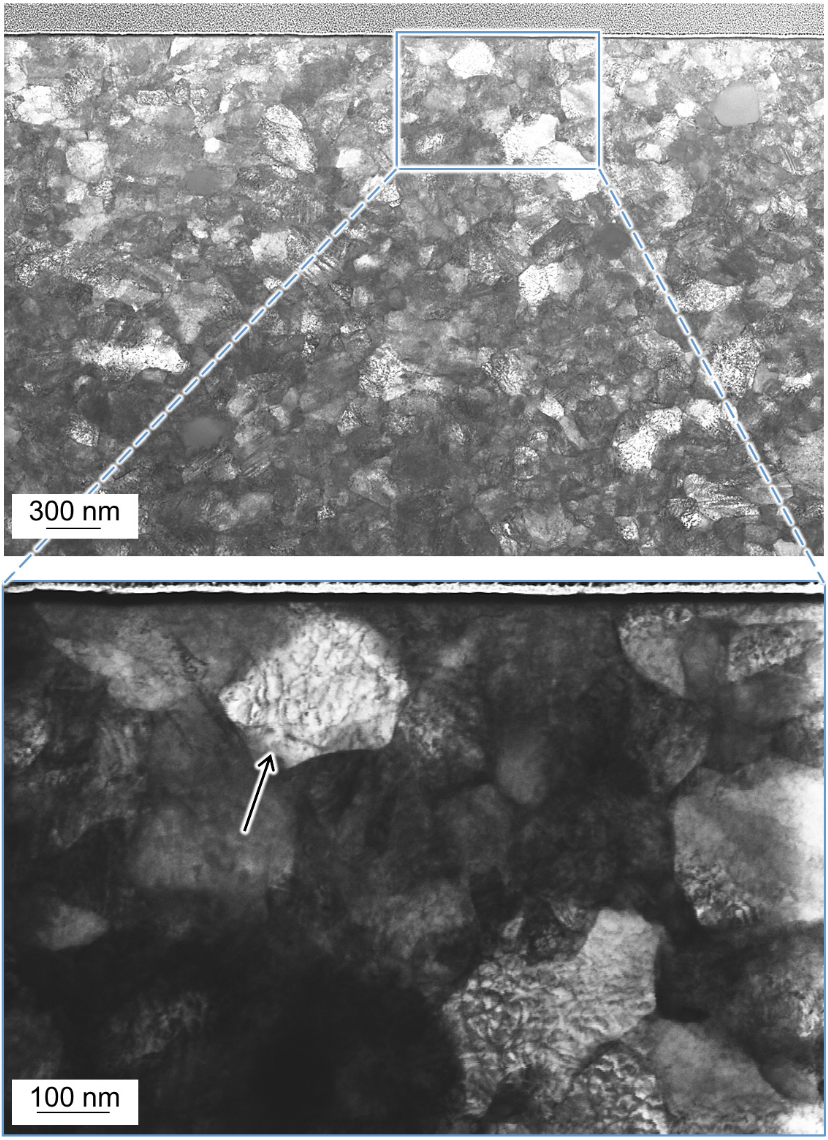

Figure 5.34 Scanning transmission electron microscopy (STEM) images of the subsurface of a specimen with a white etching layer (WEL), drilled at a cutting speed of v_c = 80 m/min and a feed of f = 0.300 mm (batch A). Black arrow: dislocations

5.3 Micromagnetic evaluation of surface integrity (SI)

In this chapter, the magnetic microstructures in the subsurfaces of deep drilled specimens will be analyzed by MBN analysis (5.3.1), Bitter technique (5.3.2), MOKE microscopy (5.3.3), and MFM (5.3.4). These complementary methods are based on fundamentally different underlying principles, have significantly different levels of complexity, and can be used to monitor magnetic microstructures on entirely different scales. In 5.3.5 the findings obtained by the different approaches will be confronted with one another. In addition to this, the findings of the micromagnetic approaches will be reviewed in close conjunction with microstructural aspects such as grain size and dislocation density, as previously assessed in 5.2.3. The motivation behind these extensive mechanism-based investigations is to gain an understanding of the mechanisms governing MBN analysis. This way, MBN analysis is qualified for a nondestructive, and quick assessment of SI of deep drilled components. An MBN-based, multi-sensory test stand is developed and used for evaluating the subsurfaces of components with the systems FracDim and Rollscan and different micromagnetic sensors.

5.3.1 Magnetic Barkhausen noise (MBN) analysis

MBN analysis was performed as a nondestructive, surface-sensitive, particularly quick, and easily applicable micromagnetic approach for a holistic characterization of SI, which does not require any special preparation of the bores. In Figure 5.35 two exemplary MBN envelopes are presented, obtained for a bore free of WEL ($v_c = 60$ m/min; $f = 0.150$ mm) and for a bore that was found to have a WEL, as it was drilled at a higher cutting speed ($v_c = 100$ m/min; $f = 0.150$ mm). For both envelopes, the parameters obtained for the maximum MBN amplitudes M_{max}, the MBN amplitudes at the remanence point M_r, and the coercive field strengths Φ_{cm} are presented.

It can be observed that the bore free of WEL exhibits a significantly higher maximum MBN amplitude of $M_{max} = 12.74$ mV, compared to $M_{max} = 4.88$ mV of a bore with a WEL. The MBN amplitude at the remanence point of $M_r = 3.19$ mV is also slightly higher for the specimen free of WEL, as $M_r = 2.41$ mV was observed for the specimen with WEL. Conversely, the coercive field strength Φ_{cm} of the specimen without WEL is at a level of $\Phi_{cm} = 2.59$ µVs and thus slightly smaller, compared to the specimen with a WEL, which is at $\Phi_{cm} = 2.98$ µVs.

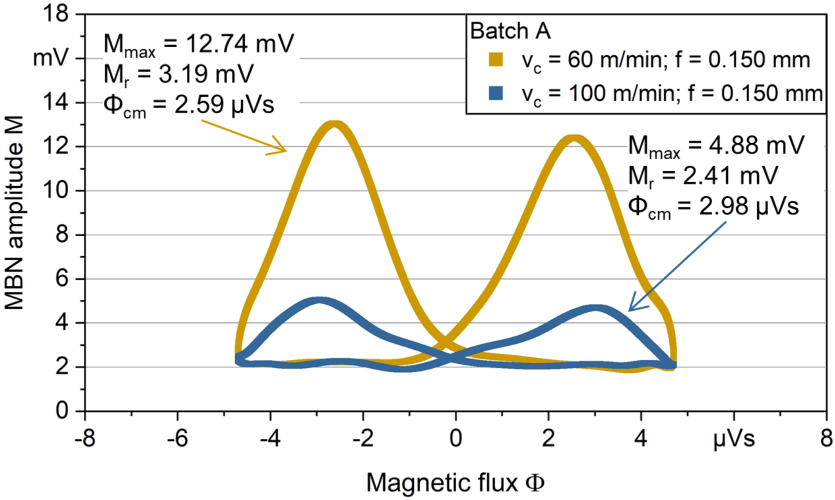

Figure 5.35 Two exemplary MBN envelopes obtained for the subsurfaces of a specimen without white etching layer (WEL) (v_c = 60 m/min; f = 0.150 mm) and a specimen with WEL (v_c = 100 m/min; f = 0.150 mm) along with the parameters obtained for M_{max}, M_r, and Φ_{cm} (batch A)

To investigate, whether the previously presented correlations observed for the two specimens also apply to additional specimens drilled at other combinations of cutting speed and feed, further experiments were performed. Following the suggestion of Stupakov et al. for an MBN-based WEL detection, multiple micromagnetic parameters were considered, as the applicability of the three parameters M_{max}, M_r, and Φ_{cm} for the detection of WEL was analyzed [81].

In Figure 5.36 the maximum MBN amplitudes M_{max} obtained for specimens drilled at different feed rates and cutting speeds are displayed. It can be seen that bores that were found to have WEL in optical microscopy lead to significantly lower MBN amplitudes of $M_{max} < 5$ mV. All bores which were found to be free of WEL led to significantly higher MBN amplitudes and a much larger scattering of the values obtained in MBN inspection around the circumference of the bore. Conversely, M_{max} values obtained for specimens with WEL show particularly low standard deviation as well as very low scattering around the circumference of the bore.

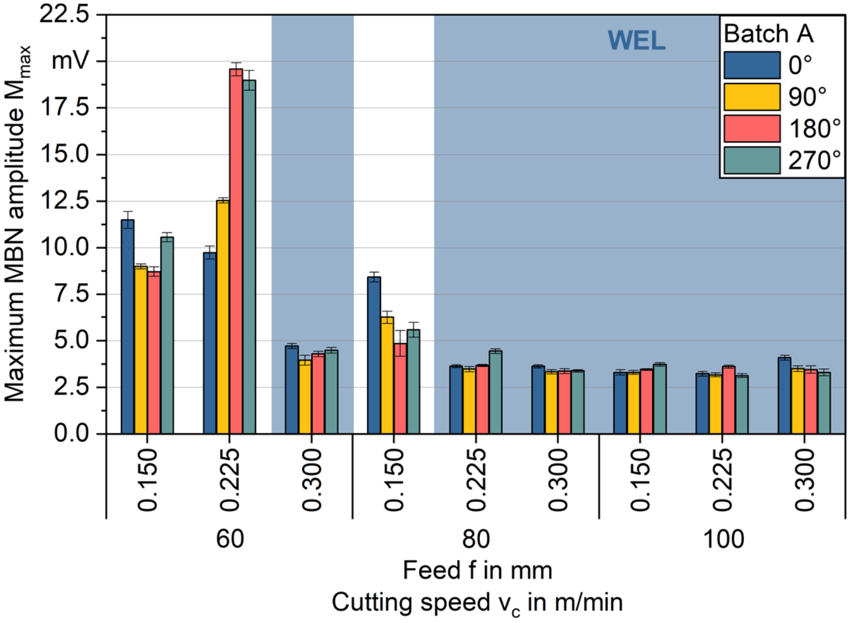

Figure 5.36 Maximum magnetic Barkhausen noise (MBN) amplitudes of specimens drilled at varying cutting speeds (v_c = 60-100 m/min) and feeds (f = 0.150-0.300 mm) at the middle of the bores (batch A). Parts of the data are published in [209]

A potential reason for the deviation in scattering might be found in the shading behavior of the WEL, covering the impact of the underlying material on MBN. Following this hypothesis, a WEL might superimpose the impact of other properties on MBN, resulting in the low scattering of M_{max} for specimens with WEL. If no WEL is present at the surface, other properties such as residual stresses might have a dominant impact on MBN analyses. This might serve as an explanation for the rather high scattering of MBN around the circumference of the bore for specimens free of WEL, for instance, the one drilled at a cutting speed of v_c = 60 m/min and a feed of f = 0.225 mm.

Another aspect that needs to be considered in this regard is the reading depths in MBN analysis. A WEL might lead to significant alterations in the relative permeability of the material and subsequently result in smaller reading depths in MBN analysis. In light of the investigations by Stupakov et al., who report on reading depths of d = 50 µm to 200 µm in martensitic steel ribbons, it might be assumed that the relative permeability inside the WEL can reduce reading depths even further [103,104]. This hypothesis corresponds to findings presented by Stupakov et al. in a different paper. In milling of AISI 52100, they observed the formation of thicker WEL with increasing flank wear. The formation of WEL resulted in a second peak in the MBN envelope. With very strong flank wear and subsequently thick WEL, the first peak originating from the bulk and a darker layer beneath the WEL vanished so that they only observed the peak originating from the WEL. Based on this observation, Stupakov et al. concluded that the presence of a WEL can limit the reading depth in MBN analysis to a few tens of micrometers [81].

To back up the hypothesis of a shading behavior of WEL, further rather mechanism-based investigations will be presented in the upcoming chapters. Utilizing advanced, micromagnetic approaches such as MOKE and MFM, the magnetic properties of WEL will be further elucidated to decouple the effects of WEL and other aspects of SI on MBN.

As micromagnetic multiparameter analyses oftentimes are superior to approaches based on a single parameter, the applicability of additional MBN parameters for the detection of WEL was evaluated. Figure 5.37 displays the Barkhausen noise amplitudes at the remanence point. It can be observed that the specimens drilled at a cutting speed of $v_c = 60$ m/min combined with a feed of $f = 0.150$ mm, respectively $f = 0.225$ mm show significantly higher MBN at the remanence point. The third specimen which was found to be free of WEL ($v_c = 80$ m/min and $f = 0.150$ mm), however, shows only slightly higher MBN at the remanence point, compared to the average values of specimens with WEL. This observation corresponds to the M_{max} values, in that this specimen also has the lowest M_{max} values of the three specimens free of WEL. This indicates that the specimen drilled at a cutting speed of $v_c = 80$ m/min combined with a feed of $f = 0.150$ mm might be more similar to the specimens with WEL in terms of SI than the other two specimens without WEL. Another indicator for this is that the FWHM values presented in Figure 5.22 are closer to the values of the specimens with WEL. Based on the poorer distinguishability between the specimens free of WEL and the ones affected by it, M_{max} is preferred over M_r and used for further analyses.

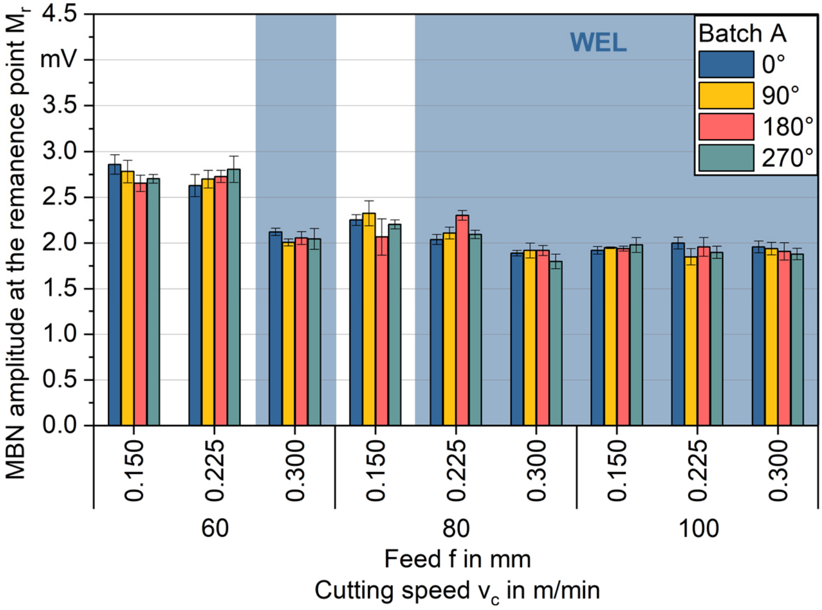

Figure 5.37 Magnetic Barkhausen noise (MBN) amplitude at the remanence point M_r of specimens drilled at varying cutting speeds (v_c = 60-100 m/min) and feeds (f = 0.150-0.300 mm) at the middle of the bores (batch A)

In addition to M_{max} and M_r, the coercive field strength Φ_{cm} was analyzed. As presented in Figure 5.38, no correlation can be observed between the coercive field strength and the presence of WEL. This is remarkable, considering the particular grain size sensitivity of this parameter and the nanocrystallinity of the WEL [23,139]. A potential explanation for this observation, might be found in the significant reduction in grain sizes also for specimens free of WEL, as evidenced in the previously presented EBSD mappings (Figure 5.11, Figure 5.24). Stupakov et al. provide conflicting results on the applicability of coercive field strength for WEL detection. In some experiments presented by them, stronger flank wear of the tool and subsequently thicker WEL after milling correlated with higher values of the coercive field strength. In others, coercive field strength is found to decrease for strong flank wear [81].

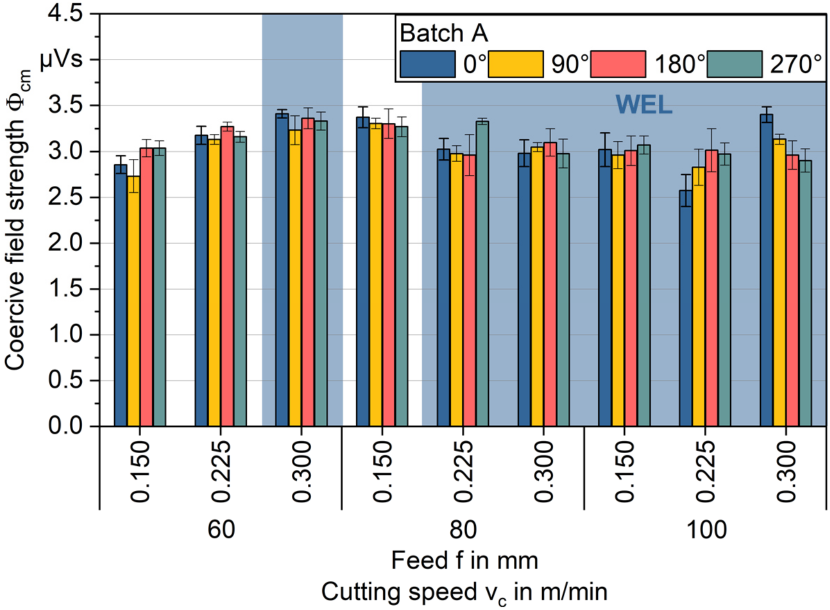

Figure 5.38 Coercive field strength of specimens drilled at varying cutting speeds (v_c = 60-100 m/min) and feeds (f = 0.150-0.300 mm) at the middle of the bores (batch A)

Figure 5.39 presents the maximum MBN amplitudes for four exemplary specimens, analyzed using different band-pass filter frequencies. Two of the four specimens have WEL, two specimens are free of WEL. In addition to the previously employed, relatively broad band-pass filter of f_{min} = 10 kHz to f_{max} = 200 kHz, seven further band-pass filters are employed, ranging from f_{bp} = 5-10 kHz, to f_{bp} = 400-500 kHz. Following the explanations provided on the skin effect in 2.2.3, varying the band-pass filter frequencies allows for altering the reading depths in MBN analysis. In general, increasing the band-pass filter frequencies reduces the reading depth in MBN analysis [73].

It can be observed, that for the lowest band-pass filter frequency of f_{bp} = 5-10 kHz only slight differences can be observed between the four specimens, with the two specimens free of WEL showing slightly lower maximum MBN amplitudes. At higher band-pass filter frequencies, the differences in maximum MBN amplitudes between the two specimens with WEL and the two specimens free of WEL become much more pronounced. When using a band-pass filter of $f_{bp} = 400$-500 kHz, the MBN amplitudes of specimens free of WEL is approx. three times higher than the maximum MBN amplitude of specimens with WEL. Following the previous remarks, the reason for this enhanced distinguishability can be found in lower reading depths when using higher band-pass filter frequencies. As outlined in 5.1, the SI is altered particularly strongly in very close proximity to the surface of the bore. Subsequently, lower inspection depths in MBN through higher band-pass filter frequencies allow for a better distinguishability of specimens. Based on these observations, it can be concluded, that for the detection of WEL, it is advisable to resort to rather high band-pass filter frequencies, as WEL are located at the very surface. When using relatively low band-pass filter frequencies, the higher influence of deeper layers complicates distinguishing between specimens with and without WEL.

These observations correspond to the findings of Baak [73]. Analyzing single-lip deep drilled specimens, he also found better distinguishability between the specimens at higher band-pass filter frequencies. He identified a stronger influence of deep hole drilling on the SI at closer distance to the surface as a reason for this [73].

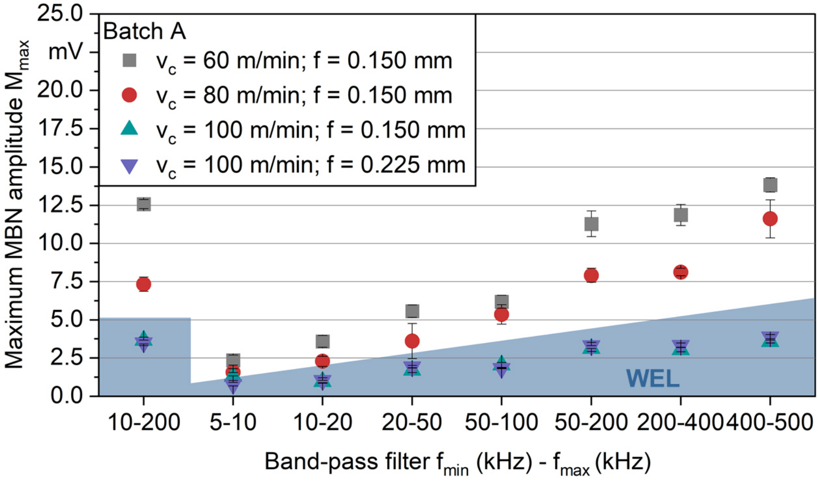

Figure 5.39 Impact of the band-pass filter frequencies on the maximum magnetic Barkhausen noise (MBN) amplitude, for two exemplary specimens without white etching layers (WEL) ($v_c = 60$ m/min; f = 0.150 mm and $v_c = 80$ m/min; f = 0.150 mm) and two specimens with WEL ($v_c = 100$ m/min; f = 0.150 mm and $v_c = 100$ m/min; f = 0.225 mm) at the middle of the bores at an angle of 0° (batch A)

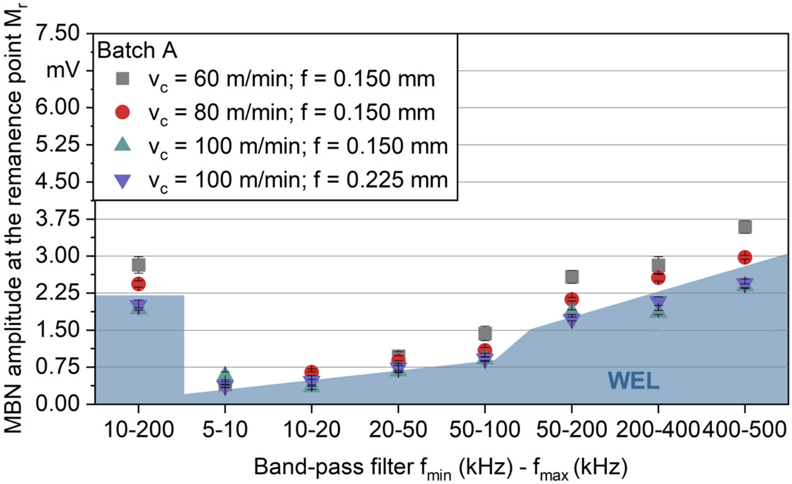

Figure 5.40 Impact of the band-pass filter frequencies on the magnetic Barkhausen noise (MBN) amplitude at the remanence point, for two specimens without white etching layers (WEL) (v_c = 60 m/min; f = 0.150 mm and v_c = 80 m/min; f = 0.150 mm) and two specimens with WEL (v_c = 100 m/min; f = 0.150 mm and v_c = 100 m/min; f = 0.225 mm) in the middle of the bores at 0° (batch A)

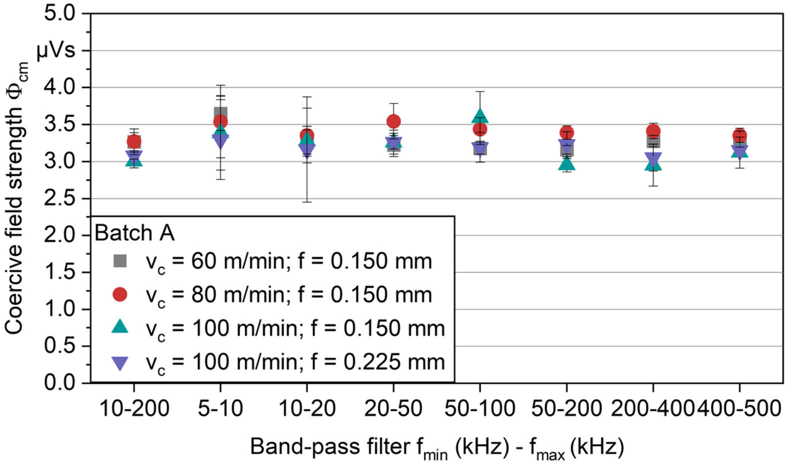

Figure 5.41 Impact of the band-pass filter frequencies on the coercive field strength, for two specimens without white etching layers (WEL) (v_c = 60 m/min; f = 0.150 mm and v_c = 80 m/min; f = 0.150 mm) and two specimens with WEL (v_c = 100 m/min; f = 0.150 mm and v_c = 100 m/min; f = 0.225 mm) in the middle of the bores at 0° (batch A)

To analyze the comparability between the micromagnetic parameters M_{max} and RMS obtained by the different systems (FracDim and Rollscan 350) further analyses were performed. The purpose of these investigations was particularly to investigate the transferability of the previously presented results, obtained using the device FracDim. For accurately positioning sensors inside of the bores and for moving them along the length of the bores, the test stand presented in Figure 4.14 was employed. The position of the sensors along the length of the bores (l_b) was evaluated using a draw wire sensor, as presented in 4.6.

Exemplary results obtained analyzing a specimen of batch B, drilled at a cutting speed of $v_c = 80$ m/min and a feed of $f = 0.150$ mm, are presented in Figure 5.42. This specimen was selected, because it shows a relatively large scattering of the values for M_{max} and RMS along the length of the bore and thus it is particularly suitable for comparison between the two systems and the different sensors.

It can be observed that both systems yield qualitatively similar results, using the respective multipurpose sensors (Figure 5.42 a). At the start of the bore, a huge scattering of M_{max} and RMS can be observed. This probably results from the unsteady cutting situation during this phase of deep hole drilling and agrees with the findings presented in [208]. After the first approx. $l_b = 25$ mm, both parameters are more stable, and show an increasing tendency until a depth of the bore of approx. $l_b = 125$ mm. At this point, a drop can be observed in both parameters. Based on the previously presented findings it can be hypothesized that this drop results from a stronger alteration of the microstructure, e.g. more severe deformation and potentially the formation of WEL. In between $l_b = 125$ and 160 mm, the values of M_{max} and RMS are relatively stable and then increase significantly before they drop again. It can be observed that the bores are not characterized at their full length. One reason for this is that the clamping of the specimens at their inner diameter prevented the sensor positioning devices from being moved any further at a certain depth. In addition to this, both sensors were placed in their respective positioning devices with a slight offset to the tip. To overcome this shortcoming of the test stand and evaluate the bores at their full length, specimens can be rotated and characterized from the end of the bores.

In addition to the comparison between the two systems, also different sensor geometries were analyzed (multipurpose sensor, drill head sensor). This way, the general adequacy of the custom-designed, miniaturized drill head sensor was assessed. It can be observed that qualitatively similar results were obtained, using both sensors. However, the drill head sensor shows a significantly higher scattering of the RMS values acquired. The relatively strong scattering observed for the drill head sensor results from various overlapping reasons. On the one hand, both multipurpose sensors have spring-mounted sensing elements. Subsequently, they are always in contact with the surface of the bore, whereas this is not the case for the drill head sensor. The slightly varying air gap between the sensor and the surface certainly contributes to the scattering observed. In addition to this, the amplifying electronics are placed outside of the sensor in an extra housing for the drill head sensor Figure 4.9 b). In contrast to this external amplification, the multipurpose sensors used contain the amplifying electronics inside the sensor housing. The length between the acquisition and amplification of the MBN signal in the multipurpose sensors is subsequently much shorter compared to the drill head sensor. Here the sensor is connected via a cable with a length of $l = 1000$ mm to the amplification.

Based on the findings presented, it can be concluded that in general, both systems are equally applicable for the characterization of subsurface zones in deep drilled bores. As a result, the findings previously presented for the FracDim probably also apply to the Rollscan 350. The custom-designed drill head sensor in general is applicable for characterizing the deep drilled surfaces. However, means need to be taken to keep conditions as constant as possible to reduce the scattering of values. In this context, it is particularly important to keep the air gap between the sensor and the surface as small and as constant as possible. A detailed account of the design of the sensor is given in [205].

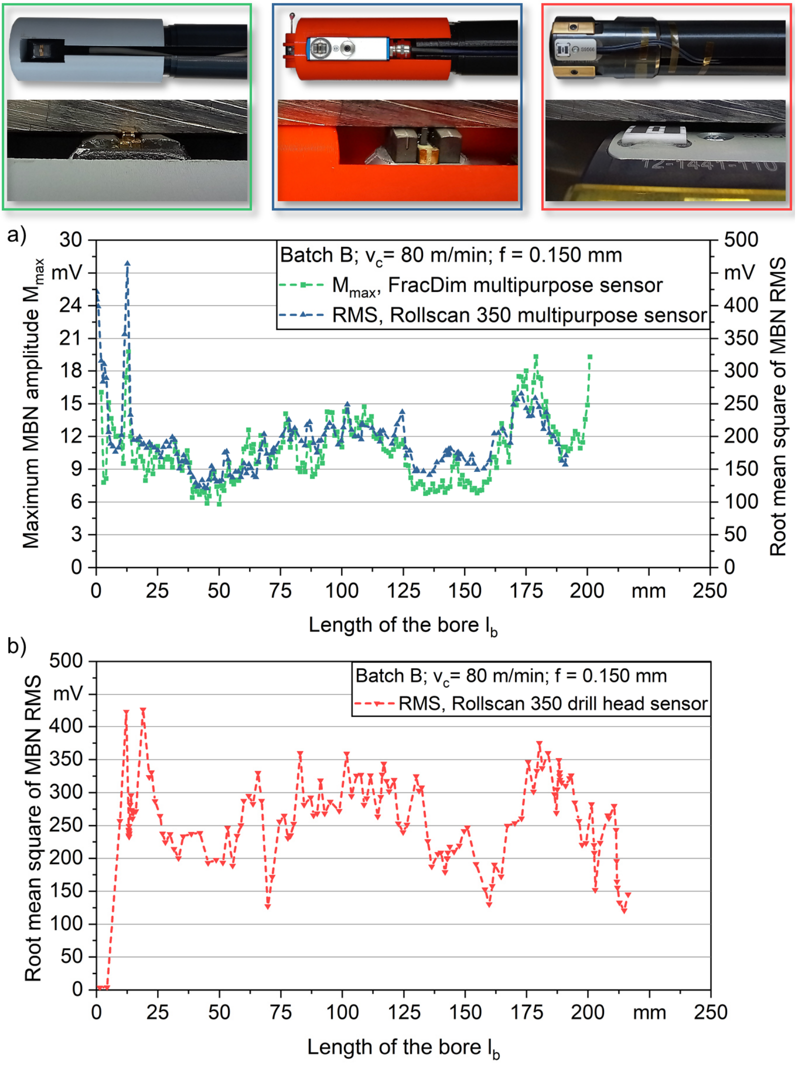

Figure 5.42 Comparison between different systems and sensors for magnetic Barkhausen noise (MBN) analysis of a specimen, drilled at a cutting speed of v_c = 80 m/min and a feed of f = 0.150 mm, along the length of the bore: a) maximum MBN amplitude M_{max} obtained by FracDim and root mean square (RMS) obtained by Rollscan 350 with multipurpose sensors; b) RMS of MBN obtained by Rollscan 350 with a custom-designed miniaturized drill head sensor (batch B)

5.3.2 Bitter technique

In addition to MBN analysis, MOKE microscopy, and MFM, the fairly straightforward Bitter technique was employed to analyze the magnetic microstructure inside the subsurface of the BTA deep drilled specimens. To assess the applicability of Bitter etching, in the first step, the bulk material was examined. Exemplary results are presented in Figure 5.43 a) and b). To assure the general adequacy of the commercially available ferrofluid employed, a specimen of AISI 1045 with a ferritic-pearlitic microstructure was analyzed by Bitter etching as a reference (Figure 5.43 c) and d).

The nital-etched cross-section of AISI 4140 reveals the typical microstructure of quenched and tempered steels (Figure 5.43 a). When analyzing this specimen by Bitter etching, it is observed that the ferrofluid is relatively evenly distributed. For instance, no major gradients or patterns can be seen (Figure 5.43b). In the micrograph of AISI 1045 a ferritic-pearlitic microstructure can be observed (c), composed of ferrite and pearlite with a lamellar structure. Using the Bitter technique, regular patterns do appear in the cross-section of AISI 1045. These resemble magnetic domain structures in steels visualized by other approaches, such as MFM [86,218,219]. Compared to the number of lamellae per grain observed in nital etching, the amount of regular neighboring patterns in the image obtained by the Bitter technique is significantly lower. In addition to this, the spacing between the regular patterns in Bitter etching does not correspond to the spacing between the lamellae of the pearlite. This indicates that the regions highlighted by the ferrofluid are domain walls dividing magnetic domains and do not derive from disturbing factors, such as the topography of the OPS-polished cross-sections. Based on this observation it can be concluded, that the ferrofluid used is well applicable for the analysis of magnetic domain structures.

In Figure 5.44 two exemplary subsurface zones analyzed by the Bitter technique are depicted along with the results of optical microscopy for specimens extracted at the same length of the same bores but at slightly different angles. In the sample free of WEL, no significant differences can be found between the Bitter patterns in the subsurface and the bulk material. In this specimen, no regular structures can be observed, apart from a few isolated dots, which might result from an incomplete distribution of the ferrofluid. In the specimen with the WEL, a clear line of agglomerated ferrofluid can be seen at a distance to the surface of approx. $d_{surf} = 12$ µm. This corresponds well to the thickness of the WEL observed in optical microscopy Figure 5.2. Based on these observations, it can be concluded that the WEL does not attract the ferrofluid, as inside the WEL almost no particles agglomerate at all. In contrast to this, the material at the interface between the WEL and the deeper subsurface does attract the ferrofluid significantly, as a dark rim can be observed below the WEL. When having a close look at the rim, one might even recognize a swept structure of the ferrofluid, similar to the swept grains observed for example in EBSD. A spot where this effect is visible is marked with A in Figure 5.44 c). However, the relatively poor resolution of optical microscopy in the classic Bitter technique, resulting from the coverslip on top of the ferrofluid, does not allow for assessing local features on such a small scale [108].

One common error in Bitter etching is that the topography of specimens impacts the agglomeration of the applied ferrofluid. Subsequently, it is vital to avoid any topographical influence, to obtain information purely from magnetic domains without any influence of topography. As OPS has a slightly etching character it is vital to avoid that the ferrofluid is impacted by polishing. If topography was significantly altered at the WEL, this would imply a drop of topography behind the WEL. As the WEL is oftentimes considered to be etch-resistant, this seems plausible. However, in an AFM-based topography assessment, no indications for such a topographic difference between the WEL and the adjacent material were found (Figure 5.54). Further information on these analyses will be given in 5.3.4.

Based on the previous remarks, it can be concluded that the Bitter technique seems to be a well-applicable, and straightforward way of visualizing the effect of a WEL on magnetic domain patterns in the subsurface of deep drilled specimens. Evidence has been provided that the WEL does not attract the ferrofluid. Instead, ferrofluid agglomerates at the interface between the WEL and the deeper subsurface regions. A potential reason for this might be found in the absence of domain walls inside the WEL and a concentration of domain walls in the material adjacent to the WEL. To further investigate this observation, results in MOKE microscopy will be presented in the upcoming section as well as results of MFM in 5.3.4.

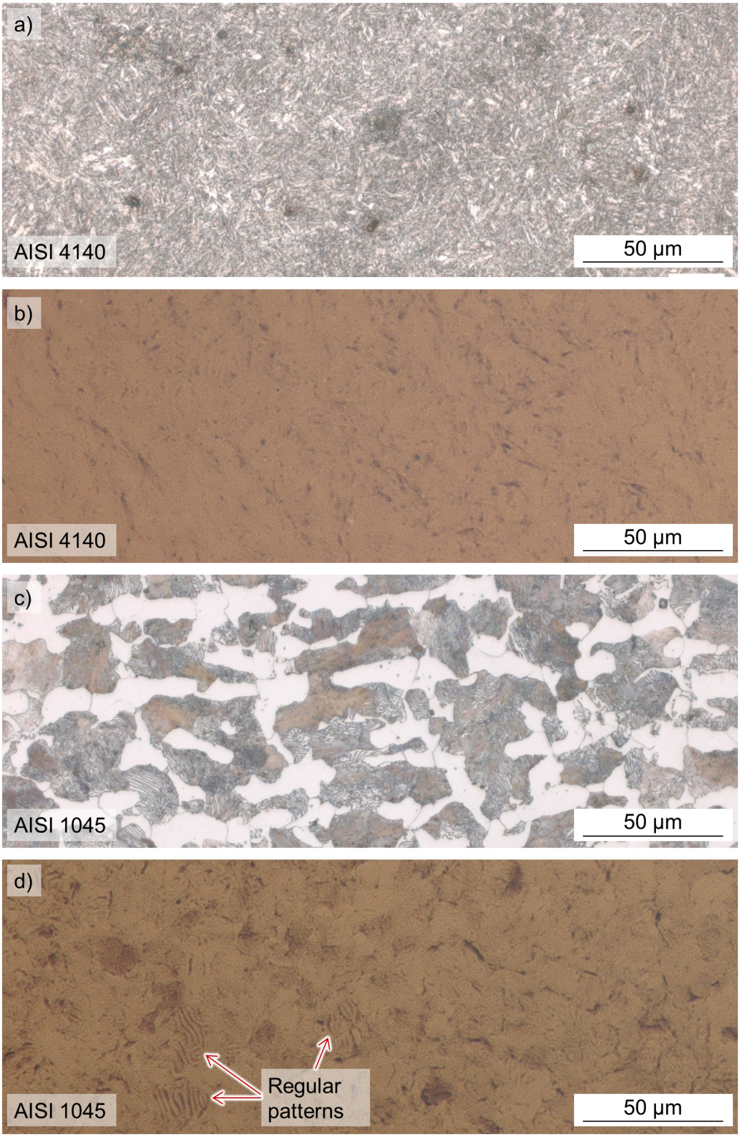

Figure 5.43 Optical microscopy and Bitter technique of different regions in: a), b) the bulk material of a specimen of AISI 4140, drilled at a cutting speed of v_c = 60 m/min and a feed of f = 0.225 mm (batch A); c, d) AISI 1045 as a reference

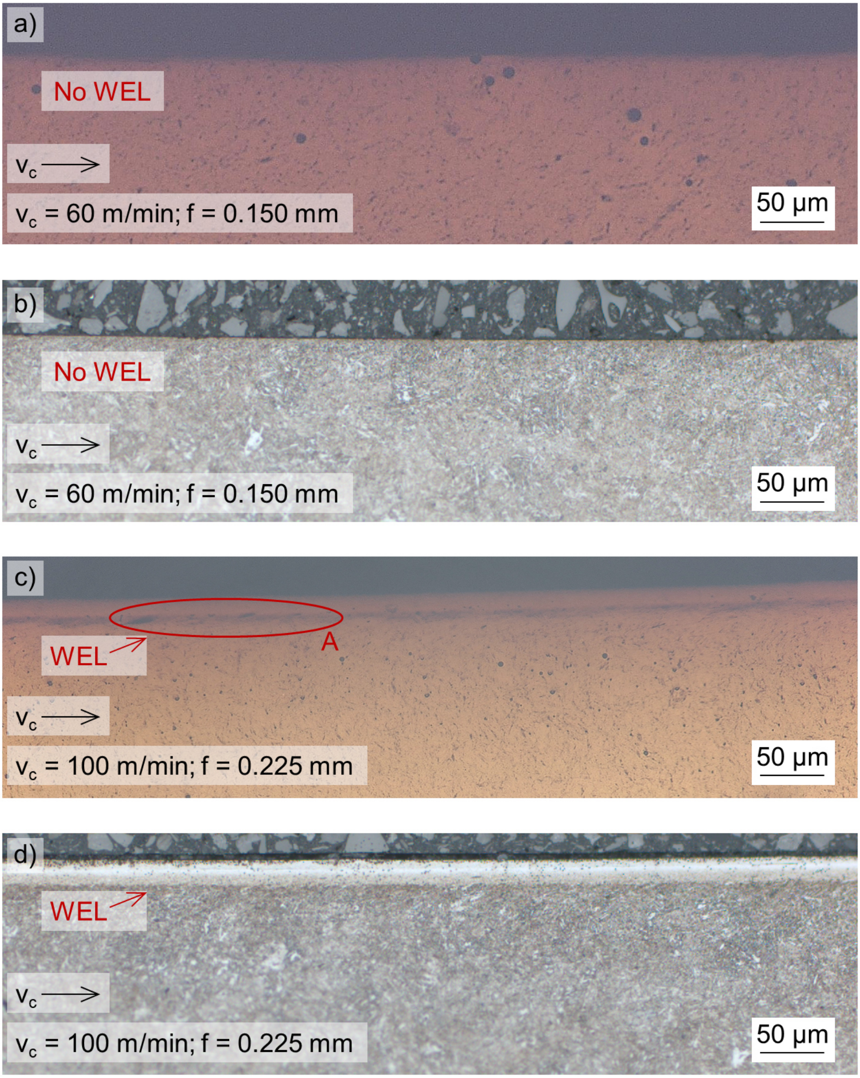

Figure 5.44 Bitter technique and optical microscopy: a), b) coss-section in transverse direction of a specimen drilled at a cutting speed of $v_c = 60$ m/min and a feed of $f = 0.150$ mm, without white etching layer (WEL); c), d) coss-section in the transverse direction of a specimen drilled at a cutting speed of $v_c = 100$ m/min and a feed of $f = 0.225$ mm, with WEL (batch A)

5.3.3 *Magneto-optic Kerr effect (MOKE) microscopy*

To further investigate on the results obtained by the Bitter technique and MBN analysis, MOKE microscopy was performed. This method allowed for in-situ observation of the evolution of magnetic domain structures in external magnetic fields at a varying field strength

As for the Bitter technique, in the first step, the magnetic microstructure inside the bulk was characterized. The results are depicted in Figure 5.45 and Figure 5.46. In Figure 5.46 a) the background is presented, which was assessed prior to magnetization. Following the method presented in 4.5, the remanence can be observed after magnetizing the specimen, then removing magnetization and subtracting the background (Figure 5.46 b). Using this method, pictures b) to l) are obtained as differential images. It can be observed, that clear patterns remain in the material at the point of remanence, when removing the external magnetic field. With increasing field strength of the external magnetic field, magnetization of the domains increases, until a relatively homogenous magnetization of the bulk is reached. This behavior of the magnetic domains can be observed for both directions of magnetization. This process is illustrated in Figure 5.46, where c) to g) present one direction of magnetization and h) to l) depict the reversed direction.

The observations correspond well to the patterns observed by Jovičević-Klug et al. for martensitic AISI M2 steel [220]. According to them, they were the first to perform MOKE microscopy for martensitic stainless steels. In their studies, they used MOKE microscopy as a tool for analyzing microstructure and were able to detect retained austenite and assess the size and morphology of martensite laths. This potential of MOKE microscopy as a tool for microstructural characterization can also be recognized in the findings presented in this thesis, as the patterns observed in MOKE microscopy resemble the quenched and tempered microstructure of the steel observed in specimens etched by nital (Figure 5.45).

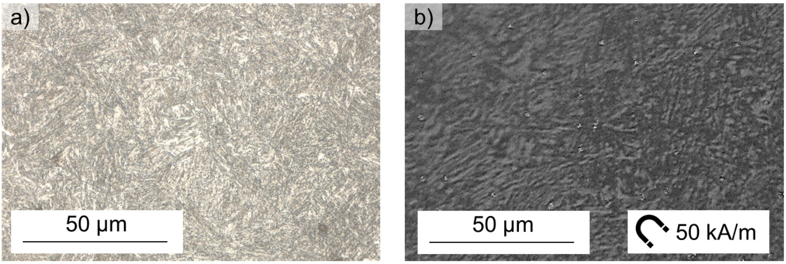

Figure 5.45 Comparison between micrographs of the bulk material obtained by microscopy: a) otpcial microscopy after nital etching; b) by magneto-optic Kerr effect (MOKE) microscopy (batch A)

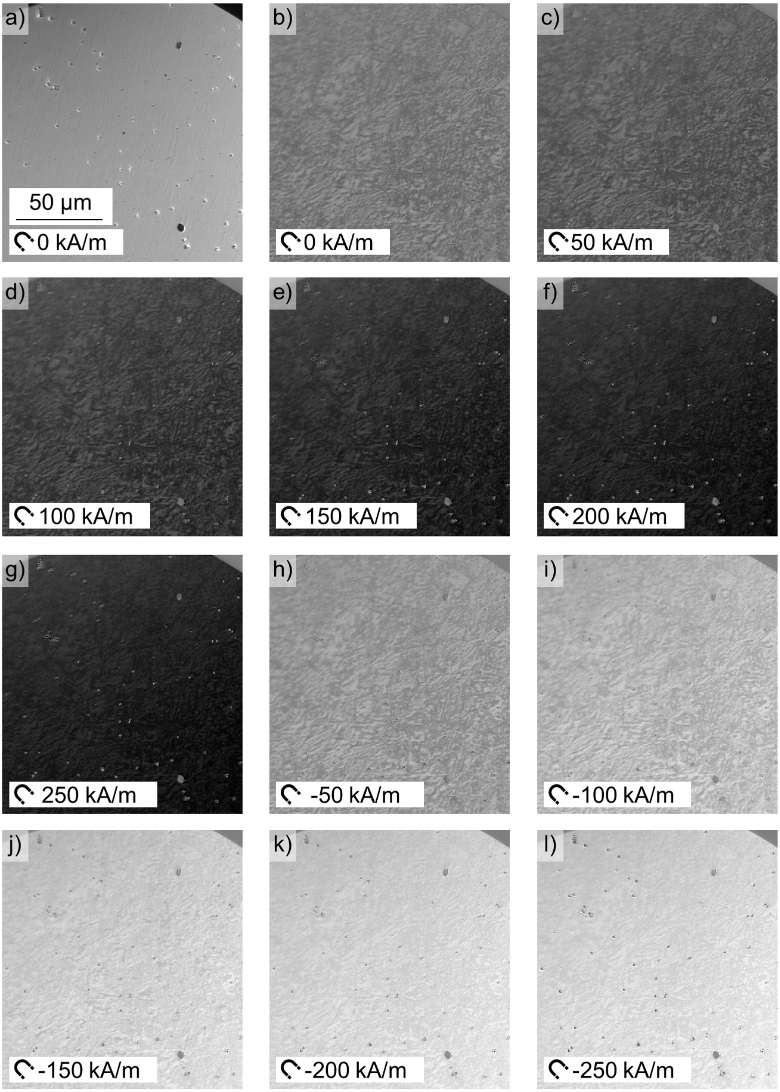

Figure 5.46 Magneto-optic Kerr effect (MOKE) microscopy for the bulk of a specimen, drilled at a cutting speed of $v_c = 80$ m/min and a feed of 0.150 mm; a) specimen before magnetization; b) remancence after magnetization; c)-g) magnezitation in one direction; h)-l) magnetization in the opposite direction (batch A)

Analyzing the subsurfaces of specimens with and without a WEL, it was found that the WEL significantly alters the magnetic microstructure in the subsurface of the bores. Exemplary results for two specimens with and without a WEL are presented in Figure 5.47 with prior magnetization, and in Figure 5.48 without prior magnetization of the specimens. The full set of images obtained when incrementally increasing the strength of the external magnetic field are presented in Figure 5.49 (specimen without WEL) and Figure 5.50 (specimen with WEL).

It can be seen that the WEL does not show any magnetic domain patterns in very close proximity to the surface of the specimen. The first domains can be detected at a distance of approx. $d_{surf} = 12$ µm to the surface (Figure 5.47 b). This distance matches the approximate thickness of the WEL (Figure 5.2). This observation also corresponds to the finding of the Bitter technique, in which no ferrofluid agglomerated in between the WEL and the coverslip. In addition to this, the shape of the magnetic domains adjacent to the WEL is remarkable, as these seem to be oriented parallel to the surface. Examples of this are indicated by arrows in Figure 5.47 and Figure 5.48. When increasing the field strength of the external magnetic field, it can be observed that the WEL stays free of magnetic domain patterns, regardless of the intensity of the external magnetic field applied to the specimen (Figure 5.48, Figure 5.50).

Analyzing the specimen free of WEL, the material close to the surface of the bore as well shows a different behavior compared to the bulk material. Domain patterns can be observed at the very surface of the specimen free of WEL. These seem larger, as less bright regions can be observed in close proximity to the surface (Figure 5.49 a).

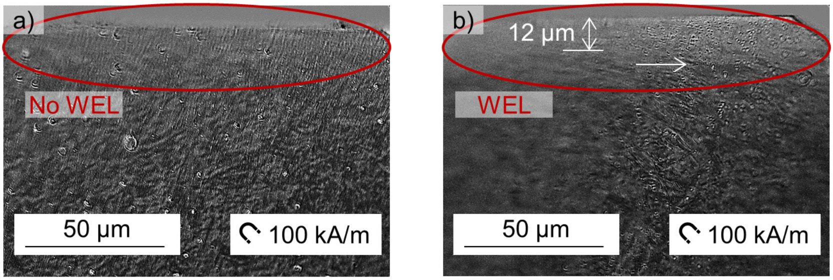

Figure 5.47 Magneto-optic Kerr effect microscopy (MOKE) microscopy after prior magnetization: a) a specimen without white etching layer (WEL) ($v_c = 80$ m/min; $f = 0.150$ mm); b) a specimen with WEL ($v_c = 100$ m/min; $f = 0.300$ mm) (batch A)

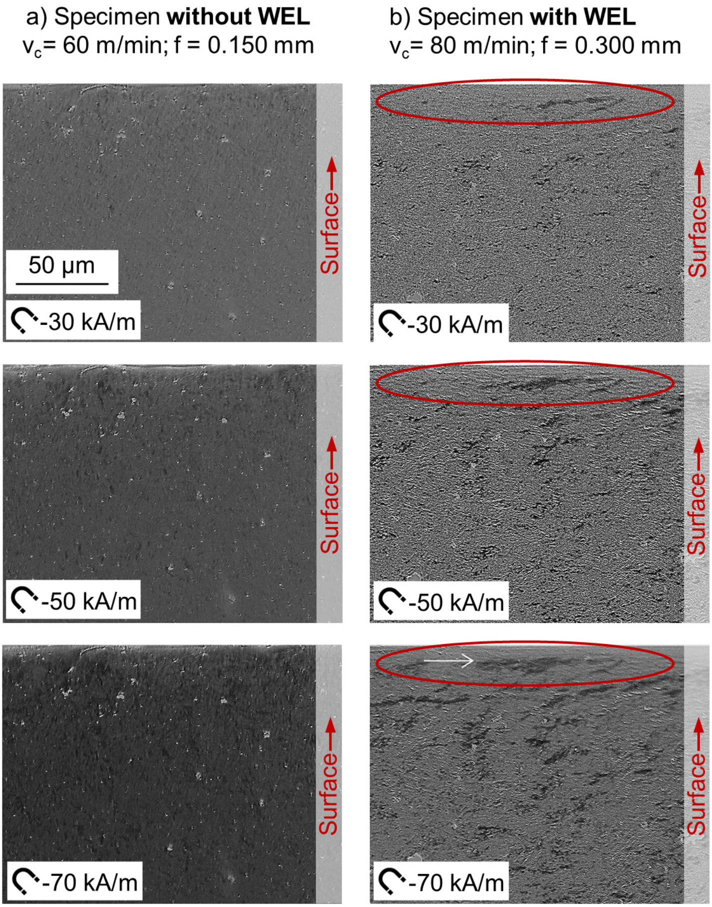

Figure 5.48 Evolution of the magnetic domains in magneto-optic Kerr effect (MOKE) microscopy without prior magnetization: a) a specimen without white etchinig layer (WEL) drilled at a cutting speed of v_c = 60 m/min and a feed of f = 0.150 mm; b) a specimen with WEL, drilled at a cutting speed of v_c = 80 m/min and a feed of f = 0.300 mm (batch A). Modified version of [198]

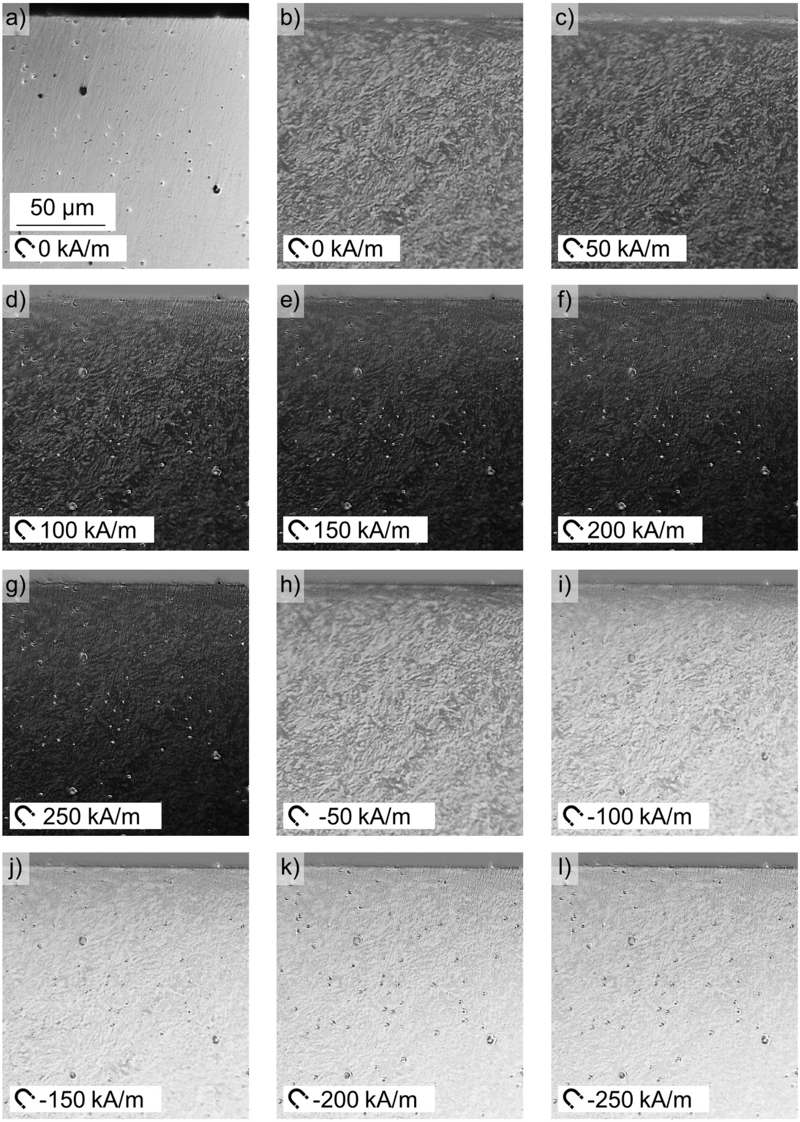

Figure 5.49 Magneto-optic Kerr effect (MOKE) microscopy for a specimen without white etching layer (WEL), drilled at a cutting speed of $v_c = 80$ m/min and a feed of 0.150 mm: a) specimen before magnetization; b) remancence after magnetization; c)-g) magnezitation in one direction; h)-l) magnetization in the opposite direction (batch A)

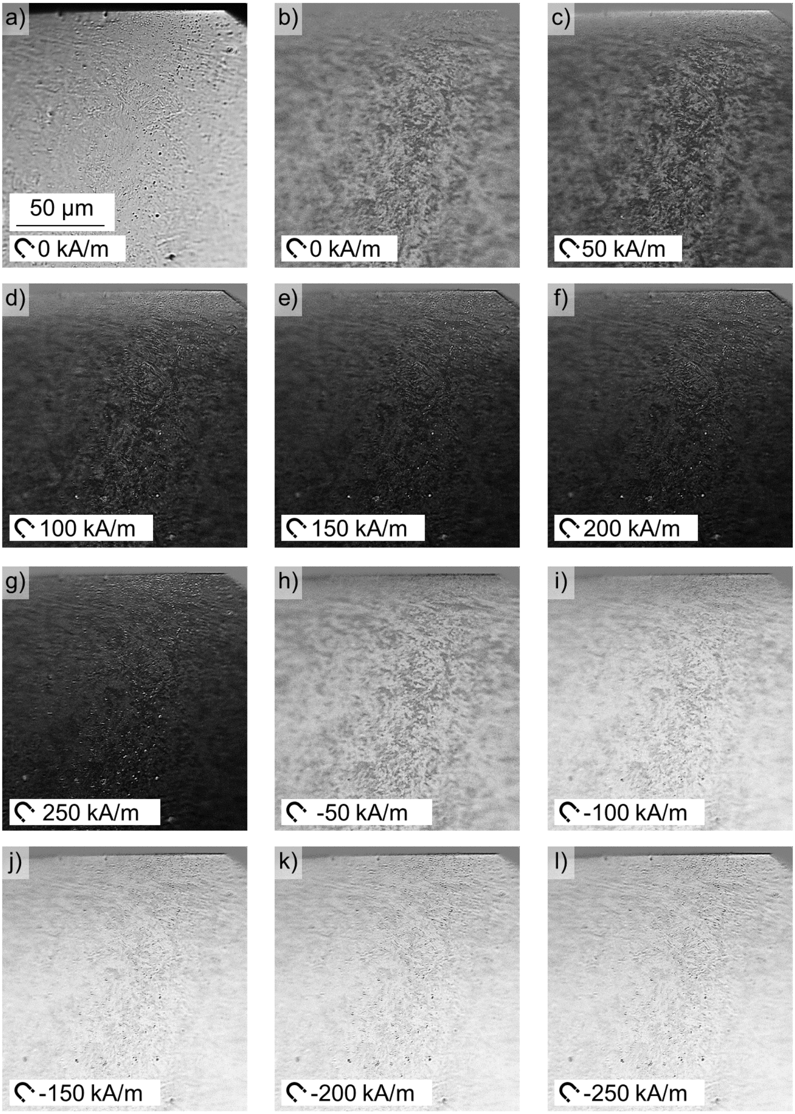

Figure 5.50 Magneto-optic Kerr effect (MOKE) microscopy for a specimen with white etching layer (WEL), drilled at a cutting speed of v_c = 100 m/min and a feed of 0.300 mm: a) specimen before magnetization; b) remancence after magnetization; c)-g) magnezitation in one direction; h)-l) magnetization in the opposite direction (batch A)

5.3.4 *Magnetic force microscopy (MFM)*

Similar to the modus operandi for the Bitter technique and MOKE microscopy, the magnetic microstructures inside the bulk material were characterized in the first step of MFM analyses. Compared to the two previously presented approaches for monitoring magnetic domains, MFM allows for a much higher lateral resolution. As the contrast between regions in a single image is the most crucial piece of information in MFM, scales are varied for the respective MFM images, to highlight the contrast between the domains as clearly as possible. Confronting the absolute values of phase shifts assessed in different images with each other can be misleading, as many factors, such as the offset have a significant impact on the absolute values in MFM.

Figure 5.51 presents exemplary results obtained for the bulk material of two specimens. Both images were obtained at a distance of $d_{surf} > 1000$ µm to the surface. Clear domain structures can be perceived in both of the images. These are relatively small and seem randomly distributed. The dark line on top of the image in Figure 5.51 b) results from errors in topography, for instance remaining OPS-particles on the surfaces. When such a flaw in topography was detected, the offset was increased to prevent any damage to the cantilever or the magnetic tip. When the topographic signal indicated an acceptable surface again, the offset was reduced to the initial value at the start of the scans. In general, the observations of MFM analyses of the bulk material are in good agreement with the results of the Bitter technique and MOKE microscopy, as no larger domain patterns were perceived and no regular structures of the domain patterns were found.

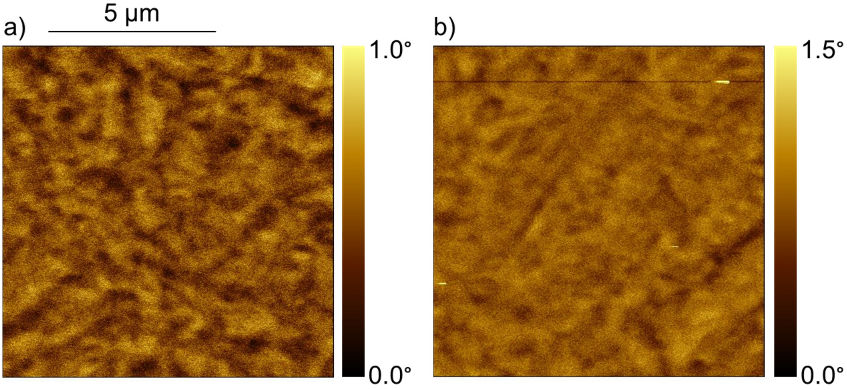

Figure 5.51 Magnetic force microscopy (MFM) images showing the domain structures inside the bulk material of two specimens: a) $v_c = 80$ m/min; $f = 0.150$ mm; b) $v_c = 80$ m/min; $f = 0.225$ mm (batch A)

In addition to the bulk material, domain patterns were analyzed in the subsurface of specimens. Exemplary results of these investigations are depicted in Figure 5.52 for a specimen free of WEL (a) and a specimen with WEL (b) at a distance to the surface of approx. $d_{surf} = 3$ µm. It can be observed that in the specimen with the WEL, no domain patterns can be identified at all in close proximity to the surface. Slight domain patterns start to show in a distance of approx. $d_{surf} = 8$ µm to the surface. Conversely to this observation, the specimen free of WEL reveals clear domain patterns with strong contrast on the entire region analyzed. Based on this observation, it can be concluded that no magnetic domains seem to exist inside the WEL, whereas in the specimen free of WEL clear domain patterns were already detected in a distance to the surface of $d_{surf} = 3$ µm. This corresponds to the previously presented findings of the Bitter technique and MOKE microscopy, which indicated the absence of magnetic domains inside the WEL in micrographs on a much larger scale. Whereas for specimens free of WEL these techniques evidenced the presence of domain patterns right at the surface of the specimens.

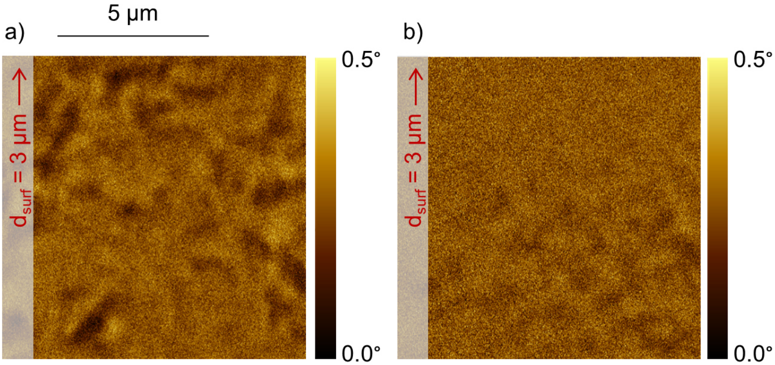

Figure 5.52 Magnetic force microscopy (MFM) of the subsurface: a) of a specimen without white etching layer (WEL), drilled at a cutting speed of $v_c = 60$ m/min and a feed of $f = 0.150$ mm; b) of a specimen with WEL, drilled at a cutting speed of $v_c = 80$ m/min and a feed of $f = 0.300$ mm (batch A). Modified version of [198]

To back up the findings presented in Figure 5.52 b), additional investigations were performed, analyzing a larger area of a specimen with WEL by MFM. This way a larger proportion of the conditioned subsurface was covered, assessing not only the WEL but also the material adjacent to it. The results of these investigations are presented in Figure 5.53. In a) a SEM image of the area analyzed is presented. The area scanned in MFM is highlighted by a red square. In the SEM image, the WEL appears featureless and has a thickness of approx. $t_{WEL} = 8$ µm. Assessing the thickness of WEL based on SEM images is particularly challenging, thus the given distance includes a relatively high uncertainty.

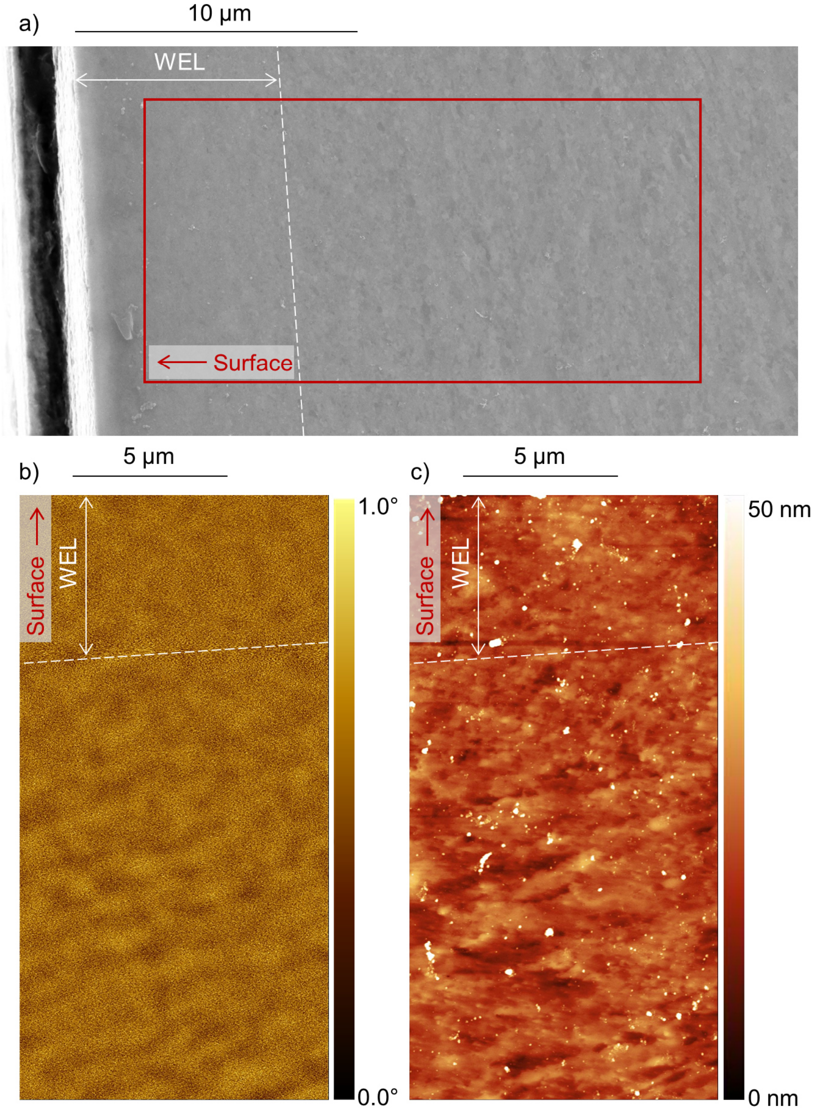

Figure 5.53 Subsurface of a specimen with a white etching layer (WEL), drilled at a cutting speed of v_c = 60 m/min and a feed of f = 0.300 mm: a) scanning electron microscopy (SEM) image; b) magnetic force microscopy (MFM) image; c) topography (batch A)

In Figure 5.53 b) the results of MFM are presented. These support the previously presented findings, as no clear domains can be observed within the WEL. In the material adjacent to the WEL, domain patterns can be visualized. This supports the validity of the measurements presented. In c) results of the topographic assessment during the first pass of the cantilever in tapping mode are presented. The surface shows relatively low roughness, with only a few flaws visible. These are most likely the remaining OPS particles. In Figure 5.54 the results of line scans of topography are presented. Three lines were evaluated. Their positioning is indicated in the top part of the figure. It can be seen that the surface is relatively smooth. The few isolated flaws have a height of approx. h = 40 nm. This size corresponds very well to the dimensions of OPS particles.

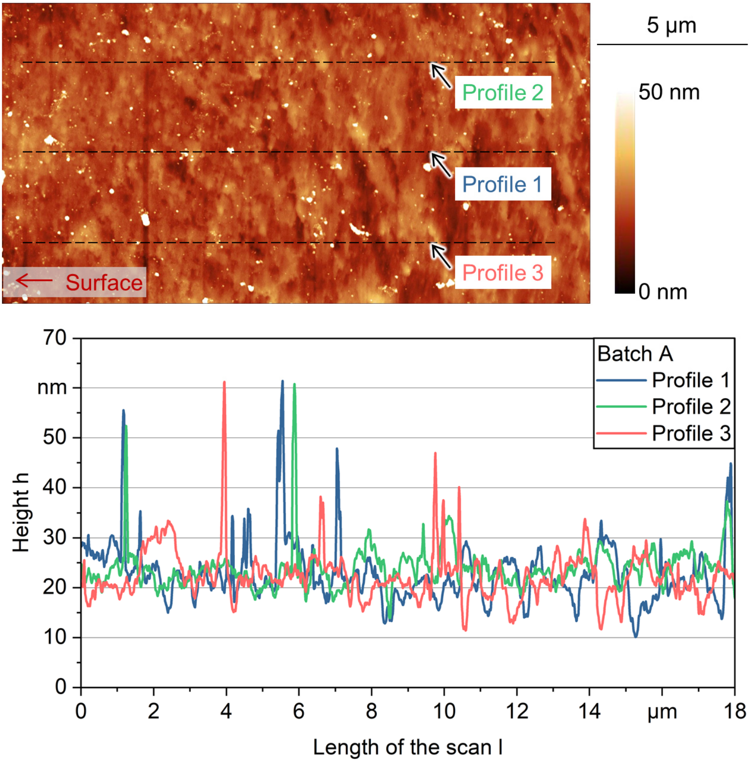

Figure 5.54 Topographic assessment of the subsurface of the specimen presented in the previous figure with a white etching layer (WEL), drilled at a cutting speed of v_c = 60 m/min and a feed of f = 0.300 mm, presenting three line-scans (batch A)

To support the previously presented finding on specimens without WEL, an additional specimen was analyzed at an even closer distance of $d_{surf} = 2$ µm to the surface. The findings presented in Figure 5.55 support the previously presented results, as also in this specimen clear domain patterns are observed in very close proximity to the surface.

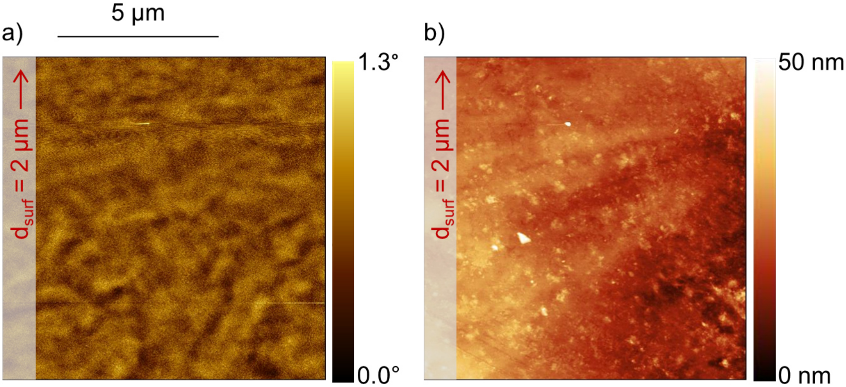

Figure 5.55 Magnetic force microscopy (MFM) of the subsurface of a specimen without white etching layer (WEL), drilled at a cutting speed of $v_c = 80$ m/min and a feed of $f = 0.150$ mm: a) MFM image; b) topography (batch A)

5.3.5 Concluding discussion of the magnetic microstructures

Based on the conclusions of the scale-bridging, multi-instrumental analysis of magnetic microstructures presented in the previous sections, the mechanisms governing domain wall motion are discussed in this section. For this purpose, the findings of the micromagnetic approaches are reviewed in close conjunction with the results of the extensive microstructural analyses presented in 5.2.3.

Dislocations act as pinning sites at which domain walls bend. Subsequently, domain walls have been found to gather in regions with high dislocation density [221]. In addition to this, dislocations act as nucleation sites for new domains [86]. Due to the change of crystallographic orientations at grain boundaries, these are well-known to be effective pinning sites as well [221]. Applying these interrelations to the findings presented in the previous chapters, the results obtained for the magnetic microstructures in the subsurfaces of bores seem plausible and consistent. The high amount of lattice defects, such as dislocations and stacking faults, and the high number of grain boundaries close to the surface of the deep drilled bores, as evidenced in the EBSD, ECCI, TKD, and STEM analyses (5.2.3), result in strong pinning of domain walls. This effect is particularly pronounced inside the WEL, for which a significantly higher number of grain boundaries, dislocations, and stacking faults is reported.

Consistent with these observations, the results of the Bitter technique, MOKE microscopy, and MFM all indicate that no regular domain patterns can be observed inside of WEL on either scale. Following the previous remarks on domain wall pinning, the reason for this absence of magnetic domains can most likely be found in a particularly strong pinning induced by the high amount of grain boundaries and lattice defects, such as dislocations and stacking faults.

In MBN analyses, significantly lower maximum MBN amplitudes were observed for specimens with WEL. These results are plausible and consistent with the other micromagnetic approaches, as it was discovered that the WEL barely contributes to the generation of MBN. MOKE microscopy provides evidence that even when applying external magnetic fields to specimens, the WEL remains free of perceivable domains. Subsequently also in the remanence state, no domains can be found inside the WEL. This provides an explanation for the observation that in addition to the maximum Barkhausen noise amplitude, also the Barkhausen noise amplitude at the remanence point allowed for distinguishing between specimens with and without WEL. Furthermore, these observations correspond to the evaluation of band-pass filter frequencies. The strongest differences between MBN amplitudes were observed for particularly high band-pass filter frequencies, which limit reading depth in MBN analysis to the very surface of specimens [81]. This agrees with the findings of the Bitter technique, MOKE microscopy, and MFM, which indicate that the strongest difference in the domain patterns of specimens with and without WEL can always be observed at the very surface of specimens.

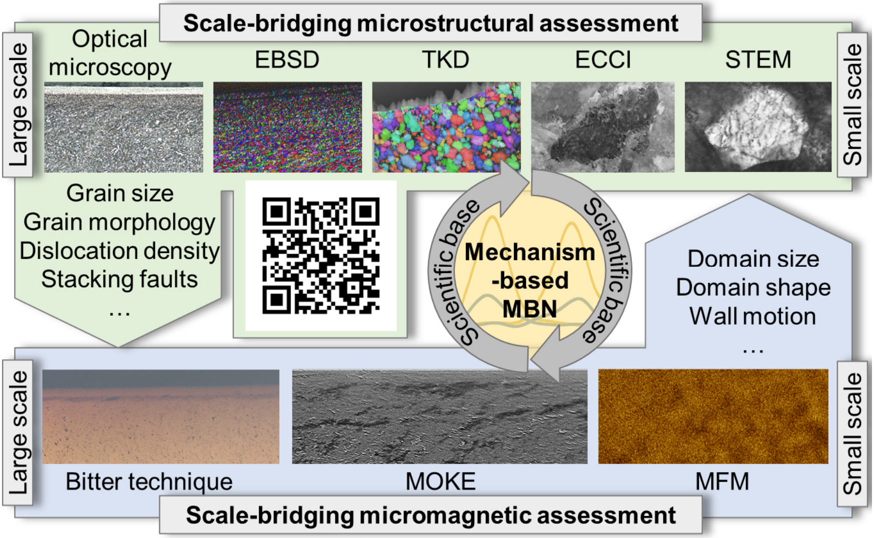

Figure 5.56 Mechanism-based magnetic Barkhausen noise (MBN) analysis through scale-bridging microstructural and micromagnetic assessment. The QR code links to an animation of the scale-bridging microstructure characterization [217]

5.4 Mechanical capability

In order to relate the previously presented findings on SI to the mechanical properties of the BTA deep drilled specimens, a test procedure was developed, which allows for quasi-static and cyclic compression testing. This procedure is inspired by the tube flattening test according to ISO 8492 and includes compression of the BTA deep drilled specimens until crack initiation is observed. To investigate the mechanisms governing deformation, the tests are instrumented. For instance, MBN and XRD analyses are performed intermittently in quasi-static and cyclic compression to assess the evolution of residual stresses induced by the deformation. In the upcoming sections, some exemplary results are presented for quasi-static (5.4.1) and cyclic compression (5.4.2).

5.4.1 Quasi-static compression

In an attempt to analyze the evolution of SI under quasi-static compression, a BTA deep drilled specimen was compressed to a displacement of $s_{QS} = 2$ mm, as this is approximately the limit of elastic deformation of the specimens [213]. Before and after compression, the specimen was characterized by means of XRD and MBN, according to the methods presented in 4.4 and 4.5. The results of these investigations are presented in Figure 5.57. It can be observed that prior to compression, significant compressive residual stresses in the range of $\sigma_{tang} = -910$ MPa to -370 MPa are present in the subsurface. After quasi-static compression to a displacement of $s_{QS} = 2$ mm, residual stresses up to $\sigma_{tang} = -90$ MPa were detected. The maximum MBN amplitude increases from an average of approx. $M_{max} = 6$ mV up to approx. 15 mV. Potential reasons for this increase in M_{max} might be found in the reduction of the intensity of compressive residual stresses. This correlation between residual stresses and MBN amplitudes has oftentimes been reported [85]. In addition to this, based on the observed relaxation of residual stresses, it seems plausible that the displacement resulted in a slight plastic deformation.

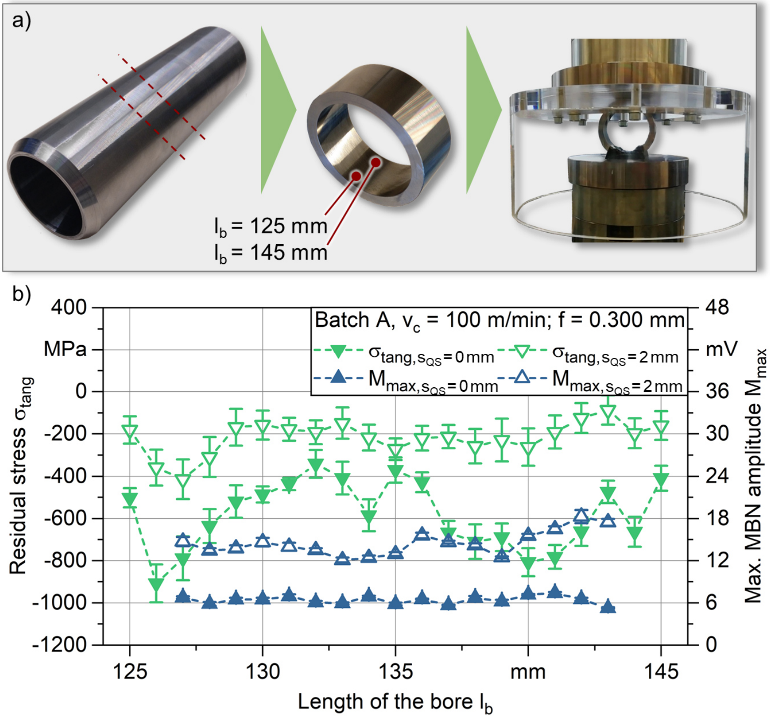

Figure 5.57 Intermittent characterization in quasi-static compression by magnetic Barkhausen noise (MBN) and X-ray diffraction (XRD) for a specimen drilled at a cutting speed of $v_c = 100$ m/min and a feed of $f = 0.300$ mm (batch A). Modified version of [207]

To analyze the impact of WEL on the quasi-static performance of the deep drilled specimens, three specimens with particularly low MBN amplitudes and four specimens with relatively high MBN amplitudes were assessed in quasi-static tests (Figure 5.58). The labeling of specimens in this figure and in Figure 5.59 is done according to the following scheme: Q stands for quasi-static test, whereas C indicates a constant amplitude test. The indices represent the feed in mm, the cutting speed in m/min and the length of the bore at which the specimen was extracted from. The length of the bore is indicated by A to E, with A being a specimen extracted at the start of the bore and E at the end of the bore. As SI varies significantly for the very start and the very end of bores, specimens were only extracted in the range of 30 mm < l_b <270 mm [207,208].

The MBN amplitudes were linked to the presence of WEL, following the correlations observed in 5.3.1. Metallographic spot checks confirmed the applicability of this MBN-based WEL prediction (Figure 5.58).

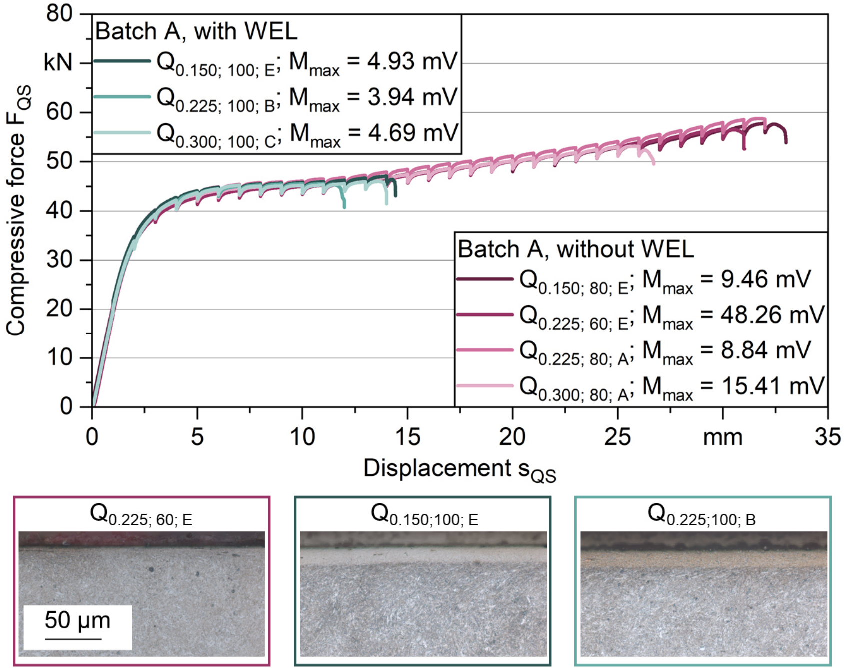

Figure 5.58 Impact of white etching layers (WEL) on the quasi-static performance of deep drilled specimens, drilled at varrying cutting speeds and feeds (batch A). Modified version of [207]

It was found that specimens with WEL show crack initiation at significantly lower displacements, compared to the specimens free of WEL. Specimens with WEL showed crack initiation at a displacement in the range of $s_{QS} = 12\text{-}14$ mm, whereas specimens free of WEL failed at significantly higher displacements in the range of $s_{QS} = 27\text{-}33$ mm [207]. The slight drops in the curves depicted result from pausing of the tests for intermittent measurements. This observation corresponds well to the hard and brittle nature of WEL. For fatigue loads, WEL are well known to promote crack initiation and propagation [56,141]. For instance, Herbert reports on WEL in nickel-based superalloys which reduced the fatigue life of specimens by more than 30 times [144].

5.4.2 Cyclic compression

In addition to quasi-static compression, cyclic compression was performed according to the methodology presented in 4.7.2. Intermittent to the fatigue tests, the subsurface of bores was characterized every 15,000 cycles by X-ray diffraction and every 5,000 cycles by MBN. An exemplary result of the investigations is presented in Figure 5.59, indicating the evolution of σ_{tang} and M_{max} with an increasing number of cycles. Additional results for cyclic testing can be found in [207].

Already in the first XRD results at 15,000 cycles, it can be observed that the residual stresses have evolved from approx. $\sigma_{tang} = -500$ MPa to approx. $\sigma_{tang} = -300$ MPa. In addition to this, in MBN analysis an increasing M_{max} is observed already after the first 5,000 cycles, indicating a relaxation of compressive residual stresses. Based on this observation it can be assumed that the residual stresses were altered already during the first few cycles.

After the initial relaxation, the residual stresses obtained by XRD as well as the M_{max} values stay relatively constant up until approx. 45,000 cycles. At this point, the values of M_{max} increase constantly up to 55,000 cycles and then drop again. In XRD, a strong increase of residual stresses was noted at 60,000 cycles, as the residual stresses rose up to approx. $\sigma_{tang} = 200$ MPa. Dye-penetrant testing revealed the formation of cracks at this stage. Analyzing the shift in M_{max}, it can be assumed that the major crack initiation started approx. in between 45,000 and 50,000 cycles, as a strong increase in M_{max} was registered at this point. Since slight increases were already observed at 30,000 cycles, it is plausible that microcrack formation started at this stage already. However, this hypothesizes is not supported by the XRD measurements. The slight increase in M_{max} at this stage might thus derive from other mechanisms. The drop in M_{max} after 55,000 cycles might result from geometrical effects due to the propagating cracks.

Based on the results presented, it can be concluded that MBN analysis is applicable for monitoring the evolution of residual stresses in the deep drilled specimens. This agrees to the findings of Baak [73]. He proposed MBN-based models for predicting and monitoring the evolution of residual stresses in single-lip deep drilled specimens, using the maximum MBN amplitude as well as the coercive field strength.

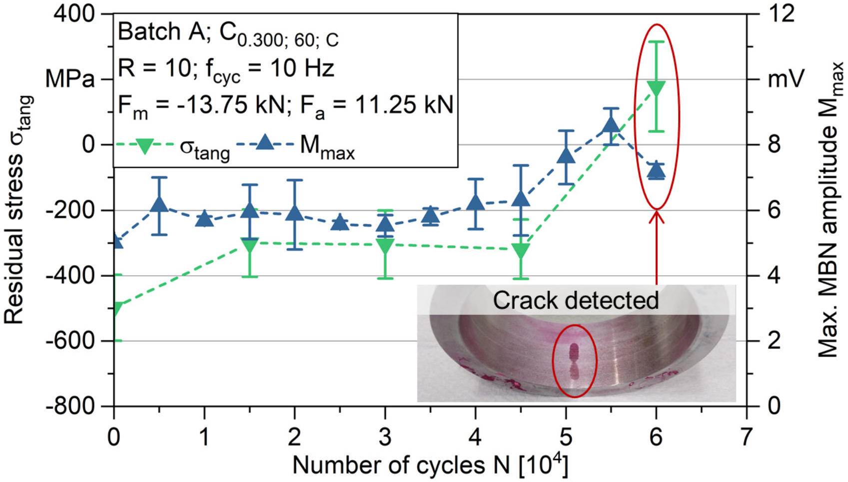

Figure 5.59 Evolution of residual stresses in constant amplitude tests of a specimen, drilled at a cutting speed of $v_c = 60$ m/min and a feed of $f = 0.300$ mm, assessed by magnetic Barkhausen noise (MBN) and X-ray diffraction (XRD) (batch A). Modified version of [207]

6 Summary

In this research work, a mechanism-based analysis of surface and subsurface conditioning in BTA deep hole drilling was presented. In the first step, the SI of deep drilled specimens was comprehensively analyzed. Results were provided, characterizing the microstructure, the microhardness, and the residual stress states in the subsurfaces.

It was found that the conditioning mechanisms in BTA deep hole drilling strongly depend on the selection of the cutting parameters. As it was observed that WEL form in drilling when using high cutting speeds and feeds, further in-depth analyses of the microstructure were performed. These aimed in particular at assessing the properties and structure of the WEL. EBSD provided evidence for severe plastic deformation in BTA deep hole drilling, which resulted in dynamic recrystallization. TKD was performed to validate the results of EBSD. In addition to this, ECCI and STEM were used to investigate further into the microstructural evolution during deep hole drilling. A particular focus was laid on the observation of lattice defects such as dislocations and stacking faults. In addition to these investigations, peak widths in XRD were analyzed, as they are particularly sensitive to grain size.

As the accessibility of the borehole wall is strongly limited, many of the conventional approaches for the evaluation of SI cannot be employed in a nondestructive way. Conversely to these, MBN analysis is based on particularly small sensors that can be positioned inside deep drilled boreholes. Thus, MBN is a highly promising approach for the nondestructive evaluation of SI in deep drilled components. As MBN is sensitive to multiple properties of materials, such as hardness, grain sizes, and residual stresses, calibration efforts are required. For this purpose, the previously obtained findings on the SI of deep drilled surfaces were complemented with a scale-bridging, multi-instrumental analysis of the magnetic microstructures and properties. The Bitter technique, MOKE microscopy, and MFM were used to determine the mechanisms governing MBN analysis on different scales.

The combined results of the extensive microstructural investigations in the first part of this work and the multi-instrumental micromagnetic evaluations presented in the second part, provide the scientific basis for a mechanism-based understanding of MBN analysis. For accurately performing MBN analysis inside of the BTA deep drilled specimens, an MBN-based, multi-sensory test stand was developed. This test stand is used to confront the results of different micromagnetic testing systems and various sensor geometries.

As the SI of a component has a major influence on its performance, capability, and life, a procedure was developed which allows for characterizing the mechanical properties of deep drilled specimens. Exemplary results are provided for specimens subjected to quasi-static and cyclic loads. Intermittently the evolution of residual stresses was assessed by XRD and MBN.

In the following sections, some of the key findings of this work are summarized. As the results obtained in the different fields are closely interconnected, they should be viewed in close conjunction.

Subsurface conditioning

A comprehensive analysis of SI in subsurfaces machined by BTA deep hole drilling was presented. Optical microscopy provided evidence that when using relatively high feed rates in combination with relatively high cutting speeds, WEL form in drilling. In large-scale micrographs of cross-sections extracted in the longitudinal direction, a periodicity in the thickness of the WEL was observed, which corresponded to the feed employed in drilling. In cross-sections extracted in the transverse direction, a periodicity in the thickness of WEL was perceived as well, resulting from the relative motion between the drill head and the specimen in drilling. EBSD analyses provided evidence of significantly refined grains close to the surface of the bores for specimens with WEL and specimens free of WEL. Specimens free of WEL revealed a grain size of $D_g = 346$ nm on average in the first $d_{surf} = 10$ µm below the surface. For specimens with WEL, an average grain size of $D_g = 272$ nm was observed in this region. Below this nanocrystalline layer, a severely deformed layer with swept grains and strong crystallographic texture was observed.

In microhardness mappings, WEL were found to have significantly high hardness, exceeding the hardness of the bulk material by more than three times. For instance, in a distance of $d_{surf} = 5$ µm to the surface of the bore, a microhardness of up to $H_m = 1340$ HV0.01 was reported on average for a specimen drilled at a cutting speed of $v_c = 100$ m/min, and a feed of $f = 0.225$ mm. Specimens free of WEL were found to have slightly increased hardness as well, resulting from work hardening. At the maximum depth of inspection of $d_{surf} = 80$ µm, the hardness observed still exceeded the hardness of the bulk material. This indicates that the effect of BTA deep hole drilling extends relatively deep into the subsurface.

The residual stresses were found to be predominantly in the compressive regime in both, axial and tangential directions. In the axial direction, exclusively compressive residual stresses were reported. In the tangential direction, evidence of moderate tensile residual stresses was provided for a few spots. Depth profiles of residual stresses revealed that the intensity of residual stresses significantly decreases after approx. $d_{surf} = 20$ µm.

Detection and assessment of white etching layers

The WEL observed in optical microscopy were further analyzed, using scale-bridging methods in optical microscopy, SEM, and XRD. To precisely assess the extent of WEL in micrographs of segments extracted in the longitudinal direction, a procedure was developed for a digital inspection of micrographs. This procedure consisted of the segmentation of the images, followed by an evaluation of the segmented images. The results were used for quantifying the periodicity of the WEL observed, as well as for identifying different shapes of WEL in the longitudinal direction.

As the nanocrystalline grain sizes observed were close to the lateral resolution of EBSD, the advanced crystallographic approaches of TKD, ECCI, and STEM were used to further investigate the microstructures underlying the WEL. Results of TKD showed good agreement with the grain sizes assessed by EBSD. For instance, an average grain size of $D_g = 260$ nm was reported for a specimen with WEL. Based on data obtained in XRD, average grain sizes were calculated using the Scherrer equation. It was found that the results of the Scherrer equation indicate much smaller grain sizes, than the actual measured grain sizes. Reasons for this can be found in additional sources of peak broadening, such as an increased dislocation density, stacking faults, and microstrains within the WEL. ECCI evidenced particularly high dislocation densities in the subsurface of deep drilled specimens with WEL. Grains were found to be surrounded by nanoscale grains. In addition to this, subgrains were observed. ECCI revealed significant voids and cracks inside the WEL at some locations of the WEL. Some cracks were observed at the interface in between the WEL and the deeper subsurface of the bulk. These cracks partly ran parallel to the surface of the bore. These observations correspond to the hard and brittle nature of the WEL, as WEL have been reported to promote crack initiation and propagation. In STEM-based investigations, the findings on grain sizes and dislocation densities of EBSD, TKD, and ECCI were confirmed. In addition to this, evidence was provided of stacking faults inside the WEL. Grains were identified that probably underwent austenitization during drilling.

The findings of the microstructural investigations correspond to the findings in the literature. Evidence was provided of severe plastic deformation in the subsurfaces of the deep drilled specimens, leading to dynamic recrystallization. The enormous amount of small-sized grains and lattice defects correspond to the observation in microhardness mappings.

Micromagnetic evaluation of surface integrity

In the scale-bridging, multi-instrumental micromagnetic evaluation of SI, MBN was qualified for nondestructively detecting WEL in the subsurfaces of BTA deep drilled components. Complementary micromagnetic approaches were used to analyze the mechanisms, governing MBN analysis.

Specimens without WEL revealed significantly higher maximum MBN amplitudes M_{max}, compared to specimens with WEL. In addition to this, the range of M_{max} was much higher for specimens free of WEL, compared to specimens with WEL. Similar correlations were observed for the MBN at the remanence point M_R. The use of higher band-pass filter frequencies resulted in an enhanced distinguishability between specimens with WEL and specimens free of WEL. The reason for this can probably be found in the reading depth in MBN analyses. As reading depth is particularly small when using high band-pass filter frequencies, the inspection is limited to the regions close to the surface. As these regions are also the parts of the subsurface where the differences between specimens with and without WEL are the strongest, it seems plausible that high band-pass filter frequencies lead to good distinguishability between the specimens.

None of the additional approaches indicated magnetic domain patterns inside the WEL. Conversely to this observation, strong domain patterns were observed close to the surfaces of specimens free of WEL. Domain structures were also revealed behind the WEL, further into the subsurface. In MOKE microscopy, evidence was provided that the WEL remains free of magnetic domains also during external magnetization. Based on this observation, it can be concluded that a major difference in the magnetic microstructures between specimens with WEL and specimens free of WEL can be found in the absence of magnetic domains inside WEL on either scale. As a result, it can be hypothesized that the low MBN detected for specimens with WEL resulted from the particularly low contribution of the WEL to the emission of MBN.

The MBN-based test stand allowed for comparing the systems FracDim and Rollscan 350 using multipurpose sensors and a custom-designed sensor that fits a BTA drill head. A good qualitative agreement was observed between the parameters RMS and M_{max} for Rollscan 350 and FracDim. Thus, it can be concluded, that the results obtained by FracDim are transferable to the Rollscan system. Using a custom-designed, miniaturized drill head sensor led to qualitatively similar results than using the multipurpose sensors. However, the scattering was much higher here. Reasons for this can be found in varying contact conditions and dimensions of the air gap in between the sensor and the surface. In contrast to the spring-loaded sensing elements of the multipurpose sensor, the BTA drill head sensor is designed for a small air gap in between the sensor and the surface.

Mechanical capability

Deep drilled specimens were subjected to quasi-static and cyclic loads, using the methodology developed in reference to the tube-flattening test. It was found that in quasi-static compression specimens with a WEL failed at significantly lower displacements compared to specimens free of WEL. It was shown that a displacement of s_{QS} = 2 mm leads to a relaxation of residual stresses in the subsurface of the specimens. This could be detected by XRD and was also indicated in the results of intermittent MBN analysis. In a constant amplitude test, it was observed that residual stresses relax during the first few cycles and then stay on a relatively constant level until crack initiation. Crack initiation was evidenced by dye-penetrant testing and could also be detected by MBN analysis.

7 Outlook: Enhanced Surface Integrity by Targeted Subsurface Conditioning

The findings presented in this thesis can be used in combination with the MBN-based test stand developed for characterizing the surface integrity in BTA deep drilled components in a fast, reliable, and nondestructive way. This way, WEL can be detected at the subsurface of deep drilled bores, without the need for time-consuming and destructive metallographic analyses by nital etching. This offers vast potential in terms of a more sustainable production. In addition to this, screening the properties of deep drilled components by MBN analysis can be performed to guarantee and even enhance SI, by a targeted, reliable subsurface conditioning for high-performance components.

In this context, the developed procedures will be used with the drill head sensor on the BTA deep hole drilling machine, to allow for assessing the SI right after machining the workpieces. This is illustrated in Figure 7.1. In the next step, an MBN-based closed-loop control will be implemented in BTA deep hole drilling. The aim of this closed-loop control is to monitor the surface integrity during machining. This way, when a detrimental alteration of SI is detected via the MBN sensor, the cutting speed and feed can be adjusted accordingly. A major challenge in these endeavors will be to reduce the relatively strong scattering resulting from the air gap between the sensor and the borehole wall.

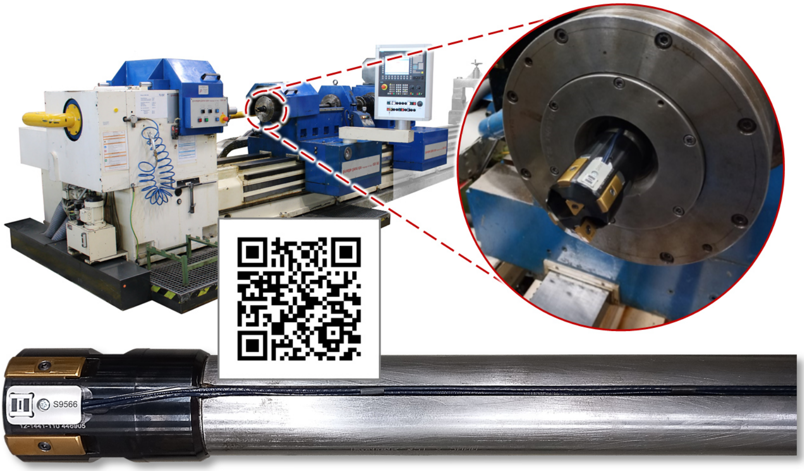

Figure 7.1 Instrumented drill head for MBN analysis mounted onto the boring bar in the deep drilling machine. The QR code links to an animation of the drill head sensor [222]

In addition to these intentions for targeted subsurface conditioning, it seems beneficial to transfer the micromagnetic approaches to the field of condition monitoring of BTA deep drilled components. As it was shown in 5.4, MBN analysis can be used to observe the evolution of residual stresses and the formation of cracks. In this context condition monitoring approaches based on MBN can be developed for example for inspecting landing gears of airplanes.

In the future, the robustness of the developed procedures for WEL detection can be improved by considering additional parameters in MBN analysis. Furthermore, additional workpiece geometries and steels should be tested.

In addition to the methods presented in this thesis for assessing the mechanical performance of deep drilled components, cyclic bending of BTA deep drilled specimens will be analyzed. A setup that was developed for performing such tests is depicted in Figure 7.2.

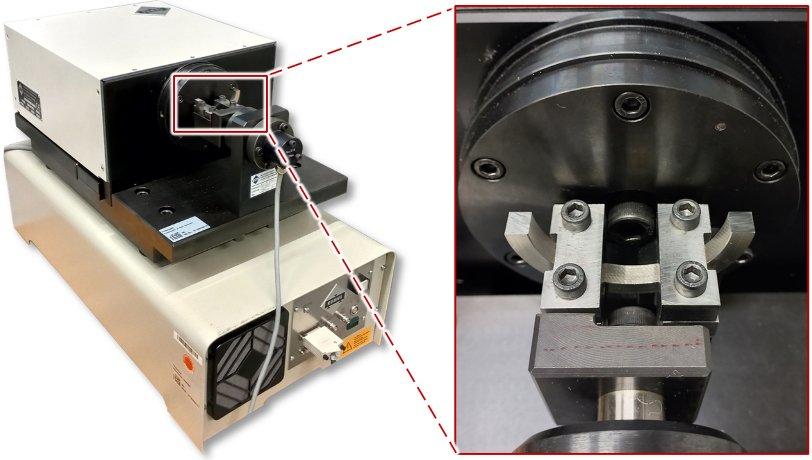

Figure 7.2 Setup developed for characterizing the BTA deep drilled specimens under cyclic bending loads, using the system Cracktronic (Russenberger Prüfmaschinen)

References

[1] United Nations Department for Economic and Social Affairs: The sustainable development goals report 2023. United Nations, New York, NY, 978-92-1-101460-0 (2023).

[2] International Energy Agency: Industry - sectoral overview. Tracking report - July 2023, https://www.iea.org/reports/industry (Checked: 15.11.2024).

[3] Tian, S.; Jiang, J.; Zhang, Z.; Manovic, V.: Inherent potential of steelmaking to contribute to decarbonisation targets via industrial carbon capture and storage. Nature communications 9, 1 (2018) 4422 doi:10.1038/s41467-018-06886-8.

[4] Ma, Y.; Bae, J.; Kim, S.-H.; Jovičević-Klug, M.; Li, K.; Vogel, D.; Ponge, D.; Rohwerder, M.; Gault, B.; Raabe, D.: Reducing iron oxide with ammonia: a sustainable path to green steel. Advanced science 10 (2023) e2300111 doi:10.1002/advs.202300111.

[5] Raabe, D.; Tasan, C.; Olivetti, E.: Strategies for improving the sustainability of structural metals. Nature 575, 7781 (2019) 64–74 doi:10.1038/s41586-019-1702-5.

[6] Allwood, J.; Cullen, J.: Sustainable materials. UIT Cambridge, Cambridge, 2012, ISBN 978-1906860059.

[7] IPCC: Climate change 2022: mitigation of climate change. Contribution of working group III to the sixth assessment report of the Intergovernmental Panel on Climate Change. IPCC, Cambridge, UK and New York, NY, USA (2022).

[8] Allwood, J.; Ashby, M.; Gutowski, T.; Worrell, E.: Material efficiency: a white paper. Resources, Conservation and Recycling 55, 3 (2011) 362–381 doi:10.1016/j.resconrec.2010.11.002.

[9] Allwood, J.: Unrealistic techno-optimism is holding back progress on resource efficiency. Nature materials 17, 12 (2018) 1050–1051 doi:10.1038/s41563-018-0229-8.

[10] La Monaca, A.; Murray, J.; Liao, Z.; Speidel, A.; Robles-Linares, J.; Axinte, D.; Hardy, M.; Clare, A.: Surface integrity in metal machining - Part II: Functional performance. International Journal of Machine Tools and Manufacture 164 (2021) 1–55 doi:10.1016/j.ijmachtools.2021.103718.

[11] Rech, J.; Hamdi, H.; Valette, S.: Workpiece surface integrity. In: Machining. Springer, London, (2008) 59–96 doi:10.1007/978-1-84800-213-5_3.

[12] Stampfer, B.; González, G.; Gerstenmeyer, M.; Schulze, V.: The present state of surface conditioning in cutting and grinding. Journal of Manufacturing and Materials Processing 5, 3 (2021) 1–17 doi:10.3390/jmmp5030092.

[13] Sasahara, H.: The effect on fatigue life of residual stress and surface hardness resulting from different cutting conditions of 0.45%C steel. International Journal of Machine Tools and Manufacture 45, 2 (2005) 131–136 doi:10.1016/j.ijmachtools.2004.08.002.

[14] Field, M.; Kahles, J.: The surface integrity of machined and ground high strength steels. DMIC Rep. 210 (1964) 54–77.

[15] Jawahir, I.; Schoop, J.; Kaynak, Y.; Balaji, A.; Ghosh, R.; Lu, T.: Progress toward modeling and optimization of sustainable machining processes. Journal of Manufacturing Science and Engineering 142, 11 (2020) doi:10.1115/1.4047926.

[16] Griffiths, B.: Manufacturing surface technology. Elsevier, 2001, ISBN 9781857180299 doi:10.1016/B978-1-85718-029-9.X5000-8.

[17] Brinksmeier, E.: Prozeß- und Werkstückqualität in der Feinbearbeitung. VDI-Verl., Düsseldorf, 1991, ISBN 9783181434024.

[18] Biermann, D.; Bleicher, F.; Heisel, U.; Klocke, F.; Möhring, H.-C.; Shih, A.: Deep hole drilling. CIRP Annals 67, 2 (2018) 673–694 doi:10.1016/j.cirp.2018.05.007.

[19] Li, B.; Huang, C.; Tang, Z.; Chen, Z.; Liu, H.; Chen, Z.; Niu, J.; Wang, Z.: Effect of drilling parameters on the hole surface integrity of low alloy steel for nuclear power during BTA deep hole drilling. The International Journal of Advanced Manufacturing Technology (2023) 1–13 doi:10.1007/s00170-023-11530-x.

[20] Holshouser, W.: Failure in aircraft parts made of ultra-high-strength steel. Journal of Failure Analysis and Prevention 22, 6 (2022) 2479–2486 doi:10.1007/s11668-022-01547-x.

[21] Cardon, M.: The marketing of Barkhausen noise analysis. The Shot Peener (2007) 18–20.

[22] Gauthier, J.; Krause, T.; Atherton, D.: Measurement of residual stress in steel using the magnetic Barkhausen noise technique. NDT & E International 31, 1 (1998) 23–31 doi:10.1016/S0963-8695(97)00023-6.

[23] Ktena, A.; Hristoforou, E.; Gerhardt, G.; Missell, F.; Landgraf, F.; Rodrigues, D.; Alberteris-Campos, M.: Barkhausen noise as a microstructure characterization tool. Physica B: Condensed Matter 435 (2014) 109–112 doi:10.1016/j.physb.2013.09.027.

[24] Astudillo, M.; Nicolás, M.; Ruzzante, J.; Gómez, M.; Ferrari, G.; Padovese, L.; Pumarega, M.: Correlation between martensitic phase transformation and magnetic Barkhausen noise of AISI 304 steel. Procedia Materials Science 9 (2015) 435–443 doi:10.1016/j.mspro.2015.05.014.

[25] Roskosz, M.; Fryczowski, K.; Schabowicz, K.: Evaluation of ferromagnetic steel hardness based on an analysis of the Barkhausen noise number of events. Materials (Basel, Switzerland) 13, 9 (2020) 1–17 doi:10.3390/ma13092059.

[26] Smithells, C.: Smithells metals reference book. Elsevier Science & Technology, Jordan Hill, 2003, ISBN 978-0-7506-7509-3.

[27] Verdeja González, J.; Fernández-González, D.; Verdeja González, L.: Physical metallurgy and heat treatment of steel. Springer International Publishing, Cham, 2023, ISBN 978-3-031-05701-4 doi:10.1007/978-3-031-05702-1.

[28] Pero-Sanz Elorz, J.; Fernández González, D.; Verdeja, L.: Structural Materials. Springer, Cham, 2019, ISBN 978-3-030-26160-3 doi:10.1007/978-3-030-26161-0.

[29] Angelo, P.; Ravisankar, B.: Introduction to steels. CRC Press Taylor & Francis Group, Boca Raton, London, New York, 2019, ISBN 9780429423598.

[30] Bargel, H.-J.; Schulze, G. (Hrsg.): Werkstoffkunde. Springer Vieweg, Berlin, Heidelberg, 2018 doi:10.1007/978-3-662-48629-0.

[31] Bergmann, W.: Werkstofftechnik 2. Hanser, München, 2009, ISBN 9783446417113.

[32] Hahn, F.: Werkstofftechnik-Praktikum. Fachbuchverl. Leipzig im Carl-Hanser-Verl., München, 2015, ISBN 978-3-446-44494-2.

[33] Hosford, W.: Iron and steel. Cambridge University Press, 2012 doi:10.1017/CBO9781139086233.

[34] Liedtke, D.; Hoferer, M.; Illgner, K.; Pirzl, N.; Stiele, H.: Wärmebehandlung von Eisenwerkstoffen. Expert Verlag, Renningen, 2017, ISBN 9783816934011.

[35] Weißbach, W.; Dahms, M.; Jaroschek, C.: Werkstoffe und ihre Anwendungen. Springer Vieweg, Wiesbaden, Heidelberg, 2018, ISBN 9783658198916.

[36] Khani Sanij, M.; Ghasemi Banadkouki, S.; Mashreghi, A.; Moshrefifar, M.: The effect of single and double quenching and tempering heat treatments on the microstructure and mechanical properties of AISI 4140 steel. Materials & Design 42 (2012) 339–346 doi:10.1016/j.matdes.2012.06.017.

[37] Berns, H.; Theisen, W.: Eisenwerkstoffe - Stahl und Gusseisen. Springer Berlin Heidelberg, Berlin, Heidelberg, 2008, ISBN 978-3-540-79955-9 doi:10.1007/978-3-540-79957-3.

[38] Wever, A.; Rose, A.: Atlas zur Wärembehandlung der Stähle. Verlag Stahleisen m. b. H., Düsseldorf, 1961.

[39] Macherauch, E.; Zoch, H.-W.: Praktikum in Werkstoffkunde. Springer Fachmedien Wiesbaden, Wiesbaden, 2014 doi:10.1007/978-3-658-05038-2.

[40] Klocke, F.: Zerspanung mit geometrisch bestimmter Schneide. Springer Vieweg, Berlin, 2018, ISBN 9783662542064.

[41] Liu, F.; Lin, X.; Song, M.; Yang, H.; Zhang, Y.; Wang, L.; Huang, W.: Microstructure and mechanical properties of laser solid formed 300M steel. Journal of Alloys and Compounds 621 (2015) 35–41 doi:10.1016/j.jallcom.2014.09.111.

[42] Boyer, R.; Cotton, J.; Mohaghegh; Schafrik, R.: Materials considerations for aerospace applications. MRS Bulletin, 40 (2015) 1055–1066 doi:10.1557/mrs.2015.278.

[43] Sahoo, G.; Singh, K.; Kumar, V.: Quenched and tempered high strength steel: a review. Journal of Metals, Materials and Minerals 4, 30 (2020) 19–29 doi:10.14456/jmmm.2020.47.

[44] Decker, K.-H.; Kabus, K.: Maschinenelemente. Hanser, München, 2018, ISBN 978-3-446-45029-5.

[45] Biermann, D.; Hartmann, H.; Terwey, I.; Merkel, C.; Kehl, D.: Turning of high-strength bainitic and quenched and tempered steels. Procedia CIRP 7 (2013) 276–281 doi:10.1016/j.procir.2013.05.047.

[46] Davim, J.: Surface integrity in machining. Springer London, London, 2010 doi:10.1007/978-1-84882-874-2.

[47] Field, M.; Kahles, J.; Cammett, J.: A review of measuring methods for surface integrity. Annals of the CIRP 21, 2 (1972) 219–238.

[48] M'Saoubi; R; Outeiro, J.; Chandrasekaran, H.; Jr., O.; Jawahir, I.: A review of surface integrity in machining and its impact on functional performance and life of machined products. International Journal of Sustainable Manufacturing 1, 1/2 (2008) 1–34 doi:10.1504/IJSM.2008.019234.

[49] Jawahir, I.; Brinksmeier, E.; M'Saoubi, R.; Aspinwall, D.; Outeiro, J.; Meyer, D.; Umbrello, D.; Jayal, A.: Surface integrity in material removal processes: recent advances. CIRP Annals 60, 2 (2011) 603–626 doi:10.1016/j.cirp.2011.05.002.

[50] Sales, W.; Schoop, J.; Da Silva, L.; Machado, Á.; Jawahir, I.: A review of surface integrity in machining of hardened steels. Journal of Manufacturing Processes 58 (2020) 136–162 doi:10.1016/j.jmapro.2020.07.040.

[51] Liao, Z.; La Monaca, A.; Murray, J.; Speidel, A.; Ushmaev, D.; Clare, A.; Axinte, D.; M'Saoubi, R.: Surface integrity in metal machining - Part I: Fundamentals of surface characteristics and formation mechanisms. International Journal of Machine Tools and Manufacture 162 (2021) 103687 doi:10.1016/j.ijmachtools.2020.103687.

[52] Astakhov, V.: Surface integrity – Definition and importance in functional performance. In: Davim, J. P. Surface Integrity in Machining, 1–35, Springer London, London, 2010 doi:10.1007/978-1-84882-874-2_1.

[53] Breidenstein, B.: Surface Integrity. In: Laperrière, Reinhart (Hg.) 2019 – CIRP Encyclopedia of Production Engineering, 1188–1199 doi:10.1007/978-3-642-20617-7_6600.

[54] Koster, W.; Field, M.; Kohls, J. et al. Manufacturing methods for surface integrity of machined structural components. Metcut research associates Inc. (1972).

[55] Varela, P.; Rakurty, C.; Balaji, A.: Surface integrity in hard machining of 300 M steel: effect of cutting-edge geometry on machining induced residual stresses. Procedia CIRP 13 (2014) 288–293 doi:10.1016/j.procir.2014.04.049.

[56] Brown, M.; Wright, D.; M'Saoubi, R.; McGourlay, J.; Wallis, M.; Mantle, A.; Crawforth, P.; Ghadbeigi, H.: Destructive and non-destructive testing methods for characterization and detection of machining-induced white layer: A review paper. CIRP Journal of Manufacturing Science and Technology 23 (2018) 39–53 doi:10.1016/j.cirpj.2018.10.001.

[57] Black, J.; Kohser, R.: DeGarmo's materials and processes in manufacturing. Wiley, Hoboken, 2019, ISBN 978-1-119-49296-2.

[58] Nickel, J.; Baak, N.; Volke, P.; Walther, F.; Biermann, D.: Thermomechanical impact of the single-lip deep hole drilling on the surface integrity on the example of steel components. Journal of Manufacturing and Materials Processing 5, 4 (2021) 1–13 doi:10.3390/jmmp5040120.

[59] Outeiro, J.: Residual stresses in machining. In: Mechanics of Materials in Modern Manufacturing Methods and Processing Techniques, 297–360, Elsevier, Amsterdam, 2020 doi:10.1016/B978-0-12-818232-1.00011-4.

[60] Stampfer, B.: Entwicklung eines multimodalen Prozessmodells zur Oberflächenkonditionierung beim Außenlängsdrehen von 42CrMo4. Dissertation. Shaker Verlag, Düren, 2022, ISBN 978-3-8440-8933-2.

[61] Maradudin, A. (Hrsg.): Light scattering and nanoscale surface roughness. Springer, New York, NY, 2007, ISBN 978-0387-25580-4.

[62] Dong, Y.: An overview of optical methods for in-process and on-line measurement of surface roughness. In: 2010 International Conference on Computer, Mechatronics, Control and Electronic Engineering, IEEE, 2010 doi:10.1109/CMCE.2010.5610235.

[63] Sackmann, D.; Heinzel, J.; Karpuschewski, B.: An approach for a reliable detection of grinding burn using the Barkhausen noise multi-parameter analysis. Procedia CIRP 87 (2020) 415–419 doi:10.1016/j.procir.2020.02.076.

[64] Goch, G.; Schmitz, B.; Karpuschewski, B.; Geerkens, J.; Reigl, M.; Sprongl, P.; Ritter, R.: Review of non-destructive measuring methods for the assessment of surface integrity: a survey of new measuring methods for coatings, layered structures and processed surfaces. Precision Engineering 23, 1 (1999) 9–33 doi:10.1016/S0141-6359(98)00021-X.

[65] Brinksmeier, E.: State-of-the-art of non-destructive measurement of subsurface material properties and damages. Precision Engineering 11, 4 (1989) 211–224 doi:10.1016/0141-6359(89)90031-7.

[66] Lucca, D.; Brinksmeier, E.; Goch, G.: Progress in assessing surface and subsurface Integrity. CIRP Annals 47, 2 (1998) 669–693 doi:10.1016/S0007-8506(07)63248-X.

[67] Teti, R.; Mourtzis, D.; D'Addona, D.; Caggiano, A.: Process monitoring of machining. CIRP Annals 71, 2 (2022) 529–552 doi:10.1016/j.cirp.2022.05.009.

[68] Schulze, V.; Zanger, F.; Stampfer, B.; Seewig, J.; Uebel, J.; Zabel, A.; Wolter, B.; Böttger, D.: Surface conditioning in machining processes. tm - Technisches Messen 87, 11 (2020) 661–673 doi:10.1515/teme-2020-0044.

[69] Schulze, V.; Aurich, J.; Jawahir, I.; Karpuschewski, B.; Yan, J.: Surface conditioning in cutting and abrasive processes. CIRP Annals 73, 2 (2024) 667–693 doi:10.1016/j.cirp.2024.05.004.

[70] Brinksmeier, E.; Gläbe, R.; Klocke, F.; Lucca, D.: Process signatures – an alternative approach to predicting functional workpiece properties. Procedia Engineering 19 (2011) 44–52 doi:10.1016/j.proeng.2011.11.078.

[71] Brinksmeier, E.; Meyer, D.; Heinzel, C.; Lübben, T.; Sölter, J.; Langenhorst, L.; Frerichs, F.; Kämmler, J.; Kohls, E.; Kuschel, S.: Process signatures - the missing link to predict surface integrity in machining. Procedia CIRP 71 (2018) 3–10 doi:10.1016/j.procir.2018.05.006.

[72] Aurich, J.; Schneider, F.; Mayer, P.; Kirsch, B.; Hasse, H.: Oberflächenerzeugungs-Morphologie-Eigenschafts-Beziehungen. Zeitschrift für wirtschaftlichen Fabrikbetrieb 111, 4 (2016) 213–216 doi:10.3139/104.111502.

[73] Baak, N.: Mikromagnetische Charakterisierung des Ermüdungsverhaltens und der Eigenspannungsrelaxation tiefgebohrter Proben des Vergütungsstahls 42CrMo4. Springer Fachmedien Wiesbaden, Wiesbaden, 2023 doi:10.1007/978-3-658-41679-9.

[74] Strodick, S.; Vogel, F.; Tilger, M.; Denstorf, M.; Kipp, M.; Baak, N.; Kukui, D.; Biermann, D.; Barrientos, M.; Walther, F.: Innovative X-ray diffraction and micromagnetic approaches for reliable residual stress assessment in deep rolled and microfinished AISI 4140 components. Journal of Materials Research and Technology 20 (2022) 2942–2959 doi:10.1016/j.jmrt.2022.07.168.

[75] Altpeter, I.; Tschuncky, R.; Szielasko, K.: Electromagnetic techniques for materials characterization. In: Hübschen, G., Altpeter, I., Tschuncky, R., Herrmann, H.-G. Materials characterization using nondestructive evaluation (NDE) methods, 225–262, Elsevier/WP Woodhead Publishing, Amsterdam, 2016 doi:10.1016/B978-0-08-100040-3.00008-0.

[76] Barkhausen, H.: Zwei mit Hilfe der neuen Verstärker entdeckte Erscheinungen. Physikalische Zeitschrift 20 (1919) 401–403.

[77] Wolter, B.; Gabi, Y.; Conrad, C.: Nondestructive testing with 3MA - an overview of principles and applications. Applied Sciences 9, 6 (2019) 1068 doi:10.3390/app9061068.

[78] Forschungsvereinigung Antriebstechnik e.V.: FVA 594 - Verfahrensanweisung Barkhausen. FVA e.V., Stresstech group, 2010.

[79] SAE International, AMS Committee K - Non Destructive Methods and Processes: Barkhausen noise inspection for detecting grinding burns in high strength steel parts ARP4462. Warrendale, PA, United States.

[80] Tomkowski, R.: The Barkhausen noise measurements good practice guide. KTH Royal Institute of Technology, 2022.

[81] Stupakov, A.; Neslušan, M.; Perevertov, O.: Detection of a milling-induced surface damage by the magnetic Barkhausen noise. Journal of Magnetism and Magnetic Materials 410 (2016) 198–209 doi:10.1016/j.jmmm.2016.03.036.

[82] Yamazaki, T.; Furuya, Y.; Nakao, W.: Experimental evaluation of domain wall dynamics by Barkhausen noise analysis in Fe30Co70 magnetostrictive alloy wire. Journal of Magnetism and Magnetic Materials 475 (2019) 240–248 doi:10.1016/j.jmmm.2018.11.011.

[83] Youssef, S.; Zimmer, C.; Szielasko, K.; Schütze, A.: Bewertung subjektiver und automatisierter Merkmalsextraktion periodischer Zeitsignale am Beispiel des 3MA-X8-Verfahrens. tm - Technisches Messen 86, 5 (2019) 267–277 doi:10.1515/teme-2018-0074.

[84] Szielasko, K.; Tschuncky, R.: Micromagnetic materials characterization. In: Ida, N., Meyendorf, N. Handbook of advanced nondestructive evaluation, 881–897, Springer International Publishing, Cham, 2019 doi:10.1007/978-3-319-26553-7_34.

[85] Baak, N.; Hajavifard, R.; Lücker, L.; Rozo Vasquez, J.; Strodick, S.; Teschke, M.; Walther, F.: Micromagnetic approaches for microstructure analysis and capability assessment. Materials Characterization 178 (2021) 111189 doi:10.1016/j.matchar.2021.111189.

[86] Santa-aho, S.; Honkanen, M.; Kaappa, S.; Azzari, L.; Saren, A.; Ullakko, K.; Laurson, L.; Vippola, M.: Multi-instrumental approach to domain walls and their movement in ferromagnetic steels – Origin of Barkhausen noise studied by microscopy techniques. Materials & Design 234 (2023) 112308 doi:10.1016/j.matdes.2023.112308.

[87] Wu, H.; Ziman, J.; Raghuraman, S.; Nebel, J.-E.; Weber, F.; Starke, P.: Short-time fatigue life estimation for heat treated low carbon steels by applying electrical resistance and magnetic Barkhausen noise. Materials (Basel, Switzerland) 16, 1 (2022) doi:10.3390/ma16010032.

[88] Augustyniak, B.; Chmielewski, M.; Piotrowski, L.: Review of recent achievements in stress state evaluation in technical element with Barkhausen effect. In: The 19th International Conference on Experimental Mechanics, 32, MDPI, Basel Switzerland, 2022 doi:10.3390/psf2022004032.

[89] Santa-aho, S.; Laitinen, A.; Sorsa, A.; Vippola, M.: Barkhausen noise probes and modelling: a review. Journal of Nondestructive Evaluation 38, 4 (2019) doi:10.1007/s10921-019-0636-z.

[90] Tschuncky, R.; Szielasko, K.; Altpeter, I.: Hybrid methods for materials characterization. In: Hübschen, G., Altpeter, I., Tschuncky, R., Herrmann, H.-G. Materials characterization using nondestructive evaluation (NDE) methods, 263–291, Elsevier/WP Woodhead Publishing, Amsterdam, 2016 doi:10.1016/B978-0-08-100040-3.00009-2.

[91] Jiles, D.: Introduction to magnetism and magnetic materials. Chapman and Hall/CRC, Boca Raton, 2015, ISBN 978-1-4822-3887-7.

[92] Brinksmeier, E.; Schneider, E.; Theiner, W.; Tönshoff, H.: Nondestructive testing for evaluating surface integrity. CIRP Annals 33, 2 (1984) 489–509 doi:10.1016/S0007-8506(16)30171-8.

[93] Cullity, B.; Graham, C.: Introduction to magnetic materials. IEEE Press; Wiley, Piscataway, NJ, Hoboken, NJ, 2009, ISBN 978-0-471-47741-9.

[94] Akagi, F.: Magnetic domain structures and techniques in micromagnetics simulation. In: Fujisaki, K. Magnetic material for motor drive systems. Engineering materials, 2021 doi:10.1007/978-981-32-9906-1.

[95] Moorthy, V.; Vaidyanathan, S.; Jayakumar, T.; Raj, B.: Microstructural characterization of quenched and tempered 0.2% carbon steel using magnetic Barkhausen noise analysis. Journal of Magnetism and Magnetic Materials 171, 1-2 (1997) 179–189 doi:10.1016/S0304-8853(97)00049-8.

[96] Neslušan, M.; Hrabovský, T.; Čilliková, M.; Mičietová, A.: Monitoring of hard milled surfaces via Barkhausen noise technique. Procedia Engineering 132 (2015) 472–479 doi:10.1016/j.proeng.2015.12.521.

[97] Baak, N.; Nickel, J.; Biermann, D.; Walther, F.: Barkhausen noise-based fatigue life prediction of deep drilled AISI 4140. Procedia Structural Integrity 18 (2019) 274–279 doi:10.1016/j.prostr.2019.08.164.

[98] Vértesy, G.; Gasparics, A.; Szenthe, I.; Rabung, M.; Kopp, M.; Griffin, J.: Analysis of magnetic nondestructive measurement methods for determination of the degradation of reactor pressure vessel steel. Materials (Basel, Switzerland) 14, 18 (2021) doi:10.3390/ma14185256.

[99] Alessandro, B.; Beatrice, C.; Bertotti, G.; Montorsi, A.: Domain-wall dynamics and Barkhausen effect in metallic ferromagnetic materials. Journal of Applied Physics 68, 6 (1990) 2908–2915 doi:10.1063/1.346424.

[100] Jiles, D.; Atherton, D.: Theory of ferromagnetic hysteresis. Journal of Magnetism and Magnetic Materials 61, 1-2 (1986) 48–60 doi:10.1016/0304-8853(86)90066-1.

[101] Jiles, D.; Sipahi, L.; Williams, G.: Modeling of micromagnetic Barkhausen activity using a stochastic process extension to the theory of hysteresis. Journal of Applied Physics 73, 10 (1993) 5830–5832 doi:10.1063/1.353541.

[102] Jiles, D.: Dynamics of domain magnetization and the Barkhausen effect. Czechoslovak Journal of Physics 50, 8 (2000) 893–924 doi:10.1023/A:1022846128461.

[103] Stupakov, A.; Perevertov, A.; Neslušan, M.: Reading depth of the magnetic Barkhausen noise. I. One-phase semi-hard ribbons. Journal of Magnetism and Magnetic Materials 513 (2020) 167086 doi:10.1016/j.jmmm.2020.167086.

[104] Stupakov, A.; Perevertov, A.; Neslušan, M.: Reading depth of the magnetic Barkhausen noise. II. Two-phase surface-treated steels. Journal of Magnetism and Magnetic Materials 513 (2020) 167239 doi:10.1016/j.jmmm.2020.167239.

[105] Hubert, A.; Schaefer, R.: Magnetic domains. The analysis of magnetic microstructures. Springer Berlin Heidelberg, Berlin, Heidelberg, 1998 doi:10.1007/978-3-540-85054-0.

[106] Bitter, F.: Experiments on the nature of ferromagnetism. Physical Review 41, 4 (1932) 507–515 doi:10.1103/PhysRev.41.507.

[107] Mee, C.: The mechanism of colloid agglomeration in the formation of Bitter patterns. Proceedings of the Physical Society. Section A 63, 8 (1950) 922 doi:10.1088/0370-1298/63/8/122.

[108] Tanasoiu, C.; Feldmann, D.; Schulz, I.: Eine neue trockene Bitter-Technik zur Beobachtung magnetischer Bereiche bis zur Grenze des lichtoptischen Auflösungsvermögens / A Dry Bitter Technique for High Resolution Studies of Magnetic Domains by Optical Microscopy. Practical Metallography 10, 4 (1973) 210–219 doi:10.1515/pm-1973-100402.

[109] Qiu, Z.; Bader, S.: Surface magneto-optic Kerr effect. Review of Scientific Instruments 71, 3 (2000) 1243–1255 doi:10.1063/1.1150496.

[110] Martin, Y.; Wickramasinghe, H.: Magnetic imaging by ‘‘force microscopy’’ with 1000 Å resolution. Applied Physics Letters 50, 20 (1987) 1455–1457 doi:10.1063/1.97800.

[111] Thomson, T.: Magnetic properties of metallic thin films. In: Metallic films for electronic, optical and magnetic applications (2014), 454–546 doi:10.1533/9780857096296.2.454.

[112] Röntgen, W.: Über eine neue Art von Strahlen. Annalen der Physik 300, 1 (1898) 12–17 doi:10.1002/andp.18983000103.

[113] Spieß, L.; Teichert, G.; Schwarzer, R.; Behnken, H.; Genzel, C.: Moderne Röntgenbeugung. Springer Fachmedien Wiesbaden, Wiesbaden, 2019, ISBN 978-3-8348-1219-3 doi:10.1007/978-3-8348-8232-5.

[114] Hossain, R.; Pahlevani, F.; Witteveen, E.; Banerjee, A.; Joe, B.; Prusty, B.; Dippenaar, R.; Sahajwalla, V.: Hybrid structure of white layer in high carbon steel - Formation mechanism and its properties. Scientific reports 7, 1 (2017) 13288 doi:10.1038/s41598-017-13749-7.

[115] Tanaka, K.; Akiniwa, Y.: Diffraction measurements of residual macrostress and microstress using X-rays, synchrotron and neutrons. JSME International Journal Series A 47, 3 (2004) 252–263 doi:10.1299/jsmea.47.252.

[116] González, G.; Plogmeyer, M.; Zanger, F.; Biehl, S.; Bräuer, G.; Schulze, V.: Effect of tool coatings on surface grain refinement in orthogonal cutting of AISI 4140 steel. Procedia CIRP 87 (2020) 176–180 doi:10.1016/j.procir.2020.02.113.

[117] Mustapha, S.; Ndamitso, M.; Abdulkareem, A.; Tijani, J.; Shuaib, D.; Mohammed, A.; Sumaila, A.: Comparative study of crystallite size using Williamson-Hall and Debye-Scherrer plots for ZnO nanoparticles. Advances in Natural Sciences: Nanoscience and Nanotechnology 10, 4 (2019) 1–8 doi:10.1088/2043-6254/ab52f7.

[118] Delbergue, D.; Texier, D.; Lévesque, M.; Bocher, P.: Comparison of two X-ray residual stress measurement methods: sin2 ψ and cos α, through the determination of a martensitic steel X-ray elastic constant. In: Proceedings of the 10th international conference on residual stresses (ICRS10), 55–60 doi:10.21741/9781945291173-10.

[119] Epp, J.: X-ray diffraction (XRD) techniques for materials characterization. In: Hübschen, G., Altpeter, I., Tschuncky, R., Herrmann, H.-G. Materials characterization using nondestructive evaluation (NDE) methods, 81–124, Elsevier/WP Woodhead Publishing, Amsterdam, 2016 doi:10.1016/B978-0-08-100040-3.00004-3.

[120] Tanaka, K.: The cosα method for X-ray residual stress measurement using two-dimensional detector. Mechanical Engineering Reviews 6, 1 (2019) 18-00378-18-00378 doi:10.1299/mer.18-00378.

[121] Strauß, T.: Ermittlung von fertigungsprozessbedingten Eigenspannungen bei komplexer Bauteilgeometrie. Dissertation. Karlsruher Institut für Technologie (KIT), Karlsruhe doi:10.5445/IR/1000034516.

[122] Scholtes, B. (Hrsg.): Eigenspannungen in mechanisch randschichtverformten Werkstoffzuständen. DGM-Informationsgesellschaft, Oberursel, 1991, ISBN 978-3-88355-170-8.

[123] Harrington, G.; Santiso, J.: Back-to-Basics tutorial: X-ray diffraction of thin films. Journal of Electroceramics 47, 4 (2021) 141–163 doi:10.1007/s10832-021-00263-6.

[124] He, B.: Two-dimensional X-ray diffraction. Wiley, Hoboken, NJ, 2018, ISBN 9781119356103.

[125] Scherrer, P.: Bestimmung der Größe und der inneren Struktur von Kolloidteilchen mittels Röntgenstrahlen. Nachrichten von der Gesellschaft der Wissenschaften, Göttingen. Mathematisch-Physikalische Klasse, 2 (1918) 98–100.

[126] Holzwarth, U.; Gibson, N.: The Scherrer equation versus the 'Debye-Scherrer equation'. Nature nanotechnology 6, 9 (2011) 534 doi:10.1038/nnano.2011.145.

[127] Eigenmann, B.; Macherauch, E.: Röntgenographische Untersuchung von Spannungszuständen in Werkstoffen Teil III. Materialwissenschaft und Werkstofftechnik 27, 9 (1996) 426–437 doi:10.1002/mawe.19960270907.

[128] Borrajo-Pelaez, R.; Hedström, P.: Recent Developments of Crystallographic Analysis Methods in the Scanning Electron Microscope for Applications in Metallurgy. Critical Reviews in Solid State and Materials Sciences 43, 6 (2018) 455–474 doi:10.1080/10408436.2017.1370576.

[129] Zaefferer, S.: A critical review of orientation microscopy in SEM and TEM. Crystal Research and Technology 46, 6 (2011) 607–628 doi:10.1002/crat.201100125.

[130] Keller, R.; Geiss, R.: Transmission EBSD from 10 nm domains in a scanning electron microscope. Journal of Microscopy 245, 3 (2012) 245–251 doi:10.1111/j.1365-2818.2011.03566.x.

[131] Geiss, R.; Keller, R.; Sitzman, S.; Rice, P.: New Method of Transmission Electron Diffraction to Characterize Nanomaterials in the SEM. Microscopy and Microanalysis 17, S2 (2011) 386–387 doi:10.1017/S1431927611002807.

[132] Geiss, R.; Keller, R.; Read, D.: Transmission Electron Diffraction From Nanoparticles, Nanowires and Thin Films in an SEM With Conventional EBSD Equipment. Microscopy and Microanalysis 16, S2 (2010) 1742–1743 doi:10.1017/S1431927610062227.

[133] Niessen, F.; Burrows, A.; Da Fanta, A.: A systematic comparison of on-axis and off-axis transmission Kikuchi diffraction. Ultramicroscopy 186 (2018) 158–170 doi:10.1016/j.ultramic.2017.12.017.

[134] Steinmetz, D.; Jäpel, T.; Wietbrock, B.; Eisenlohr, P.; Gutierrez-Urrutia, I.; Saeed–Akbari, A.; Hickel, T.; Roters, F.; Raabe, D.: Revealing the strain-hardening behavior of twinning-induced plasticity steels: Theory, simulations, experiments. Acta Materialia 61, 2 (2013) 494–510 doi:10.1016/j.actamat.2012.09.064.

[135] Gutierrez-Urrutia, I.; Zaefferer, S.; Raabe, D.: Electron channeling contrast imaging of twins and dislocations in twinning-induced plasticity steels under controlled diffraction conditions in a scanning electron microscope. Scripta Materialia 61, 7 (2009) 737–740 doi:10.1016/j.scriptamat.2009.06.018.

[136] Weidner, A.; Biermann, H.: Case studies on the application of high-resolution electron channelling contrast imaging – investigation of defects and defect arrangements in metallic materials. Philosophical Magazine 95, 7 (2015) 759–793 doi:10.1080/14786435.2015.1006296.

[137] Nellist, P.: Scanning Transmission Electron Microscopy. In: Hawkes, P. W., Spence, J. C. H. Springer Handbook of Microscopy, 49–99, Springer International Publishing, Cham, 2019 doi:10.1007/978-3-030-00069-1_2.

[138] Liu, J.: Scanning transmission electron microscopy and its application to the study of nanoparticles and nanoparticle systems. Journal of electron microscopy 54, 3 (2005) 251–278 doi:10.1093/jmicro/dfi034.

[139] Akcan, S.; Shah, W.; Moylan, S.; Chandrasekar, S.; Chhabra, P.; Yang, H.: Formation of white layers in steels by machining and their characteristics. Metallurgical and Materials Transactions A 33, 4 (2002) 1245–1254 doi:10.1007/s11661-002-0225-z.

[140] Arfaoui, S.; Zemzemi, F.; Tourki, Z.: Relationship between cutting process parameters and white layer thickness in orthogonal cutting. Materials and Manufacturing Processes 33, 6 (2018) 661–669 doi:10.1080/10426914.2017.1364849.

[141] Griffiths, B.; Furze, D.: Tribological advantages of white layers produced by machining. Journal of Tribology 109, 2 (1987) 338–342 doi:10.1115/1.3261363.

[142] Brown, M.; Crawforth, P.; M'Saoubi, R.; Larsson, T.; Wynne, B.; Mantle, A.; Ghadbeigi, H.: Quantitative characterization of machining-induced white layers in Ti–6Al–4V. Materials Science and Engineering: A 764 (2019) 138220 doi:10.1016/j.msea.2019.138220.

[143] Wusatowska-Sarnek, A.; Dubiel, B.; Czyrska-Filemonowicz, A.; Bhowal, P.; Ben Salah, N.; Klemberg-Sapieha, J.: Microstructural characterization of the white etching layer in Nickel-based superalloy. Metallurgical and Materials Transactions A 42, 12 (2011) 3813–3825 doi:10.1007/s11661-011-0779-8.

[144] Herbert, C.; Axinte, D.; Hardy, M.; Withers, P.: Influence of surface anomalies following hole making operations on the fatigue performance for a Nickel-based superalloy. Journal of Manufacturing Science and Engineering 136, 5 (2014) doi:10.1115/1.4027619.

[145] Du, J.; Liu, z.; Lv, S.: Deformation-phase transformation coupling mechanism of white layer formation in high speed machining of FGH95 Ni-based superalloy. Applied Surface Science 292 (2014) 197–203 doi:10.1016/j.apsusc.2013.11.111.

[146] Eyre, T.; Baxter, A.: The formation of white layers at rubbing surfaces. Tribology 5, 6 (1972) 256–261 doi:10.1016/0041-2678(72)90104-2.

[147] Fuß, H.: Aspekte zur Beeinflussung der Qualität von BTA-Tiefbohrungen. Dissertation. Technische Universität Dortmund, 1986.

[148] Griffiths, B.: White layer formations at machined surfaces and their relationship to white layer formations at worn Surfaces. Journal of Tribology 107, 2 (1985) 165–171 doi:10.1115/1.3261015.

[149] Zhang, B.; Shen, W.; Liu, Y.; Tang, X.; Wang, Y.: Microstructures of surface white layer and internal white adiabatic shear band. Wear 211, 2 (1997) 164–168 doi:10.1016/S0043-1648(97)00099-9.

[150] Guo, Y.; Sahni, J.: A comparative study of hard turned and cylindrically ground white layers. International Journal of Machine Tools and Manufacture 44, 2-3 (2004) 135–145 doi:10.1016/j.ijmachtools.2003.10.009.

[151] Bulpett, R.: The characterisation of white-etching layers formed on engineering steels. Ph. D. thesis, Brunel University, 1991.

[152] Zhang, F.; Duan, C.; Sun, W.; Ju, K.: Effects of cutting conditions on the microstructure and residual stress of white and dark layers in cutting hardened steel. Journal of Materials Processing Technology 266 (2019) 599–611 doi:10.1016/j.Jmatprotec.2018.11.038.

[153] Brown, M.; Ghadbeigi, H.; Crawforth, P.; M'Saoubi, R.; Mantle, A.; McGourlay, J.; Wright, D.: Non-destructive detection of machining-induced white layers in ferromagnetic alloys. Procedia CIRP 87 (2020) 420–425 doi:10.1016/j.procir.2020.02.065.

[154] Han, S.; Melkote, S.; Haluska, M.; Watkins, T.: White layer formation due to phase transformation in orthogonal machining of AISI 1045 annealed steel. Materials Science and Engineering: A 488, 1-2 (2008) 195–204 doi:10.1016/j.msea.2007.11.081.

[155] Barry, J.; Byrne, G.: TEM study on the surface white layer in two turned hardened steels. Materials Science and Engineering: A 325, 1-2 (2002) 356–364 doi:10.1016/S0921-5093(01)01447-2.

[156] Hosseini, S.; Klement, U.; Yao, Y.; Ryttberg, K.: Formation mechanisms of white layers induced by hard turning of AISI 52100 steel. Acta Materialia 89 (2015) 258–267 doi:10.1016/j.actamat.2015.01.075.

[157] Liao, Z.; Polyakov, M.; Diaz, O.; Axinte, D.; Mohanty, G.; Maeder, X.; Michler, J.; Hardy, M.: Grain refinement mechanism of nickel-based superalloy by severe plastic deformation - Mechanical machining case. Acta Materialia 180 (2019) 2–14 doi:10.1016/j.actamat.2019.08.059.

[158] Poulachon, G.; Albert, A.; Schluraff, M.; Jawahir, I.: An experimental investigation of work material microstructure effects on white layer formation in PCBN hard turning. International Journal of Machine Tools and Manufacture 45, 2 (2005) 211–218 doi:10.1016/j.ijmachtools.2004.07.009.

[159] Mehmedović, M.; Ekinović, S.; Šarić, E.; Butković, S.: Methodology for the white layer formation on the machined surface during longitudinal turning of hardened steels. In: TMT 2013 – Proceedings of the 17th conference on trends in the development of machinery and associated technology.

[160] Ramesh, A.; Melkote, S.; Allard, L.; Riester, L.; Watkins, T.: Analysis of white layers formed in hard turning of AISI 52100 steel. Materials Science and Engineering: A 390, 1-2 (2005) 88–97 doi:10.1016/j.msea.2004.08.052.

[161] Zemzemi, F.; Khochtali, H.; Salem, W.; Alzahrani, B.; Bouazizi, M.-L.: Analytical multi-physics model of microstructure changes in hard turning of AISI 52100 steel: prediction of thicknesses of white and dark layers. International Journal of Advanced Manufacturing Technology 112, 9-10 (2021) 2755–2771 doi:10.1007/s00170-020-06521-1.

[162] Cappellini, C.; Attanasio, A.; Rotella, G.; Umbrello, D.: Formation of white and dark layers in hard cutting: influence of tool wear. International Journal of Material Forming 3, S1 (2010) 455–458 doi:10.1007/s12289-010-0805-1.

[163] Zhang, H.; Ohsaki, S.; Mitao, S.; Ohnuma, M.; Hono, K.: Microstructural investigation of white etching layer on pearlite steel rail. Materials Science and Engineering: A 421, 1-2 (2006) 191–199 doi:10.1016/j.msea.2006.01.033.

[164] Griffiths, B.: An investigation in the role of the burnishing pads in the deep hole drilling process. Thesis, 1982.

[165] Brown, M.; Curtis, D.; McKee, G.; Crawforth, P.: An evaluation of non-destructive methods for detection of thermally-induced metallurgical machining defects. Procedia CIRP 108 (2022) 7–12 doi:10.1016/j.procir.2022.03.007.

[166] Brown, M.; Pieris, D.; Wright, D.; Crawforth, P.; M'Saoubi, R.; McGourlay, J.; Mantle, A.; Patel, R.; Smith, R.; Ghadbeigi, H.: Non-destructive detection of machining-induced white layers through grain size and crystallographic texture-sensitive methods. Materials & Design 200 (2021) 109472 doi:10.1016/j.matdes.2021.109472.

[167] Brown, M.; Crawforth, P.; Curtis, D.: Rapid non-destructive sizing of microstructural surface integrity features using x-ray diffraction. NDT & E International 131 (2022) 102682 doi:10.1016/j.ndteint.2022.102682.

[168] Zhang, F.; Duan, C.; Sun, W.; Ju, K.: Influence of white layer and residual stress induced by hard cutting on wear resistance during sliding Friction. Journal of Materials Engineering and Performance 28, 12 (2019) 7649–7662 doi:10.1007/s11665-019-04479-0.

[169] Koster, W.; Field, M.; Fritz, L.; Gatto, L.; Kahles, J.: Surface integrity of machined structural components. U.S. Air Force technical report AFML-TR-70-11. Metcut Research Associates Inc, Cincinnati, Cincinnati, OH, 1972.

[170] Chou, Y.; Evans, C.: White layers and thermal modeling of hard turned surfaces. International Journal of Machine Tools and Manufacture 39, 12 (1999) 1863–1881 doi:10.1016/S0890-6955(99)00036-X.

[171] VDI-Richtlinie 3210: Norm "Tiefbohrverfahren". Beuth Verlag, Berlin, 2006.

[172] Nickel, J.: Analyse und Modellierung der thermomechanischen Beeinflussung der Randzoneneigenschaften beim Einlippentiefbohren von Bauteilen aus Vergütungsstahl. Dissertation. Vulkan-Verlag GmbH, Essen, 2023, ISBN 978-3-8027-8924-3.

[173] Frazao, J.; Chandrashekhar, S.; Osman, M.; Sankar, T.: On the design and development of a new BTA tool to increase productivity and workpiece accuracy in deep hole machining. The International Journal of Advanced Manufacturing Technology 1, 4 (1986) 3–23 doi:10.1007/BF02601457.

[174] Abrahams, H.; Biermann, D.: Untersuchungen zum Führungsleistenverschleiß und zur Prozessdynamik beim BTA-Tiefbohren austenitischer Stähle. Dissertation. Vulkan-Verlag GmbH, Essen, 2016, ISBN 978-3-8027-8792-8.

[175] Rao, P.; Shunmugam, M.: Investigations into surface topography, microhardness and residual stress in Boring Trepanning Association machining. Wear 119, 1 (1987) 89–100 doi:10.1016/0043-1648(87)90100-1.

[176] Richardson, R.; Bhatti, R.: A review of research into the role of guide pads in BTA deep-hole machining. Journal of Materials Processing Technology 110, 1 (2001) 61–69 doi:10.1016/S0924-0136(00)00733-0.

[177] Schmidt, R.; Strodick, S.; Walther, F.; Biermann, D.; Zabel, A.: Influence of the process parameters and forces on the bore sub-surface zone in BTA deep-hole drilling of AISI 4140 and AISI 304 L. Procedia CIRP 87 (2020) 41–46 doi:10.1016/j.procir.2020.02.010.

[178] Schwersenz, A.; Erli, R.; Nawal, K.; Biermann, D.; Michel, S.; Schmidt, R.; Wiesweg, L.: P21 - Contactless torque measurement in BTA/STS deep hole drilling by using the Villari Effect – a first proof of concept. In: Poster, 320–321, AMA Service GmbH, Von-Münchhausen-Str. 49, 31515 Wunstorf, Germany, 2023 doi:10.5162/SMSI2023/P21.

[179] Schmidt, R.; Brause, L.; Strodick, S.; Walther, F.; Biermann, D.; Zabel, A.: Measurement and analysis of the thermal load in the bore subsurface zone during BTA deep hole drilling. Procedia CIRP 107 (2022) 375–380 doi:10.1016/j.procir.2022.04.061.

[180] Gerken, J.; Klages, N.; Biermann, D.; Denkena, B.: Development and analysis of a mechatronic system for in-process monitoring and compensation of straightness deviation in BTA deep hole drilling. Mechanical Systems and Signal Processing 170 (2022) 108838 doi:10.1016/j.ymssp.2022.108838.

[181] Biermann, D.; Abrahams, H.; Goeke, S.: Optimization of guide pads for the BTA deep hole drilling of high alloyed steels by microfinishing. Production Engineering 8, 1-2 (2014) 33–40 doi:10.1007/s11740-013-0505-z.

[182] Biermann, D.; Kessler, N.; Upmeier, T.; Stucky, T.: Modified DLC-coated guide pads for BTA deep hole drilling tools. Key Engineering Materials 438 (2010) 195–202 doi:10.4028/www.scientific.net/KEM.438.195.

[183] Zhang, H.; Shen, X.; Bo, A.; Li, Y.; Zhan, H.; Gu, Y.: A multiscale evaluation of the surface integrity in boring trepanning association deep hole drilling. International Journal of Machine Tools and Manufacture 123 (2017) 48–56 doi:10.1016/j.ijmachtools.2017.07.005.

[184] Li, X.; Zhai, C.; He, W.; Lu, Y.; Zhang, B.: Experimental investigation of tool wear and machining quality of BTA deep-hole drilling in low-carbon alloy steel SA-5083. Materials 16, 20 (2023) 6686 doi:10.3390/ma16206686.

[185] Matsuzaki, K.; Ryu, T.; Sueoka, A.; Tsukamoto, K.: Theoretical and experimental study on rifling mark generating phenomena in BTA deep hole drilling process (generating mechanism and countermeasure). International Journal of Machine Tools and Manufacture 88 (2015) 194–205 doi:10.1016/j.ijmachtools.2014.10.003.

[186] Griffiths, B.: Problems in measuring the topography of machined surfaces produced by plastic deformation mechanisms. Wear 109, 1-4 (1986) 195–205 doi:10.1016/0043-1648(86)90264-4.

[187] Milella, P.: Fatigue and corrosion in metals. Springer, Milan, Heidelberg, 2013, ISBN 978-88-470-2335-2.

[188] Lancaster, J.: Engineering catastrophes. CRC Press; Woodhead Publ, Boca Raton, Fla., Cambridge, 2005, ISBN 978-1-84569-016-8.

[189] Radaj, D.; Vormwald, M.: Ermüdungsfestigkeit. Springer, Berlin, Heidelberg, 2007 doi:10.1007/978-3-540-71459-0.

[190] Christ, H.-J. (Hrsg.): Ermüdungsverhalten metallischer Werkstoffe. Werkstoff-Informationsgesellschaft, Frankfurt Main, 1998, ISBN 3-88355-262-3.

[191] Suresh, S.: Fatigue of materials. Cambridge University Press, 2012, ISBN 9780521570466 doi:10.1017/CBO9780511806575.

[192] Lee, Y.-L.; Pan, J.; Hathaway, R.: Fatigue testing and analysis. Elsevier textbooks, s.l., 2004, ISBN 0-7506-7719-8.

[193] Starke, P.; Walther, F.; Eifler, D.: PHYBAL—A new method for lifetime prediction based on strain, temperature and electrical measurements. International Journal of Fatigue 28, 9 (2006) 1028–1036 doi:10.1016/j.ijfatigue.2005.07.050.

[194] Acosta, R.; Wu, H.; Sridaran Venkat, R.; Weber, F.; Tenkamp, J.; Walther, F.; Starke, P.: SteBLife, a new approach for the accelerated generation of metallic materials' fatigue data. Metals 10, 6 (2020) 798 doi:10.3390/met10060798.

[195] He, X.; Chen, J.; Tian, W.; Li, Y.; Jin, W.: Low cycle fatigue behavior of steam generator tubes under axial loading. Materials (Basel, Switzerland) 11, 10 (2018) doi:10.3390/ma11101944.

[196] Cristea, M.; Beretta, S.; Altamura, A.: Fatigue limit assessment on seamless tubes in presence of inhomogeneities: small crack model vs. full scale testing experiments. International Journal of Fatigue 41 (2012) 150–157 doi:10.1016/j.ijfatigue.2012.01.022.

[197] Audino, M.; Bendick, J.; Keating, J. et al. Fatigue life assessment of 155-mm M776 cannon tubes. US army armament research, development and engineering center (1999).

[198] Strodick, S.; Schmidt, R.; Donnerbauer, K.; Rozo Vasquez, J.; Zabel, A.; Macias Barrientos, M.; Biermann, D.; Walther, F.: Subsurface conditioning in BTA deep hole drilling for improved component performance. Production Engineering, 18 (2024) 299–317 doi:10.1007/s11740-023-01252-0.

[199] Berteld, K.: Charakterisierung der Mikrostruktur und Mikrohärte im Bereich der Bohrungsrandzone BTA-tiefgebohrter Probekörper aus 42CrMo4+QT und X2CrNi18-9, Project work, TU Dortmund University, 2020.

[200] Dong, X.: Characterization of the properties of white etching layers (WEL) in BTA deep drilled AISI 4140, Project work, TU Dortmund University, 2024.

[201] Hühn, F.: Charakterisierung der Eigenspannungsänderung in der Bohrungsrandzone BTA-tiefgebohrter Bauteile unter quasistatischer und zyklischer Verformung, Bachelor thesis, TU Dortmund University, 2022.

[202] Nickel, T.: Konzeptionierung, Entwicklung und Erprobung einer Vorrichtung zur exakten Positionierung und Führung mikromagnetischer Sensoriken in Tiefbohrungen, Project work, TU Dortmund University, 2024.

[203] Fuß, M.: Entwicklung eines Verfahrens zur Herstellung von tiefen nicht kreisförmigen Bohrungen, Dissertation, TU Dortmund University, 2019.

[204] Zabel, A.; Strodick, S.; Schmidt, R.; Walther, F.; Biermann, D.; Wegert, R.; Eisseler, R.; Möhring, H.-C.; Guski, V.; Schmauder, S.: Oberflächenkonditionierung beim Tiefbohren – Teil 1/Surface conditioning in deep hole drilling. wt Werkstattstechnik online 111, 01-02 (2021) 52–58 doi:10.37544/1436-4980-2021-01-02-56.

[205] Schmidt, R.; Strodick, S.; Walther, F.; Biermann, D.; Zabel, A.: Tool design for the integration of piezoelectric and micro magnetic sensors to realize in-process measurements in BTA deep hole drilling. Procedia CIRP 119 (2023) 408–413 doi:10.1016/j.procir.2023.06.196.

[206] Oezkaya, E.; Bücker, M.; Strodick, S.; Biermann, D.: A thermomechanical analysis leading to a novel flank face design providing longer tool lives for tools used in the drilling of Inconel 718. The International Journal of Advanced Manufacturing Technology 102, 9-12 (2019) 2977–2992 doi:10.1007/s00170-019-03417-7.

[207] Strodick, S.; Hühn, F.; Schmidt, R.; Biermann, D.; Zabel, A.; Walther, F.: Evolution of the residual stress state in BTA deep drilled components under quasi-static and cyclic loading. In: Proceedings of the 11th International Conference on Residual Stresses, 1–8.

[208] Strodick, S.; Schmidt, R.; Zabel, A.; Biermann, D.; Walther, F.: Evaluation of surface integrity after BTA deep-hole drilling of AISI 4140 by means of Barkhausen noise analysis. Proceedings of the 13th international conference on Barkhausen noise and micromagnetic testing (2019) 1–7.

[209] Strodick, S.; Berteld, K.; Schmidt, R.; Biermann, D.; Zabel, A.; Walther, F.: Influence of cutting parameters on the formation of white etching layers in BTA deep hole drilling. tm - Technisches Messen 87, 11 (2020) 674–682 doi:10.1515/teme-2020-0046.

[210] Strodick, S.; Steffens, D.; Walther, F.; Schmidt, R.; Zabel, A.; Biermann, D.: Towards reliable micromagnetic detection of white etching layers in deep drilled quenched and tempered steels. Proceedings of the 5th Symposium Materialtechnik (2023) 1–14 doi:10.21268/20230711-9.

[211] Strodick, S.; Schmidt, R.; Zabel, A.; Biermann, D.; Walther, F.: Automatic diagnosis and thickness determination for white etching layers in deep drilled steels based on thresholding and machine learning algorithms. Procedia CIRP 123 (2024) 30–35 doi:10.1016/j.procir.2024.05.008.

[212] Strodick, S.; Kröger, T.; Walther, F.: An animation of a test stand for the micromagnetic evaluation of surface integrity in deep hole drilled components - Supplementary material for S. Strodick: Scale-bridging micromagnetic evaluation of surface integrity and conditioning mechanisms in deep hole drilled AISI 4140 steel. https://doi.org/10.17877/tudodata-2024-m0nsoipx (2024).

[213] Strodick, S.; Schmidt, R.; Gerdes, L.; Zabel, A.; Biermann, D.; Walther, F.: Impact of cutting parameters on the mechanical properties of BTA deep drilled components under quasi-static compression. Procedia CIRP 103 (2021) 207–212 doi:10.1016/j.procir.2021.10.033.

[214] Huang, X.; Schmidt, R.; Strodick, S.; Walther, F.; Biermann, D.; Zabel, A.: Simulation and modeling of the residual stress state in the sub-surface zone of BTA deep-hole drilled specimens with eigenstrain theory. Procedia CIRP 102 (2021) 150–155 doi:10.1016/j.procir.2021.09.026.

[215] Sakai, T.; Belyakov, A.; Kaibyshev, R.; Miura, H.; Jonas, J.: Dynamic and post-dynamic recrystallization under hot, cold and severe plastic deformation conditions. Progress in Materials Science 60 (2014) 130–207 doi:10.1016/j.pmatsci.2013.09.002.

[216] Fischer, A.; Scholtes, B.; Niendorf, T.: Influence of deep rolling and induction hardening on microstructure evolution of crankshaft sections made from 38MnSiVS5 and 42CrMo4. HTM Journal of Heat Treatment and Materials 76, 3 (2021) 175–194 doi:10.1515/htm-2021-0002.

[217] Strodick, S.; Kröger, T.; Donnerbauer, K.; Kukui, D.; Walther, F.: An animation of scale-bridging microstructure characterization in deep hole drilled AISI 4140 steel - Supplementary material for S. Strodick: Scale-bridging micromagnetic evaluation of surface integrity and conditioning mechanisms in deep hole drilled AISI 4140 steel. https://doi.org/10.17877/tudodata-2024-m0ns1mhl (2024).

[218] Dille, J.; Pacheco, C.; Camerini, C.; Malet, L.; Nysten, B.; Pereira, G.; Almeida, L. de; Alcoforado Rebello, J.: Influence of heat treatments on microstructure and magnetic domains in duplex stainless steel S31803. Metallurgical and Materials Transactions A 49, 8 (2018) 3515–3524 doi:10.1007/s11661-018-4721-1.

[219] Batista, L.; Rabe, U.; Altpeter, I.; Hirsekorn, S.; Dobmann, G.: On the mechanism of nondestructive evaluation of cementite content in steels using a combination of magnetic Barkhausen noise and magnetic force microscopy techniques. Journal of Magnetism and Magnetic Materials 354 (2014) 248–256 doi:10.1016/j.jmmm.2013.11.019.

[220] Jovičević-Klug, M.; Jovičević-Klug, P.; McCord, J.; Podgornik, B.: Investigation of microstructural attributes of steel surfaces through magneto-optical Kerr effect. Journal of Materials Research and Technology 11 (2021) 1245–1259 doi:10.1016/j.jmrt.2021.01.106.

[221] Honkanen, M.; Santa-aho, S.; Laurson, L.; Eslahi, N.; Foi, A.; Vippola, M.: Mimicking Barkhausen noise measurement by in-situ transmission electron microscopy - effect of microstructural steel features on Barkhausen noise. Acta Materialia 221 (2021) 117378 doi:10.1016/j.actamat.2021.117378.

[222] Strodick, S.; Kröger, T.; Walther, F.: An animation of a BTA drill head equipped with a micromagnetic sensor - Supplementary material for S. Strodick: Scale-bridging micromagnetic evaluation of surface integrity and conditioning mechanisms in deep hole drilled AISI 4140 steel. https://doi.org/10.17877/tudodata-2024-m0nru8ta (2024).

Student works

The following student works were supervised by the author in the framework of this dissertation:

- Berteld, K.: Charakterisierung der Mikrostruktur und Mikrohärte im Bereich der Bohrungsrandzone BTA-tiefgebohrter Probekörper aus 42CrMo4+QT und X2CrNi18-9. Project work, TU Dortmund University (2020).
- Kröger, T.: Entwicklung und Erprobung von Auswertealgorithmen zur Analyse von Wirbelstromsignalen. Project work, TU Dortmund University (2021).
- Hühn, F.: Charakterisierung der Eigenspannungsänderung in der Bohrungsrandzone BTA-tiefgebohrter Bauteile unter quasistatischer und zyklischer Verformung. Bachelor thesis, TU Dortmund University (2022).
- Steffens, D.: Einfluss von Schnittgeschwindigkeit, Vorschub und Werkzeugbeschichtung auf die Surface Integrity in der Bohrungsrandzone BTA-tiefgebohrter Probekörper aus 42CrMo4+QT. Project work, TU Dortmund University (2022).
- Gasch, N.: Charakterisierung der Surface Integrity in der Bohrungsrandzone BTA-tiefgebohrter Probekörper aus 42CrMo4+QT, Project work, TU Dortmund University (2024).
- Dong, X.: Microstructure and properties characterization of white etching layers (WEL) in BTA deep drilled AISI 4140, Project work, TU Dortmund University (2024).
- Nickel, T.: Konzeptionierung, Entwicklung und Erprobung einer Vorrichtung zur exakten Positionierung und Führung mikromagnetischer Sensoriken in Tiefbohrungen. Project work, TU Dortmund University (2024).

Publications and presentations

The following articles were published by the author in the framework of this dissertation:

- Strodick, S.; Schmidt, R.; Zabel, A.; Biermann, D.; Walther, F.: Automatic diagnosis and thickness determination for white etching layers in deep drilled steels based on thresholding and machine learning algorithms. Procedia CIRP 123, (2024) 30-35.
  https://doi.org/10.1016/j.procir.2024.05.008
- Strodick, S.; Schmidt, R.; Donnerbauer, K.; Rozo Vasquez, J.; Zabel, A.; Macias Barrientos, M.; Biermann, D.; Walther, F.: Subsurface conditioning in BTA deep hole drilling for improved component performance. Production Engineering 18, 2 (2024) 299–317.
  https://doi.org/10.1007/s11740-023-01252-0
- Strodick, S.; Steffens, D.; Schmidt, R.; Zabel, A.; Biermann, D.; Walther, F.: Towards reliable micromagnetic detection of white etching layers in deep drilled quenched and tempered steels. 5. Symposium Materialtechnik, (2023) 1-14.
  https://doi.org/10.21268/20230711-9
- Strodick, S.; Hühn, F. R.; Schmidt, R.; Biermann, D.; Zabel, A.; Walther, F.: Evolution of the residual stress state in BTA deep drilled components under quasi-static and cyclic loading. ICRS 11, Proceedings of the 11th International Conference on Residual Stresses (2023) 1-8.
  https://hal.science/hal-04022501
- Strodick, S.; Schmidt, R.; Brause, L.; Zabel, A.; Biermann, D.; Walther, F.: Mikromagnetische Charakterisierung der Bohrungsintegrität. wt Werkstattstechnik online 112, 11/12 (2022) 757-761.
  https://doi.org/10.37544/1436-4980-2022-11-12-31
- Strodick, S.; Schmidt, R.; Biermann, D.; Zabel, A.; Walther, F.: Influence of the cutting edge on the surface integrity in BTA deep hole drilling - part 2: Residual stress, microstructure and microhardness. Procedia CIRP 108 (2022) 276-281.
  https://doi.org/10.1016/j.procir.2022.03.047
- Strodick, S.; Schmidt, R.; Gerdes, L.; Zabel, A.; Biermann, D.; Walther, F.: Impact of cutting parameters on the mechanical properties of BTA deep drilled components under quasi-static compression. Procedia CIRP 103 (2021) 207-212.
  https://doi.org/10.1016/j.procir.2021.10.033
- Strodick, S.; Berteld, K.; Schmidt, R.; Biermann, D.; Zabel, A.; Walther, F.: Influence of cutting parameters on the formation of white etching layers in BTA deep hole drilling. Technisches Messen 87 (11) (2020) 674-682.
  https://doi.org/10.1515/teme-2020-0046

- Strodick, S.; Schmidt, R.; Zabel, A.; Biermann, D.; Walther, F.: Evaluation of surface integrity after BTA deep-hole drilling of AISI 4140 by means of Barkhausen noise analysis. ICBM 13, Proceedings of the 13th International Conference on Barkhausen Noise and Micromagnetic Testing (2019) 1-7.
- Strodick, S.; Walther, F.; Schmidt, R.; Zabel, A.; Biermann, D.: Analyse des Eigenspannungszustands in der Bohrungsrandzone tiefgebohrter Probekörper aus 42CrMo4+QT und X5CrNi18-10. Werkstoffprüfung 2019 - Fortschritte in der Werkstoffprüfung für Forschung und Praxis, Hrsg.: H.-J. Christ (2019) 287-292.

The following presentations were given by the author in the framework of this dissertation:

- Strodick, S. (Sp.); Schmidt, R.; Zabel, A.; Biermann, D.; Walther, F.: Automatic diagnosis and thickness determination for white etching layers in deep drilled steels based on thresholding and machine learning algorithms. CIRP CSI 2024, 7th CIRP Conference on Surface Integrity, Bremen, 14.-17. May (2024).
- Strodick, S. (Sp.); Steffens, D.; Schmidt, R.; Biermann, D.; Zabel, A.; Walther, F.: Towards reliable micromagnetic detection of white etching layers in deep drilled quenched and tempered steels. 5. Symposium Materialtechnik des Clausthaler Zentrums für Materialtechnik, Clausthal-Zellerfeld, 23.-24. Feb. (2023).
- Strodick, S. (Sp.); Schmidt, R.; Zabel, A.; Biermann, D.; Walther, F.: Micromagnetic monitoring of the surface integrity for BTA deep hole drilling. ICBM 14, 14th International Conference on Barkhausen Noise and Micromagnetic Testing, Stockholm, Sweden, 27.-30. Sept. (2022).
- Strodick, S. (Sp.); Schmidt, R.; Biermann, D.; Zabel, A.; Walther, F.: Influence of the cutting edge on the surface integrity in BTA deep hole drilling - part 2: Residual stress, microstructure and microhardness. CIRP CSI 2022, 6th CIRP Conference on Surface Integrity, Lyon, 08.-10. June (2022).
- Strodick, S. (Sp.); Hühn, F. R.; Schmidt, R.; Zabel, A.; Biermann, D.; Walther, F.: Evolution of the residual stress state in BTA deep-drilled components under quasi-static and cyclic loading. ICRS 11, 11th International Conference on Residual Stresses, Web Conference, 27.-30. Mar. (2022).
- Strodick, S. (Sp.); Schmidt, R.; Gerdes, L.; Zabel, A.; Biermann, D.; Walther, F.: Impact of cutting parameters on the mechanical properties of BTA deep drilled components under quasi-static compression. CIRPe 2021, 9th CIRP Global Web Conference, Web Conference, 26.-28. Oct. (2021).
- Strodick, S. (Sp.); Schmidt, R.; Zabel, A.; Biermann, D.; Walther, F.: Influence of cutting parameters on surface integrity in BTA deep hole drilling of steel components. ICEAF 6, 6th International Conference of Engineering Against Failure, Web Conference, 23.-25. June (2021).

- Strodick, S. (Sp.); Schmidt, R.; Zabel, A.; Biermann, D.; Walther, F.: Micro-magnetic assessment of functional properties in the sub-surface zone of deep drilled AISI 4140 and 304L steels. MSE 2020, Materials Science and Engineering, Web Conference, 22.-25. Sept. (2020).
- Strodick, S. (Sp.); Walther, F.; Schmidt, R.; Zabel, A.; Biermann, D.: Analyse des Eigenspannungszustands in der Bohrungsrandzone tiefgebohrter Probekörper aus 42CrMo4+QT und X5CrNi18-10. Werkstoffprüfung 2019, Neu-Ulm, 03.-04. Dec. (2019).
- Strodick, S. (Sp.); Schmidt, R.; Zabel, A.; Biermann, D.; Walther, F.: Evaluation of surface integrity after BTA deep-hole drilling of AISI 4140 by means of Barkhausen noise analysis. ICBM13, 13th International Conference on Barkhausen Noise and Micromagnetic Testing, Prague, Czech Republic, 23.-26. Sept. (2019).